



Thomas Schmid, B.Eng.

**Development of a crossflow air classifier for validation
experiments in a modular arrangement**

MASTER'S THESIS

to achieve the university degree of

Diplom-Ingenieur

Master's degree programme: Chemical and Process Engineering

submitted to

Graz University of Technology

Supervisor

Ass.Prof. Dipl.- Ing. Dr.techn. Stefan Radl

Institute of Process and Particle Engineering

Graz, July 2016

EIDESSTATTLICHE ERKLÄRUNG

Ich erkläre an Eides statt, dass ich die vorliegende Arbeit selbstständig verfasst, andere als die angegebenen Quellen/Hilfsmittel nicht benutzt, und die den benutzten Quellen wörtlich und inhaltlich entnommenen Stellen als solche kenntlich gemacht habe. Das in TUGRAZonline hochgeladene Textdokument ist mit der vorliegenden Masterarbeit identisch.

AFFIDAVIT

I declare that I have authored this thesis independently, that I have not used other than the declared sources/resources, and that I have explicitly indicated all material which has been quoted either literally or by content from the sources used. The text document uploaded to TUGRAZonline is identical to the present master's thesis dissertation.

04.07.2016

Date

T. Seidl

Signature

Copyright © Thomas Schmid, Graz University of Technology, Institute of Process and Particle Engineering.

All rights reserved. No part of the material protected by this copyright notice may be reproduced or utilized in any form or by any means, electronically or mechanically, including photocopying, recording or by any information storage and retrieval system without written permission from the author.

Abstract

In this thesis a crossflow classifier test stand is developed for research purposes, i.e. to validate jet in crossflow (JICF) simulations, as well as for teaching purposes. Particles are perpendicularly injected into the vertical crossflow by using a pneumatic conveying system. Therefore, a novel brush feeder is designed to meter, disperse, and pre accelerate particles into the conveying system. Experiments have been performed using quartz powder with a size of the grains between 100 and 300 [μm], as well as glass beads with a grain size between 400 and 600 [μm]. Investigations by particle image velocimetry show, that a homogeneous distribution of particles, as well as near steady state conditions can be achieved at the injection point. The modularity of the test stand allows performing many different experiments, which is beneficial for research purposes, as well as for future student lab courses and project work.

Kurzfassung

Gegenstand der vorliegenden Masterarbeit ist die Konstruktion eines Querstromsichters, welcher einerseits zu Forschungszwecken genutzt werden kann, z.B. zur Validierung von Simulationen, in denen Partikel in einen Querstrom injiziert werden (jet in crossflow, JICF). Andererseits soll der Aufbau für die Lehre dienen, d.h. für verschiedene Laborübungen zur Verfügung stehen. Partikel werden mit Hilfe einer pneumatischen Förderung senkrecht in den vertikalen Querstromsichter eingebracht. Teil dieser pneumatischen Förderung ist ein neuartiger Bürstendosierer, welcher eigens zu diesem Zweck konstruiert wurde. Er dient dazu, Pulver zu dosieren, zu dispergieren, und vorbeschleunigt in die Förderleitung abzugeben. Experimente wurden sowohl mit Quarzsand (Korngröße zwischen 100 und 300 Mikrometern) als auch mit Glaskugeln durchgeführt, welche im Größenbereich von 400 bis 600 Mikrometern liegen. Versuche mittels „particle image velocimetry“ (PIV) zeigen, dass im Bereich der Partikelinjektion eine homogene Partikelverteilung über die gesamte Höhe des Förderrohres erreicht wird. Außerdem wird ermittelt, dass hierbei ein annähernd stationärer Zustand erreicht wird. Der Versuchsstand ist in Modulbauweise ausgeführt. Dadurch ergibt sich die Möglichkeit, verschiedene für die Forschung relevante Experimente an ein und demselben Versuchsstand durchzuführen. Ferner können mit Hilfe des Aufbaus unterschiedliche Studentenübungen kreiert werden.

Acknowledgement

First I want to thank Ass. Prof. Stefan Radl for the assignment of the master thesis' topic and for the intensive and encouraging supervision, including technical discussions, helpful advices and organizational support. A further big thank goes to Mr. Hans Grubbauer, who provided his tools from the workshop, manufactured a big part of the test stand and gave me several useful hints on the practical side. For all the perfect organisation regarding e.g. ordering processes a thank goes also to the office team of the institute.

I also want to thank the people around me, who are not directly involved with the thesis but still had a positive influence on the outcome of it. In this context I'd like to mention my good friend Matthias, who introduced me into the Austrian way of life. A special thanks goes thereby to my family, who supported me each morally and financially. At last I want to thank my girlfriend Nora, who always believed in me and encouraged me day for day.

Table of Content

1	Introduction	1
1.1	Goals	3
2	State of the Art.....	4
2.1	Horizontal particle conveying.....	4
2.2	Particle feeders.....	5
3	Basic calculations.....	11
3.1	Settling behaviour of particles	11
3.2	Saltation velocity	13
3.3	Stokes number and Relaxation length	15
3.4	Slip effects	17
3.5	Penetration depth	17
4	Engineering of the crossflow classifier	20
4.1	Specification and conceptual design.....	20
4.2	Basic engineering.....	21
4.3	Detail engineering.....	29
4.4	Possible operating points of the classifier.....	35
5	Engineering of the particle feeding unit.....	37
5.1	Specification and conceptual design.....	37
5.2	Detail engineering.....	43
6	Experimental.....	49
6.1	Crossflow classifier.....	50
6.2	Brush feeder.....	55
6.3	Particle image velocimetry (PIV)	56
7	Results.....	60

7.1	Air mass balance	60
7.2	Particle size analysis	62
7.3	Mass flow rate vs. brush speed	65
7.4	Particle image velocimetry	72
8	Discussion and Conclusion	86
8.1	Feeding unit	86
8.2	Classifier performance	90
9	Outlook	92
10	References	93
Appendix A	98
A.1	Data sheets of purchase parts	98
A.2	Data sheet of glass particles	100
Appendix B	102
B.1	Technical drawings	102
Appendix C	104
C.1	Calculation of settling behaviour of particles in an air counter flow	104
C.2	Calculation of saltation velocity	107
C.3	Calculation of penetration depth of particles into crossflow channel	110
C.4	Calculation of relaxation length in conveying pipe	111
C.5	Calculation of separation efficiency	121
C.6	Mass flow rate vs. brush speed – raw data	122
Appendix D	131
D.1	Mass flow diagrams	131
Appendix E	137
E.1	Temporal velocity distributions measured by PIV	137

E.2 Octave program for temporal velocity analysis	146
E.3 Program add-on for “MatPIV” written by Radl.....	148
Appendix F	150
F.1 QUICPIC report – fine fraction	150
F.2 QUICPIC report – coarse fraction	151
F.3 Octave program for particle size analysis	152

List of Figures

Figure 1-1: Chinese picture of traditional winnowing process [5].....	1
Figure 1-2: Instantaneous fluid velocity distribution of a JICF simulation (u in [m/s]) [10]. ...	2
Figure 2-1: Conveying conditions dependent on pressure gradient and gas velocity [16].	5
Figure 2-2: Principle sketch of an injector feeder [14].	6
Figure 2-3: Principle sketch of a rotary feeder [14].	6
Figure 2-4: Principal sketch of a brush feeder, as used in system RGB 1000 [30].....	8
Figure 2-5: Brush feeder "RODOS" [42].	9
Figure 2-6: Clausthal feeding and dispersing unit [28].	10
Figure 3-1: Settling velocity v_s [m/s] and Reynolds number Re depending on particle diameter d_p [μm] for glass beads with a particle density $\rho_p = 2,700$ [kg/m^3] and air with a gas density of $\rho_g = 1.2$ [kg/m^3].	12
Figure 3-2: Equivalent diameter [μm] and Reynolds number dependent on counter flow velocity w_g [m/s] of spherical glass particles with a density $\rho_p = 2,700$ [kg/m^3] and air with density $\rho_g = 1.2$ [kg/m^3].	13
Figure 4-1: Flowsheet of the crossflow classifier including its additional equipment like a mass flow controller, a particle feeder, a cyclone separator, two particle containers and a fan.	21
Figure 4-2: incoming and outgoing streams of crossflow classifying section in ideal case	22
Figure 4-3: Saltation velocity U_s [m/s] dependent on particle diameter d_p [μm] for a particle mass flow of $\dot{m}_p = 0,072$ [kg/s], a hydraulic pipe diameter of $D_T = 35.5\text{mm}$ and a pipe inner cross section of $A_T = 1456$ [mm^2] resulting in a saltation mass loading of $\mu_s \approx 7.8$ [kg/kg] for the correlation of Matsumoto, and $\mu_s \approx 5.5$ [kg/kg] for the correlation of Rizk.	25
Figure 4-4: Dimensions b (width), h (height) and t (depth) of the crossflow classifier section, showing the inlet- and outlet streams.	25
Figure 4-5: Penetration depth y [m] of particles into crossflow section calculated for three different initial particle velocities $u=5$ [m/s], $u=6$ [m/s] and $u=7$ [m/s] referring to the calculation method by Rudinger [17].	26
Figure 4-6: Cross section and hydraulic diameter of the standardized, rectangular conveying pipe.	27
Figure 4-7: Relaxation length x_e [m] and particle Reynolds number Re of accelerated particles over percentage of particle velocity U_p on gas velocity U_g [%] with superficial gas velocity U_g	

= 5 [m/s] and two different initial particle velocities $U_{p,0,1} = 0$ [m/s] and $U_{p,0,2} = 4$ [m/s] for a particle diameter $d_p = 300$ [μm].	27
Figure 4-8: Relaxation length x_e [m] of accelerated particles over U_p/U_g [%] under three different superficial gas velocities $U_{g,1} = 5$ [m/s], $U_{g,2} = 6$ [m/s] and $U_{g,3} = 7$ [m/s] for two different initial particle velocities $U_{p,0,1} = 0$ (black markers, full) and $U_{p,0,2} = 4$ [m/s] (red markers, blank, the particle diameter is $d_p = 300$ [μm]).	28
Figure 4-9: Relaxation length x_e [m] of accelerated particles over U_p/U_g [%] under three different superficial gas velocities $U_{g,1} = 5$ [m/s], $U_{g,2} = 6$ [m/s] and $U_{g,3} = 7$ [m/s] for two different initial particle velocities $U_{p,0,1} = 0$ (black markers, full) and $U_{p,0,2} = 4$ [m/s] (red markers, blank, the particle diameter is $d_p = 100$ [μm]).	29
Figure 4-10: Crossflow classifier assembly including	31
Figure 4-11: Influence of L/D ratio of square cells in reducing turbulence intensity [54].	33
Figure 4-12: Volumetric flow stream \dot{V}_1 [l/min] depending on the outlet volume stream \dot{V}_4 [l/min], for three exemplary transverse volume streams \dot{V}_3 [l/min].	35
Figure 4-13: Gas velocities U_1 [m/s] at the plant inlet, U_2 [m/s] upstream of the transverse stream inlet, and U_4 [m/s] at the plant outlet depending on the outlet volume stream \dot{V}_4 [l/min] and for two different transverse jet velocities $U_{3,1} = 5.3$ [m/s] and $U_{3,2} = 4$ [m/s].	36
Figure 5-1: Sketch of system A consisting out of a metering hopper, a conveyor belt and a rotating brush; particles are sucked into the conveying line by a ring nozzle.	39
Figure 5-2: Sketch of system A.1 resembling system A, but using two hoppers.	39
Figure 5-3: Sketch of system B as a modified RODOS feeder shown by Kaye [42].	39
Figure 5-4: Sketch of system C consisting out of two hoppers with defined outlet cross section using the simple hour-glass effect.	40
Figure 5-5: Particle mass flow [kg/h] over rotational speed of brush [min^{-1}] [41].	42
Figure 5-6: Interface between hopper and brush feeding unit.	43
Figure 5-7: Powder discharge mechanism of hopper.	44
Figure 5-8: Connection of motor to housing using a bell-shaped housing.	45
Figure 5-9: Rotary shaft seals to separate bearing seat area from powder metering area dust free.	45
Figure 5-10: Brush guiding bars.	46
Figure 5-11: Principle of brush guiding bars to pinch brush to a certain extent: a) zero pinch, b) pinch of $\xi = 4$ [mm], c) pinch of $\xi = 5$ [mm].	46
Figure 5-12: 3D model of feeding channel, see drawing number PC03000000.	47
Figure 5-13: 3D-printed powder chute to adapt a rectangular face to a circular face.	48

Figure 6-1: Glass particles, each 50x magnification, left panel: grain size 100 - 200 [μm], right panel: grain size 400 - 600 [μm].	49
Figure 6-2: Quartz sand particles, grain size 100 - 300 [μm], 50x magnification.	50
Figure 6-3: Experimental set-up in laboratory including MFC, power supply, pneumatic conveying, brush feeder, crossflow classifier section, flexible pipes, cyclone, etc.	51
Figure 6-4: Gas meter connected to classifier air inlet.....	52
Figure 6-5: Classifying experiment for particle size distribution analysis using quartz powder with a particle size between 100 [μm] and 300 [μm], particles accelerated only mechanically by brush operated with at 24 [V].....	53
Figure 6-6: Functional principle of the direct image analysis being the basic concept for QUICPIC [61].	54
Figure 6-7: Experimental setup for investigating mass flow against rotational speed of brush.	55
Figure 6-8: Experimental set-up for PIV image recording.	57
Figure 7-1: Measured volumetric flow rates \dot{V}_1 and \dot{V}_4 for maximal excess air (red and filled markers) and minimal excess air (black and voided markers) dependent on mass flow controller set up \dot{V}_3	60
Figure 7-2: Calculated gas velocities U_2 and U_4 at the corresponding cross sections for maximal excess air (red and filled markers) and for zero excess air (black and voided markers) dependent on transverse gas velocity U_3 generated by mass flow controller.....	61
Figure 7-3: Calculated equivalent diameters $d_{eq,2}$ and $d_{eq,4}$ at the corresponding cross sections for maximal excess air (red and filled markers) and for zero excess air (black and voided markers) dependent on transverse gas velocity U_3 generated by mass flow controller.	61
Figure 7-4: Q_3 distribution of fine and coarse fraction, as a result from QICPIC.	63
Figure 7-5: Probability density distribution of the fines $q_{Fi}(x)$, the coarse material $q_C(x)$ and the feed material $q_F(x)$	63
Figure 7-6: Degree of separation dependent on particle size x [μm].	64
Figure 7-7: Rotational speed of brush n [rpm] dependent on voltage signal U [V] for glass powder sized between 100 and 200 [μm], without using brush guiding bars and for all experiments performed in the first attempt (see Table 21).	65
Figure 7-8: Mass flow of particles \dot{m} [g/s] versus the measured rotational speed of the brush [rpm] (left panel) and versus the voltage signal of the power supply U [V] (right panel) for two different glass beads (i.e., 100 to 200 microns and 400 to 600 microns).....	66

Figure 7-9: Time and number averaged mass flow values $\dot{m}_{averaged}$ [g/s] including their number averaged absolute standard deviations σ versus the applied voltage U [V] for glass beads sized between 100 and 200 [μm] and without brush guiding bars.....	67
Figure 7-10: Time and number averaged mass flow values $\dot{m}_{averaged}$ [g/s] including their number averaged absolute standard deviations σ versus the applied voltage U [V] for glass beads sized between 400 and 600 [μm] and without brush guiding bars.....	67
Figure 7-11: Time and number averaged mass flow values $\dot{m}_{averaged}$ [g/s] including their number averaged absolute standard deviations σ versus the applied voltage U [V] for glass beads sized between 400 and 600 [μm] and with an adjusted brush guide bar pinch of $\zeta = 4$ [mm].....	68
Figure 7-12: Time- and number averaged mass flow values $\dot{m}_{averaged}$ [g/s] including their number averaged absolute standard deviations σ versus the applied voltage U [V] for glass beads sized between 100 and 200 [μm] and with an adjusted brush pinch of $\zeta = 4$ [mm].	69
Figure 7-13: Time- and number averaged mass flow values $\dot{m}_{averaged}$ [g/s] including their number averaged absolute standard deviations σ versus the applied voltage U [V] for glass beads sized between 100 and 200 [μm] and with an adjusted brush pinch of $\zeta = 5$ [mm]	70
Figure 7-14: Time- and number averaged mass flow values $\dot{m}_{averaged}$ [g/s] including their number averaged absolute standard deviations σ versus the applied voltage U [V] for glass beads sized between 400 and 600 [μm] and with an adjusted brush pinch of $\zeta = 5$ [mm].	70
Figure 7-15: High speed image of experiment #1.....	72
Figure 7-16: High speed image of experiment #2.....	73
Figure 7-17: High speed image of experiment #3.....	74
Figure 7-18: High speed image of experiment #4.....	74
Figure 7-19: High speed image of experiment #5.....	75
Figure 7-20: High speed image of experiment #6.....	75
Figure 7-21: High speed image of experiment #7.....	76
Figure 7-22: High speed image of experiment #8.....	76
Figure 7-23: High speed image of experiment #9.....	77
Figure 7-24: Calculated relaxation u_p/U_3 dependent on the relaxation length x_e [m] (left panel) vs. mean particle velocity profile u_p [m/s] measured by PIV and averaged over 2999 picture pairs (right panel) for experiment #1. The colours represent the magnitude of the particle velocity.....	78
Figure 7-25: Calculated relaxation u_p/U_3 dependent on the relaxation length x_e [m] (left panel) vs. mean particle velocity profile u_p [m/s] measured by PIV and averaged over 299 picture pairs	

(right panel) for experiment #2. The colours represent the magnitude of the particle velocity.	79
Figure 7-26: Calculated relaxation u_p/U_3 dependent on the relaxation length x_e [m] (left panel) vs. mean particle velocity profile u_p [m/s] measured by PIV and averaged over 299 picture pairs (right panel) for experiment #3. The colours represent the magnitude of the particle velocity.	80
Figure 7-27: Calculated relaxation u_p/U_3 dependent on the relaxation length x_e [m] (left panel) vs. mean particle velocity profile u_p [m/s] measured by PIV and averaged over 299 picture pairs (right panel) for experiment #4. The colours represent the magnitude of the particle velocity.	81
Figure 7-28: Calculated relaxation u_p/U_3 dependent on the relaxation length x_e [m] (left panel) vs. mean particle velocity profile u_p [m/s] measured by PIV and averaged over 299 picture pairs (right panel) for experiment #5. The colours represent the magnitude of the particle velocity.	81
Figure 7-29: Calculated relaxation u_p/U_3 dependent on the relaxation length x_e [m] (left panel) vs. mean particle velocity profile u_p [m/s] measured by PIV and averaged over 299 picture pairs (right panel) for experiment #6. The colours represent the magnitude of the particle velocity.	82
Figure 7-30: Calculated relaxation u_p/U_3 dependent on the relaxation length x_e [m] (left panel) vs. mean particle velocity profile u_p [m/s] measured by PIV and averaged over 299 picture pairs (right panel) for experiment #7. The colours represent the magnitude of the particle velocity.	83
Figure 7-31: Calculated relaxation u_p/U_3 dependent on the relaxation length x_e [m] (left panel) vs. mean particle velocity profile u_p [m/s] measured by PIV and averaged over 299 picture pairs (right panel) for experiment #8. The colours represent the magnitude of the particle velocity.	84
Figure 7-32: Calculated relaxation u_p/U_3 dependent on the relaxation length x_e [m] (left panel) vs. mean particle velocity profile u_p [m/s] measured by PIV and averaged over 299 picture pairs (right panel) for experiment #9. The colours represent the magnitude of the particle velocity.	84
Figure 7-33: Chosen cluster for temporal velocity trend, exemplary for experiment #1 (left panel) and for experiment #9 (right panel). The colours represent the magnitude of the particle velocity.	85
Figure 8-1: Mass flow rate \dot{m}_s [kg/h] versus rotational speed of the brush n [min ⁻¹] [41].	86

Figure 8-2: Free contact surface between powder and feeding brush.....	87
Figure 8-3: Mass flow rate of particles [mg/min] over time [s] of the particle feeder investigated by Molinder and Wiinikka [37].....	89
Figure 8-4: Correlation of the mean mass flow rate dm/dt [g/s] and the adjusted power supply voltage U [V] (left panel) compared to the correlation between mean mass flow rate [mg/min] and pusher block velocity [mm/h] of the feeder investigated by Molinder and Wiinikka [37].	89
Figure A 1: Mass flow of particles \dot{m} [g/s] versus fed mass m [g] from the hopper. Symbols represent different experimental runs (glass bead diameter: 100 to 200 [μm], without using brush guiding bars).....	131
Figure A 2: Mass flow of particles \dot{m} [g/s] versus fed mass m [g] from the hopper. Symbols represent different experimental runs (glass bead diameter: 400 to 600 [μm], without using brush guiding bars).....	132
Figure A 3: Mass flow of particles \dot{m} [g/s] versus fed mass m [g] from the hopper. Symbols represent different experimental runs (glass bead diameter: 100 to 200 [μm]; brush pinch: $\zeta = 4$ [mm] each side).....	133
Figure A 4: Mass flow of particles \dot{m} [g/s] versus fed mass m [g] from the hopper. Symbols represent different experimental runs (glass bead diameter: 400 to 600 [μm]; brush pinch: $\zeta = 4$ [mm] each side).....	134
Figure A 5: Mass flow of particles \dot{m} [g/s] versus fed mass m [g] from the hopper. Symbols represent different experimental runs (glass bead diameter: 100 to 200 [μm] brush pinch: $\zeta = 5$ [mm] each side).....	135
Figure A 6: Mass flow of particles \dot{m} [g/s] versus fed mass m [g] from the hopper. Symbols represent different experimental runs (glass bead diameter: 400 to 600 [μm] brush pinch: $\zeta = 5$ [mm] each side).....	136
Figure A 7: Temporal velocity distributions in horizontal direction (u_x) and in vertical direction (u_y) for the 20 th row and the 10 th column of the residual matrices of experiment #1, i.e., for 3000 matrices generated for the observation time of 1.5 [s].....	137
Figure A 8: Temporal velocity distributions in horizontal (x) direction (left panel) and in vertical (y) direction (right panel) for the 20 th row and the 10 th column of the residual matrices of experiment #2, i.e., for 300 matrices generated for the observation time of 1.5 [s].	138

Figure A 9: Temporal velocity distributions in horizontal (x) direction (left panel) and in vertical (y) direction (right panel) for the 20 th row and the 10 th column of the residual matrices of experiment #3, i.e., for 300 matrices generated for the observation time of 1.5 [s].	139
Figure A 10: Temporal velocity distributions in horizontal (x) direction (left panel) and in vertical (y) direction (right panel) for the 20 th row and the 10 th column of the residual matrices of experiment #4, i.e., for 300 matrices generated for the observation time of 1.5 [s].	140
Figure A 11: Temporal velocity distributions in horizontal (x) direction (left panel) and in vertical (y) direction (right panel) for the 20 th row and the 10 th column of the residual matrices of experiment #5, i.e., for 300 matrices generated for the observation time of 1.5 [s].	141
Figure A 12: Temporal velocity distributions in horizontal (x) direction (left panel) and in vertical (y) direction (right panel) for the 20 th row and the 10 th column of the residual matrices of experiment #6, i.e., for 300 matrices generated for the observation time of 1.5 [s].	142
Figure A 13: Temporal velocity distributions in horizontal (x) direction (left panel) and in vertical (y) direction (right panel) for the 20 th row and the 10 th column of the residual matrices of experiment #7, i.e., for 300 matrices generated for the observation time of 1.5 [s].	143
Figure A 14: Temporal velocity distributions in horizontal (x) direction (left panel) and in vertical (y) direction (right panel) for the 20 th row and the 10 th column of the residual matrices of experiment #8, i.e., for 300 matrices generated for the observation time of 1.5 [s].	144
Figure A 15: Temporal velocity distributions in horizontal (x) direction (left panel) and in vertical (y) direction (right panel) for the 5 th row and the 25 th column of the residual matrices of experiment #9, i.e., for 300 matrices generated for the observation time of 1.5 [s].	145

List of Tables

Table 1: Characterization of materials used for detail engineering.	23
Table 2: Selection parameter for mass flow controller: requirements against equipment data.	34
Table 3: Priority rating of criteria for benchmarking of several feeding systems.....	40
Table 4: Benchmarking no. one rating all systems referring to the corresponding criteria from "1" (bad fulfilling) to "10" (good filling), the higher the sum of points the more preferable the solution.	41
Table 5: Benchmarking no. two rating all systems referring to the corresponding criteria from "1" (bad fulfilling) to "10" (good filling), the higher the sum of points the more preferable the solution.	41
Table 6: Used powders for experiments.....	49
Table 7: Parameter set up of the brush feeder for particle size distribution experiment.....	54
Table 8: Experimental plan for PIV investigation including used powders, classifier velocities and feeder/ injection settings, pinch configuration see Figure 5-11.	59
Table 9: Masses of classified powder including fine portion f and coarse portion c	62
Table 10: Effective thickness of powder layer δ inside of brush exemplary for different brush speed n [rpm] – mass flow \dot{m} [kg/s] configurations measured for fine glass powder, $100 [\mu\text{m}]$ $\leq d_p \leq 200 [\mu\text{m}]$, and without using brush guiding bars.	88
Table 11: structured list of assemblies and parts out of own construction	102
Table 12: Calculation data sheet for calculating settling velocity v_s [m/s] numerically by using Microsoft Excel solver, dependent on particle diameter d_p [μm], drag coefficient C_d and Reynolds number Re	104
Table 13: Calculation data sheet for calculating the equivalent diameter d_{eq} [μm] of a particle in a counter flow by using Microsoft Excel solver, dependent on counter flow gas velocity v_g [m/s], drag coefficient C_d and Reynolds number.	105
Table 14: Calculation of saltation velocity for a solids mass flow $\dot{m}_p = 0,054$ [kg/s], a hydraulic pipe diameter $D_T = 0,0355$ [m] and a cross section of $A = 0,001456$ [m^2] with air as gaseous phase, referring to the correlation of Rizk [45].	107
Table 15: Calculation of saltation velocity for a solids mass flow $\dot{m}_p = 0,054$ [kg/s], a hydraulic pipe diameter $D_T = 0,0355$ [m] and a cross section of $A = 0,001456$ [m^2] with air as gaseous phase, referring to the correlation of Matsumoto.	108
Table 16: Calculation of penetration depth y [m] for different initial velocities and for different particle diameters d_p	110

Table 17: Calculation of relaxation length x_e [m] dependent on superficial gas velocity $U_g = 5$ [m/s], initial particle velocities $U_{p,0}$ (pre accelerated particles) for a step size of $(U_{p,0,calc,i} - U_{p,calc,i-1}) = 0,1$ [m/s]; the relaxation length from a certain $U_{p,0}$ to a certain percentage of U_g is calculated as the sum of relaxation lengths over the respective steps.....	111
Table 18: Calculation of relaxation length x_e [m] dependent on superficial gas velocity $U_g = 6$ [m/s], initial particle velocities $U_{p,0}$ (pre accelerated particles) for a step size of $(U_{p,0,calc,i} - U_{p,calc,i-1}) = 0,1$ [m/s]; the relaxation length from a certain $U_{p,0}$ to a certain percentage of U_g is calculated as the sum of relaxation lengths over the respective steps.....	114
Table 19: Calculation of relaxation length x_e [m] dependent on superficial gas velocity $U_g = 7$ [m/s], initial particle velocities $U_{p,0}$ (pre accelerated particles) for a step size of $(U_{p,0,calc,i} - U_{p,calc,i-1}) = 0,1$ [m/s]; the relaxation length from a certain $U_{p,0}$ to a certain percentage of U_g is calculated as the sum of relaxation lengths over the respective steps.....	117
Table 20: Calculation of separation efficiency $T(x)$ based on QICPIC results $Q_{3, Fi}(x)$ and $Q_{3, C}(x)$ dependent on given x_3 [μm] and basing on measured masses m_{Fi} of the fines and $m_{F, C}$ of the coarse particle fraction.	121
Table 21: Time averaged mass flow rate of feeder \dot{m} [g/s], rotational speed of brush n [rpm], circumferential speed of brush u_0 [m/s], current consumption of drive motor I [A], electrical power P [W] and estimated mechanical torque M [Nm] dependent on voltage signal of power supply tested with glass powder, sized between 100 to 200 [μm].	122
Table 22: Time averaged mass flow rate of feeder \dot{m} [g/s], rotational speed of brush n [rpm], circumferential speed of brush u_0 [m/s], current consumption of drive motor I [A], electrical power P [W] and estimated mechanical torque M [Nm] dependent on voltage signal of power for glass bead powder sized between 400 to 600 [μm].	125
Table 23: Time averaged mass flow rate of feeder \dot{m} [g/s], current consumption of drive motor I [A], electrical power P [W] dependent on voltage signal of power for glass bead powder sized between 400 to 600 [μm] and a brush guiding bar pinch of 4 [mm] each side.....	126
Table 24: Time averaged mass flow rate of feeder \dot{m} [g/s], current consumption of drive motor I [A], electrical power P [W] dependent on voltage signal of power for glass bead powder sized between 100 to 200 [μm] and a brush guiding bar pinch of 4 [mm] each side.....	127
Table 25: Time averaged mass flow rate of feeder \dot{m} [g/s], current consumption of drive motor I [A], electrical power P [W] dependent on voltage signal of power for glass bead powder sized between 100 to 200 [μm] and a brush guiding bar pinch of 5 [mm] each side.....	127

Table 26: Time averaged mass flow rate of feeder \dot{m} [g/s], current consumption of drive motor I [A], electrical power P [W] dependent on voltage signal of power for glass bead powder sized between 400 to 600 [μm] and a brush guiding bar pinch of 5 [mm] each side.....	128
Table 27: Time- and number averaged mass flow values $\dot{m}_{averaged}$ [g/s] including their number averaged standard deviations σ , absolute and in percent, and the corresponding number of experiments i in relation to the adjusted power supply voltage U [V] for glass powder sized between 100 to 200 [μm] and without using brush guiding bars.	128
Table 28: Time- and number averaged mass flow values $\dot{m}_{averaged}$ [g/s] including their number averaged standard deviations σ , absolute and in percent, and the corresponding number of experiments i in relation to the adjusted power supply voltage U [V] for glass powder sized between 400 to 600 [μm] and without using brush guiding bars.	129
Table 29: Time- and number averaged mass flow values $\dot{m}_{averaged}$ [g/s] including their number averaged standard deviations σ , absolute and in percent, and the corresponding number of experiments i in relation to the adjusted power supply voltage U [V] for glass powder sized between 400 to 600 [μm] and with using brush guiding bar pinch of 4 [mm].	129
Table 30: Time- and number averaged mass flow values $\dot{m}_{averaged}$ [g/s] including their number averaged standard deviations σ , absolute and in percent, and the corresponding number of experiments i in relation to the adjusted power supply voltage U [V] for glass powder sized between 100 to 200 [μm] and with an applied brush pinch of 4 [mm].	130
Table 31: Time- and number averaged mass flow values $\dot{m}_{averaged}$ [g/s] including their number averaged standard deviations σ , absolute and in percent, and the corresponding number of experiments i in relation to the adjusted power supply voltage U [V] for glass powder sized between 100 to 200 [μm] and with an applied brush pinch of 5 [mm].	130
Table 32: Time- and number averaged mass flow values $\dot{m}_{averaged}$ [g/s] including their number averaged standard deviations σ . absolute and in percent. and the corresponding number of experiments i in relation to the adjusted power supply voltage U [V] for glass powder sized between 400 to 600 [μm] and with an applied brush pinch of 5 [mm].	130

Abbreviations

CAD	computer aided design
JICF	jet in crossflow
MFC	mass flow controller
PIV	particle image velocimetry
PSD	particle size distribution
TIG	tungsten inert gas

Nomenclature

Latin Symbols

A_c [m ²]	cross section of conveying pipe
A_p [m ²]	cross section of pipe
b [m]	width of crossflow classifier
b_T [m]	width of conveying pipe
C_d [-]	drag coefficient
d [-]	parameter
d_p^* [m]	critical particle diameter
D_T [m]	tube diameter
F_d [N]	drag force
F_m [N]	gravitational force
Fr [-]	Froude number
Fr_p [-]	Froude number relating to single particle
Fr_s [-]	Froude number at saltation
Fr_{ss} [-]	Froude number relating to superficial gas velocity at saltation
g [ms ⁻²]	gravity
h_T [m]	height of conveying pipe
K_v [-]	flow parameter for valves
l_c [m]	length of conveying pipe
\dot{m}_p [kgs ⁻¹]	particle mass flow rate
p_l [bara]	supply pressure
Re [-]	Reynolds number
Re_p [-]	Reynolds number of particle
Stk [-]	Stokes number
T [K]	absolute temperature

t [m]	depth of crossflow classifier
U_1 [ms^{-1}]	gas velocity at classifier inlet
U_2 [ms^{-1}]	gas velocity below transverse flow inlet
U_3 [ms^{-1}]	gas transverse flow velocity
U_4 [ms^{-1}]	gas velocity above transverse flow inlet
U_g [ms^{-1}]	superficial gas velocity
$U_{g,c}$ [ms^{-1}]	superficial gas velocity in conveying pipe
U_{gs} [ms^{-1}]	saltation velocity
U_p [ms^{-1}]	velocity of particle
u_p [ms^{-1}]	velocity of particle
$U_{p,0}$ [ms^{-1}]	initial velocity of particle
$U_{p,x,0}$ [ms^{-1}]	initial particle velocity in x- direction
$U_{p,y,0}$ [ms^{-1}]	initial particle velocity in y- direction
U_s [ms^{-1}]	saltation velocity
\dot{V}_1 [m^3s^{-1}]	volumetric gas flow rate at classifier inlet
\dot{V}_3 [m^3s^{-1}]	volumetric gas flow rate of transverse flow
\dot{V}_4 [m^3s^{-1}]	volumetric gas flow rate above transverse flow inlet
v_s [ms^{-1}]	settling velocity
w [ms^{-1}]	gas velocity
W_s [kgs^{-1}]	mass flow rate of solids
x [-]	parameter
x [m]	particle diameter
x_e [m]	relaxation length
Y [m]	maximal penetration depth

Greek Symbols

μ [kgkg ⁻¹]	mass loading
μ_{cl} [kgkg ⁻¹]	mass loading in classifier
μ_{pn} [kgkg ⁻¹]	mass loading dependent on Froude number
μ_s [kgkg ⁻¹]	mass loading at saltation
α	constant
η_g [Pas]	gas viscosity
κ	classifier sharpness index
ζ [mm]	brush pinch
ρ_g [kgm ⁻³]	gas density
ρ_n [kgm ⁻³]	gas density
ρ_p [kgm ⁻³]	particle density
σ [-]	standard deviation
τ_f [s]	characteristic time of flow field
τ_v [s]	relaxation time
Φ [-]	drag term

1 Introduction

Air classifiers are used to separate solid particles, which are dispersed in a gaseous phase, into two or more fractions regarding to their size [1]. Klumpar et al. [2] state that classifying can also be done by particle shape, electric and magnetic properties, density and other physical properties of the particles. Furchner and Zampini [3] sum up all relevant physical properties of the particle regarding to air classifying to its settling velocity.

Air classifying has been known since the beginning of agriculture, when people had to separate the grain from its shells. Corn is thrown into the air. While the wind takes the light chaff away the heavy grain falls back on the ground. If the wind was too strong, grain would be taken away with the chaff. If the wind was too weak, the grain would contain more impurities. This prehistoric process is not very effective, as today it is applied only by primitive peoples [4]. In daily life there is a phrase “to separate the wheat from the chaff”, which presumably goes back to the air classifying process.



Figure 1-1: Chinese picture of traditional winnowing process [5]

In modern industry air classifiers come up in the end of the 19th century. Klumpar et al. [2] refer to the so called “Mumford-Moodie” separator, which was patented in 1885 to be one of the first applications of air classification. The patent of Osborne [6] also shows one early air classifier. Over the years more and more classifier geometries and classifying techniques came up. Some of them are shown in the publications of Klumpar et al. [2] and Shapiro and Galperin [7]. Next to the development of new air classifiers, also the description of the general phenomena happening between the gaseous phase and the solid phase has been advanced. These multiphase

flows are defined in the field of fluid dynamics and can nowadays, due to proceeding computer performance, be simulated. One of these flows with a high interest for industrial applications is the so called jet in crossflow (JICF). A transverse jet is injected into a crossflow. Industrial applications are for example the air jet injection in gas turbines for controlling mixture ratios and NO_x concentrations in combustion and for cooling purposes. It is also used for steering missiles and in environmental engineering, when controlling the exhaust gas from industrial chimneys [8,9].

Radl et al. [10] have developed Euler- Lagrange simulations, which allow the efficient simulation of highly loaded gas particle flows. The size distribution of the particles to be used in the simulation can be comparably broad due to numerical schemes that allow a stable integration of the governing equations. These schemes also enable the simulation of highly laden particle jets, which are injected into a crossflow (see Figure 1-2). Unfortunately, a rigorous experimental validation of these simulations was not done so far. Recently, Puttinger et al. [11] performed an experimental investigation of a highly laden particle jet, which is injected into a crossflow using a rather primitive device. The measurement is done by a camera system including an image processing program. Unfortunately, Puttinger et al. [11] did not perform systematic experiments using bi- or polydisperse mixtures of particles that help in validation of Euler-Lagrange simulations of these systems.

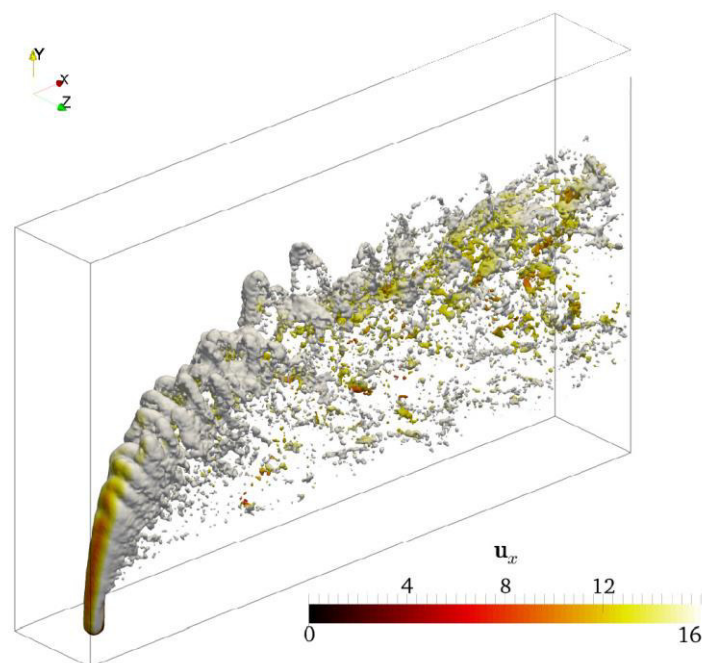


Figure 1-2: Instantaneous fluid velocity distribution of a JICF simulation (u in [m/s]) [10].

1.1 Goals

To validate JICF simulation results based on the method of Radl et al. [10] an experimental crossflow classifier needs to be designed. A transverse particle jet injected into a vertical crossflow classifier has to be realized by a horizontal pneumatic conveying system. Therefore, a conveying concept has to be found and a particle feeder has to be selected and designed. Segregation shall be prevented in the particle injection system, in order to provide time-invariant flow rates of large and small particles. Mass flow of particles and air must be adjustable, as well as the inlet velocity and mass loading of particles into the classifier shall be definable to start simulations at the inlet of the crossflow classifier. Also, there shall be possibilities for further modifications. For that reason, a modular setup is pursued. The classifier has to be started up, JICF experiments have to be performed by recording pictures of the particle bulk motions using a high speed video camera. These data will be fed into an Octave program to extract flow velocity profiles, which are needed for future validations of simulation results with the recorded experimental data.

2 State of the Art

The state of the art reviewed in the following chapter focusses on the conveying and feeding of air as homogeneous phase and solid particles as the dispersed phase. Thus, in the following presentation fluid-to-solid density ratio must be sufficiently small, resulting in large particle Stokes numbers.

2.1 *Horizontal particle conveying*

Depending on the air velocity and the mass loading of particles, different conveying conditions are documented in literature. These depend on particle mass loading and on the fluid velocity [12–16]. For high fluid velocities and low particle concentrations a homogeneous particle distribution appears inside the conveying pipe. In case the fluid velocity is decreased below a certain saltation velocity, particle concentration on the ground of the pipe increases, while its conveying velocity decreases in this area. The saltation is defined as the border between dilute phase conveying and dense phase conveying. The flow is not homogeneous anymore hereby, and is then called a degenerated homogeneous flow [17]. With decreasing velocity dunes appear on the bottom of the conveying pipe. Further decreasing results in slug flow. At the saltation velocity, the necessary pressure gradient for conveying has its minimum as it increases with increasing/ decreasing gas velocity. Wirth [12] describes this saltation point also as a “plugging limit”, because only little disturbances of a conveying condition left of the plugging limit can easily lead to a plugging of the conveying pipe. While conveying in dilute phase appears with a nearly steady-state pressure drop, dense phase conveying is unsteady. This is a reason why small system variations can destabilize the conveying system and lead to plugging of the conveying pipe. Therefore, a minimum gas velocity is required to ensure conveyance. This minimum velocity is defined by Wagner [13], who also defines the plugging limit by a certain mass loading of particles. Wirth [12] recommends not to highly exceed the minimum velocity due to increasing pressure drop, which implicates higher energy demand.

Figure 2-1 shows the pressure drop ΔP normalized over the conveying length L depending on the gas velocity. Starting at a low gas velocity the pressure gradient is rather high resulting in plug flow, i.e., a plug of particles followed by a plug of air is conveyed through the pipe at low velocities [18]. Increasing gas velocity decreases the pressure drop resulting in dune flow. Dunes, comparable to sand dunes in the desert, are moved on the ground of the pipe while dilute particles are fed above with higher velocity. At the saltation point, where the pressure drop is minimal, dunes may disappear. However, little deviations of the fluid mass flow rate or particle

mass loading can lead to dune flow again. A further increase of gas velocity ensures a dilute phase flow, where particles are distributed homogeneously over the pipe inner cross section while the pressure drop rises.

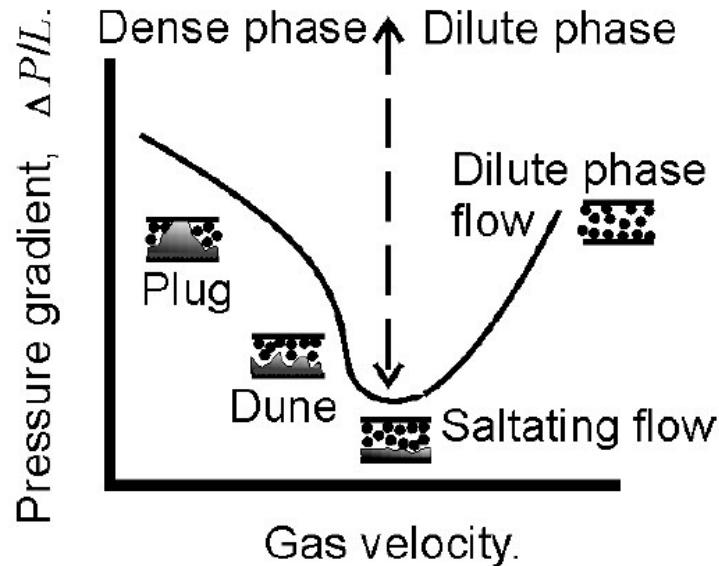


Figure 2-1: Conveying conditions dependent on pressure gradient and gas velocity [16].

There are different concepts to convey particles in an air stream. Couper et al. [19] divide them into a vacuum system, a pressure system and a push-pull system. In the vacuum system particles are sucked into the conveying pipe by vacuum using a suction feeder [14]. There can be one blower and several pickup stations for solids. The pressure system instead can be understood as one source with several destinations. In a push-pull system particles are picked up by a fan (“pull”) and then delivered to several destinations (“push”).

2.2 Particle feeders

Particles are brought into the conveying line by a particle feeder. One simple way of feeding particles into a pipe is that by a pressure vessel, which is described by Hilgraf [14] and Desai [20]. Puttinger et al. [11] use this system for investigations about particles, that are injected into a crossflow. The advantage of this system is its simplicity: there are no rotating parts, therefore no motors, bearings etc. Particles are easily dispersed inside of the conveying pipe. An essential downside of this system is, that the control of the injection velocity of the particles is rather difficult. Also, a long time investigation, i.e., ensuring a constant mass flow of particles and air over time, is a challenge. In short: a pressure vessel can only operate in batch mode. This issue can be improved by a variety of other feeders, such as gravity feeders, screw feeders [14] [21], fluidized bed feeders [22] etc.

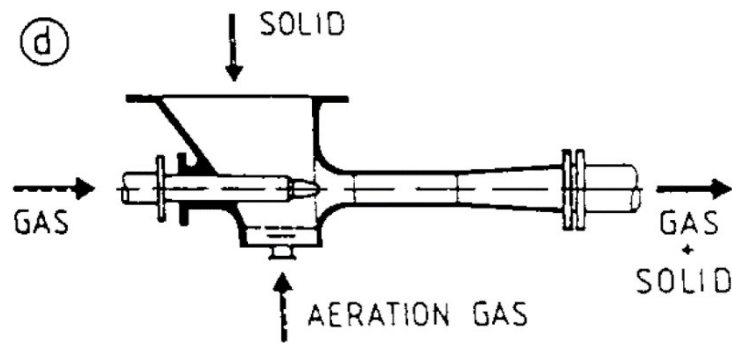


Figure 2-2: Principle sketch of an injector feeder [14].

An interesting feeder concept of a so-called injection feeder is described by Hilgraf [14] (see Figure 2-2) and was investigated by Chellappan and Ramaiyan [23]. Particles are fed from a hopper into a chamber, where they are primarily aerated and secondarily accelerated in the conveying direction. Chellappan and Ramaiyan [23] point out, that the right nozzle position is crucial for a successful feeding operation. Hilgraf [14] and Agarwal [24] show a rotary feeder, see Figure 2-3. A feeder valve including several chambers of certain geometry rotates on an axis perpendicular to the feeding direction. Bulk material moves into the chambers from above by gravity. Latter effect makes it leave the chamber when reaching the rear side at the outlet. The mass flow is controlled by chamber geometry and valve speed.

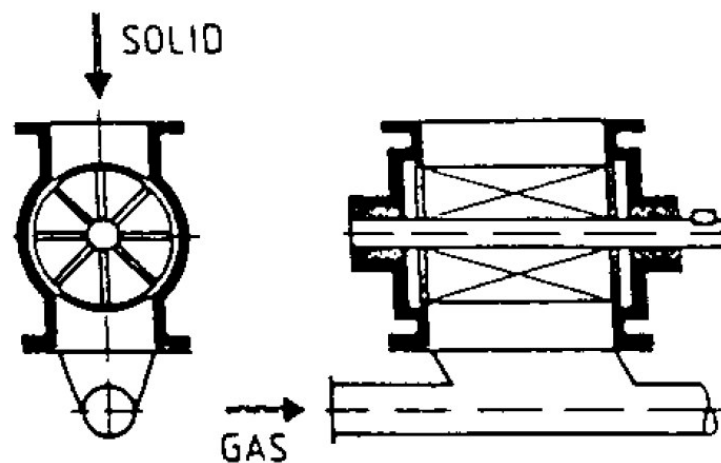


Figure 2-3: Principle sketch of a rotary feeder [14].

The rotary feeder is also called “rotary air lock” [25] due to its ability to seal the hopper upon the rotary feeder against the air flow below. Shock pressures inside the conveying pipe will not influence the particle bed in the hopper. Therefore, there is no need for closing the hopper to its environment for operational safety, i.e. to prevent dust explosions. This is only possible, if there is an interference fit between the rotary valve and the casing. In this area there is the downside

of blocking due to bigger particles which can eventually block the gap between rotary valve and housing. Johnson [26] solves this problem by implementing a flexible wall, that is mounted on a spring: if a big particle (for example a bolt) tries to block the gap between rotary valve and wall, the blocking force moves the wall to clear the way for the bigger particle. If a bulk material is cohesive, a blow through rotary feeder, as described by S.S.T. Schüttguttechnik Maschinenbau GmbH [27], is used. It is directly mounted into the conveying pipe while the axis of the rotary valve is parallel to the middle axis of the conveying line. As a result, particles are not only delivered to the conveying line by gravity, but also by the air stream itself.

A version to the rotary feeder is the so called brush feeder or brush disperser, where the valve of a rotary feeder can be imagined as replaced by a rotating brush [28], which also can produce a constant mass flow. In 1933 Wenzel [29] invented a system of a hopper including a rotating brush at its outlet connected to a blower or fan. The rotating brush is used to meter paper particles, which are scratched by the brush bristles along the casing wall. Therefore, the gap between wall and bristles has to be as small as possible. The gas stream induced by the blower discharges particles from the brush into the conveying line. Brush feeders, as invented by Lins and Verleger [30] and formulated in a VDI rule [31], are also used to feed and disperse fine, i.e. cohesive, powders for generating test aerosols. These are used, e.g., for testing cyclones [32], particle size characterization [33] [34], testing cement quality [35] and many other applications. There are different brush feeder systems: the system of Lins and Verleger [30] consists out of a powder chamber which is arranged below a rotating brush. A piston below the powder pushes the latter in direction of the rotating brush, where the bristles thereof scratch off particles of the powder bed to deliver them into a high velocity gas stream on the opposite side. The gas stream takes the particles out of the brush, see Figure 2-4. The mass flow rate of particles is set up by traverse speed of the piston, dependent on bed density and cross section of the powder chamber [31]. An industrial example for this types of feeders is the RGB 1000 from the company Palas, which operates with particle sizes from 0.1 to 100 microns while producing a mass flow of 0.04 to 430 [g/h], assuming a particle density of 1000 [kg/m³] [36].

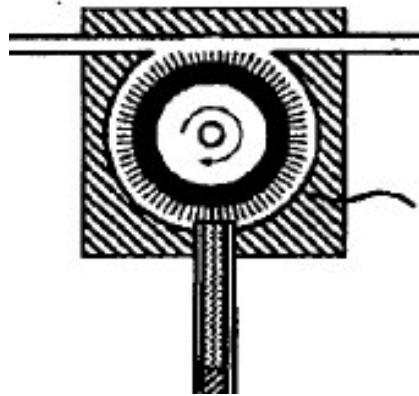


Figure 2-4: Principal sketch of a brush feeder, as used in system RGB 1000 [30].

For this system the VDI rule [31] is valid, which gives a standardized design rule for this type of brush feeder. The mass flow of particles \dot{m}_p is defined by the cross section of the piston A , the traverse speed of the piston v and the bulk density of the powder ρ_p .

$$\dot{m}_p = Av\rho_p \quad 2-1$$

Molinder and Wiinikka [37] also present a feeder, where powder mass flow is dependent on the transverse speed of an equipment device, in their apparatus a pusher block, which is continuously moved upwards by a syringe pump. This pusher block moves up a particle bed, containing biomass particles with a grain size between 75 and 1000 [μm]. The particles are filled inside a glass tube with a particle injection tube in its centre. When the particle bed moves upwards, it reaches continuously the entrance of the injection tube, where the particles are transported by a carrier gas, in their application nitrogen is used. The achieved feed rate of the apparatus is very low at 9.0 to 66.5 [mg/min], which equals 1.5 to 11.1 [10^{-4} g/s]. Similar to the system of Lins and Verleger [30], the feed rate correlates with the velocity of the pusher block.

A different brush feeder concept is presented by Woodruff et al. [38]. A brush rotates inside a hopper with its brush-shaft axis perpendicular to the rotating bottom plate of the hopper. In the centre of the bottom plate a carrier gas inlet is worked. Next to it, i.e., in the region of the outer brush diameter, there is an outlet orifice inside the bottom plate to discharge particles, as well as the carrier gas. Particles are fed into the hopper by a special loading port, which can be sealed hermetically by a loading port stopper, as well as the whole system is sealed with O-rings against gas leakage. All the technical effort is done for metering small biomass particles ($d_p < 150$ [μm]) with a high aspect ratio at steady feed rates, because those can cause interruptions when fed with many customary particle feeders. The maximum feed rate that can be gained is rather low at 2.42 [g/min].

A further method of metering powder material is shown by Leschonski et al. [39,40], where in a first step powder is filled into a rotating notch, where it is compacted to a certain level. A rotating brush delivers the powder from the notch into a pipe, where it is sucked through. In a special device downstream, where particles are forced to bounce on walls in a zigzag shaped piece of pipe, agglomerates are dispersed into their primary particulate components. An industrial example of this type of feeder is a probe dispersing device for certain measuring instrument called RODOS by the company Sympatec. Peters and Stintz [36] sum up its typical operation range to particle sizes bigger than 0.5 microns and mass flow rates between one and 15 [kg/h], referring to a particle density of 1000 [kg/m³].

While in the RODOS system the brush is fed with powder due to the rotational speed of a powder filled notch, powder can also be fed by gravity. This feeder is described in a work of Leschonski et al. [41], see Figure 2-5. A cohesive powder is filled into a flexible hose, whose walls are moved to prevent particles from sticking to the wall. The bristles of a rotating brush scrap off particles from the powder bed and deliver them along the wall of the casing directly into the conveying line, where they are discharged by an air stream. Surprisingly, this type of feeder is also found as the RODOS system in literature, as it is mentioned in the publication of Kaye [42].

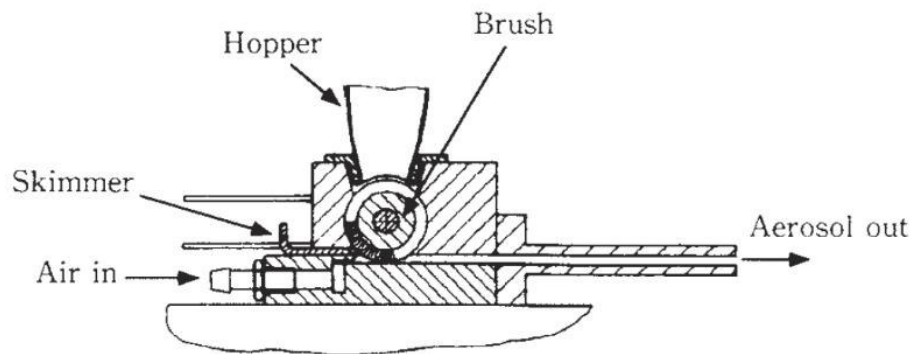


Figure 2-5: Brush feeder "RODOS" [42].

The system is also known as a part of the so called "Clausthal feeding and dispersing unit" by Leschonski [28], see Figure 2-6. The powder is metered and pre dispersed by a rotary brush (1). It enters the voids between the bristles of the brush from a hopper (2) above to be delivered to the feeding point (3). Here it is drawn out of the brush by a high velocity air stream to enter a special injector for further dispersing of the remaining agglomerates.

In this system particle mass flow is dependent on the brush rotating speed and the geometry of hopper outlet and brush. Unfortunately, there is no published design rule for this system, unlike for the system of Lins and Verleger [30] for which such a rule exists.

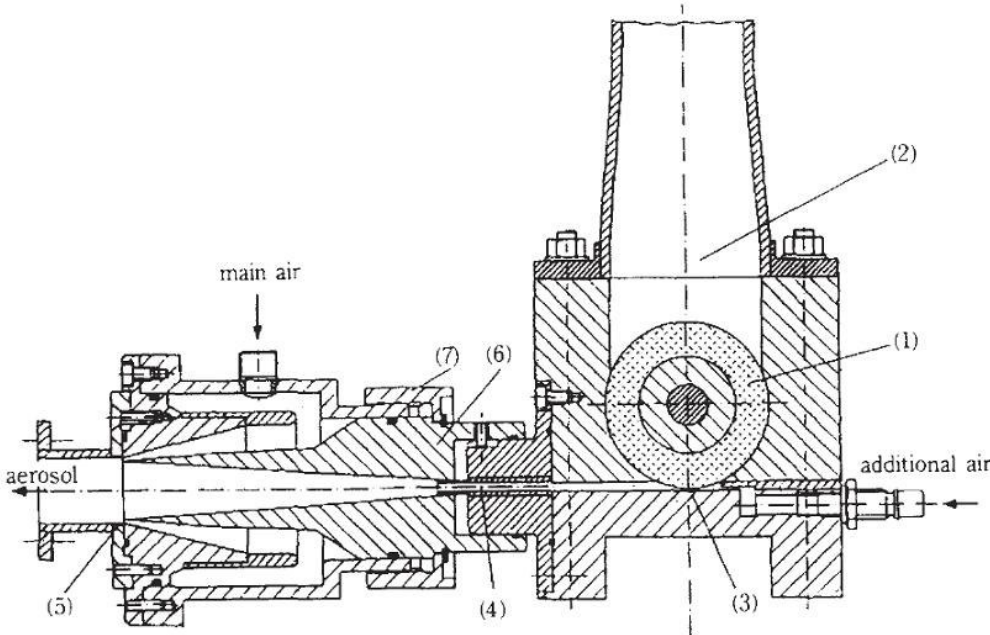


Figure 2-6: Clausthal feeding and dispersing unit [28].

3 Basic calculations

3.1 Settling behaviour of particles

The settling behaviour of spherical shaped particles depends on their density, their diameter and the counter flow velocity w_g . These are calculated by solving the balance of forces acting on a particle which is located in a counter flow. The terminal settling velocity v_s is calculated depending on the particle diameter while the equivalent particle diameter, i.e., where the particle is not moving, is calculated by setting the settling velocity equal to the counter flow velocity. The related equations are given by Furchner and Zampini [3].

$$F_m = \rho_P \frac{\pi}{6} d_P^3 g \quad 3-1$$

$$F_d = c_d \frac{\pi}{4} d_P^2 \frac{\rho_g}{2} v_s^2 \quad 3-2$$

$$v_s = 1.15 \sqrt{\frac{\rho_P d_P g}{\rho_g C_d}} \quad 3-3$$

The gravitational force F_m and the drag force F_d are set equal by ignoring the buoyancy because of the low density of air compared to the particles. It is the force balance for steady state, i.e., the particle does not accelerate. In case the settling velocity of the particle is higher than the gas velocity, the particle sediments downwards against the direction of the gas velocity and vice versa.

In a dilute flow (i.e. particle volume fractions below 1%) the drag coefficient C_d is dependent on the Reynolds number Re , which is dependent on the settling velocity v_s . The settling velocity, respectively, is dependent on the drag coefficient. This mathematical challenge can be solved numerically by using the Microsoft Excel solver, i.e., start values are guessed and their errors are minimized by the least-squares method.

Since the calculated Reynolds number lies in the transition region $1 < Re < 1000$, see equation 3-4, the corresponding drag coefficient C_d is approached by following equation 3-5, Brauer [43].

$$Re = \frac{v_s d_P \rho_g}{\eta_g} \quad 3-4$$

$$C_d = \frac{24}{Re} + \frac{4}{\sqrt{Re}} + 0.4 \quad 3-5$$

Figure 3-1 shows the calculated settling velocity v_s and the corresponding Reynolds number depending on the particle diameter d_p for particle diameters from less than 100 microns up to 500 microns. The settling velocity rises with increasing particle diameter nearly linear while the gradient of the Reynolds number starts in the region of zero rising with increasing particle diameter. A particle with a diameter of 100 microns follows a settling velocity of 0.5 [m/s] (see also Table 12 in the Appendix C), a particle diameter of 300 microns results in 2.2 [m/s] settling velocity.

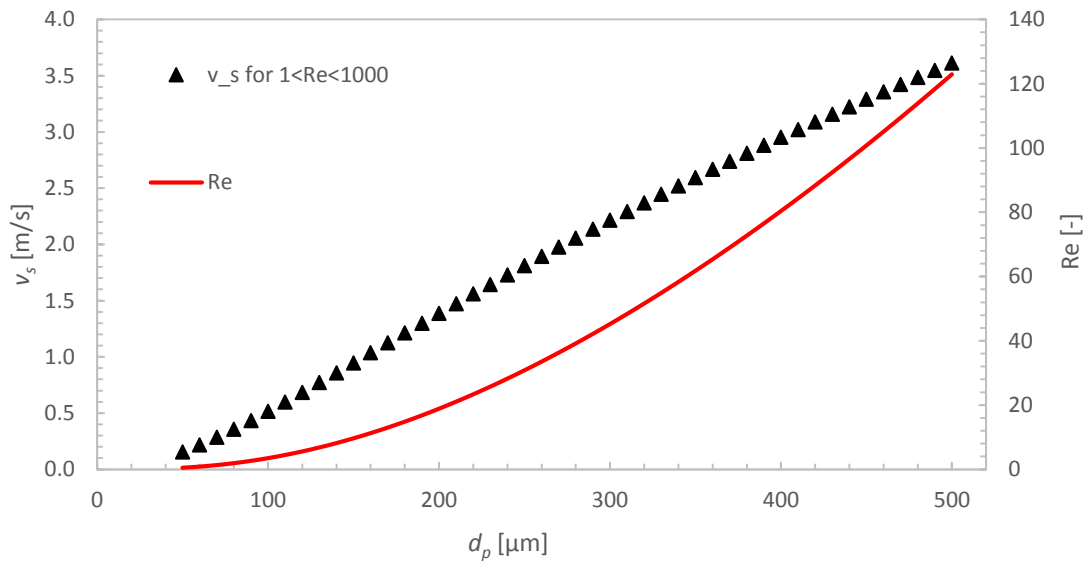


Figure 3-1: Settling velocity v_s [m/s] and Reynolds number Re depending on particle diameter d_p [μm] for glass beads with a particle density $\rho_p = 2,700$ [kg/m³] and air with a gas density of $\rho_g = 1.2$ [kg/m³].

Figure 3-2 shows the calculated equivalent diameter d_p [μm] and the corresponding Reynolds number depending on the counter flow velocity w_g [m/s] for particle diameters from less than 0.5 [m/s] up to 4 [m/s]. The equivalent particle diameter rises within these dimensions under increasing counter flow velocity nearly linear while the gradient of the Reynolds number starts in the region of zero rising with increasing counter flow velocity. A counter flow velocity of 0.5 [m/s] results in an equivalent particle diameter of ca. 100 microns (see also Table 13 in the Appendix C), a counter flow velocity of e.g. 2.2 [m/s] gives an equivalent diameter of 300 microns, respectively. Thus, both calculations, for the settling velocity and for the equivalent particle diameter, are consistent.

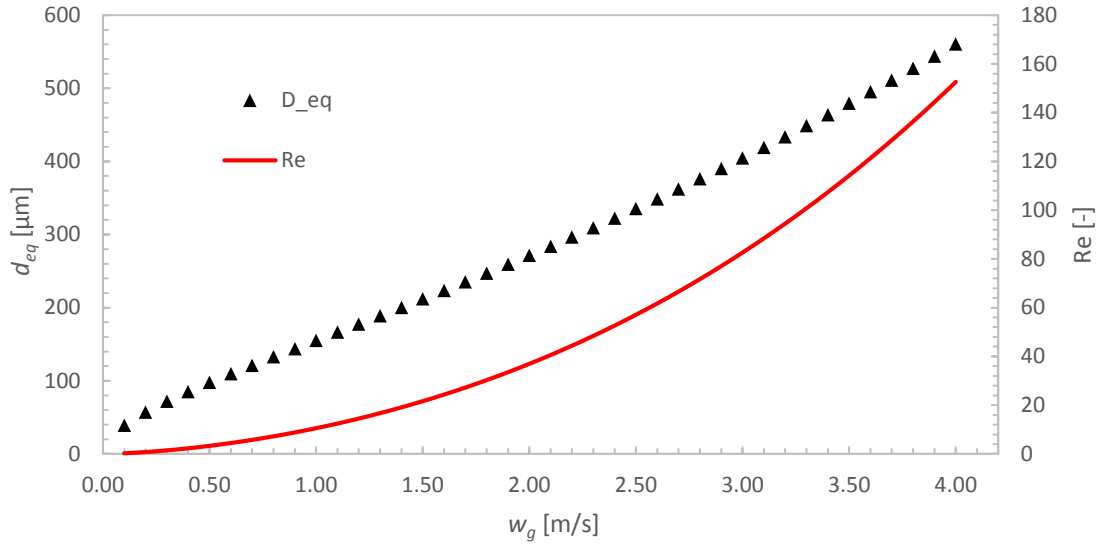


Figure 3-2: Equivalent diameter [μm] and Reynolds number dependent on counter flow velocity w_g [m/s] of spherical glass particles with a density $\rho_p = 2,700$ [kg/m^3] and air with density $\rho_g = 1.2$ [kg/m^3].

3.2 Saltation velocity

Dhodapkar and Jakob [44] suggest two correlations for calculating the saltation velocity, which represents the border between dense phase and dilute phase conveying. The saltation velocity marks the minimum conveying pressure depending on the average superficial gas velocity in conveying line or the maximum mass flow rate of particles at a certain conveying pressure, respectively. The correlation of Rizk [45] describes the saltation point by equating the mass loading of particles μ_s at saltation with the Froude number Fr at saltation adding two parameters d_R and x_R , where d_p has to be written in SI unit [m]. Dhodapkar and Jakob [44], as well as Holdich [16] propose analytical solutions for the correlation of Rizk, which can also be solved numerically by using the Microsoft Excel solver. The equation of Rizk [45] is

$$\mu_s = \frac{1}{10d_R} Fr_s^{x_R} \quad 3-6$$

with

$$d_R = 1440 \frac{d_p}{[m]} + 1.96 \quad 3-7$$

$$x_R = 1100 \frac{d_p}{[m]} + 2.5 \quad 3-8$$

while the mass loading μ is defined as

$$\mu = \frac{\dot{m}_{particles}}{\dot{m}_{air}} \quad 3-9$$

$$\mu_s = \frac{W_s}{\rho_f U_s A} \quad 3-10$$

with W_s being the mass flow rate of solids, ρ_f being the gas density and A being the cross section of the pipe. The Froude number at saltation is defined by the saltation velocity U_s and the diameter of the tube D_T .

$$Fr_s = \frac{U_s}{\sqrt{gD_T}} \quad 3-11$$

The correlation of Matsumoto et al. [46] takes also the dependency of the saltation velocity to the particle size and its density into account: the saltation velocity decreases with increasing particle diameter to a critical particle diameter d_p^* . Further increasing of particle size will cause an increase in saltation velocity. The critical diameter d_p^* is dependent on the gas and particle densities and is, according to Dhodapkar and Jakob [44], calculated as follows

$$\frac{d_p^*}{D_T} = 1.39 \left(\frac{\rho_p}{\rho_f} \right)^{-0.74} \quad 3-12$$

For $d_p \leq d_p^*$ the mass loading at saltation, μ_s , is calculated with two different Froude numbers Fr_p and Fr_{ss} . While Fr_p refers to the single particle terminal velocity U_t and the particle diameter d_p , Fr_{ss} relates to the superficial velocity at saltation conditions U_{gs} and the conveying pipe diameter D_T . [44]

$$\mu_s = 0.373 \left(\frac{\rho_p}{\rho_f} \right)^{1.06} \left(\frac{Fr_p}{10} \right)^{-3.7} \left(\frac{Fr_{ss}}{10} \right)^{3.61} \quad 3-13$$

$$Fr_p = \frac{v_s}{\sqrt{gd_p}} \quad 3-14$$

$$Fr_{ss} = \frac{U_{gs}}{\sqrt{gD_T}} \quad 3-15$$

For $d_p < d_p^*$:

$$\mu_s = 55 \left(\frac{d_p}{D_T} \right)^{1.43} \left(\frac{Fr_{ss}}{10} \right)^{4.0} \quad 3-16$$

Dhodapkar and Jakob [44] suggest a guideline for when to use the correlation of Rizk [45] or the one of Matsumoto et al. [46]. Hence for coarse particles, i.e., particles bigger than 500 microns, and a particle specific gravity of less than 3 the Rizk correlation should be used. If the

specific gravity was greater than 3 or if particles were smaller than 500 microns, the Matsumoto correlation is the right choice.

Gomes and Mesquita [47] investigate several correlations for the saltation velocity including the ones by Rizk and Matsumoto. They find the correlation of Rizk to be best for fine particles, which is in their definition for particles smaller than 200 microns. For coarse particles both above mentioned correlations give acceptable results for pipe diameters ranging between 25 to 200 [mm].

A rather simple ansatz is used by Wirth [48], who proposes the minimum gas velocity in pneumatic horizontal conveying to be at least double the settling velocity of coarse and medium fine particles. Wagner [13] suggests to keep the minimal gas velocity near the plugging limit to increase the conveying efficiency. He describes the mass loading dependent on the Froude number:

$$\mu_{pn} = \frac{2.58}{10^5} Fr^4 \quad 3-17$$

The minimal velocity referring to Wagner [13] is then defined as

$$w > 1.4 \sqrt{D_T^4 \mu_{pn}} \quad 3-18$$

3.3 Stokes number and Relaxation length

The Stokes number Stk characterizes the ability of a particle to react on velocity changes of its surrounding fluid, i.e. to converge its velocity to the fluids velocity. The lower the Stokes number, i.e. if $Stk \ll 1$, the easier above mentioned conversion will be and vice versa. The Stokes number is defined as the relaxation time (i.e., momentum response time τ_v) divided by a characteristic time of the flow field τ_f , see Crowe [49].

$$Stk = \frac{\tau_v}{\tau_f} \quad 3-19$$

with

$$\tau_v = \frac{\rho_p d^2}{18\eta_g} \quad 3-20$$

$$\tau_f = \frac{D_T}{U_g} \quad 3-21$$

Puttinger et al. [11] use a different correlation for predicting the relaxation time τ_v : the Reynolds number changes during the acceleration phase of a particle in a flow field due to the changing

relative velocity. This effect is respected in the equation of Zaichik et al. [50] as it extends the equation for the relaxation time of Crowe et al. [49] by a Reynolds number dependent term, i.e., the drag function:

$$Re_p = \frac{\rho_f d_p (U_g - U_p)}{\eta_g} \quad 3-22$$

$$\tau_v = \frac{\rho_p d_p^2}{18\eta_g \phi(Re_p)} \quad 3-23$$

$$\phi(Re_p) = \begin{cases} 1 + 0.15 Re_p^{0.687} & \text{for } Re_p \leq 10^3 \\ 0.11 \frac{Re_p}{6} & \text{for } Re_p \geq 10^3 \end{cases} \quad 3-24$$

The relaxation length is equal to the path a particle moves when accelerated by a surrounding fluid until it reaches the fluid velocity. Rudinger [17] provides the equations of motion for a particle in an arbitrary flow. As gravitational influences can be neglected, the time derivative of the particle velocity U_p dependent of the velocity of the surrounding gas $u(t)$ and the relaxation time τ_v reads

$$\frac{dU_p}{dt} = \frac{u(t) - U_p}{\tau_v} \quad 3-25$$

The solution of above differential equation for a particle initially at rest reads:

$$U_p = \exp\left(-\frac{t}{\tau_v}\right) \frac{1}{\tau_v} \int_0^t u(t') \exp\left(\frac{t'}{\tau_v}\right) dt' \quad 3-26$$

In case the surrounding gas velocity U_g is constant, the above solution simplifies to the following expression:

$$U_p = U_g \left[1 - \exp\left(\frac{-t}{\tau_v}\right)\right] \quad 3-27$$

To calculate the relaxation length of a particle, Rudinger [17] also derives a form, where particle velocity is expressed as a function of space:

$$U_p \frac{dU_p}{dx} = \frac{U_g - U_p}{\tau_v} \quad 3-28$$

Above equation can be solved by a simple ansatz:

$$\int_{U_{p,0}}^{U_{p,e}} \frac{U_p}{U_g - U_p} dU_p = \int_{x=0}^{x_e} \frac{dx}{\tau_v} \quad 3-29$$

The integration of above shown equation results in the analytical solution for x_e :

$$x_e = \tau_v [U_g \cdot \ln|U_{p,0} - U_g| + U_{p,0} - U_g \cdot \ln|U_{p,e} - U_g| - U_{p,e}] \quad 3-30$$

3.4 Slip effects

Above calculated relaxation lengths do not take into account so-called “slip effects” between particles and the surrounding fluid. Thus, the velocity of particles u_p within a horizontal conveying system will always be smaller than the superficial gas velocity U_g , see Agarwal [51]. In literature, the ratio between u_p and U_g is often defined as the slip ratio, e.g. in Narayan and Prakash [52]. While Agarwal [51] suggests the slip ratio to be ca. 0.8 for coarse particles and ca. 0.9 for fine particles, Narayan and Prakash [52] as well as Holdich [16] give different approximations for the slip ratio. While the ratio u_p/U_g presented by Holdich is the maximal possible particle velocity, based on its surrounding superficial gas velocity, Narayan and Prakash define the ratio $(U_g - u_p)/U_g$ as the difference between the particle and its superficial gas velocity, based on the superficial gas velocity. The following equations calculate the maximum particle velocity based on its superficial gas velocity, using the correlations by both above mentioned authors.

Holdich [16]:

$$u_p = U_g (1 - 0.0638x^{0.3} \sqrt{\rho_s}) \quad 3-31$$

Narayan and Prakash [52]:

$$u_p = U_g - U_g \left[6 \cdot 10^{-3} \left(\frac{\rho_s}{\rho_f} \right)^{0.5} \left(\frac{d_p^3 \rho_f^2 g}{\eta_g^2} \right)^{0.1} \right] \quad 3-32$$

3.5 Penetration depth

The penetration depth of a jet in crossflow (JICF) is dependent on the jet velocity, the crossflow velocity, and the flow arrangement relative to the direction of gravity. To simplify calculations, swarm effects of different sized particles are neglected in a first step. As a result, only one single particle entering a crossflow at a certain initial velocity $U_{p,0}$ is investigated. Also, the influence of the gas jet conveying the particle is here disregarded. Thus, the penetration depth can be

calculated as suggested by Rudinger [17]. Based on that, U_g is the vertical upwards crossflow velocity and $U_{p,x}$ is the horizontal velocity of the particle, $U_{p,y}$ the vertical, respectively. The drag function is here defined based on a correlation by Klyachko, see in [17]. The equations of motion of the particles as well as the applied drag function read as follows:

$$f(Re) = 1 + \frac{1}{6} Re^{\frac{2}{3}} \quad 3-33$$

$$\frac{dU_{p,y}}{dt} = \frac{(U_g - U_{p,y})f(Re)}{\tau_v} \quad 3-34$$

$$\frac{dU_{p,x}}{dt} = -\frac{U_{p,x}f(Re)}{\tau_v} \quad 3-35$$

In a next step, Rudinger [17] combines above equations of motion:

$$\frac{dU_{p,y}}{dU_{p,x}} = -\frac{(U_g - U_{p,y})}{U_{p,x}} \quad 3-36$$

Its integration by Rudinger [17] leads to:

$$U_g - U_{p,y} = \frac{(U_g - U_{p,y,0})U_{p,x}}{U_{p,x,0}} \quad 3-37$$

The Reynolds number based on the averaged particle velocity in both directions reads:

$$Re = \frac{\rho_g d_p}{\eta_g} \sqrt{(U_g - U_{p,y})^2 + U_{p,x}^2} \quad 3-38$$

Rudinger then combines the equation 3-33 for the drag function with the equations 3-35 to 3-38 and finds therefore the local derivation of the horizontal velocity $U_{p,x}$ dependent on a constant α . In case of Stokes drag, i.e., $Re \ll 1$, α is zero, as the second summand of the drag function represents the first factor of α . There, the Reynolds number is calculated for the initial particle velocity being perpendicular to the gas stream.

$$\frac{dU_{p,x}}{dx} = -\frac{1 + \alpha \left(\frac{U_{p,x}}{U_{p,x,0}} \right)^{\frac{2}{3}}}{\tau_v} \quad 3-39$$

$$\alpha = \frac{1}{6} \left(\frac{\rho_g d_p U_{p,x,0}}{\eta_g} \right)^{2/3} \left[1 + \left(\frac{U_g - U_{p,y,0}}{U_{p,x,0}} \right)^2 \right]^{1/3} \quad 3-40$$

In a next step, Rudinger integrates equation 3-39 by adding another variable Z . By setting Z to zero and defining $F(\alpha)$ as a function of α the calculation of the maximum penetration depth Y is simplified:

$$Z = \left(\frac{U_{p,x}}{U_{p,x,0}} \right)^{\frac{1}{3}} \quad 3-41$$

$$y = \tau_v U_{p,x,0} \frac{3}{\alpha} \left[1 - Z + \frac{\tan^{-1} \alpha^{\frac{1}{2}} Z}{\alpha^{\frac{1}{2}}} - \frac{\tan^{-1} \alpha^{\frac{1}{2}}}{\alpha^{\frac{1}{2}}} \right] \quad 3-42$$

$$Y = \tau_v U_{p,x,0} F(\alpha) \quad 3-43$$

$$F(\alpha) = \frac{3}{\alpha} \left(1 - \frac{\tan^{-1} \alpha^{1/2}}{\alpha^{1/2}} \right) \quad 3-44$$

4 Engineering of the crossflow classifier

4.1 *Specification and conceptual design*

To validate simulation results, e.g., the recirculation behind an injection point, or the separation efficiency, several boundary conditions must be set. On the one hand the vertical streaming air flow inside the crossflow classifier must be under well-defined fluid flow conditions and its fluid flow velocity must be controlled. Similar conditions have to be guaranteed for the transverse injection air stream. Also, the air and particle velocities at the particle inlet into the crossflow classifier must be controlled. Therefore, particles shall be nearly fully relaxed to their surrounding air atmosphere. Next to their velocity also the mass flow of particles and air at the inlet has to be known. This can only be done, if the particle size distribution is given. A simple way to solve this problem is using a bi-disperse powder. All particles have to be from the same material and shall have an identical shape. The minimum particle diameter is set to 100 microns, while the maximum diameter should not be larger than 1.5 [mm]. Another challenge is, that all particles shall be well mixed until they enter the crossflow classifier, i.e. segregation in the conveying system must be avoided. A further requirement is that the injection has to be perpendicular to the vertical crossflow classifier channel. To validate simulated particle trajectories, the latter have to be recorded during the physical experiment. This can be done by an optical measurement using a high speed camera system, e.g., as done by Yan and Rinoshika [53]. The latter observe particulate motions while horizontal conveying in a transparent pipeline.

Finally, the desired maximum mass loading of particles in the observation region should be up to $\mu = 3$ [kg particles/ kg air] in order to reflect industrially-relevant conditions.

4.2 Basic engineering

Figure 4-1 shows the basic flowsheet of the plant. A mass flow controller (MFC) provides a continuous and exact mass flow of secondary air in the conveying pipe. This mass flow is used to adjust the jet air velocity. Particles are metered into the conveying pipeline by a feeder. Particles and secondary air shall enter the crossflow classifier under certain conditions referring to their velocity and mass flow.

Air is sucked through the crossflow classifier via a fan located at the outlet of the system, and which is positioned after a cyclone. The air stream shall take the small fraction out, while the heavy fraction shall be energetic enough to leave the classifier channel by a side stream, which is an open channel in a certain position of the right classifier wall. Air and light fraction enter the cyclone, where the light fraction shall be separated completely.

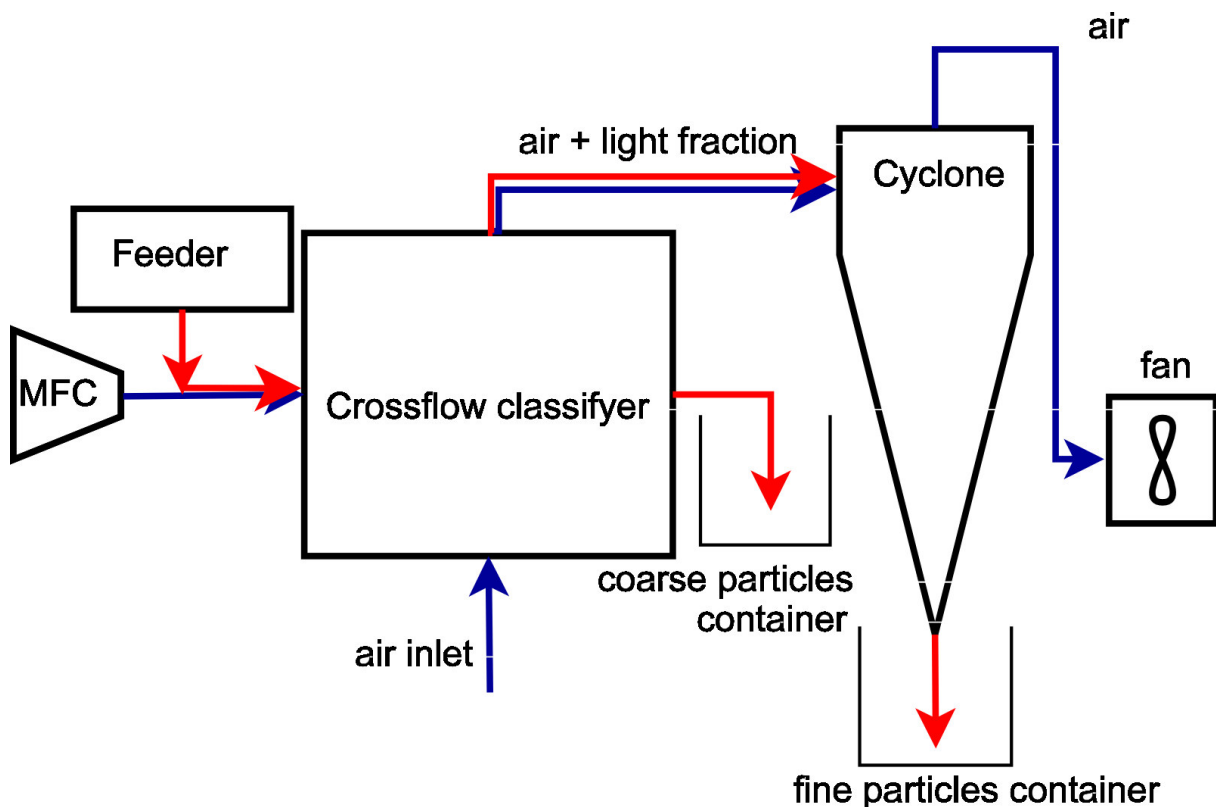


Figure 4-1: Flowsheet of the crossflow classifier including its additional equipment like a mass flow controller, a particle feeder, a cyclone separator, two particle containers and a fan.

4.2.1 Mass balance

The mass balance is performed around the crossflow classifying section. Incoming streams are on the one hand (i) the classifying air from the bottom and on the other hand (ii) the air / particle jet from the pneumatic conveying line. Outgoing streams are (i) the heavy fraction of particles, which is collected in a side bunker, and (ii) the air / fine particles stream that leaves the

classifying section on its top to be sent to the cyclone. Some of the coarse particles might not enter the side bunker. Therefore, another bunker has to be implemented on the bottom of the classifier. Figure 4-2 shows the outgoing and incoming streams of the crossflow classifying section for the ideal case, i.e. all coarse particles move into the side bunker and all fines are drawn out of the validation region with the main air stream.

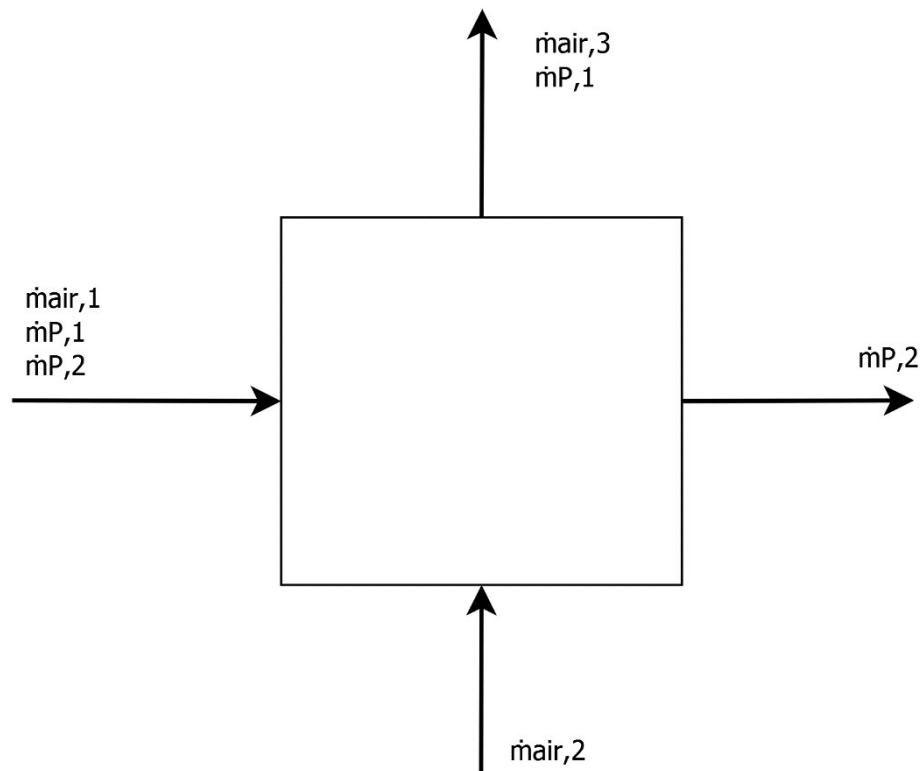


Figure 4-2: incoming and outgoing streams of crossflow classifying section in ideal case

4.2.2 Basic design aspects

As required, the crossflow air stream shall be as straight as possible. This can be realized by implementing a honey comb shaped flow straightener directly after the air inlet at the bottom of the classifier. This flow straightener should also provide a certain amount of pressure drop to keep the flow homogeneously distributed over the channel cross section. Latter can also be established by a perpendicular inlet of the air to the classifier with a rather wide cross section. This will keep on the one hand the air velocity low, and on the other hand the direction change produces a certain amount of pressure drop.

The overall cross section of the classifier should be chosen to be as small as possible to keep the mass flow rate of air small. The cross section of the pneumatic conveying line has to be defined with care. While a wide cross section causes a high amount of air needed to keep an

appropriate air velocity, a narrow cross section causes an increase of mass loading inside of the pipe, which can cause saltation.

Since there is an existing zigzag sifter test stand which will be replaced by this new experimental set up, some parts of it can be reused. There is a cyclone and a fan, the flow rate through latter is controlled by a simple valve that defines a leak air stream. To easily assembly all parts, the air / fines outlet diameter should be connected to the cyclone. The existing fan must provide enough power to produce the desired mass flow rate of air. The air mass flow rate in the pneumatic conveying pipe is set up by a mass flow controller (MFC) which is fed by the laboratory's air pressure system.

The bulk material will be test powders consisting of almost ideally spherical shaped glass beads. These should be of a particle size bigger than 100 microns. Thus, the powder can be considered as free flowing, which (i) makes the design of the feeding unit easier, and (ii) results in easier modelling problem since cohesive forces can be neglected. The parameters of powder and gas used for the apparatus engineering are shown in Table 1.

Table 1: Characterization of materials used for detail engineering.

parameter	property / value
bulk material	glass
sphericity Ψ	1
particle diameter d_p [μm]	$100 \leq d_p \leq 500$
solid density ρ_p [kg/m^3]	2,700
gas phase	air
gas density ρ_g [kg/m^3]	1.2
gas viscosity η_g [10^{-5} Pas]	1.9

4.2.3 Dimensions

The dimensions of the apparatus depend highly on the used particles and their behaviour.

Critical parameters concerning the conveying of the particles are the cross section of the conveying pipe A_c and its length l_c , the gas velocity inside of the tube $U_{g,c}$, the mass flow rate of particles \dot{m}_p and the particles' diameter. The mass flow of particles is dependent on the mass flow of gas \dot{m}_g to fulfil a certain mass loading μ_c . To keep particles airborne, i.e., to maintain dilute phase conveying, a certain minimum gas velocity, i.e. the saltation velocity $U_{g,s}$, is needed. The saltation velocity influences the mass flow of particles \dot{m}_p by having influence on the mass flow of gas $\dot{m}_{g,c}$. Also, the saltation velocity $U_{g,s}$ is influenced by the mass loading μ_c ,

which is further affected by the cross section of the conveying pipe. The mass loading μ_c inside of the conveying pipe is furthermore affected by the mass loading μ_{cl} inside of the classifier, which shall be between 0 and 3 [kg/kg]. This mass loading μ_{cl} inside the classifier section is dependent on its cross section, which itself is affected by the penetration depth of the small fraction of particles, as these shall not touch the opposite wall to the particle entry.

All these each other influencing parameters are arranged by building up a Microsoft Excel sheet varying input parameters to get a feeling for which parameters influence which geometry in what way.

Other factors that have to be considered are constructional limitations. It has to be considered, which theoretical geometrical structure can be realized in an economical way. Basic geometries, like measures for certain construction profiles, have to be taken into account.

Figure 4-3 shows the calculation of the saltation velocity U_s [m] dependent on the particle diameter for particles from 100 microns up to 500 microns for the correlations of Rizk and Matsumoto. The saltation velocity calculated with the first correlation stays almost constant for different particle diameters. The Matsumoto correlation shows a typical behaviour: the saltation velocity decreases with rising particle diameter until a critical diameter, in this case around 200 microns. A further increase of the particle diameter leads then to an increase of saltation velocity. Since Dhodapkar and Jakob [44] recommend the Matsumoto correlation for particles smaller than 500 microns, the saltation velocity should be between 5.5 and 7 [m/s].

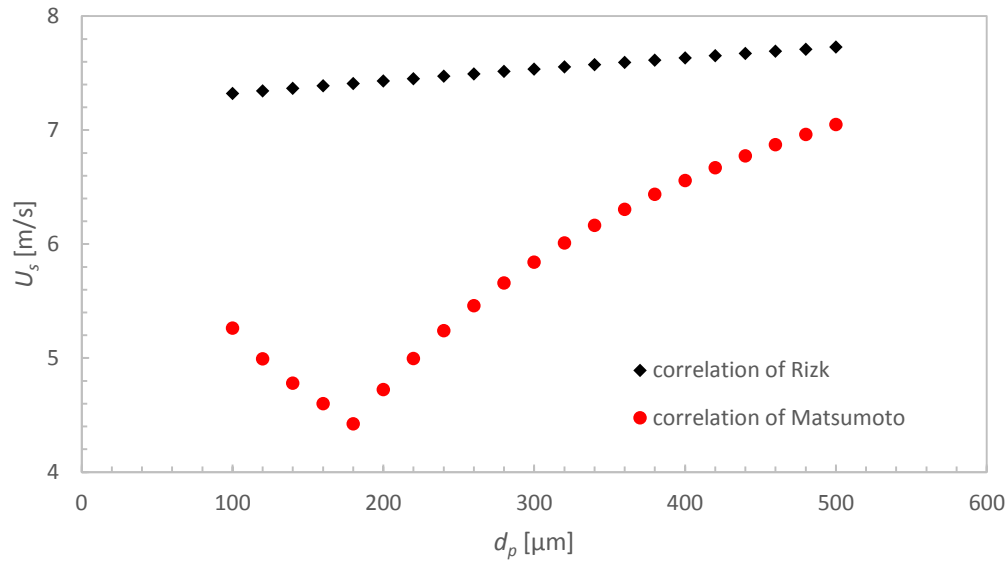


Figure 4-3: Saltation velocity U_s [m/s] dependent on particle diameter d_p [μm] for a particle mass flow of $\dot{m}_p = 0,072$ [kg/s], a hydraulic pipe diameter of $D_T = 35.5\text{mm}$ and a pipe inner cross section of $A_T = 1456$ [mm^2] resulting in a saltation mass loading of $\mu_s \approx 7.8$ [kg/kg] for the correlation of Matsumoto, and $\mu_s \approx 5.5$ [kg/kg] for the correlation of Rizk.

Having an idea of a realistic minimum velocity inside of the conveying tube, the penetration depth of particles into the crossflow classifier section can be calculated for different particle diameters, as shown in Figure 4-5. The penetration depth of the light fraction limits the minimum width b [m] of the crossflow classifier as it shall not enter the side channel to the coarse particles' container (see Figure 4-4). Particle-wall interactions, on the other hand, can immediately decrease the particle's velocity to separate it downwards into the coarse particle container at the bottom of the classifier system.

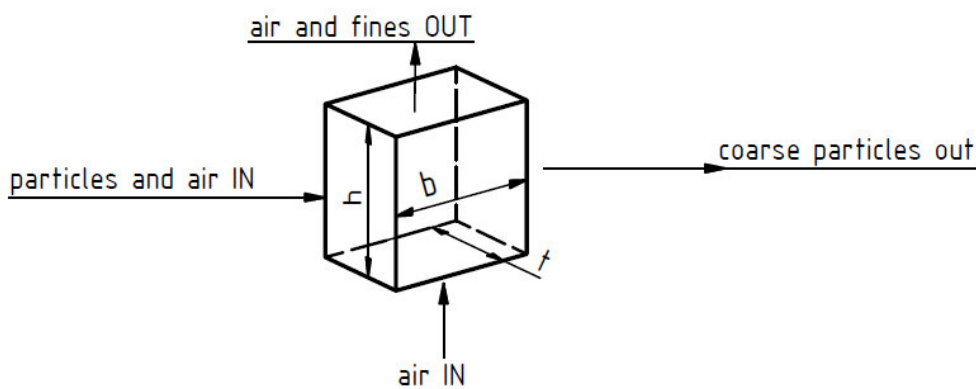


Figure 4-4: Dimensions b (width), h (height) and t (depth) of the crossflow classifier section, showing the inlet- and outlet streams.

Figure 4-5 illustrates, that particles of a diameter of 100 microns with the suggested initial velocities u [m/s] will penetrate less than 300 [mm] into the crossflow channel. Therefore, the width b for the crossflow channel is set to 300 [mm].

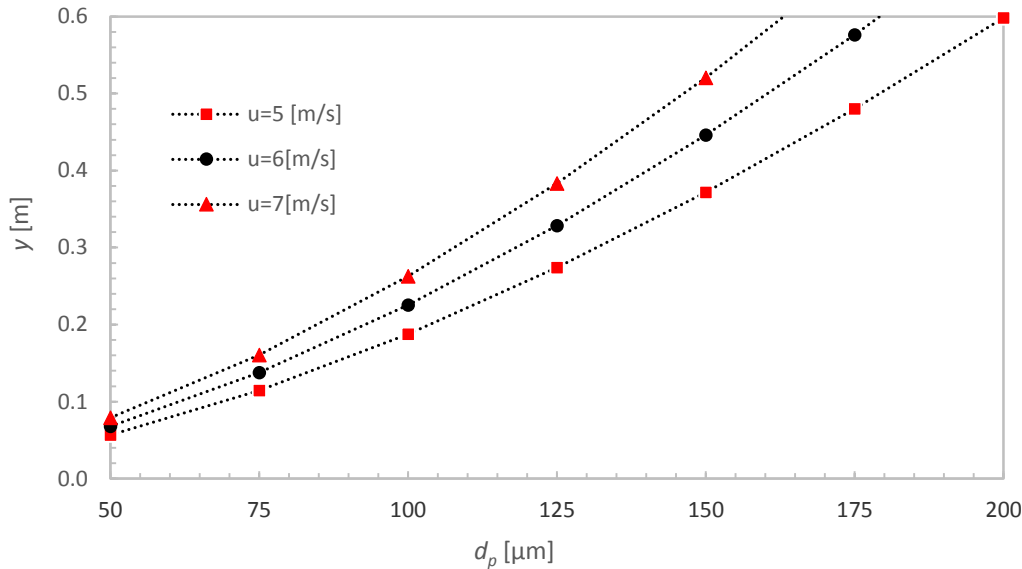


Figure 4-5: Penetration depth y [m] of particles into crossflow section calculated for three different initial particle velocities $u=5$ [m/s], $u=6$ [m/s] and $u=7$ [m/s] referring to the calculation method by Rudinger [17].

As the width b of the crossflow classifier is comparably wide, the depth t has to be kept as narrow as possible to keep the required mass flow of air in a technically feasible range. Another limit concerning the depth t of the classifier is the cross section A_c of the conveying pipe. The latter shall not be too small, as it increases the particle mass loading μ_c inside of the pipe, which causes an increase in saltation velocity U_{gs} . A satisfying compromise is found by setting the depth $t = 28$ [mm] and by using a rectangular pipe of inner width $b_T = 26$ [mm] and inner height $h_T = 56$ [mm] resulting in a hydraulic diameter of $D_T = 35.5$ [mm], which determines the Froude number Fr in the pipe. See all dimensions in Figure 4-6.

The length of the conveying pipe l_c is defined by the relaxation length of the used particles. The latter is dependent on relaxation time τ_r of particles, which is dependent on its Reynolds number Re , and is dependent on the initial velocity of the particles $U_{p,0}$. Figure 4-7 gives an example of above explained correlation for a superficial gas velocity of 5 [m/s] (of the jet), and two different initial particle velocities of zero and of 4 [m/s]. As particles accelerate, the Reynolds number, being influenced by the difference $(U_g - U_p)$, decreases. Therefore, the driving force for particle acceleration decreases. Additionally, the covered distance of particles increases with increasing velocity per unit time. Thus, the relaxation length x_e increases drastically when converging to

the superficial gas velocity U_g . Figure 4-7 shows, that the above mentioned effect is substantially decreased by a higher initial particle velocity $U_{p,0}$ (see slope of graph for $U_{p,0} = 4$ [m/s]): while a non pre accelerated particle requires a relaxation length of 1.8 [m] to approach $U_p/U_g = 88$ [%], an 80 [%] pre accelerated particle reaches this velocity within 0.78 [m].

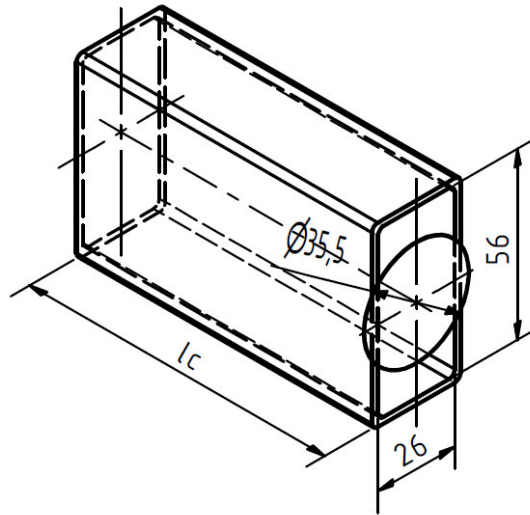


Figure 4-6: Cross section and hydraulic diameter of the standardized, rectangular conveying pipe.

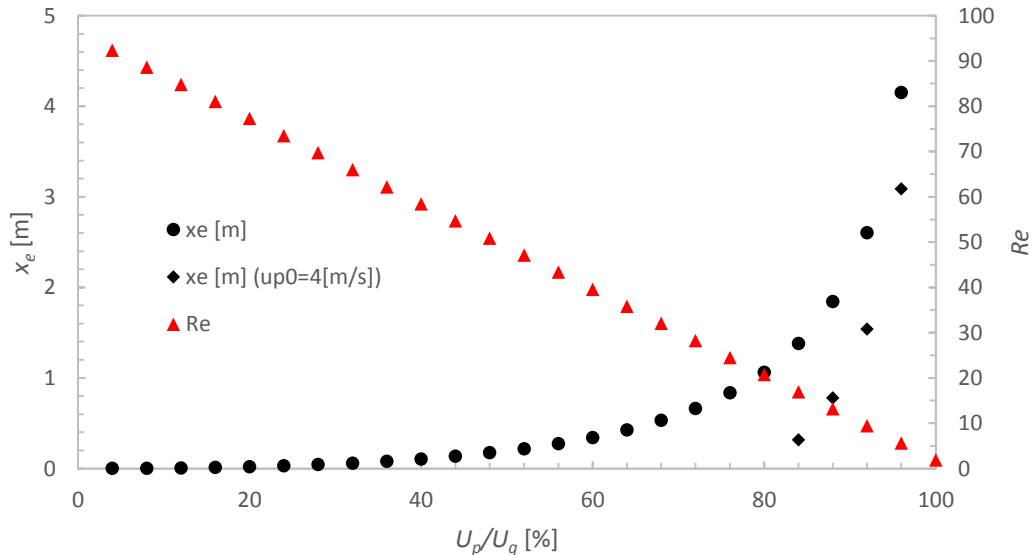


Figure 4-7: Relaxation length x_e [m] and particle Reynolds number Re of accelerated particles over percentage of particle velocity U_p on gas velocity U_g [%] with superficial gas velocity $U_g = 5$ [m/s] and two different initial particle velocities $U_{p,0,1} = 0$ [m/s] and $U_{p,0,2} = 4$ [m/s] for a particle diameter $d_p = 300$ [μm].

Figure 4-8 shows the relaxation length x_e for the desired U_p/U_g region (i.e., 80 [%] and above) for different superficial gas velocities U_g , and with or without particle pre-acceleration. On the one hand, a higher superficial gas velocity leads to longer relaxation distances while on the other hand, particle pre-acceleration reduces relaxation length. The closer the particle initial

velocity is to the superficial gas velocity, the greater is the effect of a reduction in relaxation length. This correlation can be also described by the Stokes number being $Stk \gg 1$. The Stokes number increases with increasing superficial velocity and with particle diameter.

Figure 4-9, which is calculated for $d_p = 100$ [μm], shows much smaller relaxation lengths for higher U_p/U_g rates than Figure 4-8 ($d_p = 300$ [μm]). To accelerate all particles of a binary bulk ($d_{p,1} = 100$ [μm], $d_{p,2} = 300$ [μm]), the length of the conveying pipe l_c must be very long. As a result, the l_c is chosen to be around 1.2 [m] to ensure proper velocity of small particles. Thus, the velocity of the coarse fraction when entering the crossflow classifier has to be measured in order to avoid errors introduced by an incorrect injection velocity in the simulation.

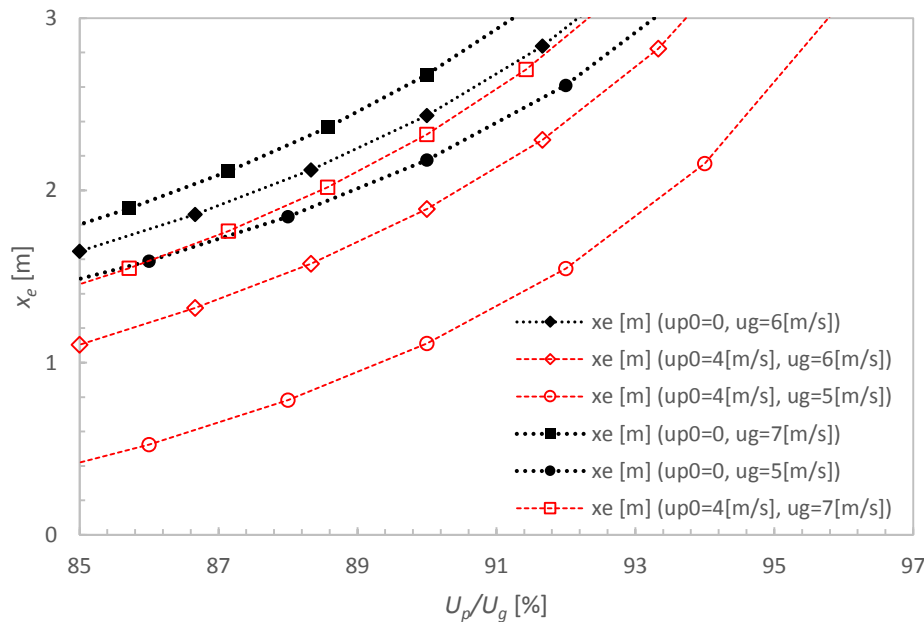


Figure 4-8: Relaxation length x_e [m] of accelerated particles over U_p/U_g [%] under three different superficial gas velocities $U_{g,1} = 5$ [m/s], $U_{g,2} = 6$ [m/s] and $U_{g,3} = 7$ [m/s] for two different initial particle velocities $U_{p,0,1} = 0$ (black markers, full) and $U_{p,0,2} = 4$ [m/s] (red markers, blank, the particle diameter is $d_p = 300$ [μm]).

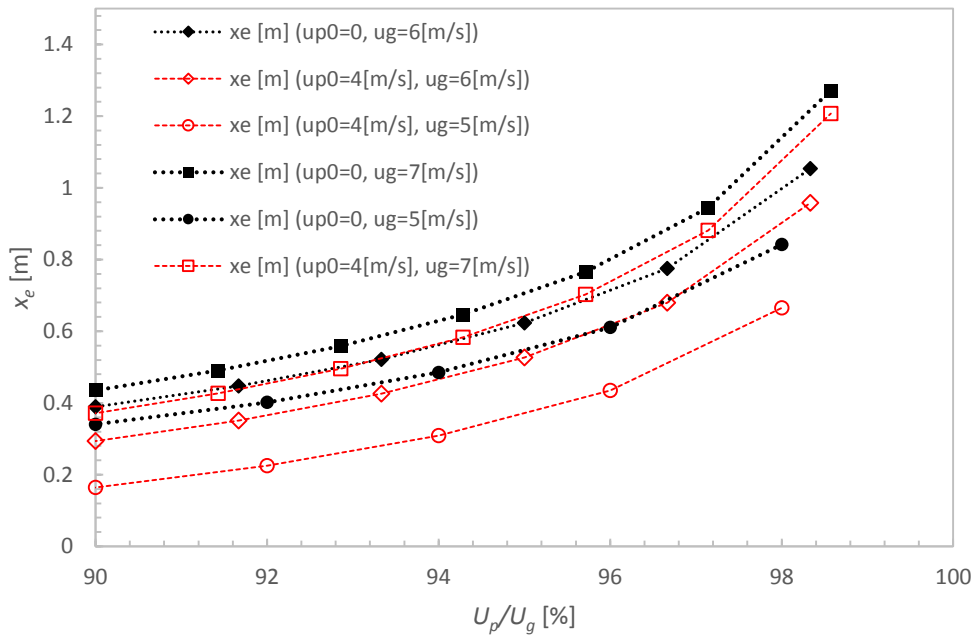


Figure 4-9: Relaxation length x_e [m] of accelerated particles over U_p/U_g [%] under three different superficial gas velocities $U_{g,1} = 5$ [m/s], $U_{g,2} = 6$ [m/s] and $U_{g,3} = 7$ [m/s] for two different initial particle velocities $U_{p,0,1} = 0$ (black markers, full) and $U_{p,0,2} = 4$ [m/s] (red markers, blank, the particle diameter is $d_p = 100$ [μm]).

4.3 Detail engineering

Detail engineering was performed for all relevant components of the crossflow classifier, since it was designed from scratch. Standardised products like O-Rings or bearings are bought by a supplier company (e.g., RS-Components). Also raw material, like steel sheets and shafts, were purchase parts. Manufacturing was performed in the institute's workshop. As some manufacturing steps like bending of rather long metal sheets etc. could not be done in the own workshop, these manufacturing steps were outsourced. For that reason, a make or buy decision has to be done for several components.

All parts, except those listed in a standard part catalogue, are modelled by using the CAD program Autodesk Inventor. These single parts are then assembled to certain assembly groups, and converted into a technical 2D component drawing. The assembly groups are assembled to either further assembly groups or to the final assembly. In addition, they are converted into technical assembly drawings.

The design of the crossflow classifier shall provide the possibility of further modifications, i.e. exchanging certain assembly groups. Therefore, the whole construction is designed in a modular way. Certain main assembly groups are assembled by simple flange connections.

These flanges are either rectangular or circular, depending on the geometries of the parts to connect.

4.3.1 Assembly groups

4.3.1.1 Classifying section – CL000000

All mean assembly groups are designed as simple sheet constructions consisting out of austenitic stainless steel of the material X5CrNi18-10, material number 1.4301. The material is well known for its corrosion resistance and for its high ductility. Therefore, its weldability is very good. In the form of thin sheet metal with a thickness of 2 [mm] it is highly applicable for bent components and for TIG (tungsten inert gas) welding. Latter process needs high practical skills of the user because of being highly mechanic rather than automatic. But therefore, it results in very fine, good looking weld seams. Figure 4-10 shows an assembly drawing of the crossflow classifier excluding pneumatic conveying pipe, cyclone and fan. All assembly groups, the coarse fraction container, the classifying air inlet section, the flow straightening section, the classifying section and the air + fines outlet section are all designed with a constant depth to not induce vortices behind overlaps. All welds are realized in spot welds to minimize warpage due to high local heat input.

The flanges and difficult geometries of the unfolded metal sheets are produced by laser cutting and the pipe ends are carried out as standard parts. Most of the metal sheets are manufactured to bent components. This brings the advantage of better stiffness, less weld joints, therefore less sealing effort and a smooth wall.

The disadvantage of the modularity of the system is its high amount of joint faces, which provide the possibility of leakages. To prevent leakage, all these faces have to be sealed properly, which is done by foam rubber flat gaskets bonded onto the flange surface. Spot welded joints are sealed with silicone.

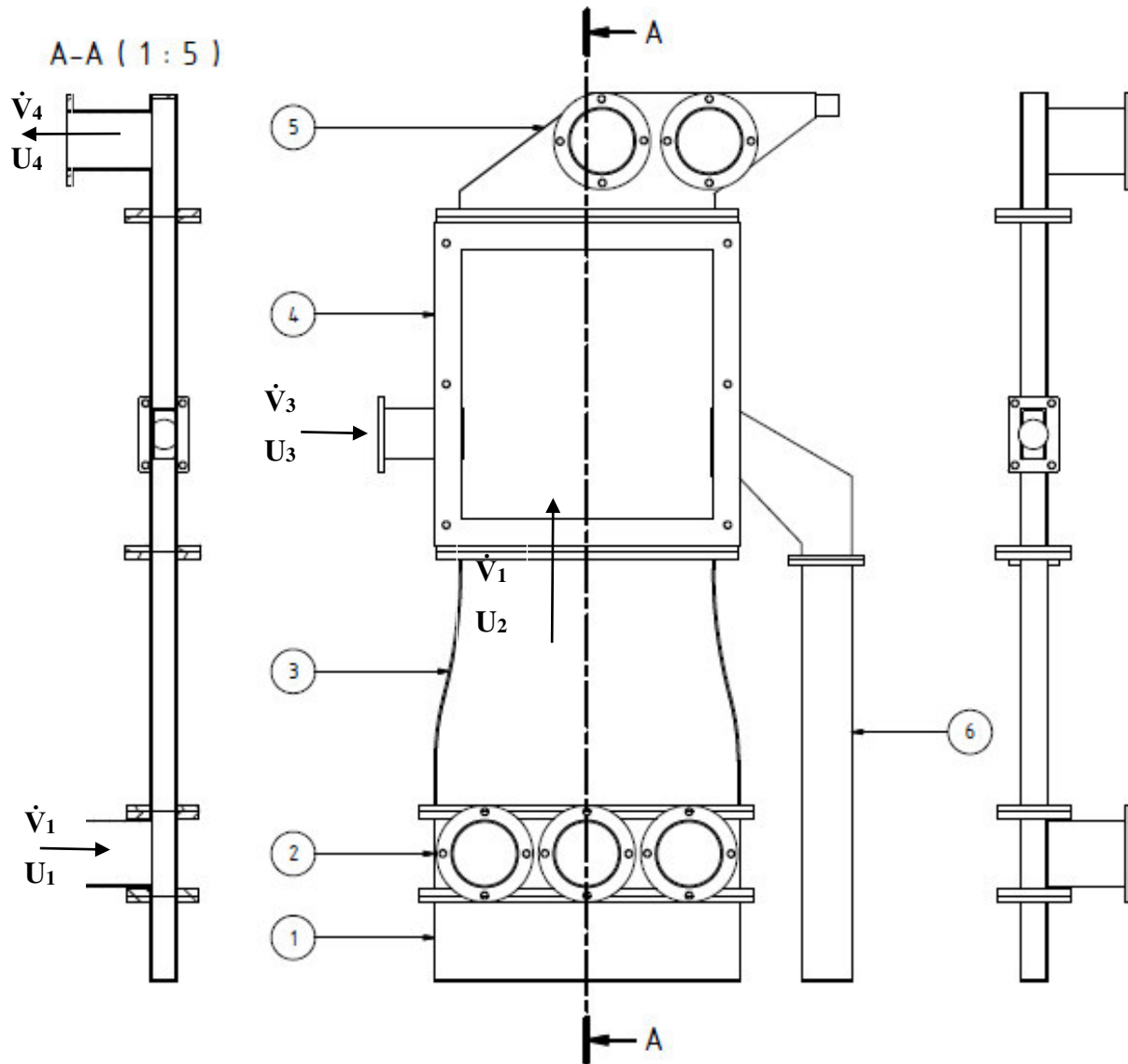


Figure 4-10: Crossflow classifier assembly including

1 and 6: coarse fraction container, 2: air inlet, 3: flow straightener part in form of nozzle, 4: classifying section including particle inlet flange, coarse fraction container and observation window, 5: fines and outlet part.

4.3.1.1.1 Coarse fraction container – CL030000/ CL060000/ CL070000

There are two coarse fraction containers: one on the bottom of the classifier to collect particles, in case they do not follow the desired paths either into the coarse fraction container on the right side of the classifier or into the fines outlet. Its cross section has the same dimension as the one of the air inlet above, it can collect particles until a bulk volume of 1 [dm³]. The other container is assembled to the desired exit for coarse particles of the crossflow classifier section. It consists of the same pipe as it is used for pneumatic conveying pipe to save costs and manufacturing effort. The pipe is closed by a metal sheet on its ground and is mounted by a rectangular flange, same as the alternative coarse material container. Its bulk volume is 0.73 [dm³].

4.3.1.1.2 Classifying air inlet – CL050000

The inlet section for the classifying air is realized as a flow channel, manufactured by a bent component and a laser cut metal sheet including three pipes of 76 [mm] diameter to keep the inlet velocity and therefore the dynamic pressure into the flow channel low. This is important to induce a proper pressure drop within the flow straightener above the air inlet to straighten and to distribute the air over the whole cross section. Circular flanges on the outer side of the inlet pipes enable to close them with blind flanges. This will be important for further modifications.

4.3.1.1.3 Flow straightener section in form of nozzle – CL020000

This section consists of two laser cut metal sheets as front and back wall and two sheet metal strips as side walls. On the lower side of the section a flow straightener in form of a honeycomb out of aluminium is inserted to reduce turbulence and to distribute the velocity profile. Its cells have a cell size of 1.6 [mm] and a cell length of 28 [mm]. This results in a L/D ratio of 17.5. Li et al. [54] show, that an increase of L/D ratio of square cells implemented into a flow can reduce its turbulence intensity, see Figure 4-11. This is proved for different cell lengths.

Also Mehta and Bradshaw [55] recommend a high L/D ratio for honeycombs in small low speed wind tunnels. They suggest an optimum value of about 6-8. As the current L/D value is more than double the recommended by latter authors, the performance of the flow straightener is expected to be sufficient.

The nozzle form of the assembly group is designed to ensure, that coarse particles fall down into the coarse particle container due to a lower velocity on the lower end of the flow straightener section. This is also important due to a decrease of the free cross sectional area in the honeycomb flow conditioner.

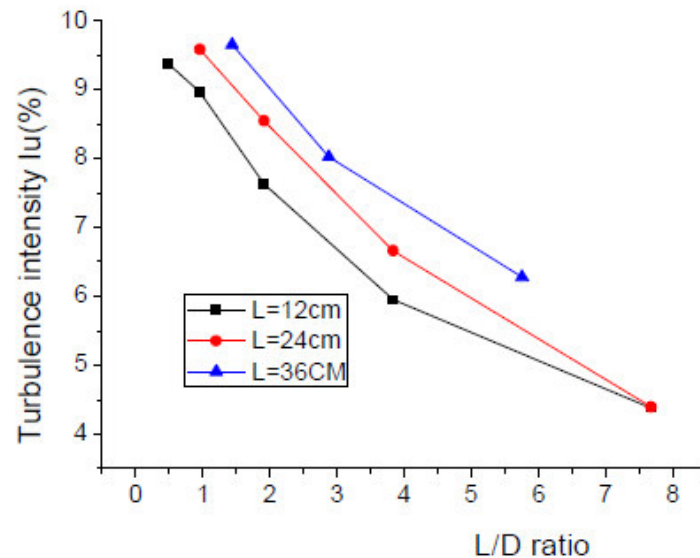


Figure 4-11: Influence of L/D ratio of square cells in reducing turbulence intensity [54].

4.3.1.1.4 Classifying section – CL040000/ CL080000

The classifying section includes an inspection window out of acrylic glass to allow the observation of particle motions using a high speed camera. There is each a socket on the right and left side of the classifier. On the left socket the particle conveying tube is mounted by flange connection. On the right a deflection channel is welded to lead coarse particles into the powder container, which is also fixed with rectangular flanges. To save manufacturing effort, both flange sizes, the one of the particle inlet and the one of the coarse fraction container, are equal. The container has ergo the dimensions of the conveying tube.

4.3.1.1.5 Air and fines outlet part – CL010000

The outlet section of fine particles includes two different outlet opening sizes. The small tube on the right side is designed in dependence on the hose system from classifier to cyclone of the previously existing zigzag sifter in the laboratory. The bevelled form of the housing in direction to the small outlet tube should give the air a direction and prevent particles of colliding against a wall. Thus a high mass flow of air and particles will be forced through a tube of comparably small diameter, a high pressure drop is expected in this part of the system. Therefore, two big tubes are placed into the front panel of the outlet section, which can optionally be used or blended by blind flanges.

4.3.2 Equipment selection

4.3.2.1 Mass flow controller

As the cross section and the desired air velocity for dilute phase conveying inside of the relaxation pipe is defined, the required volumetric flow rate is calculated to select an appropriate mass flow controller. The second selection criteria for a mass flow controller is its K_v -value. This value is a flow parameter for valves and is calculated related to the user manual regarding general hints for digital mass flow controller and pressure measuring / controlling devices in a laboratory [56]. K_v is standardized by DIN EN 60534-1:2005-07. In the following formula \dot{V} is the volumetric flow rate through the valve of the mass flow controller in [m³/h], p_1 is the supply pressure from the laboratory's pressure system in [bar] (absolute), ρ_n is the gas density in [kg/m³] and T is the absolute temperature in [K].

$$K_v = \frac{\dot{V}}{257 \cdot p_1} \sqrt{\rho_n T} \quad 4-1$$

The critical data of the chosen mass flow controller of the type Bronkhorst EL Flow F203 AV is listed in Table 2. The required data is estimated by assuming the absolute system pressure p_1 being 8 [bar] and the system temperature at room temperature of 293 [K], respectively. The required volumetric flow rate results from an estimated conveying air velocity between 4 [m/s] and 7 [m/s].

Table 2: Selection parameter for mass flow controller: requirements against equipment data.

	EL Flow F203 AV	required
\dot{V} [ln/min]	8...1000 (nominal)	350...600
K_v	0.15...1.5	0.19...0.33

4.3.2.2 Fan and cyclone

The fan as well as the cyclone can be adapted from an already existing zigzag classifier test stand. The fan in form of an industrial vacuum cleaner (RUWAC WS2000) is equipped with two drive motors offering a power of each 800 [W]. One downside of this vacuum cleaner is, that its generated volumetric flow rate cannot be varied. This variation is done by an external secondary air control in form of a valve inside of a tee connector. The only way to set up a certain desired volumetric flow rate is to measure it simultaneously with a gas meter.

The cyclone is of the type Mini CV06 and can, according to the manufacturer "Clear Vue Cyclones", separate particles bigger than 5 microns to a degree of 99.9% [57]. The structure of

the cyclone is rather simple: the upper separation part is made out of transparent plastic, which is mounted to the particle container only by a plug connection. This simplifies its handling.

4.4 Possible operating points of the classifier

If a particle is separated inside of the classifier depends mostly on the air velocity surrounding it. This velocity is defined by the volumetric flow rate of air, which differs within the classifier section, see Figure 4-12. While the volume stream induced by the fan \dot{V}_4 is increased, the inlet stream at the bottom of the plant \dot{V}_1 increases, too. When turning on the transverse stream generated by the mass flow controller \dot{V}_3 , the whole curve decreases. This might lead to a negative flow \dot{V}_1 streaming outwards of the plant.

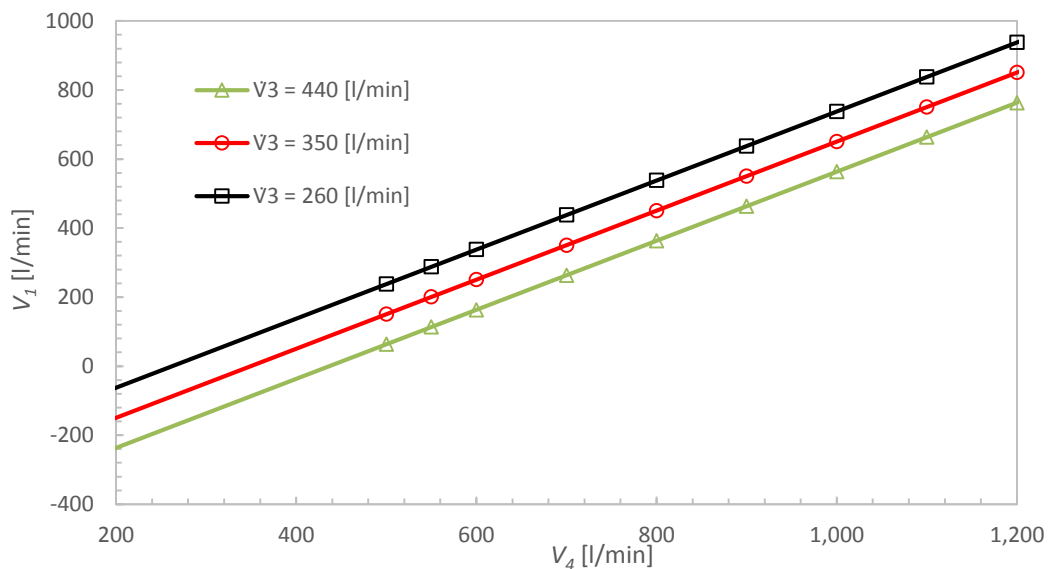


Figure 4-12: Volumetric flow stream \dot{V}_1 [l/min] depending on the outlet volume stream \dot{V}_4 [l/min], for three exemplary transverse volume streams \dot{V}_3 [l/min].

Based on the mass balance, possible velocity configurations can be calculated and are shown in Figure 4-13 exemplary for two rather useful transverse flow velocities U_3 . It can be seen, that an increase of U_3 leads to an increase of U_1 and U_2 . The difference between U_4 and U_2 , being the velocities deciding whether a particle goes with the air stream or leaves the classifier as coarse product, decreases with decreasing U_3 . The higher U_3 , the worse the prediction of a sharp separation grain, assuming a particle to not enter the coarse particle container across from the jet inlet: if the settling velocity of a particle lies between both values, separation depends on the probability of the particle to move below the transverse jet influenced region or not. This leads to the idea of an operation region instead of an operation point. For example, if particles with small diameter (p_{small}) shall be separated of particles of a big diameter (p_{big}), the minimum velocity $U_{4,min}$ must be higher than the settling velocity of p_{small} . The maximum velocity $U_{4,max}$

shall be lower than the settling velocity of p_{big} . The minimum velocity $U_{2,min}$ must be higher than the settling velocity of p_{small} and its maximum velocity $U_{2,max}$ has to be lower than the settling velocity of p_{big} . Consequently, both, the maximum velocity $U_{2,max}$, and the minimum velocity $U_{4,min}$ are not relevant as they are covered by $U_{2,min}$ and $U_{4,max}$.

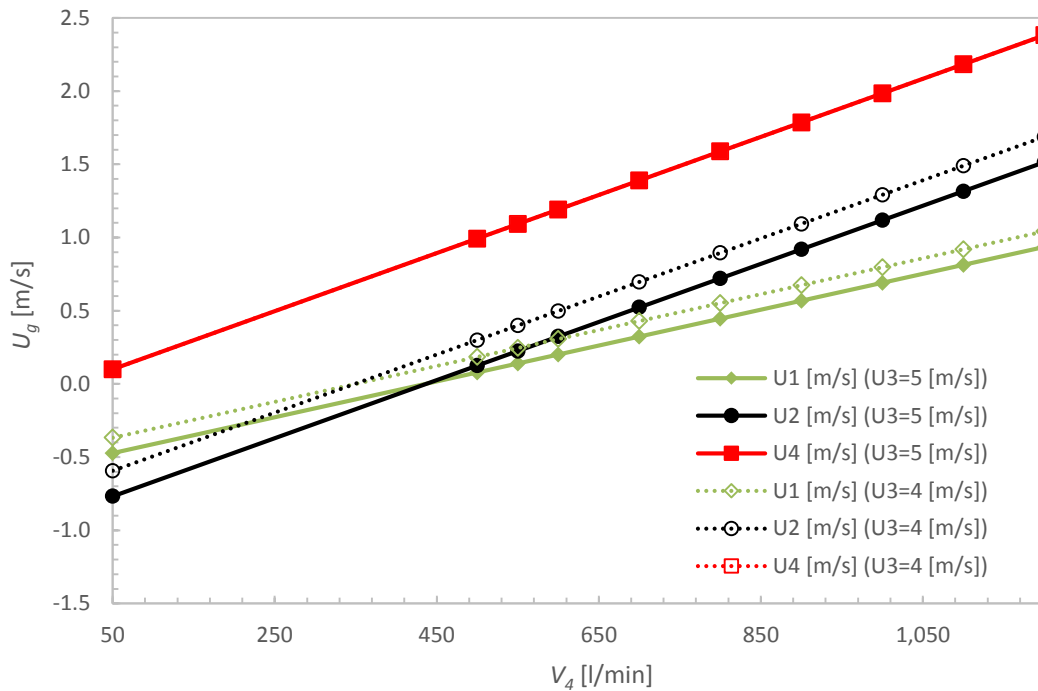


Figure 4-13: Gas velocities U_1 [m/s] at the plant inlet, U_2 [m/s] upstream of the transverse stream inlet, and U_4 [m/s] at the plant outlet depending on the outlet volume stream \dot{V}_4 [l/min] and for two different transverse jet velocities $U_{3,1} = 5.3$ [m/s] and $U_{3,2} = 4$ [m/s].

5 Engineering of the particle feeding unit

5.1 Specification and conceptual design

Shinohara et al. [58], as well as Engblom et al. [59] show, that particle size segregation of an at least binary bulk material begins already when filling and emptying a hopper. Therefore, feeding both the light and the heavy fraction from one bunker will lead to a certain degree of segregation. To prevent segregation from the beginning, it is decided to feed each particle size from a separate hopper. The segregation inside of the conveying line is considered to be negligible. In fact, a mixing process of both particle fractions inside of the pipe is aimed at. To eliminate segregation processes to its maximum, two independent feeders are set up either next to each other or behind each other. Since both particle feed points shall not influence each other, the latter position is the preferred one.

The feeding unit has got two jobs to fulfil. On the one hand bulk material has to be metered to set the desired mass flow. On the other hand, particles must be brought into the conveying pipe under prevention of leak air. There are many systems available on the market that are able to meter bulk materials. Few of them are able to do both jobs at once. Rotary feeders have the ability to do that: constant mass flow is set by valve speed and size, leakage is prevented by an interference fit formed by valve and housing. Thus, a rotary valve consists out of a small number of chambers which are filled and emptied when entering the upper and lower point. Unfortunately, this will cause a spatial and temporal particle distribution that is not homogeneous.

Above described circumstance should be improved by increasing the number of chambers. This is somehow the fact in the rotating brush of a brush feeder. Here particles will find their place between the voids of the bristles of the brush. The number of confined chambers is enormous. Therefore, spatial particle distribution is considered to be rather homogeneous. Replacing a rotary valve by a brush feeder the most convenient system found in literature is the so called "RODOS" system [42] by Leschonski et al. [41], see Figure 2-5 and Figure 2-6, respectively. The downside of not preventing air leakage has to be solved. This is done by sealing the cap of the hopper, i.e., a simple operation of the feeder in batch mode.

There are several feeding systems found that come into consideration. To find the most proper one, a benchmarking is done. Therefore, a number of decision criteria is set up to rate each system. The found criteria are the segregation prevention, manufacturing, simplicity, few turning parts, good metering action and good dispersing action. Since found criteria do not have

all equal priority, this can also be set in advance, i.e. a rating of “1” stands for a lower priority and a rating of “2” stands for a higher priority. Referring to this all systems are rated depending on the corresponding criteria with numbers from 1 to 10. “1” stands for worst fulfilling of the criteria, “10” stands for best fulfilling of the criteria. Each point referring to a rated system and a corresponding criterion is multiplied by the priority factor of the certain criterion. To keep the subjective prioritisation of certain systems low, the benchmarking is done independently by two persons, the author and the supervisor.

A rotary valve feeder as it is implemented in the existing zigzag sifter set up is excluded from this list, because it can only generate a constant mass flow over a certain time interval, but not a time-discrete constant mass flow of particles.

System A shows a modification of an invention by Leschonski and Röthele [40] in 1994. Powder is metered out of one bunker by making use of the hourglass principle for free flowing bulk materials, like, e.g., Staron et al. [60] state in their work, that granular material flows continuously through an hour-glass while the amount of particles above the opening decreases. After being metered, the particles are transported by a conveyor belt to a rotary brush, where they are brought into the conveying channel. This should provide a good dispersion and a mechanical pre acceleration of particles by the rotational speed of the brush, see Figure 5-1. Segregation is only minimized by implementing cones at the inlet of the hopper and at the outlet, respectively.

System A.1 is almost equal to system A, since it prevents metering segregation by using two hoppers instead of one, see Figure 5-2.

Figure 5-3 shows system B, which is a modification of the RODOS feeder shown by Leschonski et al. [41] in 1995 and by Kaye [42]. The hopper should not be made as a flexible hose, since particles are free flowing. System B.1 is almost equal to system B with the only difference, that it prevents segregation by using two feeding units behind each other.

System C consists out of two hoppers set up behind each other, which discharge particles homogeneously by making use of the hour-glass effect, see Figure 5-4.

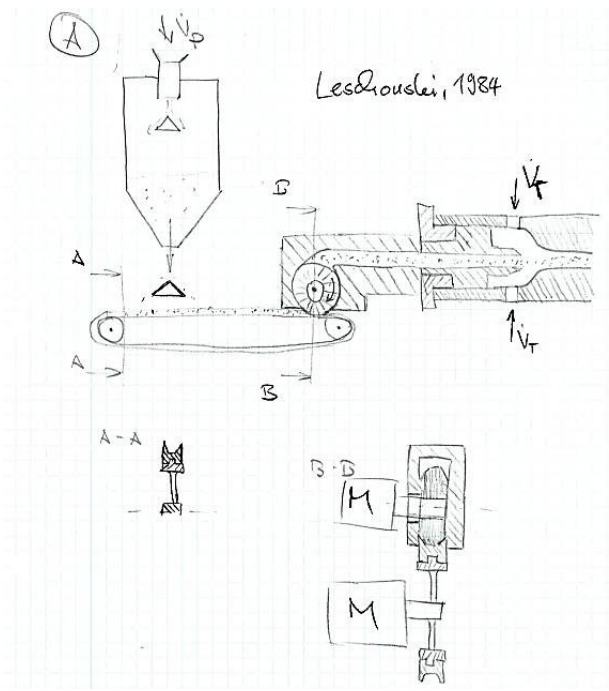


Figure 5-1: Sketch of system A consisting out of a metering hopper, a conveyor belt and a rotating brush; particles are sucked into the conveying line by a ring nozzle.

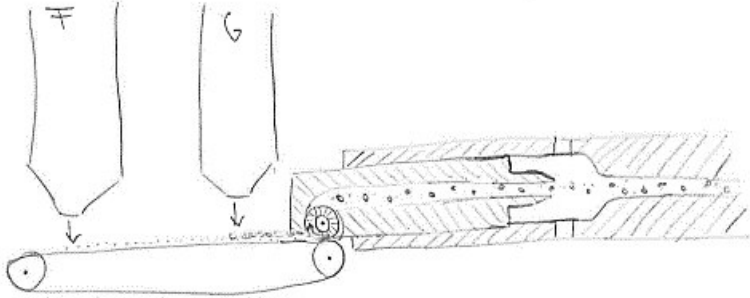


Figure 5-2: Sketch of system A.1 resembling system A, but using two hoppers.

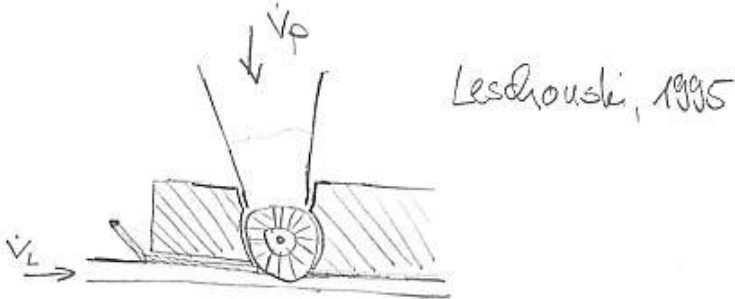


Figure 5-3: Sketch of system B as a modified RODOS feeder shown by Kaye [42].

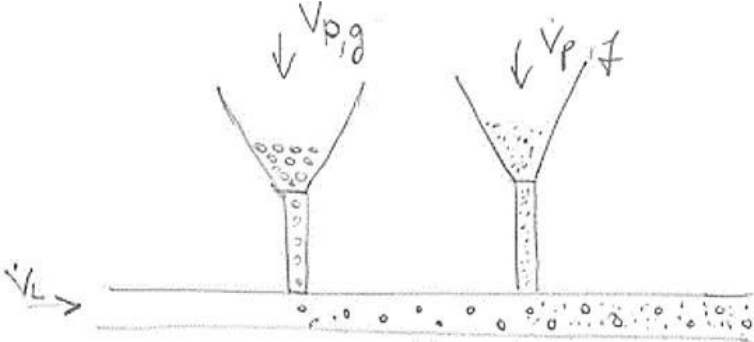


Figure 5-4: Sketch of system C consisting out of two hoppers with defined outlet cross section using the simple hour-glass effect.

Table 3 shows the priority rating of the criteria. High priority comes to the prevention of segregation, as this is one basic requirement on the validation quality. The metering action is also crucial for latter. Since the construction is a prototype which has to be manufactured in an appropriate amount of time, this is also an issue of high priority. The dispersing action is not a limiting factor as the used non cohesive bulk materials should not form agglomerates. Due to “few rotating parts” stand for a simple construction these two points should not get too prioritized.

Table 3: Priority rating of criteria for benchmarking of several feeding systems.

<i>segregation prevention</i>	2
<i>manufacturing</i>	2
<i>construction. simplicity</i>	1
<i>few rotating parts</i>	1
<i>good dispersing</i>	1
<i>good metering</i>	2

The sums of rating points are rather similar comparing both benchmarks. The two related systems A and A.1 get in both benchmarks the lowest numbers of points and are therefore the losers in this match. The opinion to system B differs between both benchmarks, as it reaches in the first case comparably few points and in the other case a rather high rating. Both evaluators estimate the segregation prevention in system B rather bad, while their opinions concerning its metering and dispersing functionality differ. Benchmark one sees it rather good while benchmark two rates it as best. The prioritisation of both criteria influences this difference further. System B.1 is the winner over system C as second place in benchmark 1. Benchmark 2 sees latter two systems equal in their quality. Both evaluators agree that system C provides best

properties in its simplicity and therefore in its low expected manufacturing effort, which is worse in system B.1. Both systems are expected to prevent segregation to a maximum.

Table 4: Benchmarking no. one rating all systems referring to the corresponding criteria from "1" (bad fulfilling) to "10" (good filling), the higher the sum of points the more preferable the solution.

Benchmarking 1	system A	system A.1	system B	system B.1	system C
segregation prevention	3	8	3	9	9
manufacturing	3	3	5	4	7
constr. simplicity	2	3	5	4	8
few rotating parts	2	2	5	5	8
good dispersing	8	8	7	8	2
good metering	7	7	6	10	3
sum	38	49	45	63	56

Table 5: Benchmarking no. two rating all systems referring to the corresponding criteria from "1" (bad fulfilling) to "10" (good filling), the higher the sum of points the more preferable the solution.

Benchmarking 2	system A	system A.1	system B	system B.1	system C
segregation prevention	3	7	3	10	10
manufacturing	2	5	7	7	10
constr. simplicity	2	4	7	5	10
few rotating parts	1	1	6	4	10
good dispersing	10	10	10	10	3
good metering	5	5	10	10	5
sum	33	49	63	73	73

Since system B.1 and system C are the two most preferable in this benchmarking, these two have to be investigated more detailed. The segregation prevention is rated very high in both systems, as in both each particle fraction is metered by a separate feeding unit. Particles will then mix inside of the conveying tube. The manufacturing and constructional simplicity are better rated in system C, as it only consists out of two hoppers with a defined orifice to the conveying line while system B.1 requires a sealing concept, a housing of the brush and so on. This makes it rather complicated in its construction and therefore also rather extensive in manufacturing. System C does not contain any rotating parts which makes it cheaper and less complex while system B.1 has a rotating drive shaft which requires a motor, eventually a

gearbox and a bearing arrangement. The dispersing of particles, i.e. the disintegration of agglomerates and distribution of particles is better in system B.1, because this is applied by the interaction of particles with the bristles of the rotating brush and the housing wall. System B.1 provides the possibility to set the mass flow rate by adjusting the driving speed of the brush, as it is shown by Leschonski [41], see Figure 5-5. The mass flow in system C is fix by its orifice geometry.

The ultimate task of the feeding unit is metering of powder into a conveying pipe. Since this task is estimated to be fulfilled best by system B.1, latter is the winner of the benchmarking.

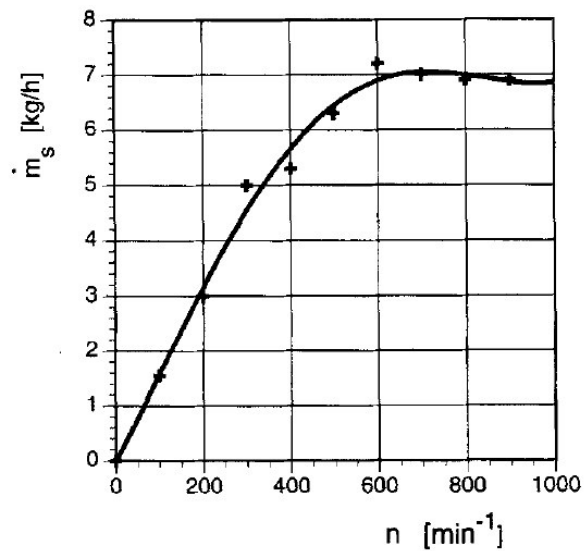


Figure 5-5: Particle mass flow [kg/h] over rotational speed of brush [min^{-1}] [41].

5.2 Detail engineering

A hopper, including a chute and a powder plug is mounted on top of a brush feeding unit. The mass flow of particles is set by a certain speed of the rotating brush. Particles are drawn into the interference fit between the nylon bristles and the aluminium housing (see Figure 5-6) to be discharged into the conveying tube underneath the feeder. Thereby a mechanical pre acceleration of particles while providing a sufficient metering should be guaranteed. A plug allows keeping particles back inside of the hopper to accelerate the brush before feeding powder to it. This is done to decrease initial torque and to not feed powder into the classifier before reaching the state of normal operation. The sealing within all interfaces is also realized by flat gaskets and silicone, respectively.

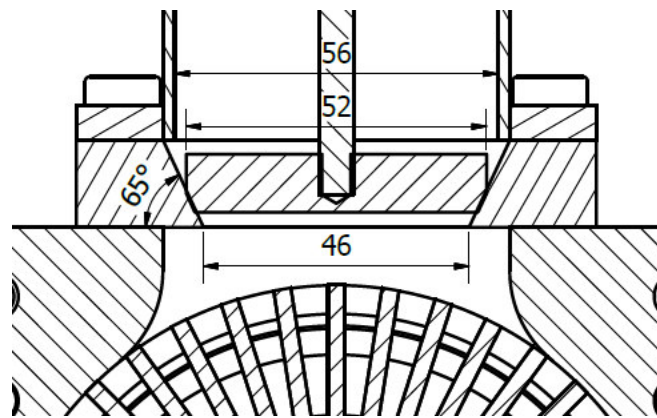


Figure 5-6: Interface between hopper and brush feeding unit.

5.2.1 Hopper

The hopper wall is realized as a tube of same dimensions as the conveying tube. Therefore, the same kind of flanges can be used for connections. The lower flange is mounted to the housing of the feeder with a 3D-printed chute in between. The chute lowers the width of the hopper to the desired inlet width of the feeder. A plug pressed into the cone of the chute prevents powder to flow through it. The interruption of powder flow is needed to separate hopper filling and brush feeding operation into two processes. When the hopper is filled with powder, the plug is lifted by a shaft being connected to the plug and reaching out of the hopper. Once the plug is lifted, it is locked by a simple mechanism in upper position until all powder has run out. The locking is realized by a rotary mounted metal sheet secured by a screw nut in axial direction. To prevent air streaming into the hopper, latter has to be sealed against air leakage. On top of the hopper this is done by screwing down a polychloroprene membrane, also known under the name neoprene. The plug shaft is put through a hole inside of the middle of the membrane. Latter is fixed to the shaft by a jam nut connection and another flange screws down the membrane to the flange of the hopper. As neoprene is a rather elastic material, the shaft can be

lifted by deforming the membrane to provide proper sealing while starting the feeding operation. See the mechanism in Figure 5-7.

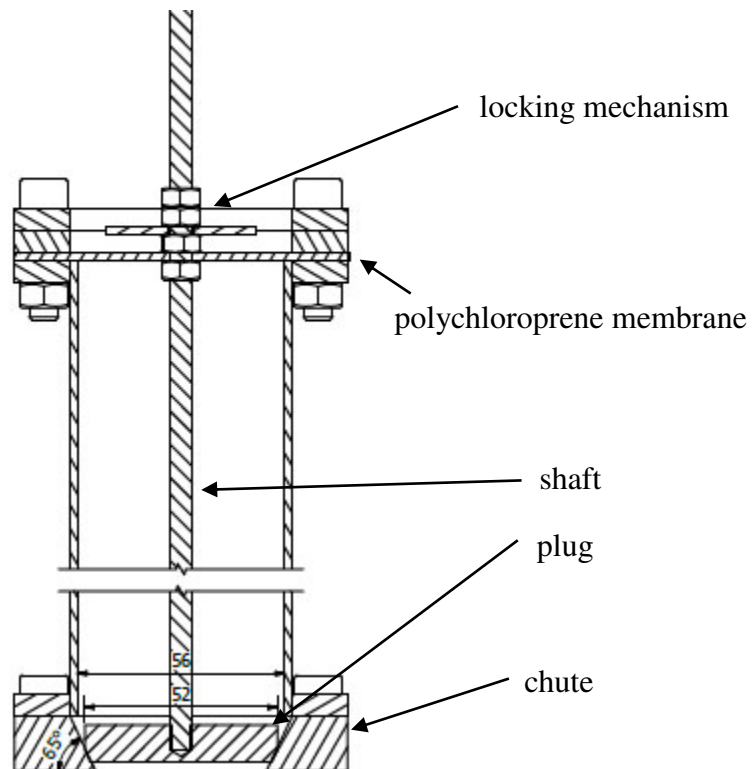


Figure 5-7: Powder discharge mechanism of hopper.

5.2.2 Feeding unit

The feeding unit consists out of a rotary brush mounted on a drive shaft driven by a direct current motor. The voltage of the motor is varied to vary its rotational speed. The drive shaft is pivot mounted inside a housing, arranged by a fixed and a floating bearing. To prevent statically over determination (locking) by fixing the motor to the housing, a coupling is mounted between motor shaft and drive shaft. It is also useful to compensate manufacturing tolerances in axial and in radial direction, respectively. To keep both sealing and connection capabilities of the interface motor/ housing compatible with manufacturing feasibility, a bell-shaped housing is designed, see Figure 5-8. The motor is mounted to a flange, which has a greater outer diameter than the motor itself. Motor and flange are then mounted to the coupling, which has been fixed to the drive shaft before. Within the coupling a small gap of two millimetres is planned to compensate manufacturing tolerances and to prevent the connection from locking. A bell shaped casing is mounted to the motor flange and to the housing of the brush feeding unit. O-Rings in both interfaces guarantee an oil and dust-free chamber. Both grooved ball bearings are equipped with a gasket on each side to prevent leakage of bearing oil on the one side, but also to protect the bearing from particle contamination.

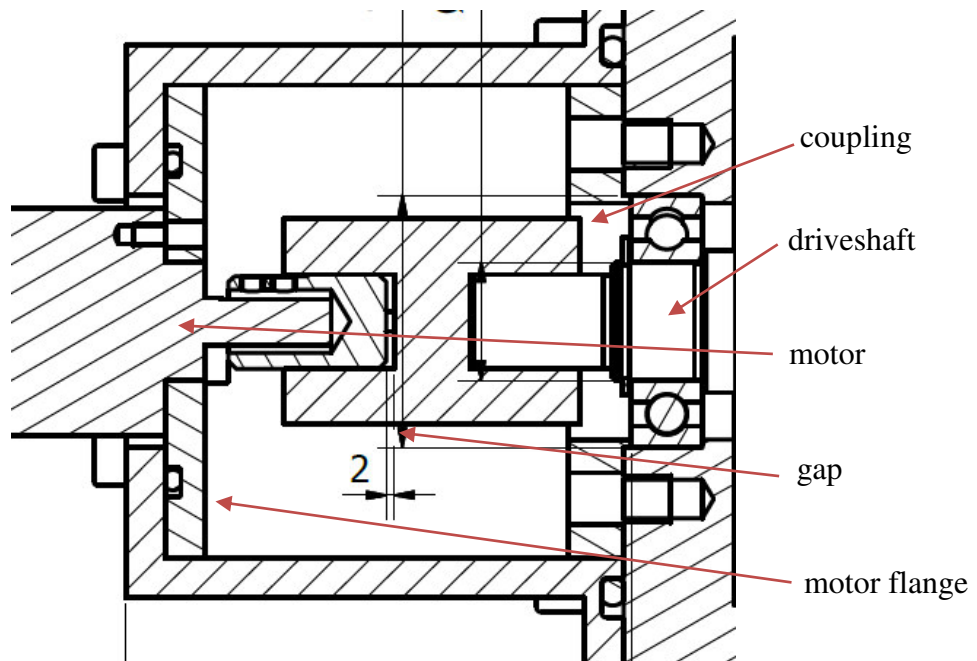


Figure 5-8: Connection of motor to housing using a bell-shaped housing.

Another sealing effort is done within the feeding chamber. To prevent powder from entering the area of bearing seats, rotary shaft seals are mounted between the rotating drive shaft and the housing, see Figure 5-9. Two disks are needed to bring the rotating drive shaft to the outer diameter of the brush. Therefore, particles cannot grind in the interfaces of a rotary and a still standing surface.

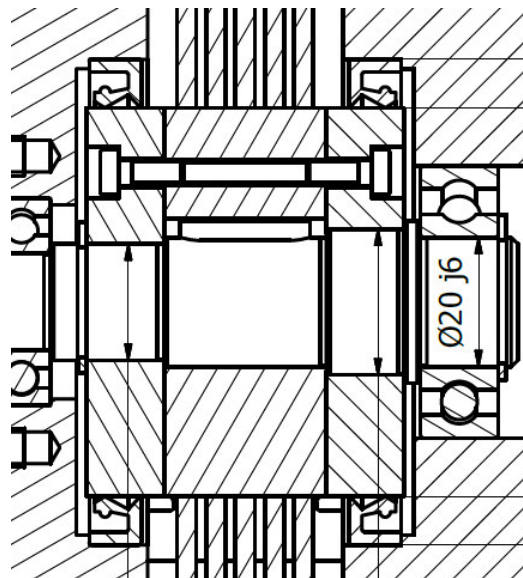


Figure 5-9: Rotary shaft seals to separate bearing seat area from powder metering area dust free.

To set up different mass flows there are three different setting parameters. The first one is the geometry of the powder chute regulating the mass flow of particles moving towards the rotating brush. If the open surface of the lower end is decreased, particle mass flow should also decrease.

The second possibility are brush guiding bars to pinch the bristles of the brush. Therefore, the brush becomes denser at the outer diameter, the mass flow of particles is expected to decrease. The bars can be adjusted at different positions by clamping them with grub screws. At the lower end of the brush the guiding bars end to let the brush open. This should cause an improved particle dropping into the conveying pipe. To not damage the brush when entering the guided section, the guide bars have a smooth chamfer.

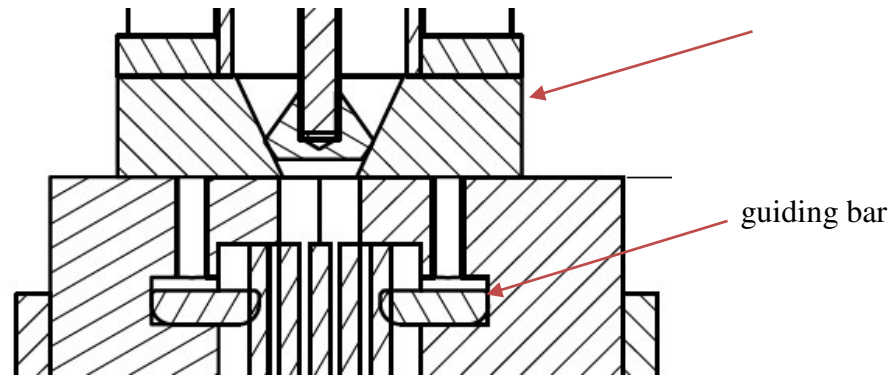


Figure 5-10: Brush guiding bars

The position of these guiding bars is specified by the resulting width of the brush as it is pinched to a certain level. A clear definition of the brush pinch is important for further investigation. The principle of the brush pinch is shown in Figure 5-11. For a pinch of zero, the guiding bars are simply left out. The measure of the pinch ζ is explained in panel c), showing a pinch of $\zeta = 5$ [mm] each side. The 19 [mm] wide brush reduces its width to 9 [mm]. Thus, bristles are pinched together to make it harder for particles to enter.

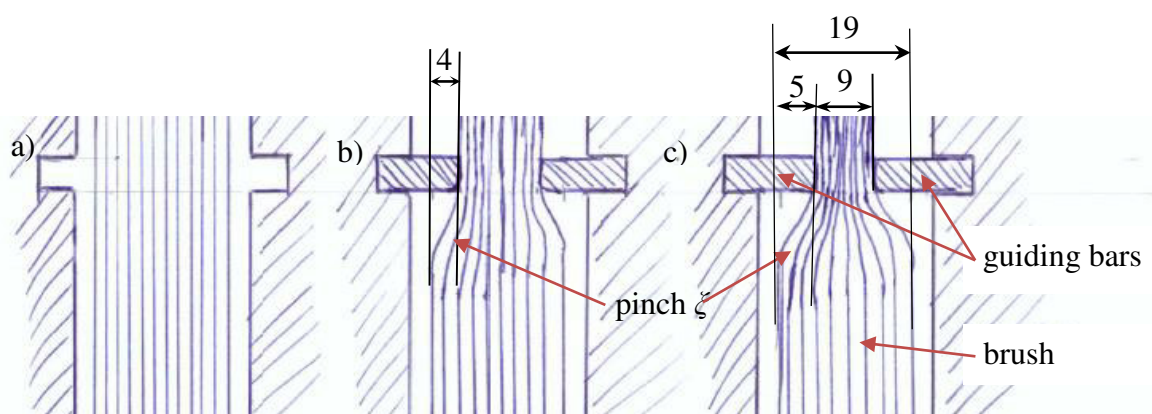


Figure 5-11: Principle of brush guiding bars to pinch brush to a certain extent: a) zero pinch, b) pinch of $\zeta = 4$ [mm], c) pinch of $\zeta = 5$ [mm].

The third possibility of adjusting a desired mass flow is setting the brush speed to a certain value. This will not only change the mass flow, but also the initial velocity of particles inside of the pneumatic conveying pipe.

5.2.3 Support of the feeding unit

As the feeder shall accelerate particles into a channel, the feeder must be mounted on top of this channel. Therefore, to keep the whole construction as modular as possible, a separate feeding channel, which can be easily assembled to the relaxation pipe by simple flange connection, is designed. It consists of a rectangular hollow profile, same dimensions as the relaxation pipe, with a hole of appropriate size. The feeder is mounted via a bolt connection to the bars, the latter of which are welded to the hollow pipe. The brush enters the hollow pipe for 20 [mm] to ensure that particles are discharged into the channel. A 3D-model of the feeding channel can be seen in Figure 5-12.

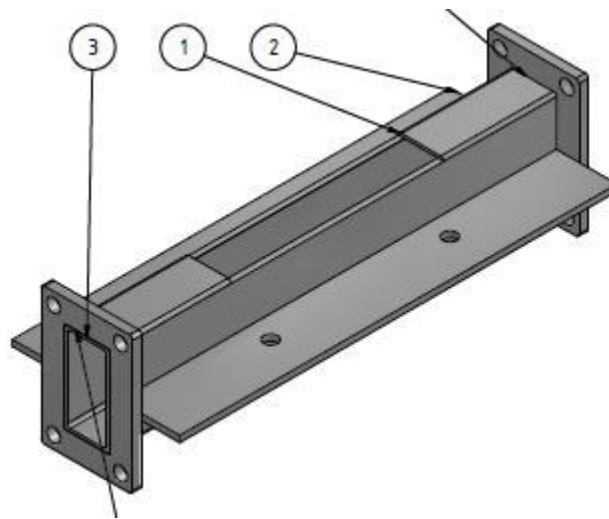


Figure 5-12: 3D model of feeding channel, see drawing number PC03000000.

5.2.4 Optional support of the feeding unit

There is an already existing zigzag sifter in the laboratory. As the sifter itself is well designed and is working as desired. However, the rotary feeder to this sifter works rather unpredictable, it is adapted to the new designed brush feeder. Therefore, a chute has to be designed to connect the brush feeder outlet (without using the acceleration channel) to the zigzag sifter inlet. The connecting face of the brush feeder outlet has a rectangular shape, while the particle inlet pipe of the zigzag sifter is circular. To solve the challenge of adapting a rectangular cross section to a circular cross section a 3D- printed chute is designed, see Figure 5-13.

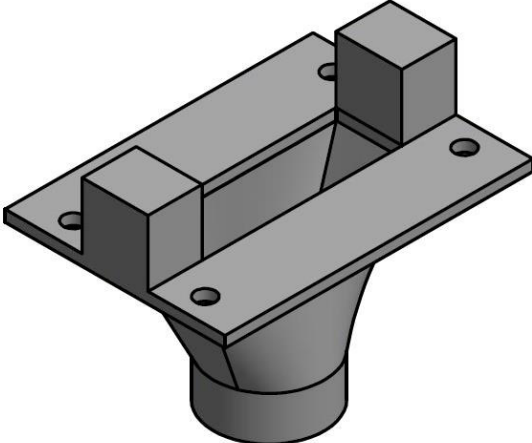


Figure 5-13: 3D-printed powder chute to adapt a rectangular face to a circular face.

6 Experimental

For first experiments of the brush feeder prototype and the crossflow classifier only one brush feeder is manufactured. There are three different powders available for experiments, see Table 6.

Table 6: Used powders for experiments.

description	material	particle sizes d_p [μm]	density ρ_p [kg/m^3]
glass beads	lime natron glass	$100 < d_p < 200$	2500
glass beads	lime natron glass	$400 < d_p < 600$	2500
quartz sand	quartz	$100 < d_p < 300$	2500

The glass beads are ordered from “Sigmund Lindner GmbH” (Type S, see data sheet in the Appendix A.2). Their structure is illustrated in Figure 6-1. Most of the illustrated particles are rather spherical, while some of them appear as agglomerates, consisting of two or three glass beads, which seem to have agglomerated during manufacturing.

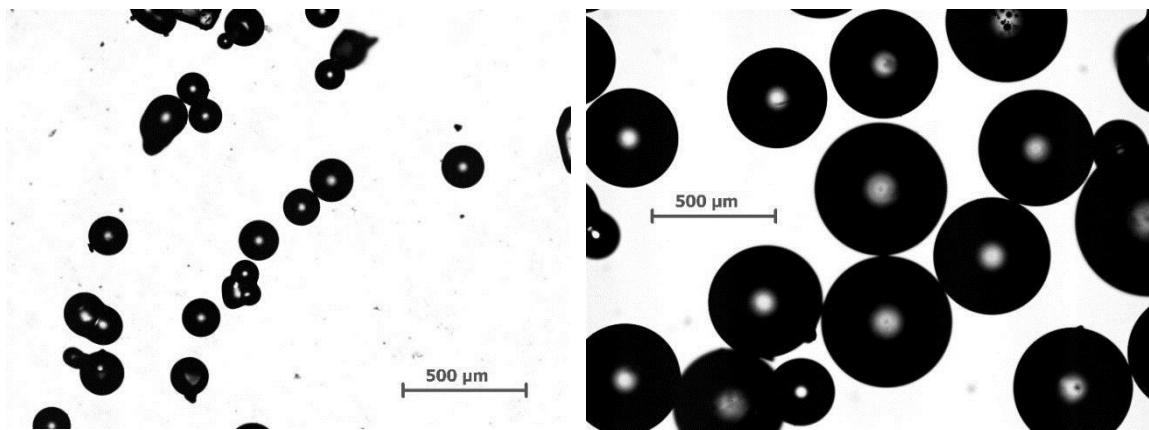


Figure 6-1: Glass particles, each 50x magnification, left panel: grain size 100 - 200 [μm], right panel: grain size 400 - 600 [μm].

The third used powder is quartz sand, which is bought as ordinary aquarium sand (Fa. SaMore GmbH, “0.1-0.3 mm AQUARIENKIES HOCHREIN NATURWEISS”). Its structure can be seen in Figure 6-2. The shape of these particles differs from the glass beads: while the glass beads have a spherical, smooth shape, the quartz particles are irregular, and are slightly elongated.

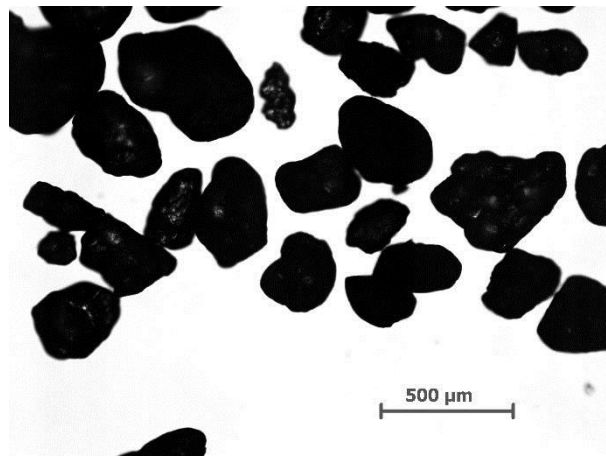


Figure 6-2: Quartz sand particles, grain size 100 - 300 [μm], 50x magnification.

6.1 Crossflow classifier

6.1.1 Experimental set-up

Figure 6-3 shows the experimental set-up in the laboratory. The crossflow classifier including its rack out of aluminium profiles, as well as the mass flow controller is mounted directly to a black coloured rack on rolls. As a consequence, the whole test stand is mobile within the laboratory. The pneumatic conveying, as it is a 1.2 [m] long lever with an additional weight at its end, is additionally supported by an arm in form of an aluminium profile mounted to the suspension of the mass flow controller. Thus, the bending moment applied to the bolts connecting the pneumatic acceleration pipe to the inlet flange of the classifier is decreased to a tolerable extent. The power supply for the drive motor of the brush feeder, as well as the computer for controlling the mass flow controller are placed on a table in front of the rack. The mass flow controller is connected to the laboratory's air pressure system and to the air inlet of the pneumatic conveying both with a flexible hose. It offers a maximum volumetric flow rate of 1,670 [$\text{l}_\text{r}/\text{min}$] and operates within a K_v -value of 0.15 to 0.5. The cyclone is of type "Mini CV06" ("Clear Vue Cyclones", Australia). It is very useful for separating fine dust and its structure is rather simple: the transparent cyclone part is mounted to the powder container only by a plug-in connection. The connection between crossflow classifier outlet and cyclone inlet by a flexible pipe can be realised either from one of the two perpendicular orientated additional big outlet pipes, as it is shown in Figure 6-3, or from the smaller outlet pipe on the right upper end of the classifier. To connect both different dimensioned flexible pipes for above mentioned options with the cyclone inlet, two different plastic- adapters are manufactured in the work shop. The outgoing flexible pipe of the cyclone leads to a tee connector, which is used for false air control. The perpendicular part of the tee is equipped with a valve. The outlet of the tee is

connected to the fan again by a flexible pipe. The fan is an industrial vacuum cleaner of the type RUWAC WS2000. Its two motors offer a power of each 800 [W].

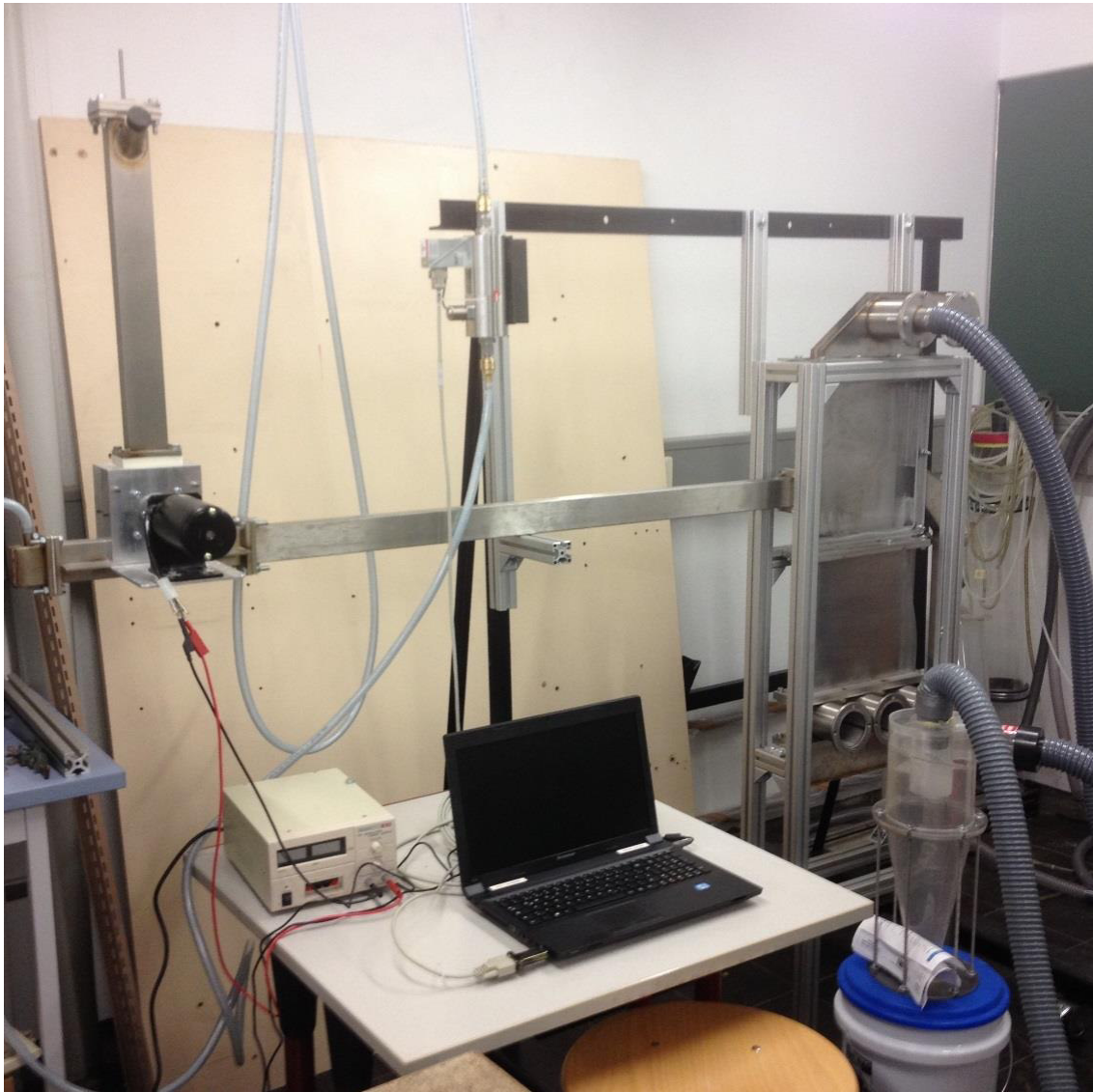


Figure 6-3: Experimental set-up in laboratory including MFC, power supply, pneumatic conveying, brush feeder, crossflow classifier section, flexible pipes, cyclone, etc.

6.1.2 Air mass balance

The air mass balance of the crossflow classifier is investigated by varying the volumetric flow rate induced by the mass flow controller as well as the one induced by the fan. While the mass flow controller is adjusted via a computer program, the volume flow regulation of the fan occurs by mechanic false air regulation. Therefore, two boundary values for each MFC configuration are documented by opening/closing the false air valve completely, i.e. resulting in maximum and minimum amount of excess air. The volumetric flow rate of the inlet of the classifier is measured by using a gas meter. While the gas meter is connected to one of the three air inlet openings of the classifier, all other openings except the outlet of the classifier connected with

the cyclone are closed with blind flanges. Having measured these volumetric flow rates $\dot{V}_{1,i}$ the flow rates $\dot{V}_{4,i}$ at the outlet of the classifier and the air velocities $U_{1,i}$ to $U_{4,i}$ can be calculated for different cross sections of the crossflow classifier and for different transverse jet velocities induced by the mass flow controller $U_{3,i}$. In addition, a maximum and minimum equivalent diameter can be calculated for each velocity.



Figure 6-4: Gas meter connected to classifier air inlet.

6.1.3 Particle size analysis

To investigate if the designed and manufactured crossflow classifier is able to separate particles concerning their size, a particle size distribution analysis is performed. Therefore, one experiment, having the feeder directly mounted to the classifier, i.e., not using the relaxation pipe, is executed. The used powder is quartz sand with a manufacturer- documented particle size between 100 and 300 microns. The volumetric flow rate of air is set to $\dot{V}_1 = 600$ [l/min] resulting in a calculated equivalence diameter of $d_{eq} = 177$ [μm], as the volumetric flow rate \dot{V}_3 is zero. An image of the running experiment can be seen in Figure 6-5. Particles transport within the conveying tube takes place mainly at the bottom of the pipe, i.e., particles are accelerated to a certain velocity but not homogeneously distributed within the pipe. The upwards deflection of a big part of the quartz particles by the classifier air can be seen in the picture. The main stream of particles penetrates the classifier to a depth of ca. 200 [mm]. Nevertheless, there are also particles observed in the area of the right hand coarse particle container inlet, moving either upwards or downwards. There are also particles observed being nearly at rest. An also rather

big amount of powder deflects downwards to the lower coarser fraction container. The parameters of the brush feeder in this experiment are listed in Table 7.

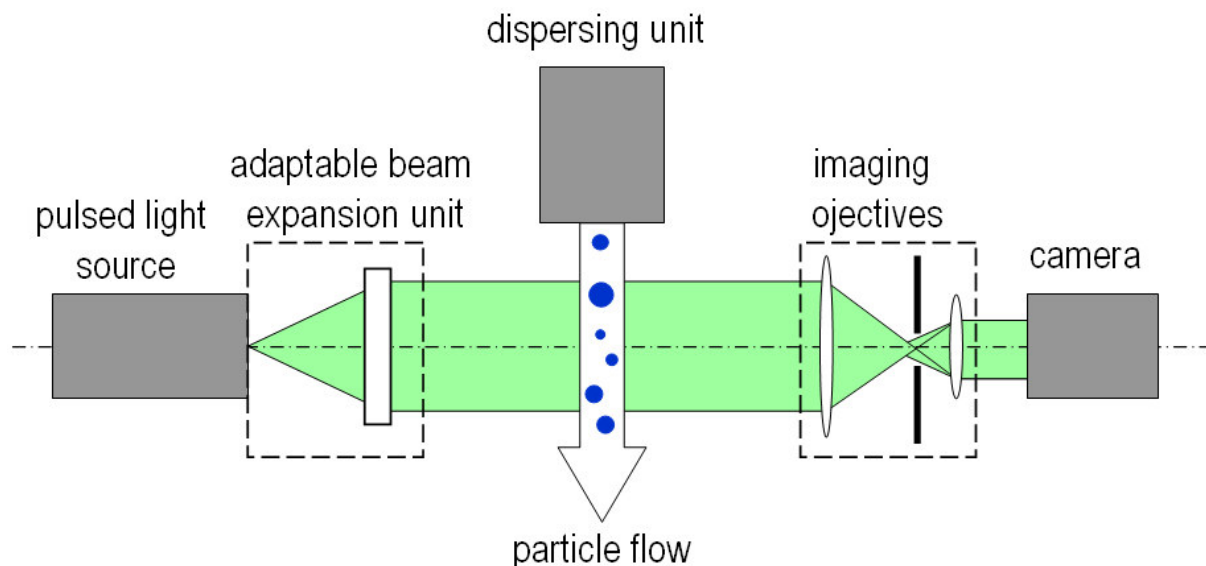


Figure 6-5: Classifying experiment for particle size distribution analysis using quartz powder with a particle size between 100 [μm] and 300 [μm], particles accelerated only mechanically by brush operated with at 24 [V].

Table 7: Parameter set up of the brush feeder for particle size distribution experiment.

applied voltage U [V]	24
rotational speed n [rpm]	1200 - 1230
calculated initial speed of particles $u_{p,0}$ [m/s]	7.5 – 7.8
guide bar pinch ξ [mm]	4 mm each side
estimated mass flow \dot{m}_p [g/s]	12.95 ± 0.55

As a result, the lower coarse fraction container and the fine fraction container are rather equally filled, while the side coarse fraction container is almost empty. The particle size distribution of all the fractions is performed using an optical particle measuring device Sympatec QUICPIC, described by Witt et al. [61]. In this device powder is filled into a little hopper and is then transported to a dispersing unit by a vibrating chute. The dispersion unit is based on the RODOS disperser, developed by Leschonski et al. [39]. Particles are dispersed at very high velocities, up to 100 [m/s]. A special illumination technique in form of a pulsed light source with an exposure time less than 1[ns] and an adaptable beam expansion unit to reach the required illumination of the fast passing particles combined with a high speed camera allows it to investigate particle size distributions and to also perform a particle shape analysis in a very short time and with a high accuracy.

**Figure 6-6: Functional principle of the direct image analysis being the basic concept for QUICPIC [61].**

6.2 Brush feeder

6.2.1 Mass flow rate vs. brush speed

Mass flow rate experiments are carried out by documenting the increase of mass fed by the brush feeder at a certain rotational speed into a particle container, which stands on top of a scale. The scale signal is documented over time in form of a video. These videos are evaluated by taking one pair of values, i.e. mass signal of the scale and the related time signal of the camera, every five seconds. The experimental set up is shown in Figure 6-7: while the particle container stands on top of the scale, the feeder including its powder chute must not touch the container. Therefore, a table containing a rectangular hole is found to support the feeder while feeding through the hole of the table. To ensure an appropriate prediction about the reproducibility of the experiments, each investigated brush speed setting is repeated for eight times for glass beads sized between 100 [μm] and 200 [μm]. As these results show a rather repeatable trend, all other experiments using particles sized between 400 [μm] and 600 [μm] or testing the brush guiding bars at different positions are only repeated twice.

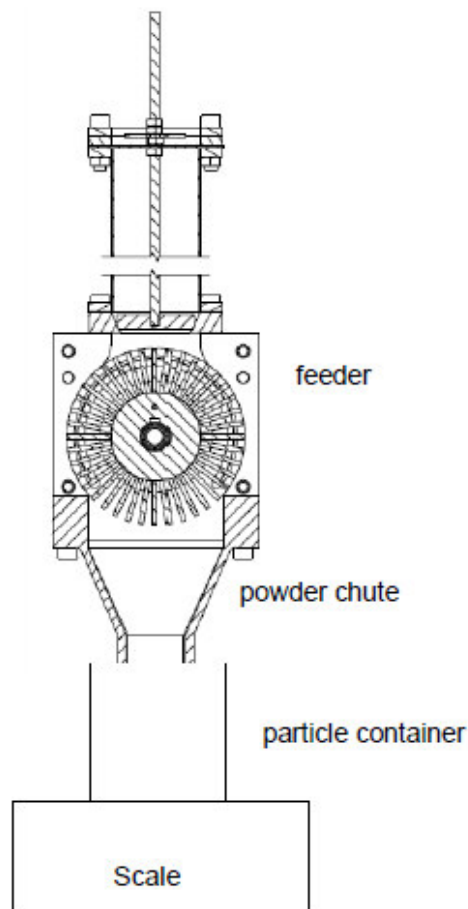


Figure 6-7: Experimental setup for investigating mass flow against rotational speed of brush.

The rotational speed of the brush is adjusted by setting up a certain speed to the drive motor. The drive motor is controlled by varying the output voltage of the corresponding power supply. The absorbed current of the motor as well as the rotational speed of the drive shaft, measured with an optical tachometer, are documented. The absorbed electrical power P [kW] of the drive motor is calculated as follows:

$$P_{el} = U \cdot I \quad 6-1$$

Assuming the efficiency of the motor being ca.1, the induced torque of the system can be estimated:

$$M = \frac{P_{mech}}{2\pi n} \quad 6-2$$

6.2.2 Pre-acceleration of particles

The pre-acceleration of particles by the rotational speed of the brush is tested in two steps: first it is only investigated, if the brush accelerates particles. This is done by feeding particles into the feeding channel (drawing number PC030000) without having the feeding channel connected to the classifier. Though particles were obviously thrown out of the channel, pre-acceleration can be guaranteed qualitatively. To quantify the acceleration of particles, the feeding channel including brush feeder is directly mounted to the inlet flange of the classifier section, i.e. the relaxation pipe is left out. Particles are accelerated only mechanically into the classifying section, where their motions are recorded by a high speed camera in order to detect particle velocities by particle image velocimetry (PIV).

6.3 Particle image velocimetry (PIV)

To investigate the velocity vectors of the particles injected into the crossflow, particle motions are recorded using a high speed camera MotionXtra Os8-S3 connected to the computer program "Motion Studio". To increase the contrast between background and particles a white paper is taped on the classifier wall. Thereby, also reflections caused by the surface of the steel wall are avoided. The recording frequency of the camera is 2,000 [Hz] in each experiment, while its shutter time is 10 [μ s] to avoid motion artefacts. To be able to realize such a small shutter time, a sufficient illumination of the observed space is required. This is realized by a high power LED lamp offering a power of 100 [W], which is mounted above the camera. The exact position of the lamp is found by trial and error: the observed space must be homogeneously illuminated, free of reflections. The experimental set-up of the image recording is shown in Figure 6-8.

For every investigated experiment 3,000 images with a pixel size of 1,600x1,200 are recorded, i.e., 1.5 [s] real time resulting in a data volume of around 5.4 [GB]. Via the PIV program “MatPIV”, version 1.7.1, introduced by Sveen and Kolaas [62] and modified by Radl, see Appendix E.3, particle motions are found by comparing two image pairs. The program runs on the open source software “Octave”. Particles in the second picture with the highest probability of having been the same particle in the picture before are detected. Thereupon directions and distances, i.e., vectors are generated. Knowing the recording frequency, i.e. the time between two images, velocities can be calculated. Therefore, a reference length in form of a coordinate system has to be defined. Latter is done by drawing three rectangular coordinates in form of dots on a white paper, e.g., with a distance of 5 [cm]. The paper is taped on the observation glass of the classifier to be recorded as one picture by the camera. After having recorded the reference for following experiments, the camera as well as the test stand must not be moved.



Figure 6-8: Experimental set-up for PIV image recording.

The PIV program saves its results as matrices in mat-files. For each investigated image pair a mat-file is generated including matrices for the respective velocities in horizontal and in vertical direction. To show, if the particles are injected into the classifier at steady state, the velocity in x- and y direction at a certain place within the observed window is plotted over time. The

smaller the slope of thereby generated curve, the higher the probability of the injection being in steady state. There is not an already existing program for latter investigation. Therefore, a new program has been implemented to load the mat-files within a loop and then print the results, see Appendix E.2.

Images are recorded for different settings for (i) the brush feeder, (ii) the velocity U_3 within the pneumatic conveying pipe, and (iii) the velocities U_2 and U_4 . The latter has been set by adjusting the volumetric flow rate \dot{V}_1 at the inlet of the classifier. Also the used powder was varied. As fine glass powder does not offer the best observability with the camera system, also quartz powder sized between 100 and 300 [μm] was used for PIV. Table 8 shows the experimental set up for all 9 PIV experiments including the used powders, the feeder set up, the adjusted velocities in the injection pipe, and in the classifier and the resulting mass loadings dependent on the feeder set up. The estimated mass flow is calculated with based on the correlation developed earlier. The calculated mass loadings relate to the median of the estimated mass flow and to the velocities U_3 and U_4 . For those experiments, where the feeder is mounted directly to the classifier with U_3 being zero, the mass loadings are estimated with the expected initial dropping velocities of the particles $u_{p,0}$.

As the evaluation of the image pairs is rather time consuming, the first experiment is fully evaluated, while all other experiments are investigated by comparing every 10th pair of images.

The conveying pipe is electrically grounded to prevent electrostatic charging of the conveyed powders. While there is not a great danger when conveying glass beads, explosive bulk materials like flour or carbon dust can easily be ignited by electrostatics. Still, when performing several classifying pre-tests electrostatic charging of the inspection glass is observed. Thereby particles stick to the acryl glass and hide the room to inspect. This challenge is solved by spraying commercially available anti-static spray of type “ANTISTATIK 100” (“CRC Industries Deutschland GmbH”) on top of the inner side of the glass.

Table 8: Experimental plan for PIV investigation including used powders, classifier velocities and feeder/injection settings, pinch configuration see Figure 5-11.

#	powder		feeder/ injection				classifier velocities			mass loadings	
	mat	d_p [μm]	U [V]	$u_{p,0}$ [m/s]	ξ [mm]	\dot{m}_{est} [g/s]	U_3 [m/s]	U_2 [m/s]	U_4 [m/s]	μ_{Co} [kg/kg]	μ_{Cl} [kg/kg]
1	quartz	100-300	22	6.7	4	13.2 ± 0.3	5	1.5	2.4	1.51	0.55
2	quartz	100-300	22	6.7	4	13.2 ± 0.3	6	1.4	2.4	1.26	0.55
3	glass	400-600	22	6.7	4	16.9 ± 1.2	4	1.6	2.3	2.42	0.7
4	glass	400-600	22	6.7	4	16.9 ± 1.2	5	1.5	2.4	1.94	0.7
5	glass	400-600	12	2.8	4	22.9 ± 0.7	5	1.5	2.4	2.61	0.95
6	glass	400-600	0	0	4	ca. 1	5	1.5	2.4	0.14	0.05
7	glass	400-600	22	6.7	4	16.9 ± 1.2	0	2.2	2.2	1.44	0.76
8	glass	400-600	18	5.3	4	21.2 ± 1.2	0	2.2	2.2	2.44	0.96
9	quartz	100-300	22	6.7	4	13.2 ± 0.3	0	2.2	2.2	1.13	0.59

7 Results

7.1 Air mass balance

The measured volumetric flow rate \dot{V}_1 , as well as the calculated flow rate \dot{V}_4 , being the sum out of \dot{V}_1 and \dot{V}_3 , are shown in Figure 7-1 for different transverse flow rates \dot{V}_3 and for completely open (index “min”) or closed (index “max”) false air valve. For both valve positions the volumetric flow rate at the inlet \dot{V}_1 decreases with increasing transverse flow rate \dot{V}_3 while the outlet flow rate \dot{V}_4 slightly increases. Both observations can be interpreted as follows: the increase of the outlet flow rate is a result of a pressure drop reduction in form of a pressure rise due to the volume increase at the point of the transverse jet injection. This has the effect of a drag decrease for the fan. Therefore, its operation point shifts to a higher volumetric flow rate. The spread between \dot{V}_1 and \dot{V}_4 increases with increasing \dot{V}_3 beginning from zero. Thus, also the velocity spread, as well as the spread of equivalence diameter within the classifier rises, see Figure 7-2 and Figure 7-3, respectively. E.g. for closed false air valve and a \dot{V}_3 of 500 [l/min], the equivalence diameter inside of the classifier varies between ca. 300 [μm] upstream the injection point, and ca. 200 [μm] downstream of the injection point.

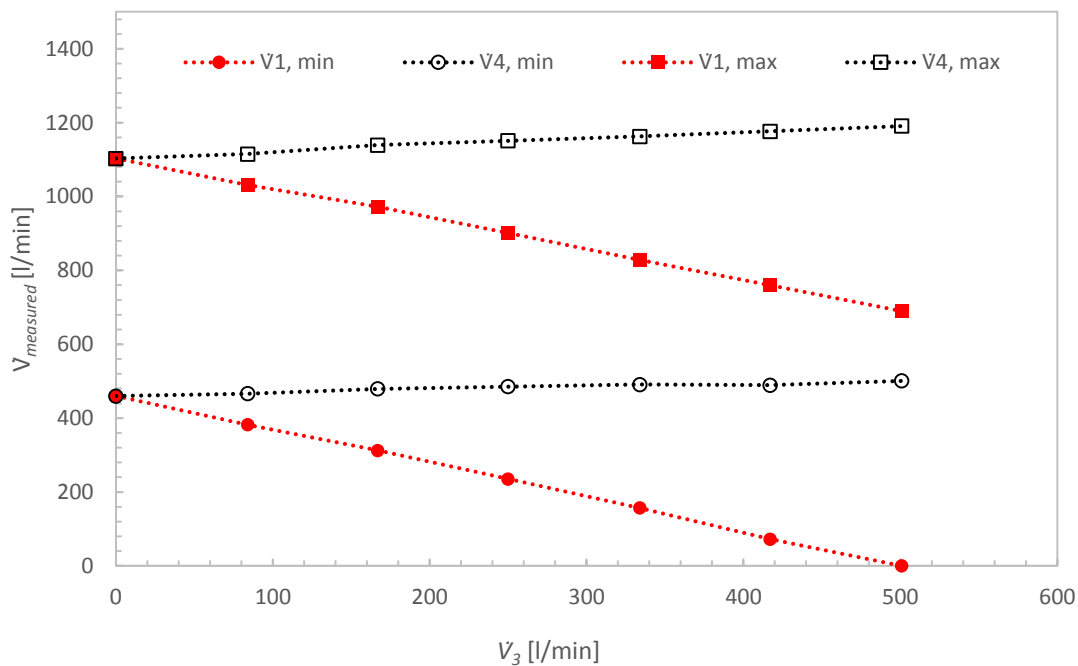


Figure 7-1: Measured volumetric flow rates \dot{V}_1 and \dot{V}_4 for maximal excess air (red and filled markers) and minimal excess air (black and voided markers) dependent on mass flow controller set up \dot{V}_3 .

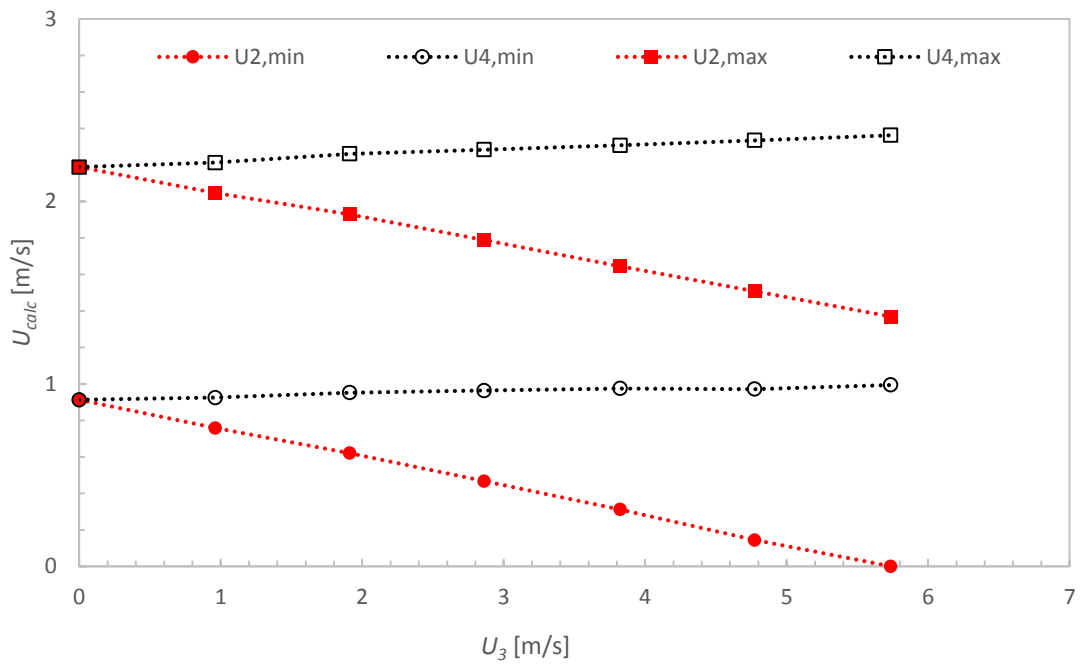


Figure 7-2: Calculated gas velocities U_2 and U_4 at the corresponding cross sections for maximal excess air (red and filled markers) and for zero excess air (black and voided markers) dependent on transverse gas velocity U_3 generated by mass flow controller.

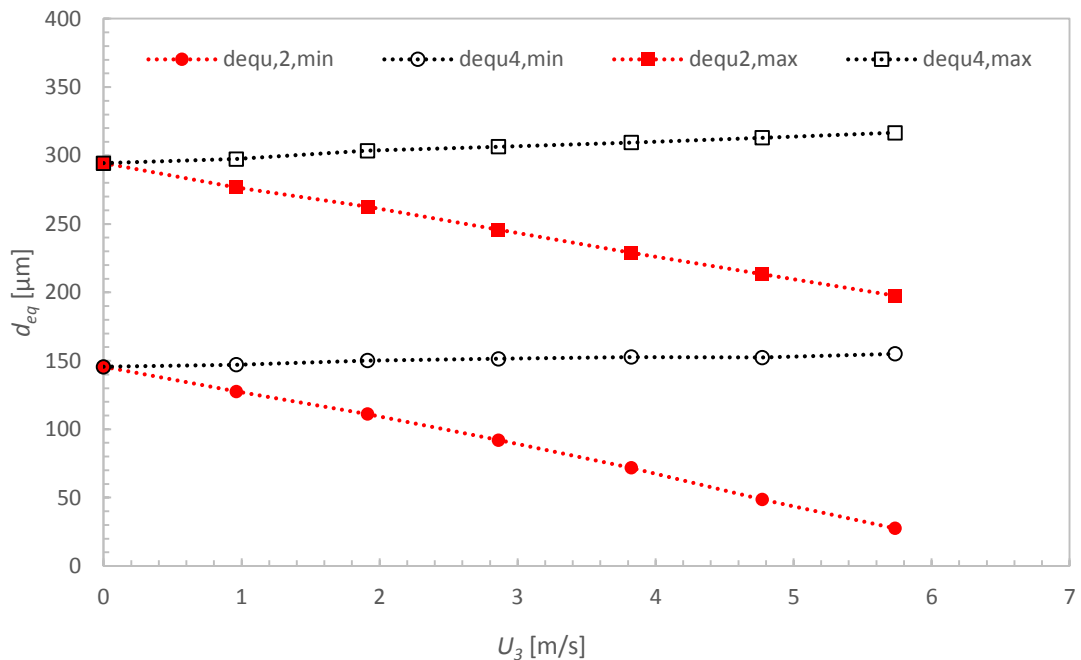


Figure 7-3: Calculated equivalent diameters $d_{eq,2}$ and $d_{eq,4}$ at the corresponding cross sections for maximal excess air (red and filled markers) and for zero excess air (black and voided markers) dependent on transverse gas velocity U_3 generated by mass flow controller.

7.2 Particle size analysis

To calculate a separation efficiency of the classifier experiment, the size distribution of the classified particles, i.e., the fine fraction residing inside of the cyclone container m_{Fi} and the coarse fraction m_C , residing in the coarse fraction container, were analysed. The sum of both gives the mass of the feed m_F . The portion of fines f and the portion of coarse particles c can then be easily calculated. The results are summed up in Table 9.

Table 9: Masses of classified powder including fine portion f and coarse portion c .

m_C [g]	534
m_{Fi} [g]	315
m_F [g]	849
c	0.63
f	0.37

Small samples of these two fractions are investigated with QICPIC to obtain the Q_3 -distributions dependent on x_3 [μm], see QICPIC -reports in Appendix F.1 (fine fraction) and Appendix F.2 (coarse fraction). From this data a csv-file is generated, which is loaded into an Octave program, see Appendix F.3. In a first step, the cumulative Q_3 -distributions are plotted, see Figure 7-4. The curves are typically s-shaped, the gap between both lines indicates that a separation has taken place.

The probability density distributions of the coarse, the fine and of the feed material are shown in Figure 7-5. The distribution of the fines has a modal particle size of 220 [μm]. The coarse fraction is rather narrow and has a modal particle size of 286 [μm]. The intersection between the density distribution of the coarse and the fine fraction indicates the median cut off $x_{50} = 247$ [μm].

The adjusted equivalent diameter d_{eq} in the experiment (defined by the average gas velocity) was set to 177 [μm] in the experiment. Therefore, particles bigger than 177 microns are expected to be the coarse fraction, smaller particles are seen as fine fraction. As the measured median cut off x_{50} is much bigger than the theoretically “adjusted” cut off diameter, more of the coarse particles, i.e. particles bigger than d_{eq} are expected to be in the fine particles container than vice versa. This expectation is nicely documented with the probability density distribution. There are almost no fine particles, i.e., particles smaller than d_{eq} , found within the coarse fraction, while the fine fraction is heavily polluted with coarse particles.

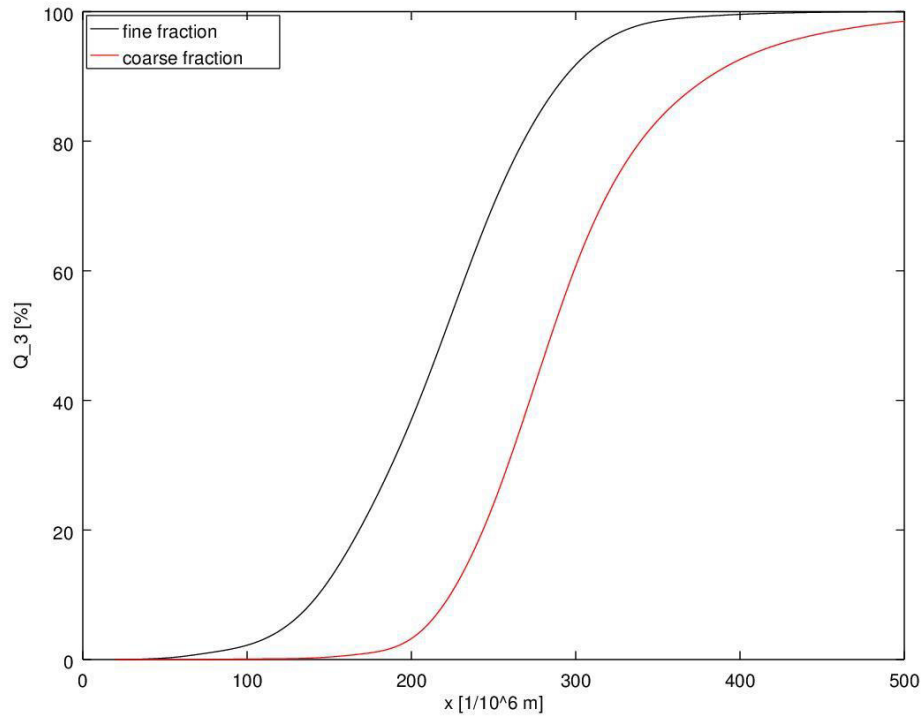


Figure 7-4: Q_3 distribution of fine and coarse fraction, as a result from QICPIC.

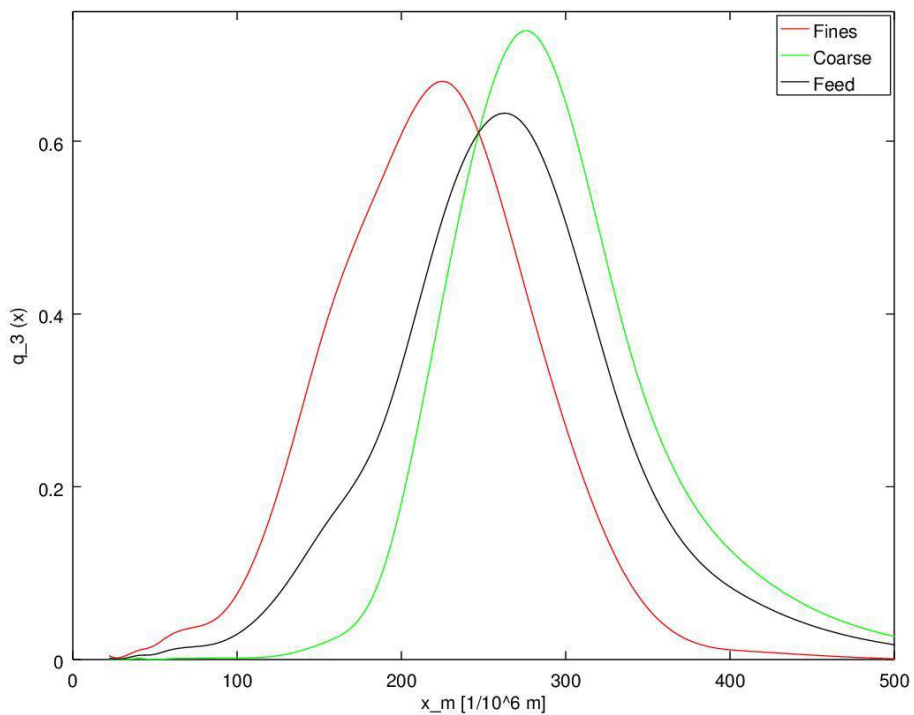


Figure 7-5: Probability density distribution of the fines $q_{Fi}(x)$, the coarse material $q_C(x)$ and the feed material $q_F(x)$.

From these data the curve for the degree of separation can be calculated. It is shown in Figure 7-6. Its slope is an indicator for the efficiency of the separation. This classifier sharpness index κ can be calculated as follows:

$$\kappa = \frac{x_{25}}{x_{75}} = \frac{190.8 [\mu m]}{313.9 [\mu m]} = 0.61 \quad 7-1$$

The nearer κ goes to unity, the better, i.e. the sharper, is the separation. For the crossflow classifier a sharpness index of 0.61 seems to be quite desirable, as Tomas [63] documents κ -values for a laboratory zigzag sifter, which can be understood as a cascade of crossflow classifiers, as each bend of the sifter is understood as a separate stage. For comparably coarse particles he measures sharpness indices between 0.7 and 0.8. As a result, the classifier designed in this work operates rather good.

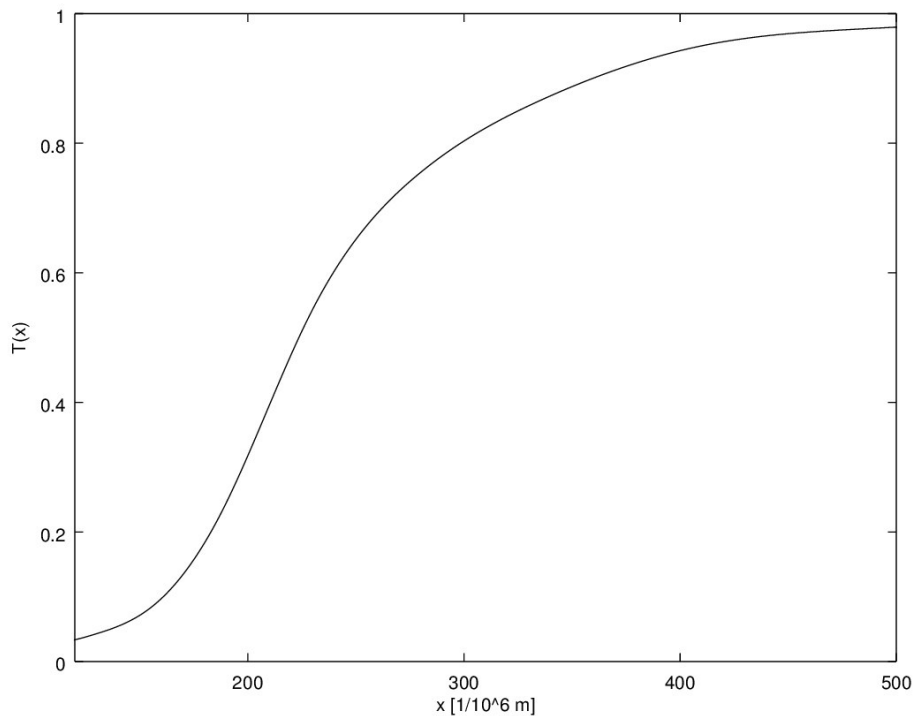


Figure 7-6: Degree of separation dependent on particle size x [μm].

7.3 Mass flow rate vs. brush speed

7.3.1 Correlation between voltage and rotational speed

Figure 7-7 shows the correlation between the applied voltage U [V] of the power supply and the optically measured rotational speed of the drive shaft n [rpm] for 88 performed experiments distributed over different voltage settings. The figure shows qualitatively, that the reproducibility of n [rpm] increases with higher voltage settings, as the spread of the points in the graph decreases. Over all experiments a linear correlation between the adjusted voltage signal at the power supply and the measured rotational speed of the drive shaft of the brush can be found.

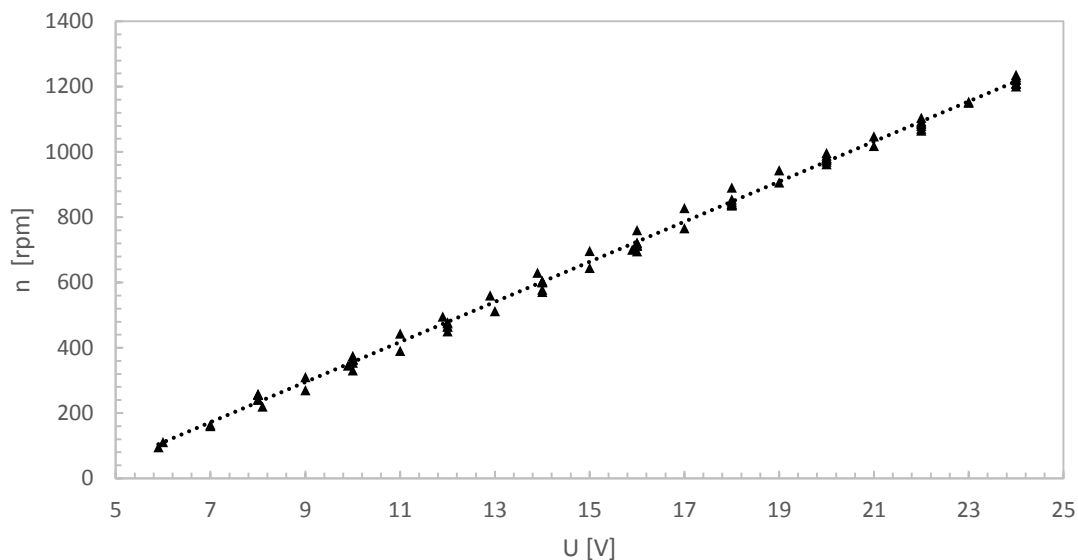


Figure 7-7: Rotational speed of brush n [rpm] dependent on voltage signal U [V] for glass powder sized between 100 and 200 [μm], without using brush guiding bars and for all experiments performed in the first attempt (see Table 21).

Figure 7-8 shows time averaged measured mass flows for 88 experiments carried out with glass beads sized between 100 to 200 microns and with 14 experiments carried out with glass beads sized between 400 to 600 microns. The mass flow data \dot{m} [g/s] is on the one hand plotted over measured rotational speed of brush n [rpm], and on the other hand plotted over adjusted voltage U [V]. Both plots show a very similar shape, i.e., a linear correlation between brush speed and voltage. Therefore, and because of the only possibility of direct influence to the feeder by adjusting the voltage of the power supply, the following feeder experiments are investigated by plotting mass flow against voltage.

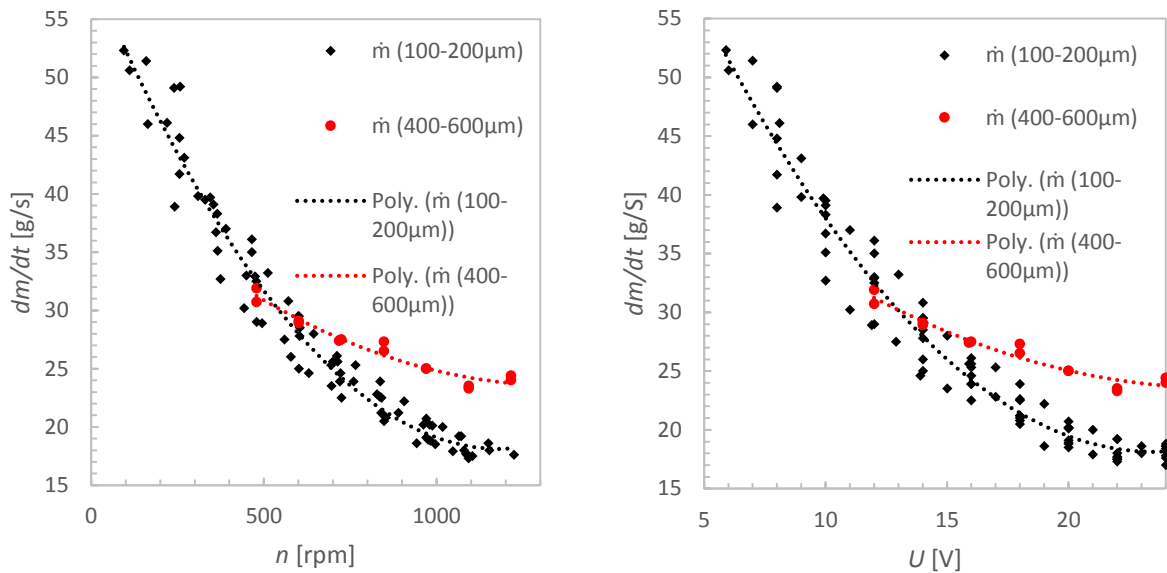


Figure 7-8: Mass flow of particles \dot{m} [g/s] versus the measured rotational speed of the brush [rpm] (left panel) and versus the voltage signal of the power supply U [V] (right panel) for two different glass beads (i.e., 100 to 200 microns and 400 to 600 microns).

7.3.2 Time and number averaged mass flow rates versus voltage

The time and number averaged mass flow values for the 100 to 200 [μm] glass beads, without use of brush guide bars, dependent on the adjusted power supply voltage (seen Figure 7-9). The mass flow decreases with increasing voltage, from ca. 45 [g/s] at 8 [V] to ca. 20 [g/s] at 20 [V], to maintain at nearly constant mass flow of ca. 18 [g/s] for voltages above 22 [V]. The standard deviation σ decreases with increasing voltage U . While a voltage setting of 8 [V] results in an averaged mass flow of 45 [g/s] \pm 3.7 [g/s], i.e., a standard deviation of 8.3 [%], a voltage setting of 24 [V] gives a mean mass flow of 18.1 [g/s] \pm 0.4 [g/s], i.e., a standard deviation of 2.3 [%]. Thus, the reducibility of experimental data increases with increasing voltage setting.

Figure 7-10 shows the time and number averaged mass flow for glass beads in a size range of 400 to 600 [μm], without using a brush guiding bar, as a function of the voltage. The plotted curve is qualitatively similar to the one shown before for the finer powder: the mass flow reduces with increasing voltage until ca. 20 [V]. Instead of being constant from that point, the mass flow reaches a minimum at 22 [V] to rise again at a voltage of 24 [V]. The standard deviations do not behave like for the fine powder. They are smaller on average, and do not show the tendency to decrease with increasing voltage.

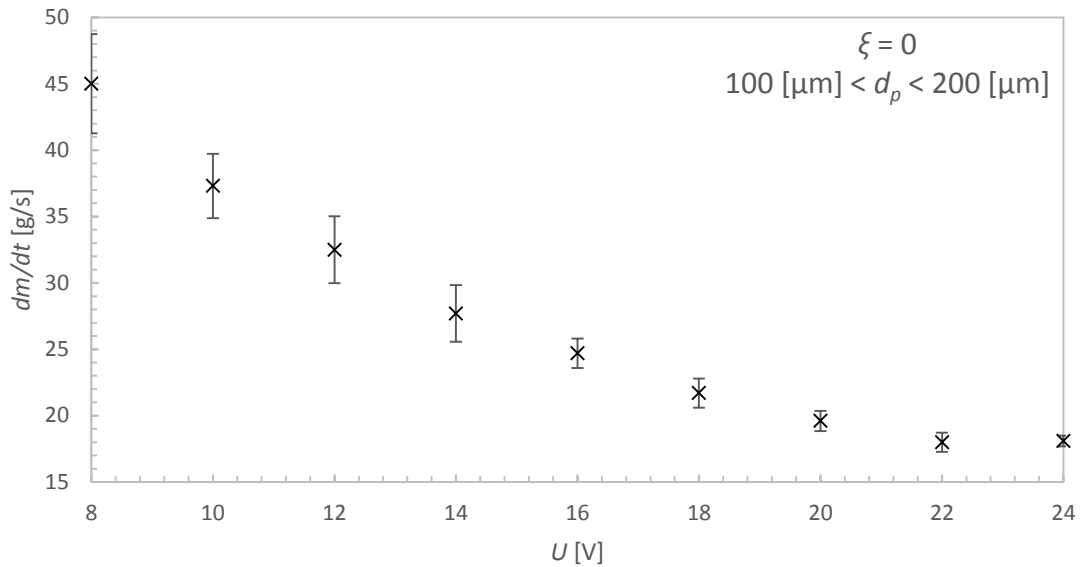


Figure 7-9: Time and number averaged mass flow values $\dot{m}_{averaged}$ [g/s] including their number averaged absolute standard deviations σ versus the applied voltage U [V] for glass beads sized between 100 and 200 μm and without brush guiding bars.

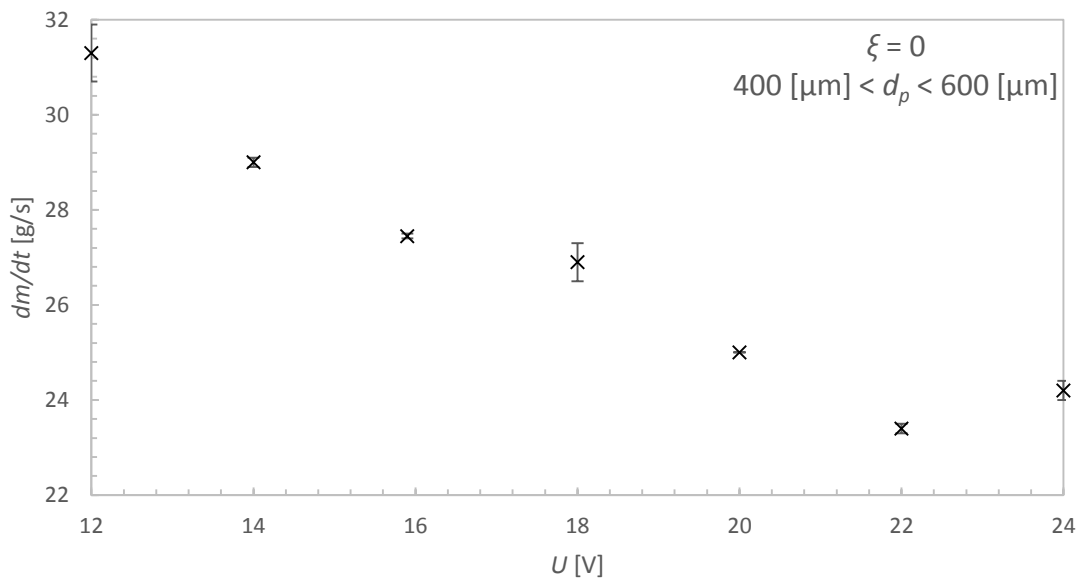


Figure 7-10: Time and number averaged mass flow values $\dot{m}_{averaged}$ [g/s] including their number averaged absolute standard deviations σ versus the applied voltage U [V] for glass beads sized between 400 and 600 μm and without brush guiding bars.

The documented mass flow over voltage of the fine glass powder starts at 45 [g/s] for 8 [V] and ends at 18 [g/s] at 22 [V], resulting in an averaged slope of 1.9 [g/Vs]. The averaged mass flow slope of the coarse glass powder is ca. 0.9 [g/Vs], i.e. being smaller.

To reduce the mass flow values in the operation line of the feeder, brush guiding bars are designed. Figure 7-11 shows the mass flow over voltage for 400 to 600 μm glass beads and for a brush pinch ζ of 4 [mm]. Comparing it with Figure 7-10, it can be seen, that both operation

lines show a decrease of mass flow with increasing voltage within 14 [V] and 22 [V]. The described minimum at 22 [V] for the experiment without guiding bars can be also observed in Figure 7-11. The greatest qualitative difference is the observed slight increase of mass flow from 12 [V] to 14 [V] which differs from the operation line of Figure 7-10. Quantitatively, a brush pinch of 4 [mm] reduces the mass flow for each voltage setting. The maximal reached mass flow reduces from 31 [g/s] without guide bars to 23 [g/s] with a brush pinch of 4 [mm], while the minimum mass flow reduces from 23 [g/s] to 17 [g/s]. The averaged slope, being 0.8 [g/Vs] when applying 4 [mm] brush pinch, does not differ dramatically from the experiment without guide bars. The averaged standard deviations increase.

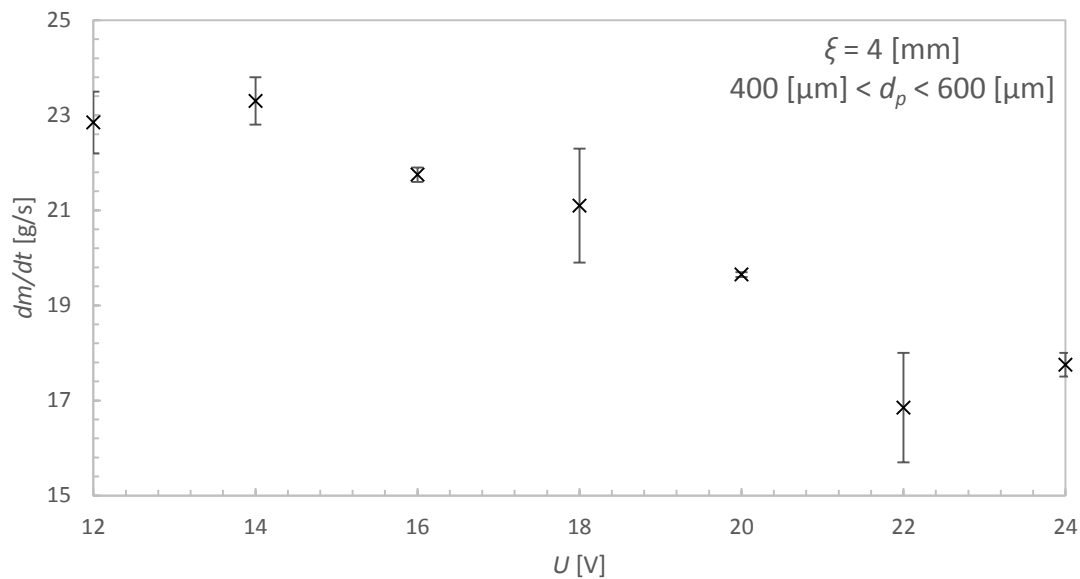


Figure 7-11: Time and number averaged mass flow values $\dot{m}_{averaged}$ [g/s] including their number averaged absolute standard deviations σ versus the applied voltage U [V] for glass beads sized between 400 and 600 μm and with an adjusted brush guide bar pinch of $\xi = 4$ [mm].

A similar situation can be observed in Figure 7-12, which shows the mass flow over voltage for the fine 100 to 200 μm glass powder and a brush pinch of $\zeta = 4$ [mm]: The characteristic decrease of mass flow with voltage is only valid between 16 [V] and 22 [V], instead of continuously decreasing between 8 [V] and 22 [V], see Figure 7-9. The maximal mass flow decreases from 45 [g/s] without guide bars to 20 [g/s], being even smaller than maximum reached for the coarse powder with the same brush pinch. The minimal mass flow also decreases from 18 [g/s] to 13 [g/s]. The averaged slope between 16 [V] and 22 [V] is ca. 1 [g/Vs] being around half of the slope investigated for the experiment without brush pinch. The standard deviations show the tendency to decrease with voltage, which meets the found tendency for the experiment without guide bars.

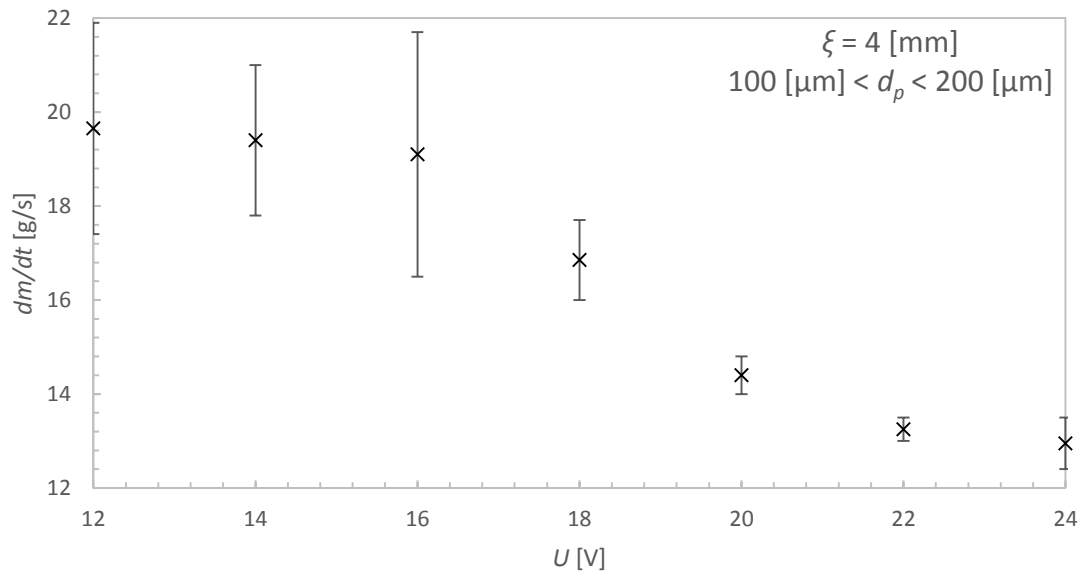


Figure 7-12: Time- and number averaged mass flow values $\dot{m}_{averaged}$ [g/s] including their number averaged absolute standard deviations σ versus the applied voltage U [V] for glass beads sized between 100 and 200 μm and with an adjusted brush pinch of $\xi = 4$ [mm].

The result of a further increase of brush pinch to $\xi = 5$ [mm] on each side can be seen in Figure 7-13 for the fine glass powder sized between 100 and 200 microns. While the maximum of the reached mass flow decreases from 20 [g/s] to 17.5 [g/s], the minimum of the reached mass flow increased from 13 [g/s] to 15 [g/s]. The averaged mass flow decreases nearly linear from 12 [V] to 24 [V] without showing any constant section as it is observed in the experiments before.

The mass flow curve for the coarse glass powder metered with a brush pinch of $\xi = 5$ [mm] behaves completely different. Its maximum mass flow increases from 23 [g/s] to 27 [g/s] by increasing pinch from 4 [mm] to 5 [mm], while its minimum mass flow at 24[V] also increases from 17 [g/s] to 20 [g/s], i.e. the whole operation curve increases. Its qualitative behaviour is not as linear as it is observed for the fine glass powder at the same brush pinch setting.

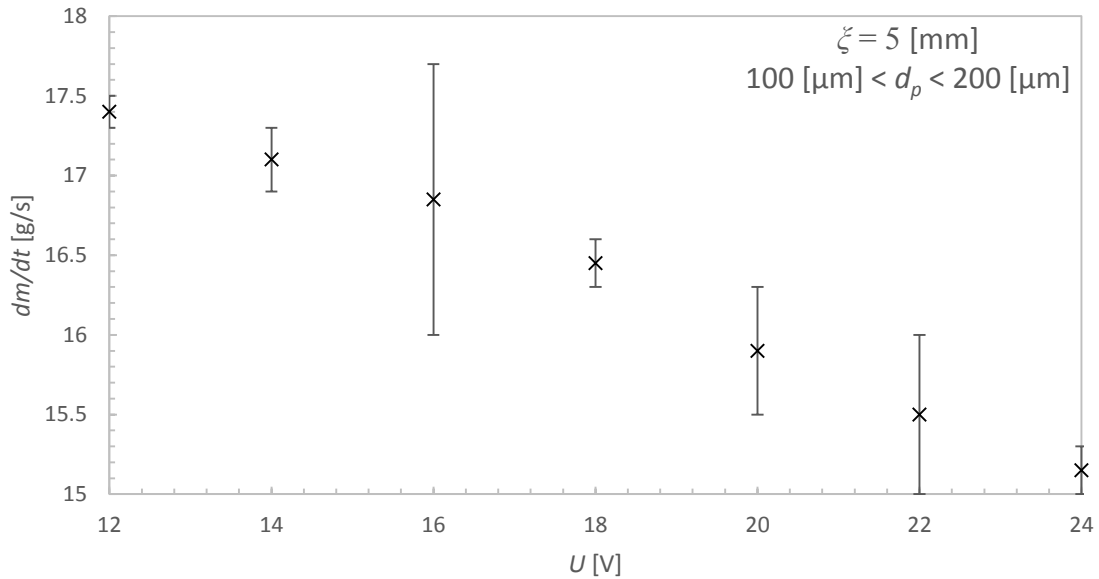


Figure 7-13: Time- and number averaged mass flow values $\dot{m}_{averaged}$ [g/s] including their number averaged absolute standard deviations σ versus the applied voltage U [V] for glass beads sized between 100 and 200 μm and with an adjusted brush pinch of $\zeta = 5$ [mm]

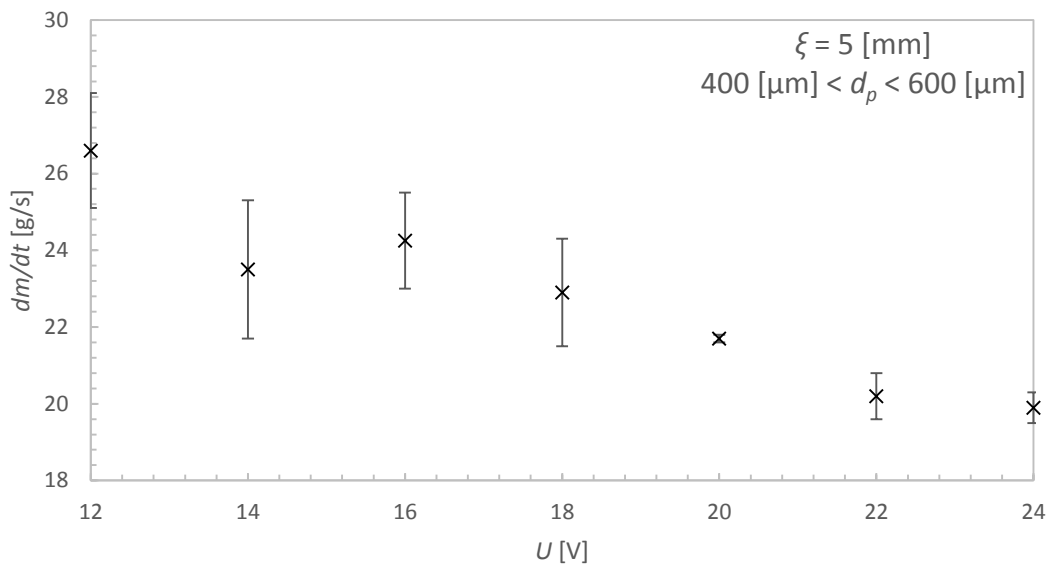


Figure 7-14: Time- and number averaged mass flow values $\dot{m}_{averaged}$ [g/s] including their number averaged absolute standard deviations σ versus the applied voltage U [V] for glass beads sized between 400 and 600 μm and with an adjusted brush pinch of $\zeta = 5$ [mm].

A possible reason for the rather unexpected increasing mass flow rate at an increased brush pinch might be, that by pinching the brush further, additional free room next to the brush is generated. The powder might not be fed only between the interface of the outer surface of the brush and the housing, but also within the generated (unwanted) gap next to the side walls of the brush.

7.3.3 Behaviour of mass flow dependent on filling height and feeding time

Figure A 1, see Appendix D.1, shows exemplary the mass flow rates of several experiments over fed particle mass, i.e., the mass difference divided by time difference at its actual scale signal. Therefore, the results of this investigation should only be interpreted in a qualitative way. All experiments in this figure are performed without using any brush guiding bars, and only for glass beads between 100 and 200 [μm] diameter. For an adjusted voltage at the power supply of 10 [V] the mass flow rates fluctuate between ca. 33 [g/s] and 43 [g/s]. Also, a slight downward slope, i.e., the mass flow rate tends to decrease with decreasing fill height, can be observed. This slight tendency cannot be found within all other experiments at different voltage settings. The mass flow fluctuation at a certain voltage setting decreases with increasing voltage: at a voltage of 24 [V] the mass flow rates fluctuate between 17 [g/s] and 20 [g/s].

Mass flow rates generated with the coarse glass powder (400 to 600 [μm]) and without using brush guiding bars do generally not show any tendency of positive or negative gradient, except the results found with a voltage of 20 [V]. These mass flow curves are directed slightly downwards, while all other mass flow curves are horizontal on average.

Using brush guiding bars and pinching the brush for 4 [mm] at each side, the mass flow curves for the fine powder are more or less horizontal on average, the curves for 12 [V] and for 14 [V] show a significant negative gradient. The mass flow curves for the coarse glass powder are found to be rather constant in mass flow over filling height.

An increase of brush pinching to $\zeta = 5$ [mm] at each side of the brush results in a rather undesired behaviour of the mass flow curves for the fine glass powder, because all curves show a significant slope downwards, i.e. mass flow decreases with decreasing filling height. The coarse powder instead flows out of the hopper nearly independent from hopper filling height. All mass flow curves are nearly horizontal in average.

7.4 Particle image velocimetry

7.4.1 Qualitative analysis of recorded images

To investigate how setting parameters of the pneumatic conveying system or of the classifying air influence the behaviour of particle injection, high speed image recordings of the injection area are made. Figure 7-15 shows one of these images for the first experiment (exp. #1). The upper and lower border of the injection pipe is marked by the visible weld seam and by the high particle concentration (i.e., the white spot on the bottom of the left corner of the picture). These particles indicate dunes in the conveying pipe. Thus, the particle concentration is observed to be rather homogeneously distributed over the whole height of the inlet pipe. The flow is interpreted as a “degenerate homogeneous flow”, according to the classification of Rudinger [17]. It is also visible, that the particle concentration on the top of the picture is nearly zero, and increases in the direction of gravity. Thus, a high particle concentration along the whole bottom line of the image can be observed.

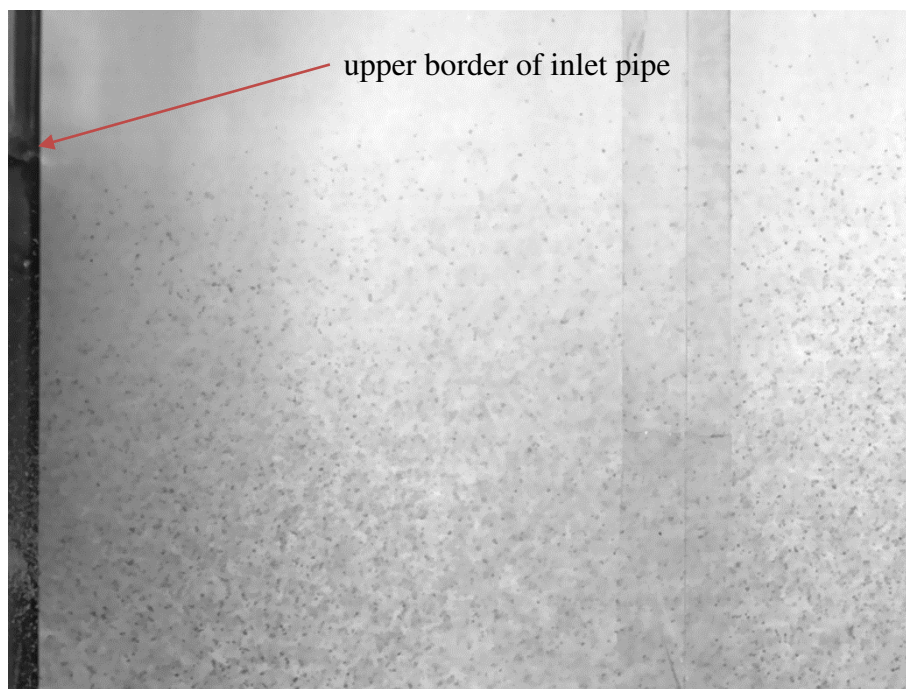


Figure 7-15: High speed image of experiment #1.

Figure 7-16 shows a high speed image of the second experiment (exp. #2). The vertical borders of the inlet pipe can also be seen and are marked by red lines. There is no high particle concentration at the lower end of the inlet pipe, i.e. there is no evidence for dunes in this configuration. The particle concentration is homogeneously distributed along the height of the inlet pipe. Again, the upper edge of the picture is free of particles. However, there are also almost no particles in the lower left corner of the picture. Some particles in the upper right end

of the image are moving upwards, while a major part of the particles move downwards and horizontally.

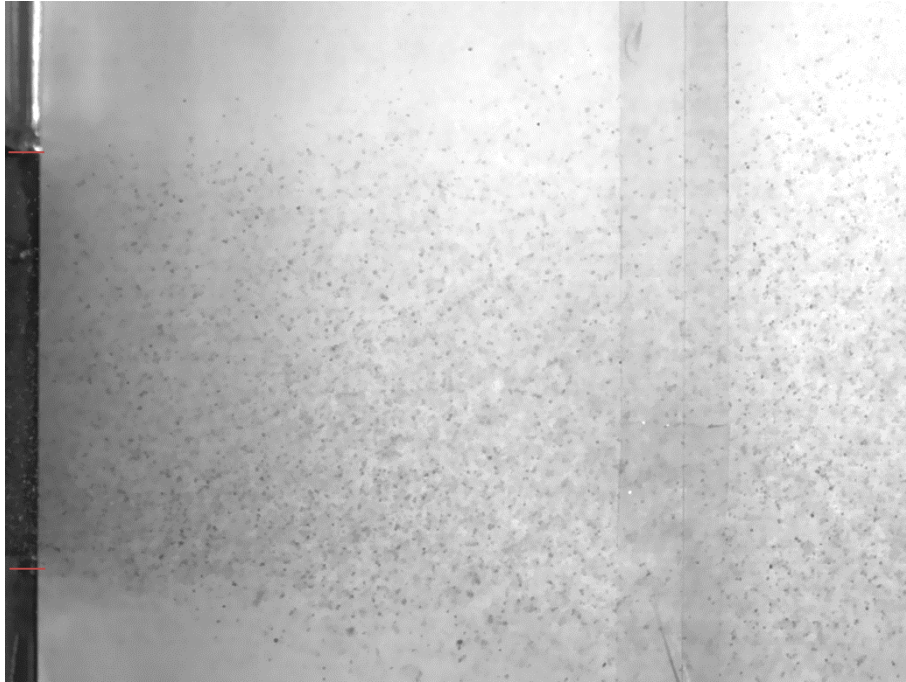


Figure 7-16: High speed image of experiment #2.

From Figure 7-17 to Figure 7-20 the geometry of the inlet pipe cannot be seen anymore, because the camera has been moved a bit to the right. While its distance to the observation window has stayed the same, the used powder is changed to glass beads sized between 400 and 600 [μm]. The first of these four pictures shows a high particle concentration in the lower left corner, while there are only sporadic particles in the right upper corner. Thus, dunes have formed in the inlet pipe. Comparing it to the second picture, i.e. Figure 7-18, there are less particles in the upper half of the image. The particle concentration in the lower left corner of the image decreases dramatically from experiment #3 to experiment #4, where a dilute conveying regime was observed. No significant qualitative differences can be observed between the pictures of experiment #4 and experiment #5. Here, a quantitative investigation should bring more information. In experiment #6 the particle concentration is significantly lower than in all other recorded experiments. Particles are observed to be homogeneously distributed over the whole image. For the last three experiments (exp. #7-9) the feeder is mounted directly to the inlet pipe of the classifier, i.e., the relaxation pipe is left out, and the gas velocity U_3 is set to zero. The first two pictures show experiments with glass powder, 400 to 600 [μm]. In both images particles are homogeneously distributed over the whole picture, and a dilute flow was observed. Experiment #9 was performed with quartz powder, resulting in a very high particle concentration at the bottom of the inlet pipe, i.e., a dense phase conveying regime was present.

This dense stream is deflected by the classifying air in upwards direction. There are only sporadic particles located above the dense stream.

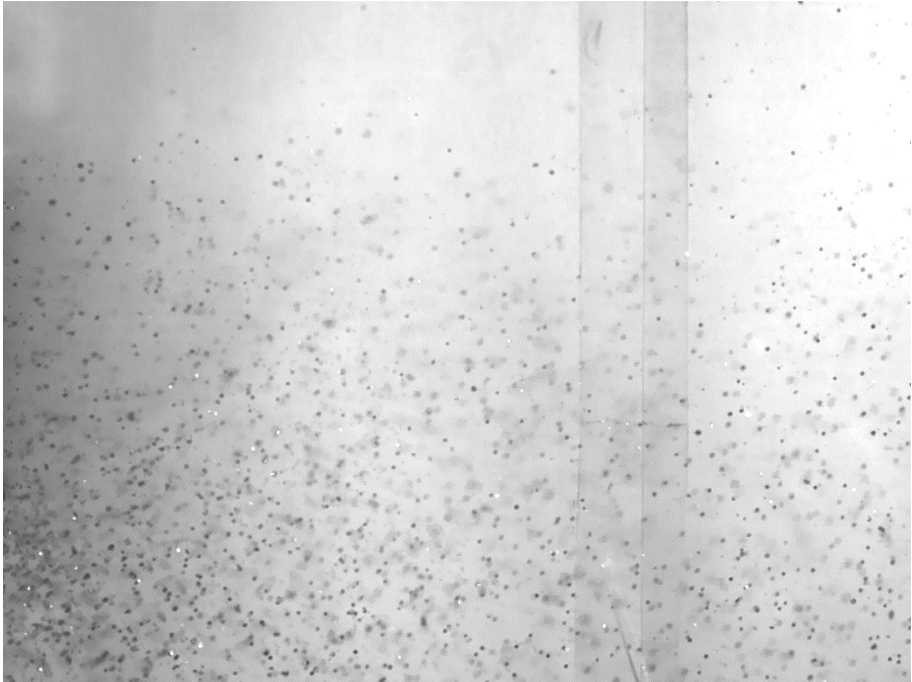


Figure 7-17: High speed image of experiment #3.



Figure 7-18: High speed image of experiment #4.

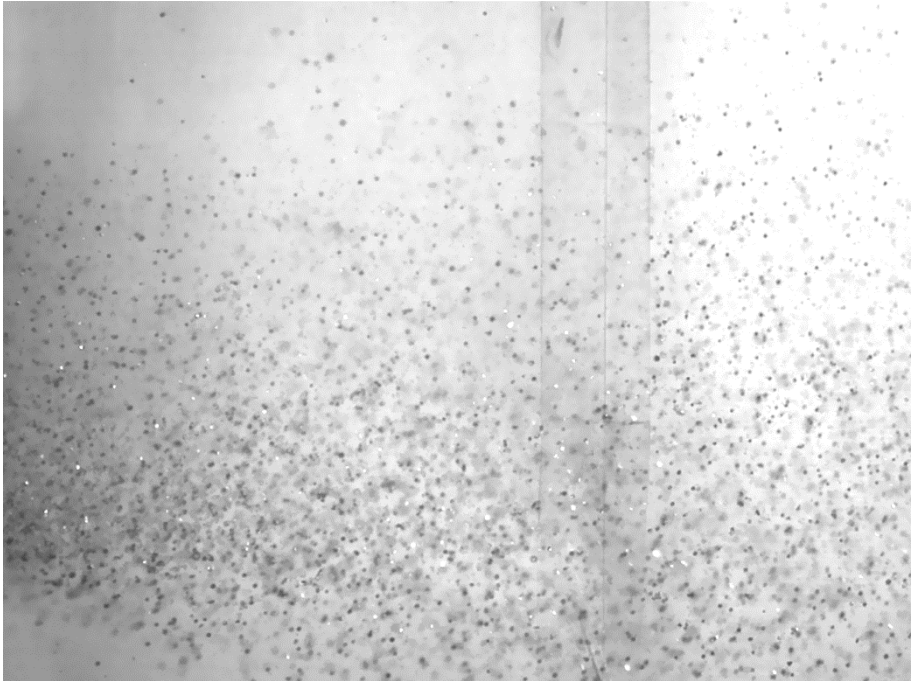


Figure 7-19: High speed image of experiment #5.

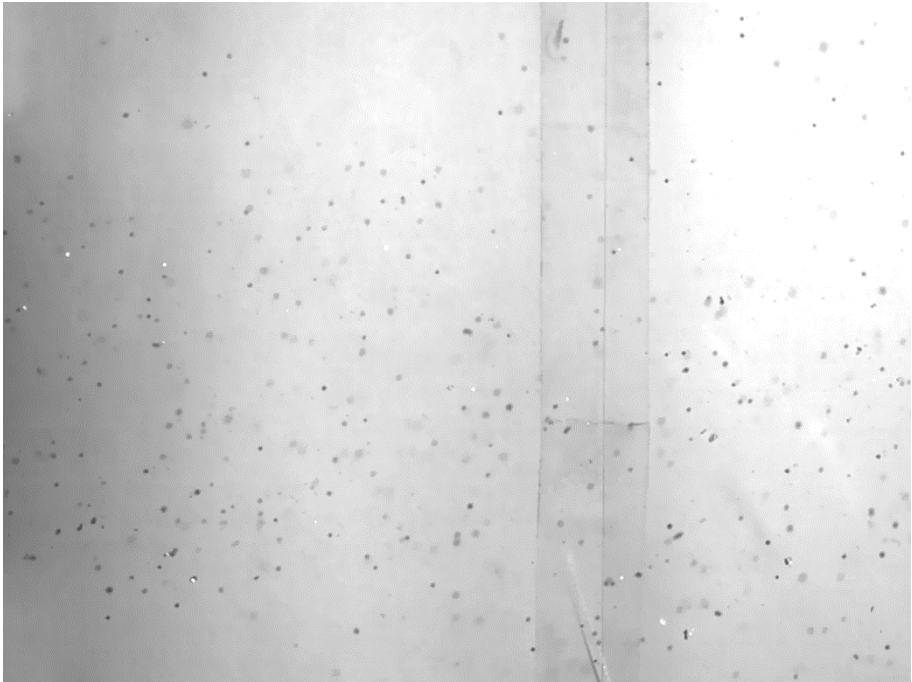


Figure 7-20: High speed image of experiment #6.



Figure 7-21: High speed image of experiment #7.



Figure 7-22: High speed image of experiment #8.



Figure 7-23: High speed image of experiment #9.

7.4.2 Quantitative analysis of the particle flow field

7.4.2.1 *Spatial velocity distribution*

In order to support the experimentally-determined data, the relaxation of the particles in the relaxation tube was calculated for every experimental setting. These calculations take the particle's pre-acceleration (due to the motion of the brush) into account. Also, these calculations are performed assuming an infinitely dilute gas-particle suspension, and hence do not consider effects induced by the high particle mass loadings.

Figure 7-24 compares the calculated relaxation curves with the experimentally-determined velocity field, illustrated as a contour plot including velocity vectors, at the inlet of the transverse flow into the classifier (i.e., at $x_e = 1.45$ [m]) for experiment #1. The initial velocity of particles $u_{p,0}$ was assumed to be equal the circumferential speed of the brush, in this case 6.7 [m/s]. The gas speed U_3 is adjusted to 5 [m/s]. The calculation predicts that the smallest particles ($d_p = 100$ [μm]) approach to the superficial gas velocity within the available relaxation length. The biggest particles will still be 5.8 [m/s] fast. The fastest measured averaged velocity for this experiment is slightly smaller than 5 [m/s], and is located in a rather limited area of the picture. As a result, all particles measured in this experiment are slower than the estimated minimum velocity of the particles being 5 [m/s], i.e., they have not relaxed to the superficial gas velocity. One reason for that could be, that the gas velocity decreases by false air, although all interfaces between flanges and feeder are equipped with seals. It could also be possible, that the initial velocity of particles differs from the expected velocity being the circumferential speed of the

brush. Another reason for particles being slower than expected by relaxation calculations are slip effects. The slip ratios calculated by the correlations of Holdich [16] and Narayan and Prakash [52] assume, that particles are accelerated by air to reach a force balance, as shown by Brauer [43]. This force balance defines the slip ratio between particle and gas velocity. As the initial velocity of particles is expected to be higher than the superficial gas velocity, and though the calculated relaxation of particles will not be completed within the length of the pipe, the correlations for slip are difficult to apply. Particle relaxation and slip effects interfere with each other. If particles relaxed to the maximum particle velocity defined by the slip ratio, they would, relating to the correlation of Holdich [16], have a velocity of $3.7 \text{ [m/s]} < u_p < 4.0 \text{ [m/s]}$. This meets the measured particle velocities by PIV.

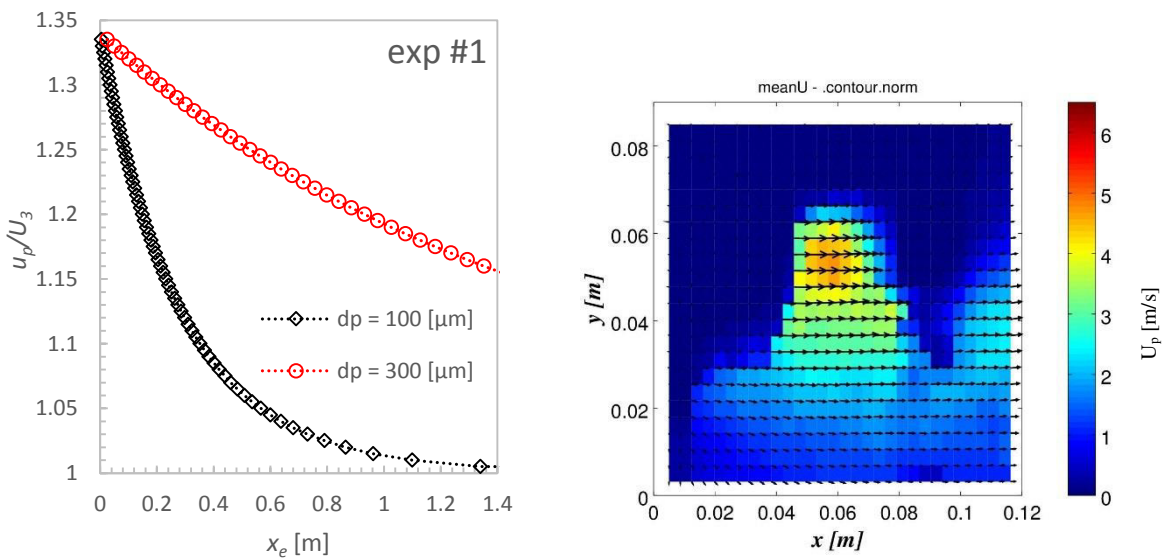


Figure 7-24: Calculated relaxation u_p/U_3 dependent on the relaxation length x_e [m] (left panel) vs. mean particle velocity profile u_p [m/s] measured by PIV and averaged over 2999 picture pairs (right panel) for experiment #1. The colours represent the magnitude of the particle velocity.

Figure 7-25 shows the above explained comparison between calculated and experimental data for experiment #2. The experimental parameters are equal except for the superficial gas velocity U_3 being now 6 [m/s]. The velocity field shows higher values over a larger area of the image. As illustrated in experiment #1, the velocity values decrease from top to bottom of the observed area. The lower vectors point downwards, same as in experiment #1. Generally, the comparison between both experiments makes sense, as the averaged particle velocity in experiment #2 is higher than in experiment #1. The calculated particle velocity due to slip lies between 4.3 [m/s] and 4.7 [m/s], assuming that the slip effects interfere the relaxation effect in a way to reach the status of balanced forces. The maximum velocities found by PIV are around 5 [m/s].

The measured velocity profiles of experiment #1 and experiment #2 both show large regions of zero velocity. Compared to the original pictures of the particle distributions in Figure 7-15 and Figure 7-16, these zero-values do not make sense in a physical way. Possible reasons for that zeros might be, that the contrast between particles and background was too small in these regions for the camera system in combination with the PIV algorithm to detect particles. Another error source is, that rather fine particles have been used in these experiments, which are more difficult to detect as bigger ones.

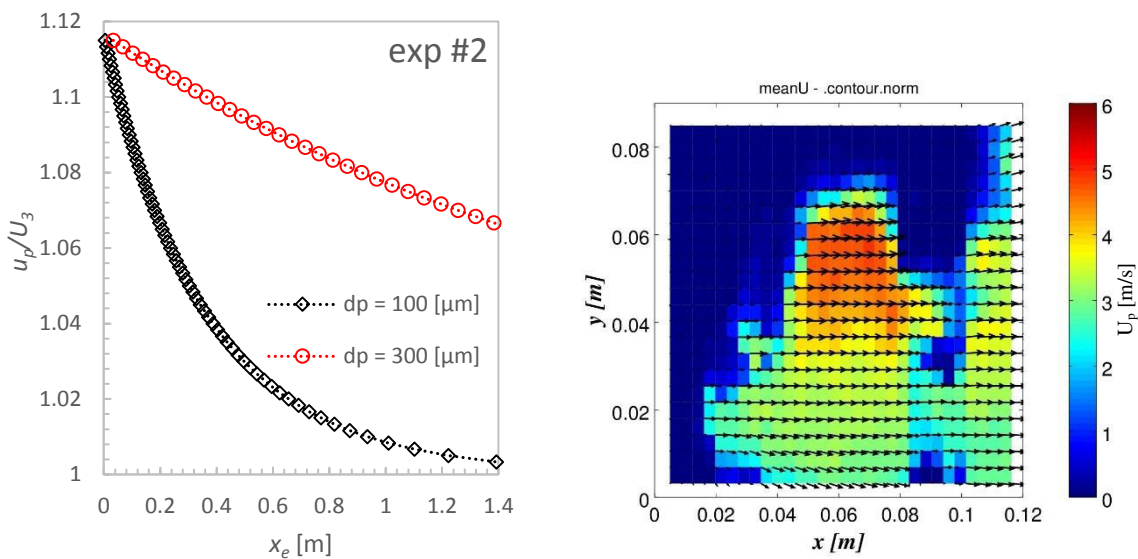


Figure 7-25: Calculated relaxation u_p/U_3 dependent on the relaxation length x_e [m] (left panel) vs. mean particle velocity profile u_p [m/s] measured by PIV and averaged over 299 picture pairs (right panel) for experiment #2. The colours represent the magnitude of the particle velocity.

The corresponding values for experiment #3 are shown in Figure 7-26. The calculated inlet velocities of the particles are 1.4 times respectively 1.5 times the superficial gas velocity $U_3 = 4$ [m/s] for each the finest and the coarsest particles. Thus, calculated particle velocities lie between 5.6 [m/s] and 6 [m/s]. The calculated equilibrium particle velocities due to slip lie between 2.6 [m/s] and 2.7 [m/s], relating to the correlation of Holdich [16]. The measured values lie in between those calculated values, as the highest measured velocity lies at ca. 4 [m/s]. This might be a result of interfering effects between relaxation and slip. The velocity field fills out almost the whole area of the picture, compared to the previous two experiments and, can be separated in three characteristic regions. While in the upper half of the image particles move rather horizontally with velocities above 2 [m/s], the lower part of the picture shows mainly velocity vectors pointing flat downwards at velocities smaller than 2 [m/s]. The area in the lower left edge shows particles moving steeply downwards at velocities smaller than 1 [m/s]. These regions meet the dense phase conveyance regime found in the qualitative

investigation of the corresponding image. While the dunes are falling down at the lower edge of the inlet pipe, the free flowing particles flow into the classifier above the dunes with higher velocities.

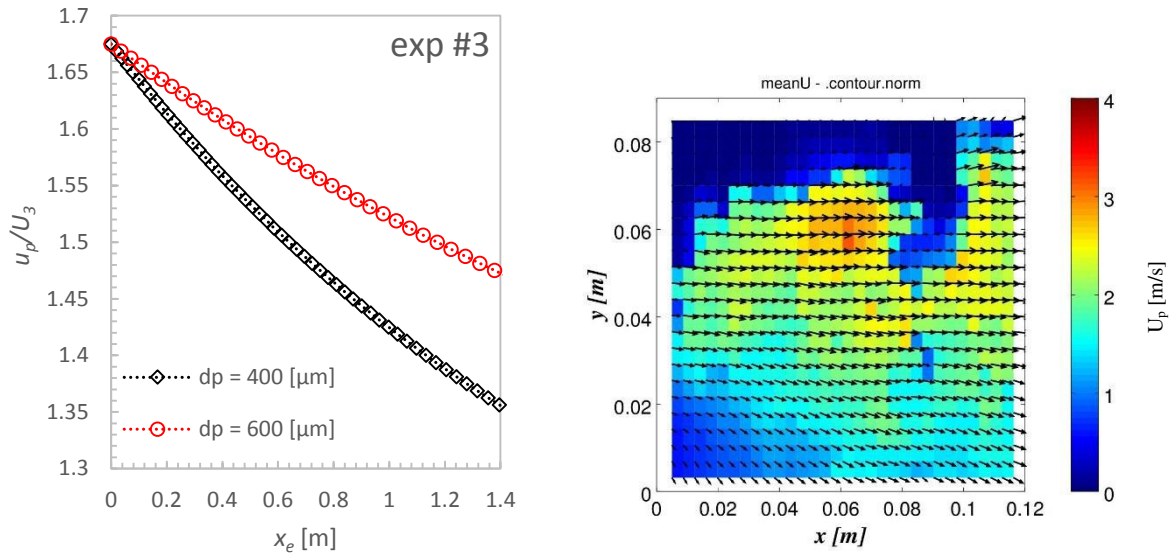


Figure 7-26: Calculated relaxation u_p/U_3 dependent on the relaxation length x_e [m] (left panel) vs. mean particle velocity profile u_p [m/s] measured by PIV and averaged over 299 picture pairs (right panel) for experiment #3. The colours represent the magnitude of the particle velocity.

Experiment #4 is carried out at the same conditions as exp #3, but the superficial gas velocity U_3 is increased to 5 [m/s]. The result is a much more homogeneous velocity profile and velocities higher than 2 [m/s]. The downward movement of the particles in the lower left edge of the image is less pronounced. Qualitatively, the measured results meet the observed particle behaviour in the qualitative investigation of this experiment rather good. The calculated inlet velocities differ again from the measured ones.

In experiment #5, see Figure 7-28, the expected initial velocity of particles is decreased to 3 [m/s] at a superficial gas velocity of 5 [m/s], while its mass loading within the conveying pipe has increased to a higher value compared to experiment #3. In the latter experiment the dune conveying regime as observed. This cannot be observed in experiment #5, neither in the qualitative observation of particle motion, nor in the measured velocity field. Comparable to experiment #4, a rather homogeneous velocity profile was observed. Unlike to the previous experiments, the calculated velocities caused by relaxation, which lie at 4.1 [m/s] meet the averaged maximum of the measured velocities rather good. The calculated equilibrium velocity caused by slip effects is between 3.2 [m/s] and 3.4 [m/s], which lies also within the measured maximum values.

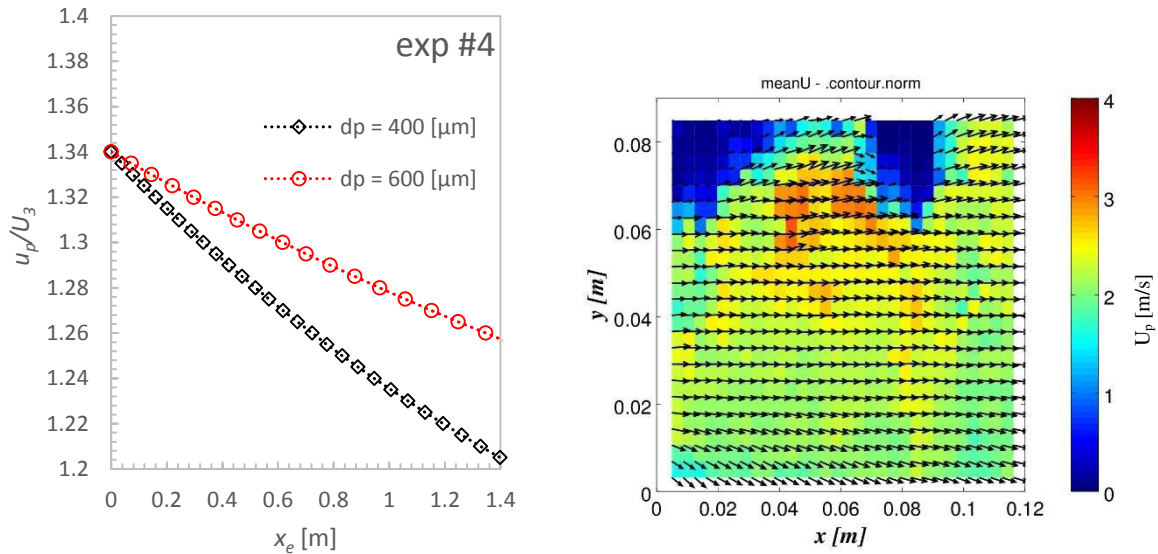


Figure 7-27: Calculated relaxation u_p/U_3 dependent on the relaxation length x_e [m] (left panel) vs. mean particle velocity profile u_p [m/s] measured by PIV and averaged over 299 picture pairs (right panel) for experiment #4. The colours represent the magnitude of the particle velocity.

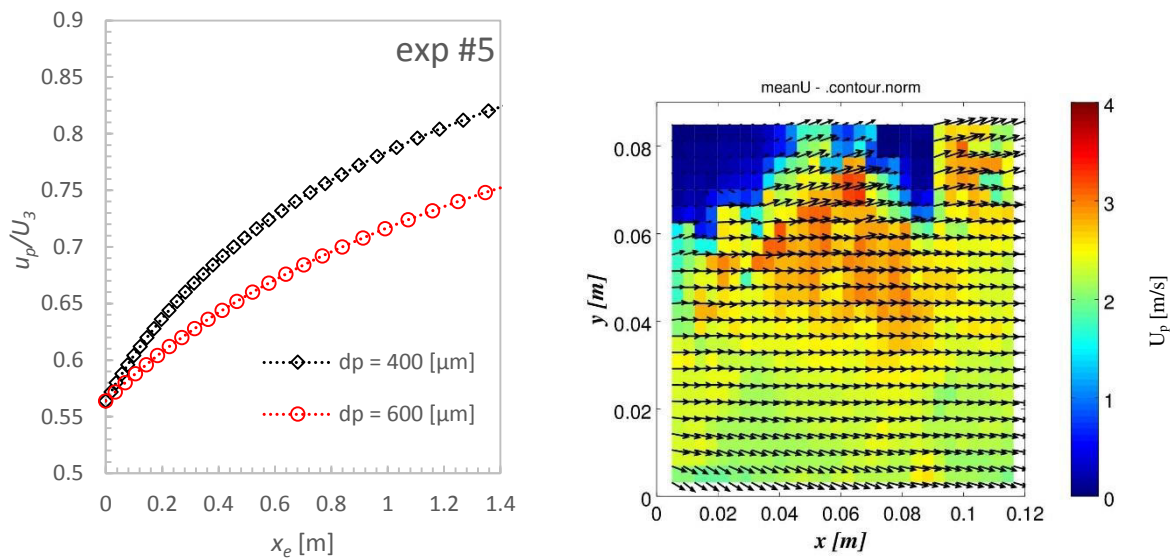


Figure 7-28: Calculated relaxation u_p/U_3 dependent on the relaxation length x_e [m] (left panel) vs. mean particle velocity profile u_p [m/s] measured by PIV and averaged over 299 picture pairs (right panel) for experiment #5. The colours represent the magnitude of the particle velocity.

In experiment #6 the brush speed is set to zero, while the superficial gas velocity stays at 5 [m/s]. Probably due to the very low mass loading in the classifying section with $\mu < 0.1$ the camera did not detect all particles, as there are certain regions showing zero velocities. Compared to the real image showing the particles flowing into the classifier, see Figure 7-20, there are two vertical stripes within the picture with a darker background: on the one hand a little shadow is thrown by the side wall of the classifier in the inlet region, on the other hand the vertically positioned tape holding the white background in position, appears darker than the

rest of the background. This lack of illumination combined with a rather low particle mass loading might lead to these peculiar PIV results. However, the measured maximum velocities meet the calculated values rather good.

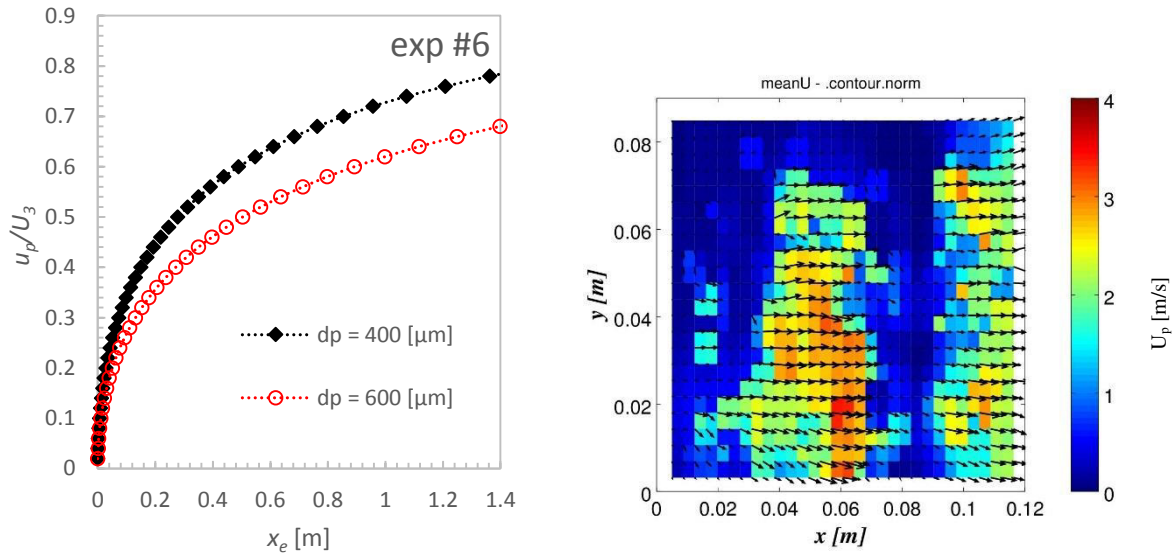


Figure 7-29: Calculated relaxation u_p/U_3 dependent on the relaxation length x_e [m] (left panel) vs. mean particle velocity profile u_p [m/s] measured by PIV and averaged over 299 picture pairs (right panel) for experiment #6. The colours represent the magnitude of the particle velocity.

In experiment #7, see Figure 7-30, the superficial gas velocity U_3 is set to zero and the length of the conveying pipe is reduced to 0.25 [m]. This is done by leaving the relaxation pipe out. The velocity field fills nearly completely the whole picture except of a small vertical stripe on the left, an erroneous measurement occurred. In the x-direction a velocity reduction can be observed. Particles on the upper edge of the observed image tend to move upwards, while the vectors on the lower edge of the picture point in a downwards direction. The maximal velocities measured are ca. 2 [m/s], while the calculated values due to rotational speed of brush and relaxation within the small length of 0.25 [m] lie between 5.7 [m/s] and 6.2 [m/s]. Thus, the gap between measured and calculated values is comparably huge. This fuels the suspicion, that the simple estimation of the initial velocity of the particles $u_{p,0}$ being equal the circumferential velocity of the brush is not precise.

In experiment #8, see the data in Figure 7-31, the circumferential speed, and therefore the expected initial speed of the particles, is decreased to 5.4 [m/s]. The velocities in the velocity profile decrease compared to that observed in experiment #7. This makes physically sense. In the left bottom corner of the image of experiment #8 also the dark background of the inlet geometry can be seen. Unlike the result for experiment #7, particle velocities are detected here. These particle velocities are very small, i.e., less than 1 [m/s], but increasing when leaving

above mentioned dark region. This is unrealistic, since particles velocities should rather decrease than increase when entering the classifier section.

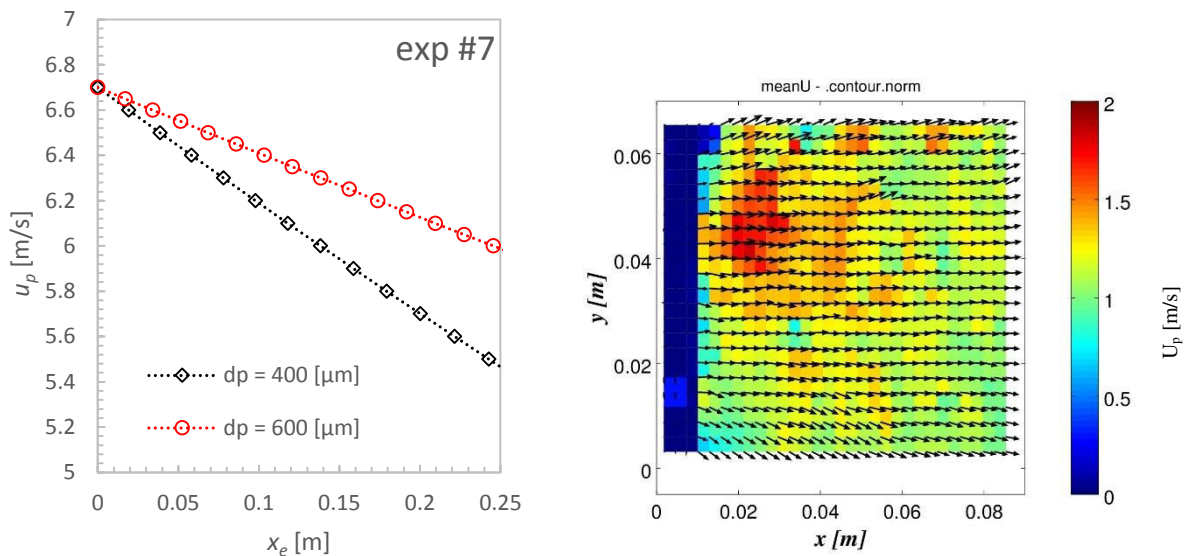


Figure 7-30: Calculated relaxation u_p/U_3 dependent on the relaxation length x_e [m] (left panel) vs. mean particle velocity profile u_p [m/s] measured by PIV and averaged over 299 picture pairs (right panel) for experiment #7. The colours represent the magnitude of the particle velocity.

Figure 7-32 shows the calculated and experimental data for experiment #9. The calculated particle velocity of the smallest particles decreases within the available relaxation length to a velocity smaller than 1 [m/s], while the coarsest particles still have a speed larger than 5 [m/s]. Thus, the speed of the particle cloud should have velocities within these boundaries. The measured velocity field shown in Figure 7-32 shows large regions with zero velocities, indicating that the PIV algorithm was unable to determine the particle velocity in these regions. The vertical region on the left of the picture is explained by the visible frame geometry of the inspection glass of the classifier. In the upper left corner there are almost no particles visible on the original image (see Figure 7-23). The dark blue region in the middle of the image can be explained by the highly loaded particle stream in this area: in this dense cloud particles cannot be detected neither by the eyes of the author nor by PIV. The particle strand consisting out of rather small particles relaxes rather fast to the classifying air velocity, as particles move rather steep upwards. Particle velocities around 5 [m/s] cannot be detected by the PIV. Thus, the difference between calculated values and measured values can be either explained by (i) an incorrect estimate of the initial particle speed induced by brush speed, or (ii) by the fact, that a strongly developed strand conveyance occurred and many particles stayed inside of the pipe after the experiment stopped.

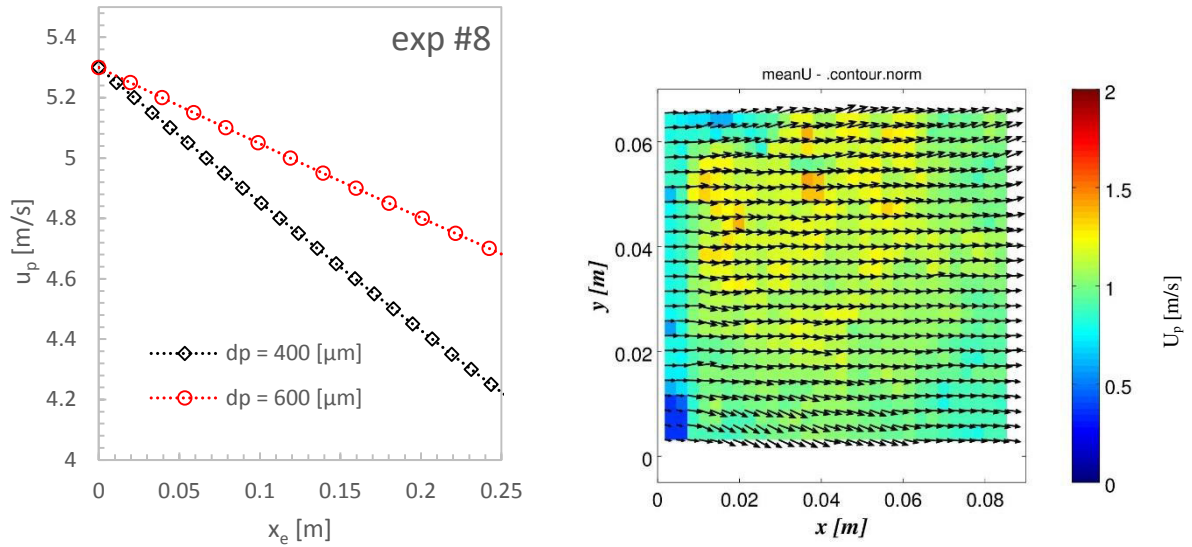


Figure 7-31: Calculated relaxation u_p/U_3 dependent on the relaxation length x_e [m] (left panel) vs. mean particle velocity profile u_p [m/s] measured by PIV and averaged over 299 picture pairs (right panel) for experiment #8. The colours represent the magnitude of the particle velocity.

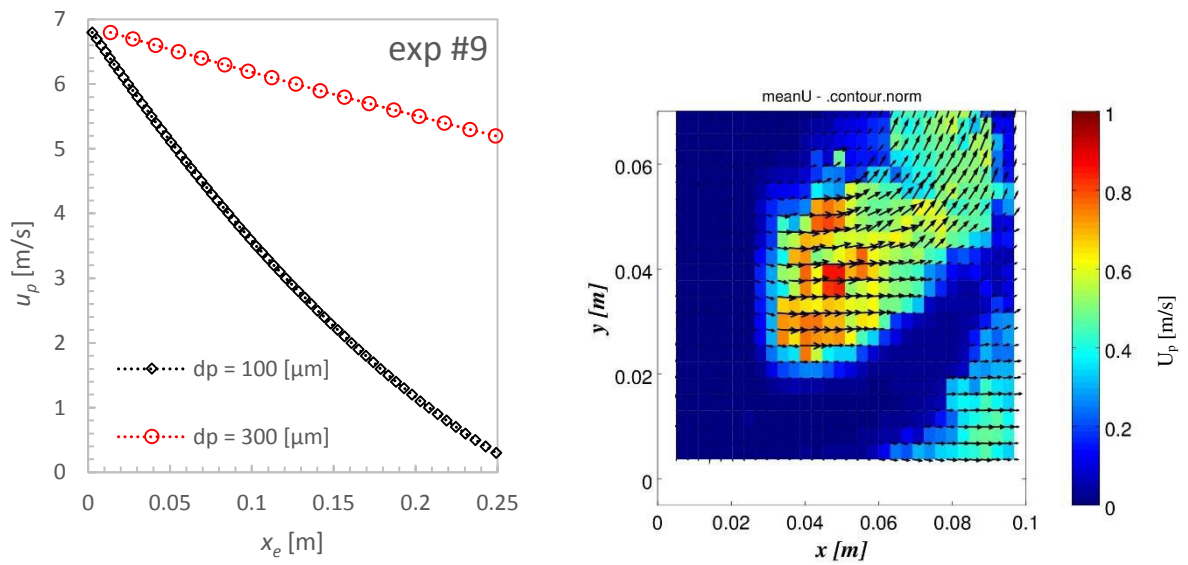


Figure 7-32: Calculated relaxation u_p/U_3 dependent on the relaxation length x_e [m] (left panel) vs. mean particle velocity profile u_p [m/s] measured by PIV and averaged over 299 picture pairs (right panel) for experiment #9. The colours represent the magnitude of the particle velocity.

7.4.2.2 Temporal evolution of the particle velocity

The above figures showed the time-averaged local mean particle velocity distributions. They do not allow an interpretation if the experiment was performed in the quasi steady state, i.e., if the same local (time-averaged) velocity distribution would have been observed at another observation time window. Therefore, velocities, separated in their x and y direction, were plotted over the observation time. This time was 1.5 [s] for each experiment, i.e., 3,000 images have been recorded with a frequency of 2,000 [Hz]. The local velocity distribution is not averaged, but for each experiment only the velocity in one interrogation window (out of the 31 x 23 windows) is plotted over time. For experiment #1 to #8 the same position of this window is chosen, i.e., the 20th row in the 10th column, see the red circle in Figure 7-33, left panel. For experiment #9 the camera system did not detect particle velocities in this region. Thus, for experiment #9 the 5th row in the 25th column is chosen; see Figure 7-33, right panel.

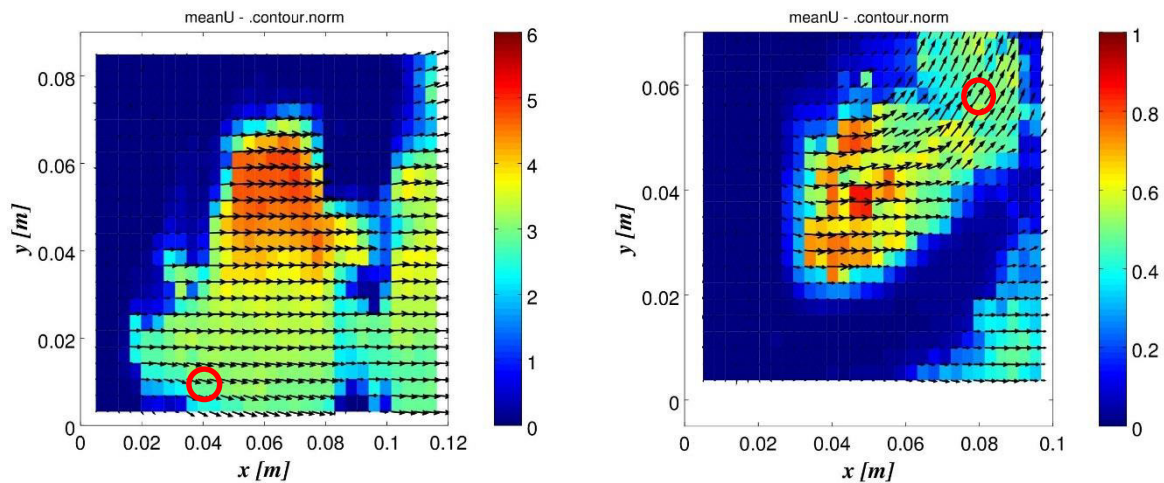


Figure 7-33: Chosen cluster for temporal velocity trend, exemplary for experiment #1 (left panel) and for experiment #9 (right panel). The colours represent the magnitude of the particle velocity.

The thereby detected velocity values are summarized in Appendix E.1, showing the velocity components versus time. In summary, the averaged velocity for each experiment stays rather constant over time based on a qualitative analysis with the naked eye. Thus, a quasi-steady state was present for all experimental data recorded.

8 Discussion and Conclusion

8.1 Feeding unit

Compared with the mass flow curves found by Leschonski [41], the current feeder does not work with the initially desired operation curve: while for Leschonski's feeder the mass flow increases with increasing rotational speed, the current feeder does the opposite: the mass flow reduces with increasing rotational speed. One reason for that is, that the feed materials are very different for both feeders: while Leschonski feeds very fine (i.e., cohesive) TiO_2 powder with a particle size in the range of 1 $[\mu\text{m}]$, the current experiments were performed with free flowing particles with a diameter larger than 100 $[\mu\text{m}]$. Leschonski presumes that a higher rotational speed of the brush might lead to a decrease of fill rate, as particles are filled between the voids of the brush. He finds the desired operation curve between a brush speed of 100 and 600 $[\text{rpm}]$. With further increase of the brush speed, the mass flow stays constant at ca. 1.9 $[\text{g/s}]$ and even reduces slightly, see the red circle in Figure 8-1.

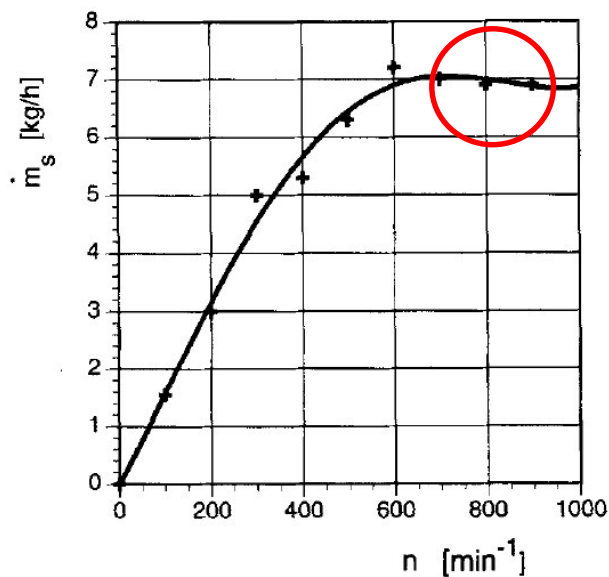


Figure 8-1: Mass flow rate \dot{m}_s [kg/h] versus rotational speed of the brush n [min^{-1}] [41].

The current feeder operates at feed rates between 12 $[\text{g/s}]$ (ca. 43 $[\text{kg/h}]$) and 45 $[\text{g/s}]$ (ca. 160 $[\text{kg/h}]$) with a minimal rotational speed of 95 $[\text{rpm}]$. The latter corresponds to a power supply voltage of 8 $[\text{V}]$. The maximum rotational speed is ca. 1200 $[\text{rpm}]$ corresponding to 24 $[\text{V}]$. Thus, a rather big range of different brush speeds can be covered with the current feeder (i.e., a 12.6-fold increase of the speed). Unfortunately, rotational speeds below 95 $[\text{rpm}]$ could not be tested.

The thickness of the effective powder layer inside the brush, as suggested by Leschonski, is also calculated for the current feeder. The brush surface A_b facing the downward moving powder stream is approximated with the arc length (corresponding to the opening angle of 77°) shown in Figure 8-2, and the width of the brush w_b .

$$A_b = l_\varphi w_b = d_b \pi w_b \frac{\varphi}{360^\circ} \quad 8-1$$

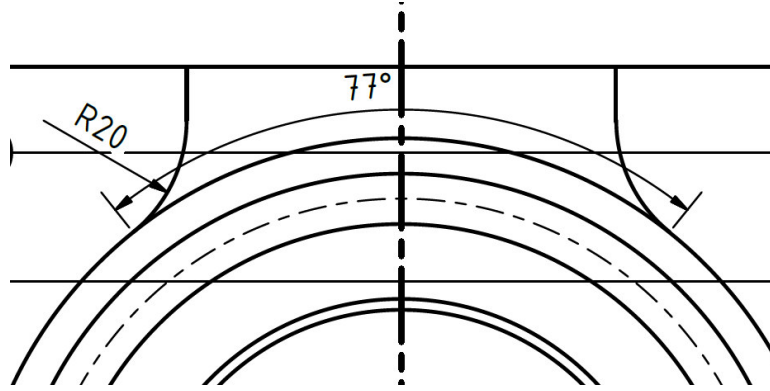


Figure 8-2: Free contact surface between powder and feeding brush.

This surface multiplied with the powder layer thickness δ results in the volume of powder inside of this part of the brush. The powder volume can be transformed into a powder mass by dividing it by bulk density ρ_b . The rate of filling of the brush section n_φ is calculated via the brush' rotational speed n [1/s], taking into account that only the opening angle φ is filled with particles:

$$n_\varphi = n \frac{360^\circ}{\varphi [^\circ]} \quad 8-2$$

$$\dot{V} = V n_\varphi \quad 8-3$$

$$\delta = \frac{\dot{m}}{\rho_b n_\varphi A_b} = \frac{\dot{m} \varphi}{\rho_b n 360^\circ d_b \pi \varphi w_b} 360^\circ = \frac{\dot{m}}{d_b \pi w_b \rho_b n} \quad 8-4$$

Table 10 shows the effective powder thickness within the brush, calculated from the experimental data collected for fine glass beads ($100 [\mu\text{m}] < d_p < 200 [\mu\text{m}]$), and without using brush guiding bars. The brush is filled completely in the first five test runs shown in Table 10, because the thickness δ exceeds the biggest diameter in the bulk. In the last two test runs the smallest particle diameter ($d_p = 100 [\mu\text{m}]$) exceeds the thickness δ . Therefore, the brush is not filled completely here. Compared with Figure 8-1, this does not reinforce the indication for the current brush feeder to operate far right from the characteristic operation line found by Leschonski.

Table 10: Effective thickness of powder layer δ inside of brush exemplary for different brush speed n [rpm] – mass flow \dot{m} [kg/s] configurations measured for fine glass powder, $100 [\mu\text{m}] \leq d_p \leq 200 [\mu\text{m}]$, and without using brush guiding bars.

n [rpm]	\dot{m}_p [g/s]	δ [μm]
250	45	1062
355	37	615
475	32,5	404
600	27,7	272
710	24,7	205
850	21,7	151
975	19,6	119
1080	18	98
1210	18,1	88

It is worth noting that Leschonski feeds fine and cohesive powder from a hopper made of flexible rubber, which is agitated at different positions to move the powder bulk downwards and to prevent bridging. Therefore, a certain downwards force is transmitted to the powder. There is no such force applied in the current system. The only reason for a decreasing powder fill with increasing rotational speed can be the increasing centrifugal force, which is increasing with rotational speed:

$$F_C = m\omega^2 r = m(2\pi n)^2 r \quad 8-5$$

Next to the above explained discrepancy to the referred feeder by Leschonski, the designed feeder operates rather reproducible for high voltage settings and without brush guiding bars. The reduction of voltage to values below 15 [V] lead to a rather undesirable standard deviation of the measured mass flow rates. One possible reason for that might be also that the error made by investigating the experimental data can rise with an increasing mass flow rate. Every 5 [s] a certain mass value displayed by the scale was noted. The instant in time when pressing stop, i.e., defining the 5 [s] varies maximal within one second. The mass flowing within this one second increases with increasing mass flow rate. Therefore, the error made by investigation should also be taken into account.

The relatively high spreads of mass flow rate over fed mass, which is documented in Appendix D.1, are also found in the publication of Molinder and Wiinikka [37]. In this latter publication a feeder is presented, which was designed to feed fuel particles at low and stable mass flow rates into a reactor, see Figure 8-3. Though the time discrete mass flow rates vary rather intensively, i.e., between less than 15 [mg/min] and more than 40 [mg/min], Molinda and Wiinikka [37] defined the feed rate as “stable”.

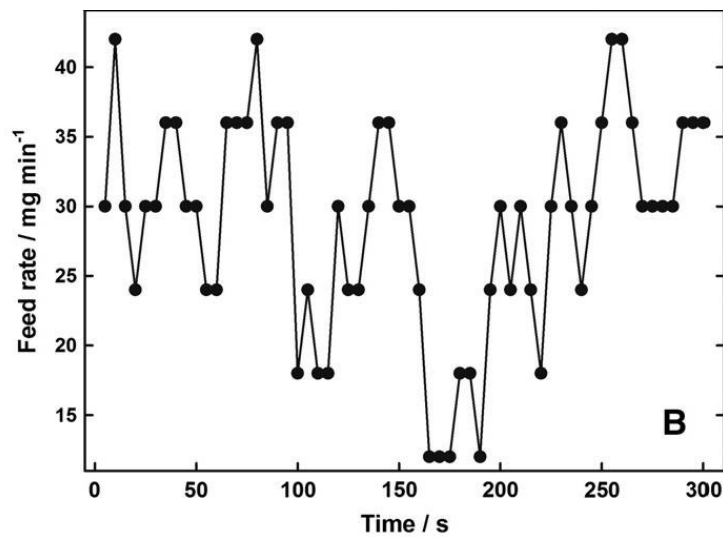


Figure 8-3: Mass flow rate of particles [mg/min] over time [s] of the particle feeder investigated by Molinder and Wiinikka [37].

Molinder and Wiinikka [37] benchmarked their investigated feeder with the regression coefficient R^2 , i.e., how much the mean mass flow rate of the feeder correlates with its corresponding setting parameter. The latter was the pusher block velocity in their study. The comparison of the measured regression coefficient for the brush feeder designed in the present work, where the power supply voltage is the setting parameter, shows that the designed brush feeder works rather well ($R^2 = 0.998$ for a polynomial regression function of 2nd order, see Figure 8-4). In case the regression is performed linearly, the regression coefficient decreases to $R^2 = 0.92$.

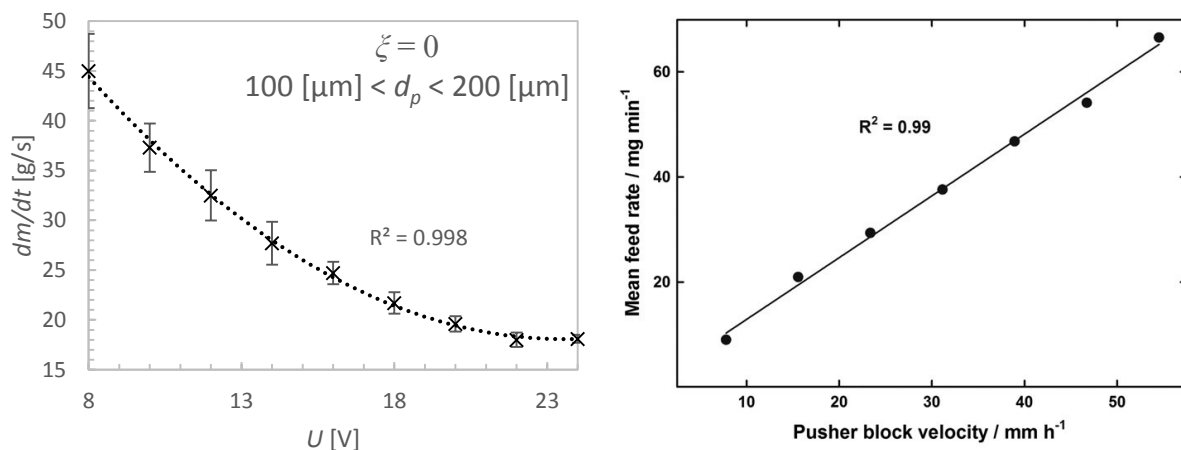


Figure 8-4: Correlation of the mean mass flow rate dm/dt [g/s] and the adjusted power supply voltage U [V] (left panel) compared to the correlation between mean mass flow rate [mg/min] and pusher block velocity [mm/h] of the feeder investigated by Molinder and Wiinikka [37].

The expected reduction of the mass flow rate when pinching the brush is only partly confirmed: a brush pinch to 4 [mm] reduces the mass flow rates, while a further increase of the pinch increases it again. This phenomenon is not considered to be an effect by the brush pinch itself,

but by the thereby changed geometry of the powder inlet. Another interesting phenomenon is that for a brush pinch of 5 [mm] the mass flow rate of particles decreases with decreasing fill height of the hopper in case the fine powder is used (100 [μm] – 200 [μm]). This phenomenon is not observed for the larger particles. Thus, it is speculated that the fine powder is able to trickle into a void region of the brush, leading to a fill height-dependent mass flow.

The obtained mass loadings realized by the present brush feeder – classifier combination are minimal $\mu_{min,cl} = 0.5$ [kg/kg] for the highest air flow rates of $\dot{V}_3 = 500$ [l/min] and $\dot{V}_4 = 1190$ [l/min], and for the lowest measured particle feed rate of $\dot{m}_p = 13$ [g/s] (using a brush pinch of $\xi = 4$ [mm]). The theoretical maximal possible mass loading $\mu_{max,cl} = 4.5$ [kg/kg] is realized for the highest possible particle mass flow rate of the brush feeder (i.e., $\dot{m}_p = 45$ [g/s]) and in case the minimum volumetric flow rate within the classifier (i.e., $\dot{V}_4 = 460$ [l/min]) is set.

8.2 Classifier performance

The present classifier test stand has to fulfil two tasks at once: on the one hand the tough minimal requirements concerning its feeding have to be complied to guarantee experimental data of high quality. On the other hand, several different student exercises have to be performed with the test stand. Therefore, a high modularity of the test stand is required, i.e., many possible experiment configurations have to be adjustable.

For mass loadings inside of the conveying pipe greater than 1.9 [kg/kg] (i.e., greater than 0.7 [kg/kg] in the classifier), and when using spherically shaped glass beads with a diameter between 400 [μm] and 600 [μm], useful experimental data could be produced. To scientifically investigate the behaviour of smaller particles, a sufficient illumination of the observed area is one of the limiting factors: the installed 100 [W] LED lamp appears to be appropriate for coarse particles, however, for fine particles a lens with magnification needs to be used, which requires a more extreme light source.

A dilute flow regime was observed for velocities lower than the expected saltation velocity, which demarcates the minimum velocity to realize a dilute flow. From this it can be concluded that the pre acceleration of particles helps to decrease the saltation velocity within the observed conveying length: Thus, particles have already a rather high kinetic energy when thrown into the conveying pipe via the brush feeder.

The investigation about the temporal velocity distribution of particles in the inlet area of the classifier in combination with the temporal distribution of mass flow rates of the feeder shows that the required steady state for JICF simulations can be guaranteed.

The new test stand brings also several possibilities for future laboratory exercises: the separation efficiency of the classifier can be investigated by varying the mass loading, the initial velocity of particles, the mass flow rate of the conveying air, the mass flow of the classifying air, as well as the material to be separated. Additionally, the length of the conveying pipe can be varied, and the results of these investigations can be compared to experiments performed with the zigzag sifter. The latter can be easily adapted to the current system. Next to that, PIV investigations can be performed for different settings.

Finally, a number of outlets covered with blind flanges was installed, which allow further permutations of the experimental setup. Explorative experiments performed using one of these outlets at the top of the classifier show an interesting behaviour: due to the larger size of this outlet the particles do not completely follow the air flow, but collide with the upper wall of the classifier. These particles are then collected in the coarse fraction container after flowing downwards following rather complex trajectories. Even this could be interesting for a laboratory exercise, in order to guide students in the correct design of outlets for classifiers.

9 Outlook

As the whole test stand is a prototype, there is still room for future investigations and for further development. For example, it could be tested how the brush feeder works for lower brush speeds, or in case different brushes are used. Furthermore, different powder chute geometries can be tested, which can be adapted to the brush pinch. The aim of these investigations should be to smoothen the mass flow curves versus the brush speed, and to increase the reproducibility for these settings. Another possible modification of the brush feeder could be an apparatus inside of the hopper pressing the powder towards the brush. The speed stability of the brush could be improved by using an incremental encoder to measure, and subsequently control the brush speed via adjusting the power supply's voltage. A CFD simulation, taking into account all conveying influences, i.e., the relaxation of particles, the slip velocity, particle-particle and particle-wall impacts, etc., could eventually give more detailed information about the prediction of the particle velocity at the outlet of the conveying pipe.

10 References

- [1] K. Leschonski, Die Technik des Windsichtens, in: GVC (Ed.), Tech. Der Gas/Feststoff-Strömung; Sichten, Abscheiden, Fördern, Wirbelschichten, Verein Deutscher Ingenieure, VDI- Gesellschaft Verfahrenstechnik und Chemieingenieurwesen, 1986.
- [2] I. V Klumpar, F. Currier, T. Ring, Air classifier, [http://www.che.utah.edu/~ring/Papers/Air Classif. Artic. \(1986\) 77–92](http://www.che.utah.edu/~ring/Papers/Air Classif. Artic. (1986) 77-92).
- [3] B. Furchner, S. Zampini, Air classifying, in: Ullmann's Encycl. Ind. Chem., Wiley-VCH, Weinheim, 2012: pp. 215–234.
- [4] K. Leschonski, Windsichter , verfahrenstechnische Maschinen zur Herstellung definierter pulverförmiger Produkte, in: Jahrb. 1988 Der Braunsch. Wissenschaftlichen Gesellschaft, Erich Goltze KG, Göttingen, 1988: pp. 175–196.
- [5] F.M. Feldhaus, Die Technik der Vorzeit, der geschichtlichen Zeit und der Naturvölker, Heinz Moos Verlag, München, 1965.
- [6] W. Osborne, Air and Dust Separator, U.S. Patent 880,161, 1908.
- [7] M. Shapiro, V. Galperin, Air classification of solid particles: A review, Chem. Eng. Process. Process Intensif. 44 (2005) 279–285.
- [8] A.R. Karagozian, The jet in crossflow, Phys. Fluids. 26 (2014).
- [9] A.R. Karagozian, Transverse jets and their control, Prog. Energy Combust. Sci. 36 (2010) 531–553.
- [10] S. Radl, B. Gonzalez, C. Goniva, S. Pirker, State of the Art in Mapping Schemes for Dilute and Dense Euler-Lagrange Simulations, 10th Int. Conf. CFD Oil Gas, Metall. Process Ind. (2014) 1–9.
- [11] S. Puttinger, G. Holzinger, S. Pirker, Investigation of highly laden particle jet dispersion by the use of a high-speed camera and parameter-independent image analysis, Powder Technol. 234 (2013) 46–57.
- [12] K.E. Wirth, Pneumatische Förderung - Grundlagen, in: GVC, VDI-Gesellschaft (Eds.), Tech. Der Gas/Feststoff- Strömung; Sichten, Abscheiden, Fördern, Wirbelschichten, Verein Deutscher Ingenieure, VDI- Gesellschaft Verfahrenstechnik und Chemieingenieurwesen, Köln, 1986: pp. 157–182.
- [13] W. Wagner, Lufttechnische Anlagen, 2nd ed., Vogel Industrie Medien, Würzburg, 2007.
- [14] P. Hilgraf, Pneumatic Conveying, in: D. Chulia, M. Deleuil, Y. Pourcelot (Eds.), Powder

- Technol. Pharm. Process., Elsevier B.V., 1994: pp. 319–346.
- [15] O. Molerus, Overview: Pneumatic transport of solids, *Powder Technol.* 88 (1996) 309–321.
- [16] R.G. Holdich, *Fundamentals of Particle Technology*, Midland Information Technology and Publishing, Loughborough, U.K., 2002.
- [17] G. Rudinger, *Fundamentals of Gas-Particle Flow*, Elsevier B.V., New York, 1980.
- [18] S. V. Dhodapkar, S.I. Plasynski, G.E. Klinzing, Plug flow movement of solids, *Powder Technol.* 81 (1994) 3–7.
- [19] J.R. Couper, W.R. Penney, J.R. Fair, S.M. Walas, *Transfer of Solids*, 3rd ed., Elsevier B.V., 2010.
- [20] M.K. Desai, *Flow assessment of powders in pneumatic conveying: a bench top assessment*, University of Wollongong, 1992.
- [21] K. Mcknight, E. Bacorn, K.W. White, *Methods of combustion of powdered fuels and powdered fuel dispersions*, U.S. Patent US 2009/0214992 A1, 2009.
- [22] A. Suri, M. Horio, A novel cartridge type powder feeder, *Powder Technol.* 189 (2009) 497–507.
- [23] S. Chellappan, G. Ramaiyan, Experimental Study of Design Parameters of a Gas-Solid Injector Feeder, *Powder Technol.* 48 (1986) 141–144.
- [24] A. Agarwal, *Rotary Valves in Pneumatic Conveying Systems*, Chem. Eng. (2013).
- [25] J.P. Tailor, Rotary air lock, U.S. Patent 3151784, 1964.
- [26] O. Johnson, Rotary feeder, U.S. Patent 2317274, 1943.
- [27] S.S.T. Schüttguttechnik GmbH, Durchblasschleuse: Lösung für pneumatische Förderung, *CHEManager.* (2007) 20.
- [28] K. Leschonski, Classification of Particles in the Submicron Range in an Impeller Wheel Air Classifier, *KONA Powder Part. J.* 4 (1996) 52–60.
- [29] E.H. Wenzel, Feeding Hopper for Pneumatic Conveyers, U.S. Patent 1903304, 1933.
- [30] G. Lins, J. Verleger, Verfahren und Vorrichtung zur Erzeugung eines Pulveraerosols sowie deren Verwendung, U.S. Patent EP 1 095 169 B1, 2002.
- [31] VDI 3491, Particulate Matter Measurement - Generation of Test Aerosols with a Rotating Brush Generator, in: *Vdi-Handb. Reinhaltung Der Luft*, Band 4, Verein

- Deutscher Ingenieure, 1989: pp. 1–8.
- [32] C. König, H. Büttner, F. Ebert, Design data for cyclones, Part. Part. Syst. 8 (1991) 301–307.
- [33] H. Buttner, Measurement of Particle Size Distributions in Gas Flows with an Optical Particle Counter, 2 (1985) 20–24.
- [34] K. Leschonski, On-Line Analysis , Its Potential and Its Problems, Part. Characterisation. 1 (1984) 7–13.
- [35] U. Kesten, Control and Optimisation of Cement Quality with Laser Diffraction Particle Size Analysis and Dry Dispersion, Sympatec GmbH. (1997) 1–20.
- [36] C. Peters, M. Stintz, Untersuchungen zur Trockendispergierung im Partikelgrößenbereich um 1 μm , Chem. -Ing. -Tech. 65 (1993) 728–733.
- [37] R. Molinder, H. Wiinikka, Feeding small biomass particles at low rates, Powder Technol. 269 (2015) 240–246.
- [38] R.B. Woodruff, P. Kreider, A.W. Weimer, A novel brush feeder for the pneumatic delivery of dispersed small particles at steady feed rates, Powder Technol. 229 (2012) 45–50.
- [39] K. Leschonski, S. Roethele, U. Menzel, A Special Feeder for Diffraction Pattern Analysis of Dry Powders, Part. Part. Syst. Charact. 1 (1984) 161–166.
- [40] K. Leschonski, S. Röthele, Method for producing a gas-solid two phase flow jet having a constant mass or volume flow rate and predetermined velocity, U.S. Patent 4660986, 1987.
- [41] K. Leschonski, B. Benker, U. Bauer, Dry Mechanical Dispersion of Submicron Particles, Part. Part. Syst. Charact. (1995) 295–298.
- [42] B.H. Kaye, Generating Aerosols, KONA Powder Part. J. 15 (1997) 68–80.
- [43] H. Brauer, Grundlagen der Einphasen- und Mehrphasenströmungen, Verlag Sauerländer, Aarau und Frankfurt am Main, 1971.
- [44] S. Dhodapkar, K. Jacob, Pneumatic Conveying, in: C.T. Crowe (Ed.), Multiph. Flow Handb., CRC Taylor & Francis, Boca Raton, London, New York, 2006.
- [45] F. Rizk, Pneumatic conveying at optimal operation conditions and a solution of Barth's equation, in: Proc. Pneumotransp. 3, 1977.
- [46] S. Matsumoto, M. Kikuta, A.S. Maeda, Effect of particle size on the minimum transport

- velocity for horizontal pneumatic conveying of solids, *J. Chem. Eng. Japan.* (1977) 273–279.
- [47] L.M. Gomes, a. L.A. Mesquita, On the prediction of pickup and saltation velocities in pneumatic conveying, *Brazilian J. Chem. Eng.* 31 (2014) 35–46.
- [48] K.E. Wirth, Die Grundlagen der pneumatischen Förderung, *Chem. -Ing. -Tech.* 55 (1983) 110–122.
- [49] C.T. Crowe, General Features of Multiphase Flows, in: C.T. Crowe (Ed.), *Multiph. Flow Handb.*, CRC Taylor & Francis, Boca Raton, London, New York, 2006.
- [50] L. Zaichik, V. Alipchenkov, E. Sinaiski, *Particles in Turbulent Flows*, Wiley-VCH, 2008.
- [51] A.T. Agarwal, Theory and Design of Dilute Phase Pneumatic Conveying Systems, *Powder Handl. Process.* 17 (2005) 18–23.
- [52] S. Narayan, O. Prakash, Prediction of slip velocity in the pneumatic conveyance of solids in the horizontal conduit, *Int. J. Adv. Res. Eng. Technol.* 4 (2013) 191–196.
- [53] F. Yan, A. Rinoshika, Application of high-speed PIV and image processing to measuring particle velocity and concentration in a horizontal pneumatic conveying with dune model, *Powder Technol.* 208 (2011) 158–165.
- [54] C. Li, J.C.K. Cheung, Z.Q. Chen, V. Scholar, Effect of square cells in improving wind tunnel flow quality, in: *Seventh Asia-Pacific Conf. Wind Eng.*, Taipei, 2009: pp. 1–8.
- [55] R.D. Mehta, P. Bradshaw, Technical Notes - Design rules for small low speed wind tunnels, *Aeronaut. Journal.* (1979) 443–449.
- [56] Fa. Bronkhorst, *Benutzer-Handbuch Allgemeine Hinweise digitale Massedurchfluss- und Druckmesser / -regler*, 2006.
- [57] B. Pentz, <http://www.clearvuecyclones.com/cv06-mini/71-cv06-mini-system.html>, (n.d.).
- [58] K. Shinohara, K. Shoji, T. Tanaka, Mechanism of Size Segregation of Particles in Filling a Hopper, *Ind. Eng. Chem. Process Des. Dev.* 11 (1972) 369–376.
- [59] N. Engblom, H. Saxen, R. Zevenhoven, H. Nylander, G. Enstad, M. Murto, Effects of Material Properties on Segregation of Binary and Ternary Powder Mixtures in a Small Scale Cylindrical Silo, *Ind. Eng. Chem. Res.* 50 (2011) 11097–11108.
- [60] L. Staron, P.-Y. Lagrée, S. Popinet, The granular silo as a continuum plastic flow: The

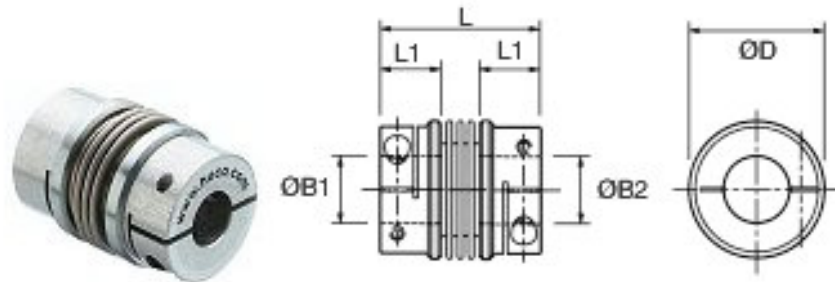
-
- hour-glass vs the clepsydra, *Phys. Fluids*. 24 (2012) 103301.
- [61] W. Witt, U. Köhler, J. List, Direct Imaging of Very Fast Particles Opens the Application of the Powerful (Dry) Dispersion for Size and Shape Characterization, (2004) 1–4.
- [62] J.K. Sveen, J. Kolaas, An introduction to MatPIV v. 1.7, (2014) 29.
- [63] J. Tomas, Gravity Separation of Particulate Solids in Turbulent Fluid Flow, *Part. Sci. Technol.* (2004) 1–19.

Appendix A

A.1 Data sheets of purchase parts

Flex-B

Stainless Steel Bellows Couplings, 3 Convolution with Clamp Style Fixing



Dimensions and Order Codes

	Coupling Size	Coupling Ref	ØD	L ±1.0	L1 (1)	ØB1, ØB2 max	Fasteners			Moment of inertia (3)	Mass (3)
			mm	mm	mm	mm	Screw	Torque (2)	Wrench	kgm ² × 10 ⁻⁸	kg × 10 ⁻³
								Nm	mm		
more	20	536.20	20	31	11	8	M2.5	1.32	2	90	16
more	26	536.26	26	37.5	14	12	M3	2.43	2.5	330	34
more	34	536.34	34	40	14	16	M3	2.43	2.5	925	56
more	41	536.41	41	49.7	18	20	M4	5.66	3	2390	99

Table Notes:

Length of supported through bore. Shafts can near butt.
Maximum recommended tightening torque.
Values apply with max bores.

Materials & Finishes

Hubs:

Al. Alloy 2014 T6, Clear anodised finish.

Bellows:

Spring quality stainless steel.

Joint assembly:

Copper C106, heat treated Zinc plate, black chromate.

Fasteners:

Alloy Steel, black oiled

Temperature Range

-40°C to +120°C

Performance

	Coupling Size	Ref.	Peak torque (4)	Max compensation			Flexural stiffness			
				Angular (5)	Radial (5)	Axial (5)	Torsional (6)	Angular	Radial	Axial
			Nm	deg	mm	mm	Nm/rad	N/deg	N/mm	N/mm
more	20	536.20	2	2	0.06	0.35	315	1.03	115	17.7
more	26	536.26	3.2	2	0.06	0.36	755	1.27	238	5.7
more	34	536.34	7.5	2.5	0.1	0.6	1740	1.34	227	6.6
more	41	536.41	10	2.5	0.15	0.8	2880	1.58	144	13.1

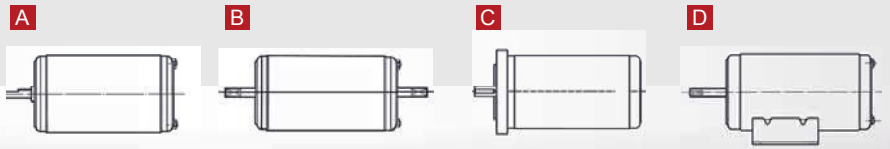
Table Notes:

Peak torque. Select a size where Peak Torque exceeds the application torque x service factor.
Max. compensation values are mutually exclusive.
Torsional stiffness values apply at 50% peak torque with no misalignment, measured shaft-to-shaft with largest standard bores. Note that in some vendors' catalogues the given torsional stiffness applies to the un-mounted bellows element only, an unrepresentative calculated value.

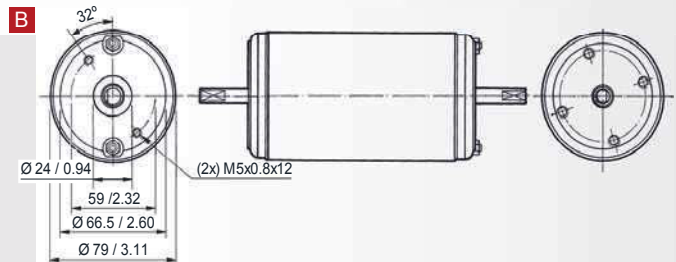
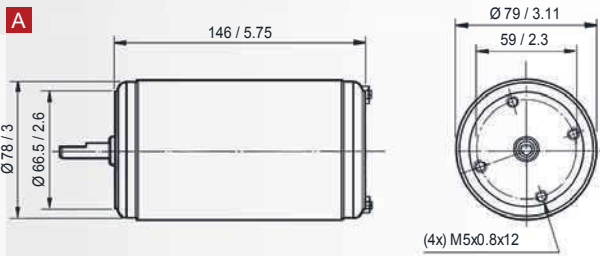


PLANETARY GEAR

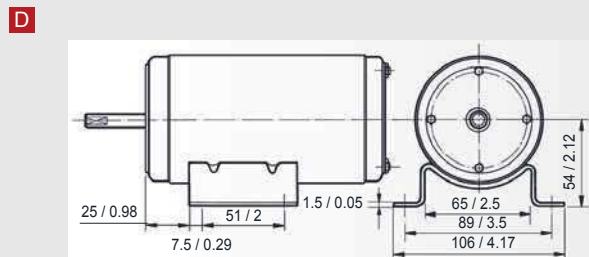
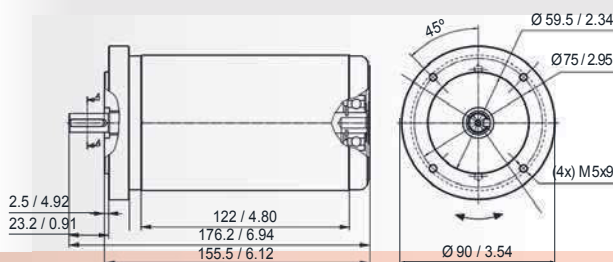
- REDUCTORES PLANETARIOS: combinables con la serie 168. Ver sección especial en catálogo.
- PLANETARY GEARS: combinable with 168 series. See special section in catalogue.
- REDUCTEURS PLANETAIRES: combinables avec la série 168. Consultez section spécial du catalogue.
- PLANETENGETRIEBE: Mit der Reihe 168 kombinierbar. Sehen Sie Sonderabschnitt im Katalog.



REFERENCIA REFERENCE REFERENZNUMMERN	TENSION NOMINAL NOMINAL VOLTAGE TENSION NOMINALE NENNSPANNUNG	PAR NOMINAL NOMINAL TORQUE COUPLE NOMINAL DREHMOMENT NOMINAL	VELOCIDAD NOMINAL NOMINAL SPEED VITESSE NOMINALE GESCHWINDIGKEIT NOMINAL	CORRIENTE NOMINAL NOMINAL CURRENT COURANT NOMINAL NOMINALSTROM	PAR DE ARRANQUE STARTING TORQUE COUPLE DE DEMARRAGE ANZUGSDREHMOMENT	CORRIENTE DE ARRANQUE STARTING CURRENT COURANT DE DEMARRAGE ANLAUFSTROM	EE SHAFT ARRE WELLE	CONEXIONES CONNECTIONS CONNEXIONS ANSCHLUSSART	ESQUEMA ELECTRO WIRING DIAGRAM SCHEMATIC SCHALTBLIND	PESO APROXIMADO APPROXIMATE WEIGHT POIDS APPROXIMATIF GEWICHT (ca.)	GRADO DE ESTANQUEIDAD WATERTIGHTNESS ETANCHÉITÉ FEUCHTIGKEITSSCHUTZKLASSE	DISEÑO: A, B DESSIN: A, B ZEICHNUNG: A, B	CURVA CURVE KURVE
	Un (V)	Mn (N.m./lbf.in)	Pn (r.p.m.)	In (A)	Ma (N.m./lbf.in)	Ia (A)				P (kg/lb.t)	IP		
168.4105.20.04	12	0.50 / 4.42	1900	14	3.0 / 26.5	64	E8	C8	EE1	2.6 / 6.9	IP40	a	37
168.4105.30.04	24	0.50 / 4.42	1900	7	3.0 / 26.5	32	E8	C8	EE1	2.6 / 6.9	IP40	a	37
168.4108.20.04	12	0.45 / 3.98	2800	19	3.0 / 26.5	100	E9	C9	EE4	2.6 / 6.9	IP40	a	39
168.4108.30.04	24	0.45 / 3.98	2800	10	3.0 / 26.5	52	E9	C9	EE4	2.6 / 6.9	IP40	a	39
168.4111.20.04	12	0.75 / 6.64	1000	11	2.8 / 24.8	36	E11	C9	EE2	2.6 / 6.9	IP40	a	40
168.4111.30.04	24	0.75 / 6.64	1000	5.5	2.8 / 24.8	18	E11	C9	EE2	2.6 / 6.9	IP40	a	40
168.4112.20.04	12	0.70 / 6.19	1500	14	3.0 / 26.5	56	E12	C11	EE2	2.6 / 6.9	IP40	a	42
168.4112.30.04	24	0.70 / 6.19	1500	7	3.0 / 26.5	28	E12	C11	EE2	2.6 / 6.9	IP40	a	42
168.4115.30.04	24	0.50 / 4.42	3000	11	3.0 / 26.5	70	E13/E41	C13	EE2	2.6 / 6.9	IP40	a	41
168.4116.20.04	12	0.50 / 4.42	1900	14	3.0 / 26.5	64	E8	C8	EE1	2.6 / 6.9	IP40	d	37
168.4116.30.04	24	0.50 / 4.42	1900	7	3.0 / 26.5	32	E8	C8	EE1	2.6 / 6.9	IP40	d	37
168.4121.30.04E	24	0.50 / 4.42	3000	11	3.0 / 26.5	70	E11/E11	C13	F2	2.6 / 6.9	IP40	b	41
168.4122.30.04	24	0.75 / 6.64	1000	5.5	2.8 / 24.8	18	E13/E41	C13	EE2	2.6 / 6.9	IP40	a	40
168.4123.20.04	12	0.50 / 4.42	2100	16	3.0 / 26.5	76	E13/E41	C13	EE2	2.6 / 6.9	IP40	a	43
168.4123.30.04	24	0.50 / 4.42	2100	8	3.0 / 26.5	38	E13/E41	C13	EE2	2.6 / 6.9	IP40	a	43
168.4134.30.04	24	0.30 / 2.65	750	1.5	1.5 / 13.3	7	E59	C9	EE2	2.6 / 6.9	IP40	a	44
168.4136.30.00E	24	0.75 / 6.64	1000	5.5	2.8 / 24.8	18	E63	C42	F2	2.6 / 6.9	IP40	c	40



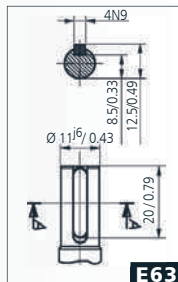
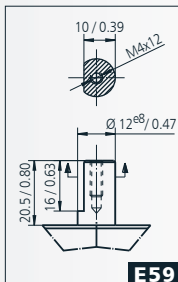
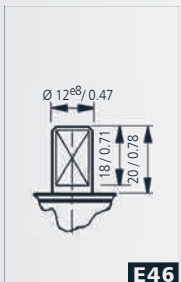
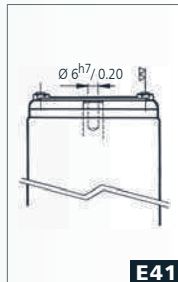
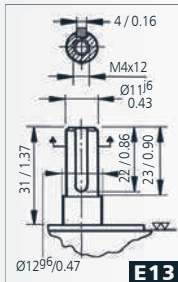
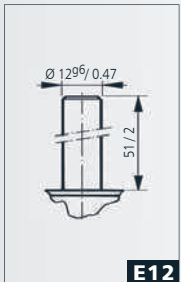
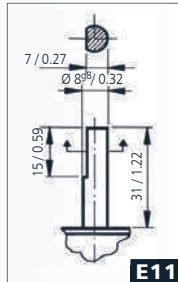
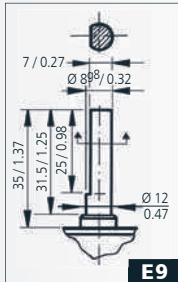
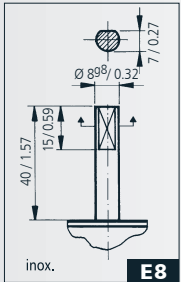
C Flange according to IEC 63 B14 - Puntos de anclaje según IEC 63 B14



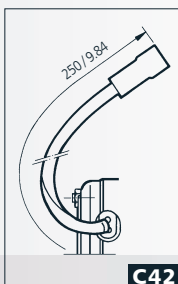
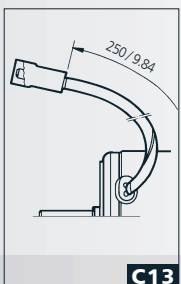
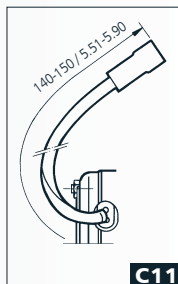
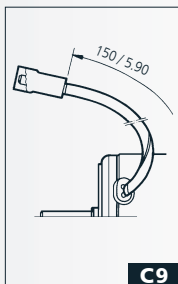
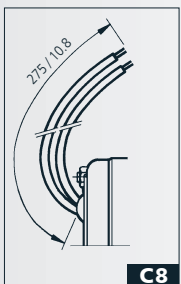
mm / inch

DOGA

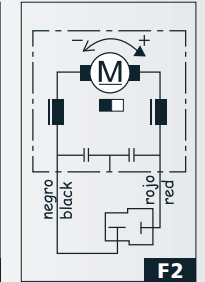
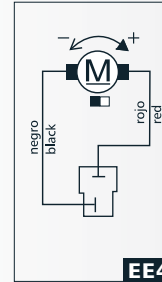
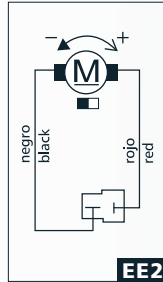
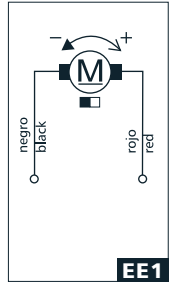
EJE - SHAFT - ARBRE - WELLE



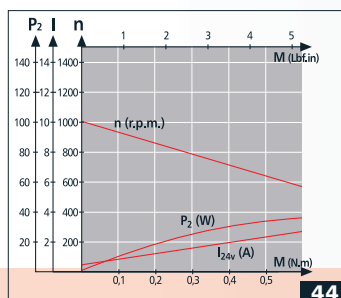
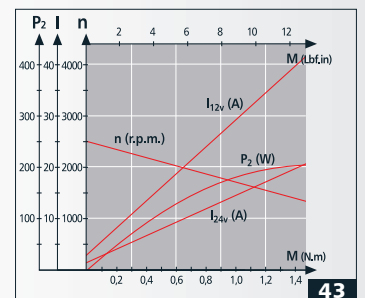
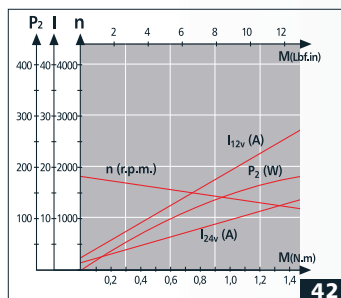
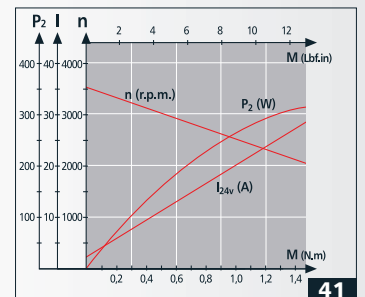
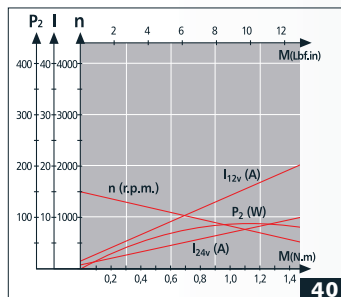
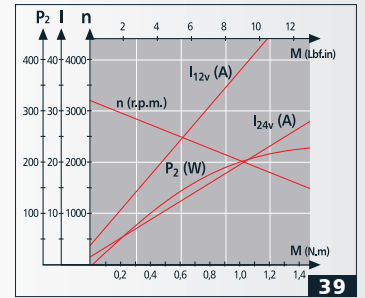
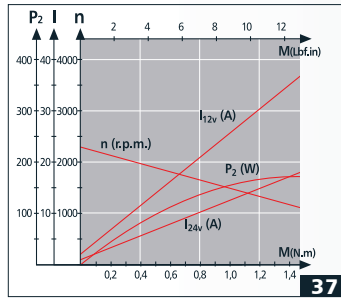
ESQUEMA ELÉCTRICO - WIRING DIAGRAM
SCHEMA ÉLECTRIQUE - SCHALTBIKD ESQUEMA ELÉCTRICO



CONEXIONES - CONNECTIONS - CONNEXIONS - ANSCHLUSSART



CURVAS - CURVES - COURBES - KURVEN



Gemplan® G 340 mit hoher Festigkeit

Gemplan® G 340 werden aus der Legierung 7xxx (Al Zn Mg) gefertigt

Die Legierung Al Zn Mg ist eine aushärtbare Knetlegierung mit folgender gewichteter chemischer Zusammensetzung:

Si	Fe	Cu	Mn	Mg	Cr	Zn	Ti
< 0,3	< 0,4	< 0,1	0,15 - 0,30	0,70 - 1,20	0,2	5,00 - 6,00	0,15

Die typische Anwendung der Gemplan® G 340 plus sind höher beanspruchte Maschinenteile in Vorrichtungen, Sondermaschinen und Schweißkonstruktionen. Die Festigkeit dieser Platte liegt bei einem Richtwert von R_m 340 N/mm² und damit im Bereich von Walzplatten mittlerer Festigkeit. Gegenüber Walzplatten bieten diese Gussplatten eine wesentlich bessere Ebenheit, Rauheit, Dickentoleranz, Parallelität und Verzugsarmut. Die Auslieferung des Werkstoffes erfolgt im Zustand T1, welcher für diesen Legierungstypen hinsichtlich des Korrosionsverhaltens den stabilsten Zustand darstellt. Gemplan® G 340 benötigt zur Einstellung der maximalen mechanischen Eigenschaften keine Vollaushärtung, durch die Vermeidung eines Abschreckprozesses in Wasser ist das Material besonders spannungsarm.

Dichte [kg/dm ³]	2,77
Elektrische Leitfähigkeit [MS/m]	20 – 23
Wärmeleitfähigkeit [W/mK]	110 – 120
Thermischer Ausdehnungskoeffizient [10 ⁻⁶ /K]	20,0 – 24,0
E – Modul [GPa]	70 ± 2
Temperaturbereich	-60 bis +120 °C

Die Schweißbarkeit von Gemplan® G 340 ist gut, als Schweißdraht sind möglichst ähnliche Legierungen zu verwenden. Wir empfehlen Drähte der Legierungen AlZn4,5Mg oder AlMg4,5MnZr. Gemplan® G 340 hat den Vorteil, dass Schweißnaht und Wärmeeinflusszone nach dem Abkühlen durch Kaltaushärtung wieder die ursprünglich vorhandenen mechanischen Eigenschaften erreichen. Für die Aushärtung ist ein Zeitraum von ca. 3 bis 4 Wochen erforderlich. Die Auslagerung sollte möglichst bei Raumtemperatur erfolgen. Der Bereich der Schweißnaht darf zum rascheren Abkühlen des Bauteiles nicht mit Wasser gekühlt werden, ansonsten steigt die Neigung zur Spannungsrissskorrosion.

mechanische Eigenschaften	Zugfestigkeit R_m [N/mm ²]	0,2% Dehngrenze $R_{p0,2}$ [N/mm ²]	Bruchdehnung A_5 [%]	Brinellhärte HB
Gemplan® G 340	~340	~300	~5	~115

Die Schweißbarkeit von Gemplan® G 340 ist gut, als Schweißdraht sind möglichst ähnliche Legierungen zu verwenden. Wir empfehlen Drähte der Legierungen AlZn4,5Mg oder AlMg4,5MnZr. Gemplan® G 340 hat den Vorteil, dass Schweißnaht und Wärmeeinflusszone nach dem Abkühlen durch Kaltaushärtung wieder die ursprünglich vorhandenen mechanischen Eigenschaften erreichen. Für die Aushärtung ist ein Zeitraum von ca. 3 bis 4 Wochen erforderlich. Die Auslagerung sollte möglichst bei Raumtemperatur erfolgen. Der Bereich der Schweißnaht darf zum rascheren Abkühlen des Bauteiles nicht mit Wasser gekühlt werden, ansonsten steigt die Neigung zur Spannungsrissskorrosion.

Weitere besondere Eigenschaften der Legierung AlZnMg:

- Ausgezeichnete Spannungsarmut
- Ausgezeichnet beständig gegen Wasser
- Gut beständig gegen Meerwasser
- Gut beständig gegen Witterung
- Ist gut schweißbar (siehe oben)
- Geringste Mikroporositäten: Gute Gas- und Öldichtigkeit für Hydraulik- und Vakuumtechnik
- Ist sehr gut spanbar
- Ist sehr gut polierbar
- Gut geeignet für das Schutzanodisieren
- Bedingt geeignet für das optische Anodisieren (bei entsprechender Vorbehandlung)

Lieferbare Formate und Stärken:

Gemplan® PLUS feinstgefräst

Dicke	Großformat	G 340
8	1520 x 3020	●
10	1520 x 3020	●
12	1520 x 3020	●
15	1520 x 3020	●
20	1520 x 3020	●
25	1520 x 3020	●
30	1520 x 3020	●
35	1520 x 3020	●
40	1520 x 3020	●
50	1520 x 3020	●

Dickentoleranz	Feinstgefräst (bis ± 0,05 mm auf Anfrage)	± 0,1 mm
Planheit	Feinstgefräst 0,40 mm / m für Dicken 0,15 mm / m für Dicken	≤ 15 mm > 15 mm
Rauigkeit	Feinstgefräst	Ra ≤ 0,40 µm

Es können auch Ihren Anforderungen entsprechend andere Stärken geliefert werden.

Pro gewünschter Stärke ist nur eine Mindestmenge von einer einzelnen Tafel erforderlich.

Außerdem kann die Stärkentoleranz von ± 0,1 mm auf bis zu ± 0,05 mm eingeschränkt werden.

Bitte legen Sie uns Ihren Bedarf vor. Gerne klären wir die Möglichkeiten und Termine.

Nutzen Sie unseren in jeder Niederlassung verfügbaren leistungsstarken Zuschnittservice

Datasheet F-203AV

Mass Flow Controller for Gases

> Introduction

Bronkhorst High-Tech model F-203AV Mass Flow Controllers (MFCs) are suited for precise control of virtually all conventional process gases. The MFC consists of a thermal mass flow sensor, a precise control valve and a microprocessor based PID controller with signal and fieldbus conversion. As a function of a setpoint value, the flow controller swiftly adjusts the desired flow rate. The mass flow, expressed in normal litres per minute or normal cubic metres per hour, is provided as analog signal or digitally via RS232 or fieldbus. The flow range, wetted materials and orifice size for the control valve are determined depending of the type of gas and the process conditions of the application.

Although all specifications in this datasheet are believed to be accurate, the right is reserved to make changes without notice or obligation.



EL-FLOW Mass Flow Controller model F-203AV

> Technical specifications

Measurement / control system

Accuracy (incl. linearity) (Based on actual calibration)	: $\pm 0,5\%$ Rd plus $\pm 0,1\%$ FS
Turndown	: 1 : 50 (in digital mode up to 1:187,5)
Multiple fluid capability	: storage of max. 8 calibration curves
Repeatability	: $< \pm 0,2\%$ Rd
Settling time (controller)	: 2...4 seconds
Control stability	: $\leq \pm 0,1\%$ FS
Kv-value	: 0,15...1,5
Temperature range	: -10...+70°C
Temperature sensitivity (nominal range)	: zero: $< \pm 0,05\%$ FS/°C; span: $< \pm 0,05\%$ Rd/°C
Leak integrity (outboard)	: $< 2 \times 10^{-9}$ mbar l/s He
Attitude sensitivity	: max. error at 90° off horizontal 0,2% FS at 1 bar, typical N ₂
Warm-up time	: 30 min. for optimum accuracy 2 min. for accuracy $\pm 2\%$ FS

Mechanical parts

Material (wetted parts)	: stainless steel 316L or comparable
Pressure rating	: 64 bar abs
Surface quality (wetted parts)	: 0,8 μm Ra typical
Process connections	: compression type or face seal male
Seals	: standard : Viton; options: EPDM, Kalrez
Ingress protection (housing)	: IP40

Electrical properties

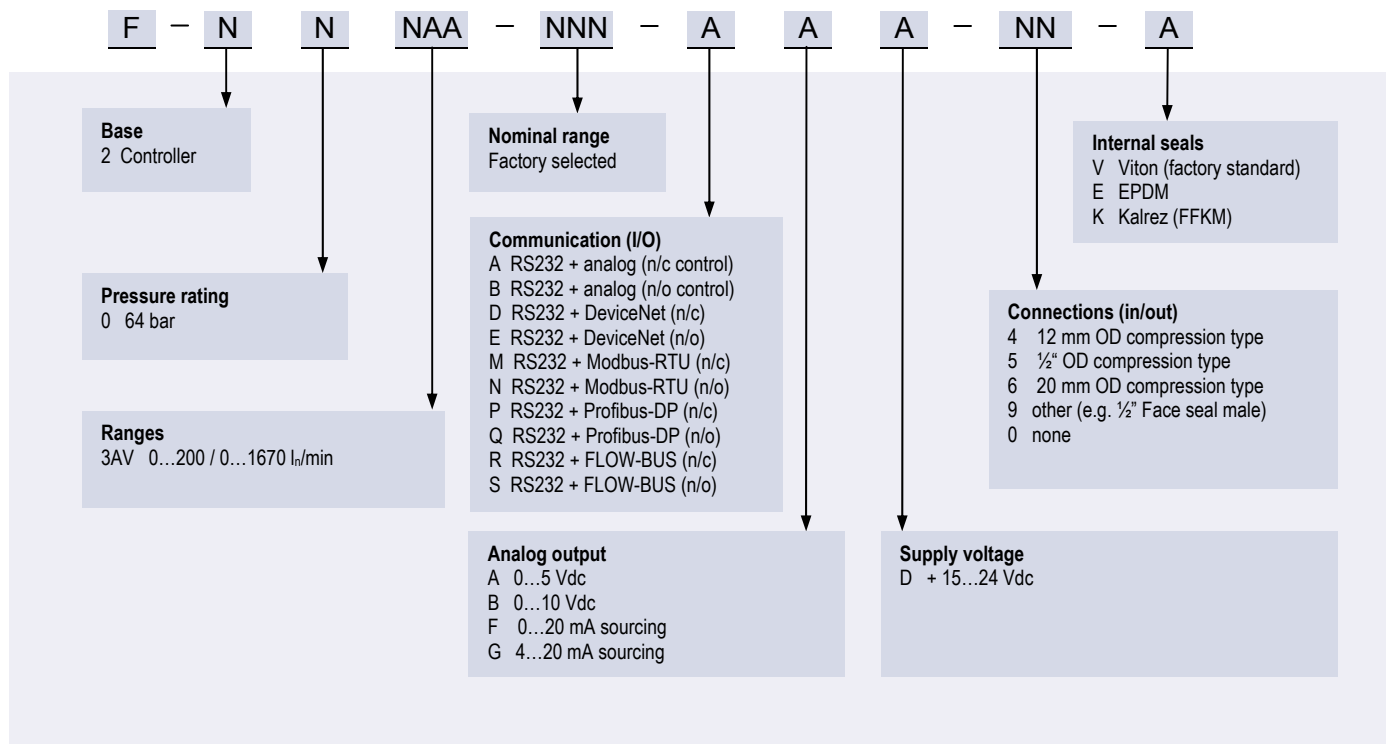
Power supply	: +15...24 Vdc $\pm 10\%$
Power consumption	: max. 320 mA; add 50 mA for Profibus, if applicable
Analog output	: 0...5 (10) Vdc, min. load impedance $> 2 \text{ k}\Omega$; 0 (4)...20 mA (sourcing), max. load impedance $< 375 \Omega$
Analog setpoint	: 0...5 (10) Vdc, min. load impedance $> 100 \text{ k}\Omega$; 0 (4)...20 mA, load impedance $\sim 250 \Omega$
Digital communication	: standard RS232 ; options: Profibus-DP®, DeviceNet™, Modbus-RTU, FLOW-BUS

> Ranges (based on Air)

Model	minimum	nominal	maximum
F-203AV-M50	4...200 l _n /min	4...500 l _n /min	4...750 l _n /min
F-203AV-1M0	8...400 l _n /min	8...1000 l _n /min	8...1670 l _n /min

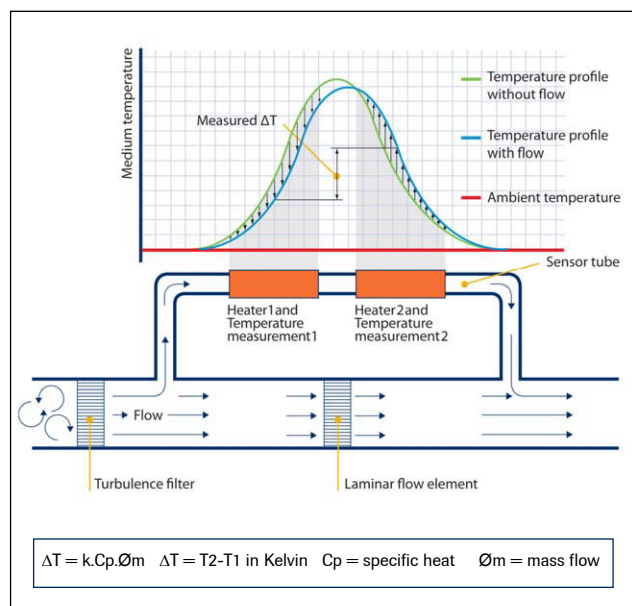
Intermediate ranges are available

> Model number identification



> Thermal mass flow measuring principle

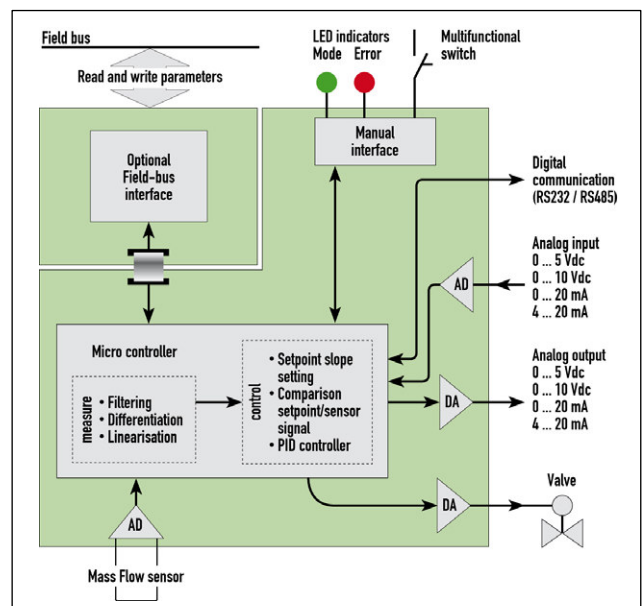
The heart of the thermal mass flow meter/controller is the sensor, that consists of a stainless steel capillary tube with resistance thermometer elements. A part of the gas flows through this bypass sensor, and is warmed up heating elements. Consequently the measured temperatures T_1 and T_2 drift apart. The temperature difference is directly proportional to mass flow through the sensor. In the main channel Bronkhorst High-Tech applies a patented laminar flow element consisting of a stack of stainless steel discs with precision-etched flow channels. Thanks to the perfect flow-split the sensor output is proportional to the total mass flow rate.



Functional scheme of the thermal mass flow sensor

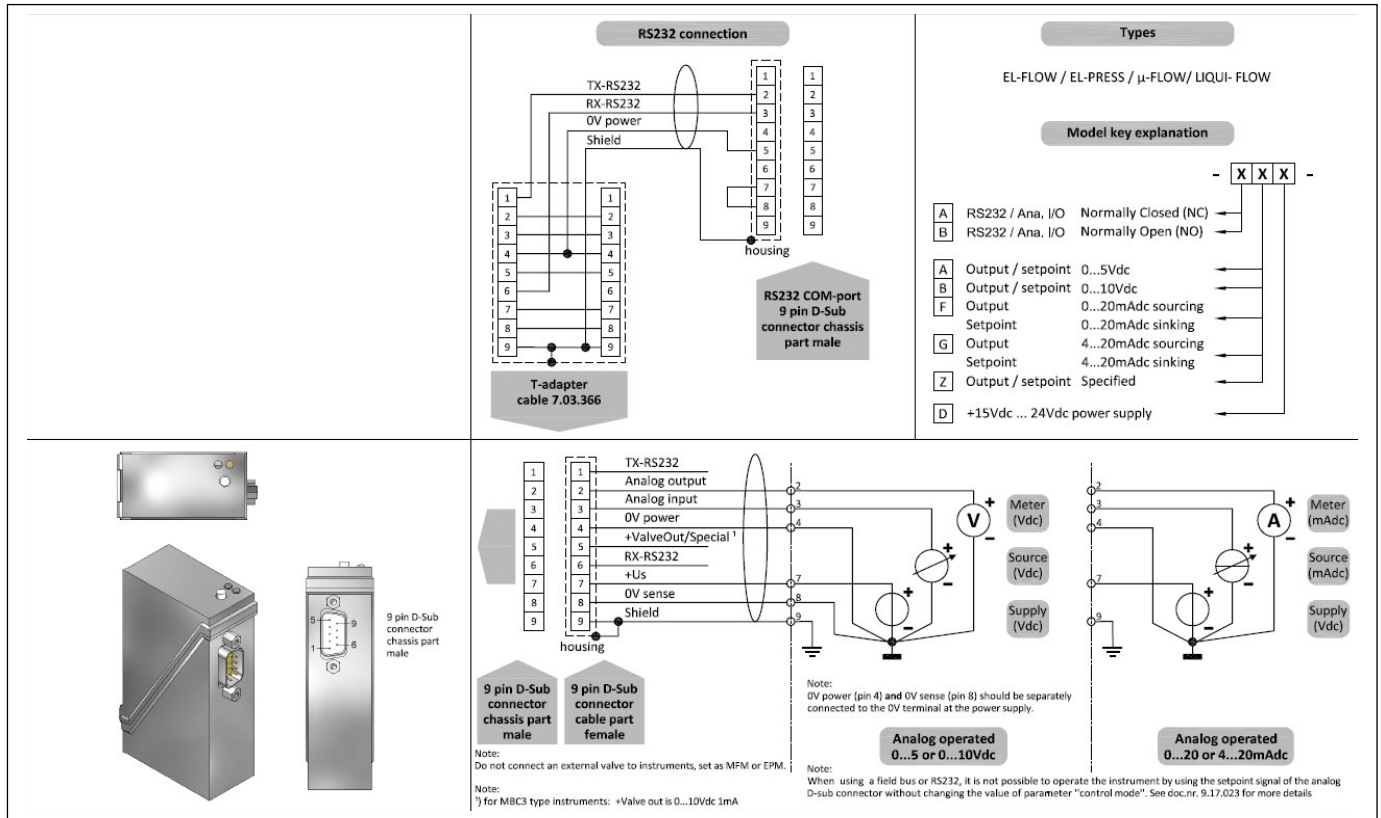
> State of the art digital design

Today's EL-FLOW[®] series are equipped with a digital pc-board, offering high accuracy, excellent temperature stability and fast response (settling times t_{98} down to 500 msec). The basic digital pc-board contains all of the general functions needed for measurement and control. In addition to the standard RS232 output the instruments also offer analog I/O. Furthermore, an integrated interface board provides DeviceNet[™], Profibus-DP[®], Modbus-RTU or FLOW-BUS protocols.



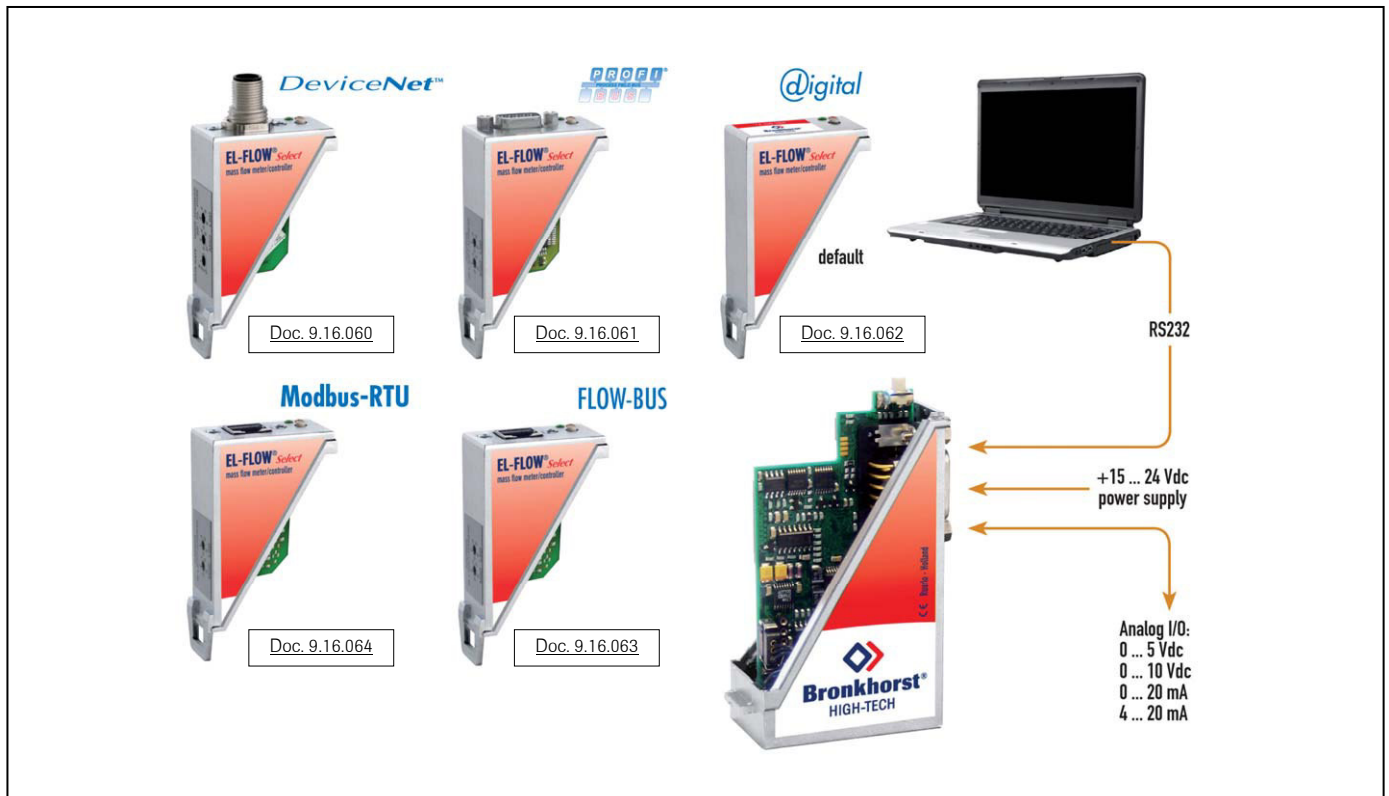
Functional scheme of the digital PC-board

> Hook-up diagram for analog or RS232 communication

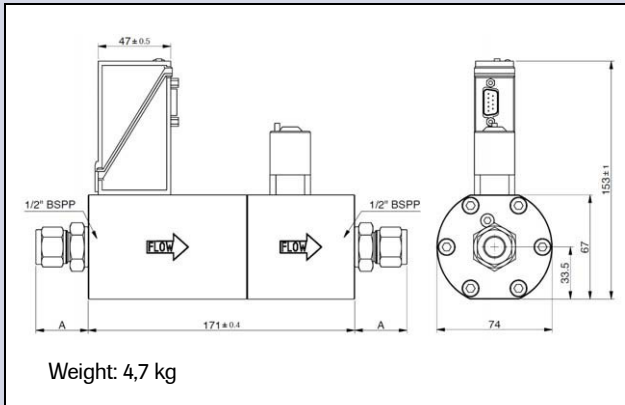


> Hook-up diagrams for fieldbus communication

For the available fieldbus options we refer to the various hook-up diagrams as indicated below. If you are viewing this datasheet in digital format, you may use the hyperlink to each of the drawings. Otherwise please visit the download section on www.bronkhorst.com or contact our local representatives.

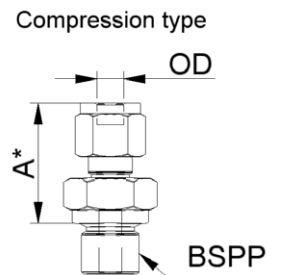


> Dimensions (mm) and weight (kg)



Dimension table adapters (RS-type)

		1/2"BSPP
Compression type		Size A
adapter 10 mm OD		31.0
adapter 12 mm OD		33.5
adapter 20 mm OD		36.5
adapter 25 mm OD		42.0
adapter 3/8" OD		30.7
adapter 1/2" OD		33.5
adapter 3/4" OD		34.8
		1/2"BSPP
Face-seal male		A
adapter 1/2" inlet		27.6
adapter 3/4" inlet		36.5



*) Dimension A is typical finger-tight.

> Options and accessories

<ul style="list-style-type: none"> - Multi-Gas / Multi-Range option, with free configuration software. - Free software support for operation, monitoring, optimizing or to interface between digital instruments and windows software. 	
<ul style="list-style-type: none"> - IN-LINE filters for protection against particulates 	
<ul style="list-style-type: none"> - BRIGHT compact local Readout/Control modules - E-5700 / E-7000 Power Supply 	
<ul style="list-style-type: none"> - Interconnecting cables for power and analog/digital communication 	

> Alternatives

<ul style="list-style-type: none"> - IN-FLOW MFC with industrial (IP65) housing 	
<ul style="list-style-type: none"> - IN-FLOW^{CTA} direct (no by-pass), industrial (IP65) Mass Flow Meter with close-coupled Control Valve 	

Technische Daten

	WS 2210	WSZ 2210	WS 2220	WSZ 2220	WS 2310	WSZ 2310	WS 2320	WSZ 2320	WS 3310	WS 3320
Gehäuse	GFK	GFK	GFK	GFK	GFK	GFK	GFK	GFK	GFK	GFK
Motorleistung (kW)	2,0	2,0	2,4	2,4	3,0	3,0	3,6	3,6	3,0	3,6
Spannung (Volt)	230	230	230	230	230	230	230	230	230	230
Unterdruck (mbar)	-195	-195	-210	-210	-185	-185	-210	-210	-185	-210
Luftleistung (m³/h) (gemessen mit 3m Schlauch)	270	270	290	290	430	430	460	460	430	460
Schalldruckpegel (dB(A)) (DIN EN ISO 3744)	64	64	67	67	69	69	72	72	69	72
Taschenfilter Staubklasse L, M (m²)	1,2/2,6	-	1,2/2,6	-	1,2/2,6	-	1,2/2,6	-	4,5	4,5
Zellenfilter Staubklasse L, M (m²)	-	1,0	-	1,0	-	1,0	-	1,0	-	-
Reststaubfilter Staubklasse H (m²)	3,2	3,2	3,2	3,2	3,2	3,2	3,2	3,2	3,2	3,2
Höhe (mm) (Zellenfilter 1,0 m² Staubklasse L, M)	-	890	-	890	-	890	-	890	-	-
Höhe (mm) (Taschenfilter 1,2 m² Staubklasse L,M)	890	-	890	-	890	-	890	-	-	-
Höhe (mm) (Taschenfilter 2,6 m² Staubklasse L,M)	1.200	-	1.200	-	1.200	-	1.200	-	-	-
Höhe (mm) (Taschenfilter 4,5 m² Staubklasse L,M)	-	-	-	-	-	-	-	-	1.570	1.570
Höhe (mm) (Zellenfilter 1,0 m² Staubklasse H)	-	1.010	-	1.010	-	1.010	-	1.010	-	-
Höhe (mm) (Taschenfilter 1,2 m² Staubklasse H)	1.010	-	1.010	-	1.010	-	1.010	-	-	-
Höhe (mm) (Taschenfilter 2,6 m² Staubklasse H)	1.340	-	1.340	-	1.340	-	1.340	-	-	-
Höhe (mm) (Taschenfilter 4,5 m² Staubklasse H)	-	-	-	-	-	-	-	-	1.626	1.626
Breite (mm)	520	520	520	520	520	520	520	520	730	730
Länge (mm)	850	850	850	850	850	850	850	850	920	920
Schutzart IP	x4	x4	x4	x4	x4	x4	x4	x4	x4	x4
Fassungsvermögen (Liter)	35	35	35	35	35	35	35	35	90	90
Sauganschluss (mm)	50	50	50	50	70	70	70	70	70	70

Unterschiedliche Entsorgungssysteme



Entsorgungswanne mit Deckel



Staubfilterbeutel



Einlegetüte

Ruwac
Industriesauger

RUWAC
Industriesauger GmbH
Westhoyeler Str. 25
49328 Melle-Riemsloh



Telefon: 0 52 26 - 98 30-0
Telefax: 0 52 26 - 98 30-44
www.ruwac.de
ruwac@ruwac.de

Die Industriesauger sind in explosionsgeschützter Ausführung nach ATEX 94/9/EG lieferbar.



DIN EN 60335-2-69, Anh. CC

ATEX 94/9/EG

DIN EN 60335-2-69, Anh. AA

14-122-000-10.2015

A.2 *Data sheet of glass particles*

Produktdatenblatt

 Erstmalig erstellt am: 16.07.2015
 Nächste Prüfung am: 30.06.2016

 Aktualisiert am: 16.07.2015
 Gedruckt am: 16.07.2015

Produkt	SiLibeads Glaskugeln Typ S; Microglaskugeln
Material	Polierte Glaskugeln aus Kalknatronglas Dichte: 2,50 kg/dm ³ Hydrolytische Klasse an Glaskugeln: HGB 1 (in Anlehnung nach DIN ISO 719) Säurebeständigkeitsklasse an Glaskugeln: S3 (nach DIN 12116) Laugenbeständigkeitsklasse an Glaskugeln: A1 (nach DIN ISO 695)
Einsatzgebiete	Mahl und Dispergierkugel für Farbstoffe, Pigmente, Tinte, Agrochemikalien und Mineralien. Füllstoff in der Chemikalien, Papier- und Kunststoffindustrie. Füllkugel zur Erhöhung der physikalischen Eigenschaften in Thermoplaste und Duroplaste. Reflexkugel > 0,8mm zur Straßenmarkierung, insbesondere für Spezialmarkierungen zur Erhöhung der Nachtsichtbarkeit bei Regen. Polierkugel in der Optik für Interokularlinsen. Strahl- und Beschichtungsmaterial zur mechanischen Oberflächenbearbeitung von Metall, Kunststoff und Holz.
Technische Daten	
Rundheit (Standard)	Artikel 52xx im Größenbereich 0,1 - 0,8 mm: ≥ 0.89 (Verhältnis Breite zu Länge (x_{min}/x_{max})) Artikel 45xx im Größenbereich 1,0 - 3,0 mm: ≥ 0.95 (Verhältnis Breite zu Länge (x_{min}/x_{max}))
Druckfestigkeit	bis zu 2.100 N (abhängig von der Größe)
Brechungsindex	1,52
Größen	Microglasperlen im Größenbereich von 0 bis 800 μm Glaskugeln Typ S im Größenbereich von 0,25 – 4,40 mm (siehe Tabelle Standardgrößen)
Transformationstemperatur	549 °C
Erweichungstemperatur	734 °C
Schmelztemperatur	1.446 °C
Wärmeleitfähigkeit	1,129 W/km
Thermische Ausdehnung	$9,05 \cdot 10^{-6} \text{ K}^{-1}$ [20 °C] (Längenausdehnungskoeffizient α)
Wärmekapazität	1,329 kJ/kg K [>600 °C]
Elastizitätsmodul	63 GPa
Härte nach Mohs	≥ 6

Lebensmittelrechtliche Bewertung

Bei den geprüften Glaskugeln handelt es sich um einen Bedarfsgegenstand im Sinne §2 Abs. 6 Nr. 1 Lebensmittel-, Bedarfsgegenstände- und Futtermittelgesetzbuch (LFGB). Die Glaskugeln unterliegen somit den lebensmittelrechtlichen Anforderungen.

Die Glaskugeln entsprechen den Anforderungen des §31 LFGB und des Artikel 3 der Verordnung (EG) Nr. 1935/2004.

Die Grenzwerte nach EU-Richtlinie 2011/65/EG (RoHS) werden eingehalten.

Blei < 1000 ppm	Cadmium < 100 ppm	Chrom VI < 1000 ppm	Quecksilber < 1000 ppm
-----------------	-------------------	---------------------	------------------------

Produktdatenblatt

 Erstmalig erstellt am: 16.07.2015
 Nächste Prüfung am: 30.06.2016

 Aktualisiert am: 16.07.2015
 Gedruckt am: 16.07.2015

Standardgrößen - Sondersiebungen auf Anfrage möglich

Artikel	Größenbereich	Druckfestigkeit *)	Schüttgewicht	Stück pro kg
5209-7	0 – 20 µm	-----	0,70 kg/dm ³	-----
5210-7	0 – 50 µm	-----	1,30 kg/dm ³	-----
5211-7	40 – 70 µm	-----	1,33 kg/dm ³	-----
5212-7	70 – 110 µm	-----	1,37 kg/dm ³	-----
5213-7	90 – 150 µm	-----	1,40 kg/dm ³	-----
5214-7	100 – 200 µm	-----	1,42 kg/dm ³	-----
5215-7	150 – 250 µm	-----	1,43 kg/dm ³	-----
5216-7	200 – 300 µm	-----	1,44 kg/dm ³	-----
5220-7	200 – 400 µm	-----	1,45 kg/dm ³	-----
5223-7	300 – 400 µm	-----	1,46 kg/dm ³	-----
5218-7	400 – 600 µm	-----	1,47 kg/dm ³	-----
5219-7	400 – 800 µm	-----	1,49 kg/dm ³	-----
4501	0,25 – 0,50 mm	-----	1,46 kg/dm ³	14.486.600
45015	0,40 – 0,60 mm	-----	1,47 kg/dm ³	6.111.500
4502	0,50 – 0,75 mm	-----	1,49 kg/dm ³	3.129.100
4503	0,75 – 1,00 mm	-----	1,50 kg/dm ³	1.140.300
4504	1,00 – 1,30 mm	250 – 350 N	1,51 kg/dm ³	502.300
4505	1,25 – 1,65 mm	350 – 500 N	1,51 kg/dm ³	250.580
4506	1,55 – 1,85 mm	500 – 650 N	1,52 kg/dm ³	155.490
4507	1,70 – 2,10 mm	600 – 750 N	1,52 kg/dm ³	111.370
4508	2,00 – 2,40 mm	750 – 900 N	1,53 kg/dm ³	71.740
4510	2,40 – 2,90 mm	950 – 1100 N	1,53 kg/dm ³	41.050
4511	2,85 – 3,45 mm	1100 – 1450 N	1,53 kg/dm ³	24.440
4512	3,40 – 4,00 mm	1450 – 1650 N	1,53 kg/dm ³	15.080
4513	3,80 – 4,40 mm	1700 – 2100 N	1,53 kg/dm ³	11.080

*) Druckfestigkeit: interne Prüfung mit Druckprüfeinrichtung No. 10004.1, Fabrikat Hegewald & Peschke

Chemische Analyse; Glaskugeln aus Kalknatronglas; CAS-Nr. 65997-17-3 / EINECS 266-046-0

Hauptbestandteile	Methode	Anteil (Referenzwerte)	CAS-Nr.	EINECS
Siliciumdioxid SiO ₂	DIN 51001	72,30 %	7631-86-9	231-545-4
Natriumoxid Na ₂ O	DIN 51001	13,30 %	1313-59-3	215-208-9
Calciumoxid CaO	DIN 51001	8,90 %	1305-78-8	215-138-9
Magnesiumoxid MgO	DIN 51001	4,00 %	1309-48-4	215-171-9
sonstige		1,50 %		

Hinweise

Lagerung	Produkt trocken und bei Raumtemperatur im geschlossen (Original-)Behälter aufbewahren.
Entsorgung	Bei Entsorgung sind die nationalen Gesetze und örtlichen Vorschriften zu beachten.
Arbeitssicherheit	Verschüttetes Produkt führt zu erhöhter Rutschgefahr.
Mitgeltende Unterlagen	Musterkarte SiLibeads ... glass beads for technical applications Sicherheitsdatenblatt SiLibeads Typ S, Microglas; Prüfberichte
Hersteller/Lieferant	Sigmund Lindner GmbH; Oberwarmensteinacher Straße 38; 95485 Warmensteinach Phone: +49-9277-9940 Web: www.sili.eu Fax: +49-9277-99499 E-Mail: sili@sigmund-lindner.com

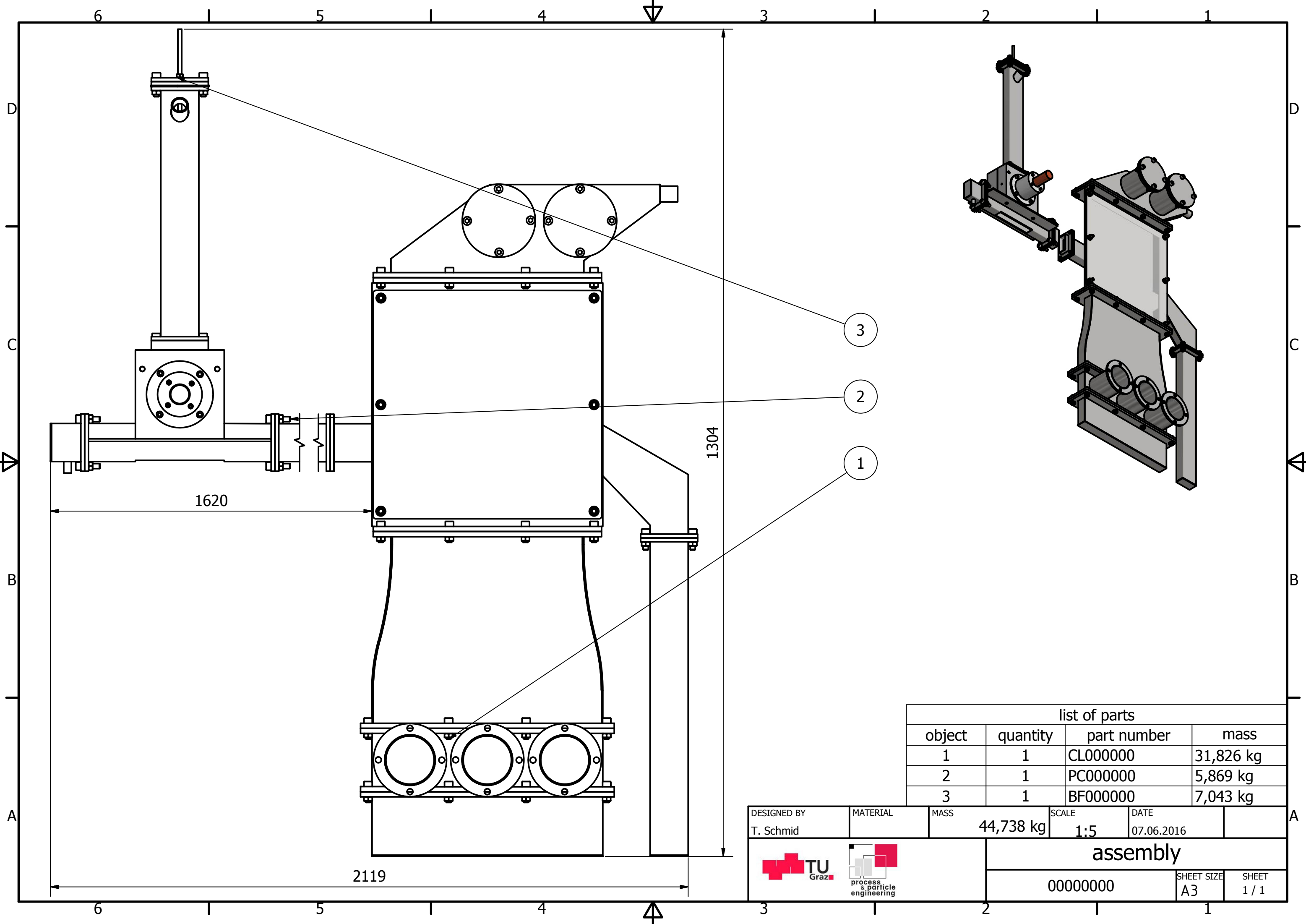
alle Daten sind Referenzwerte – Änderung vorbehalten

Appendix B



B.1 Technical drawings

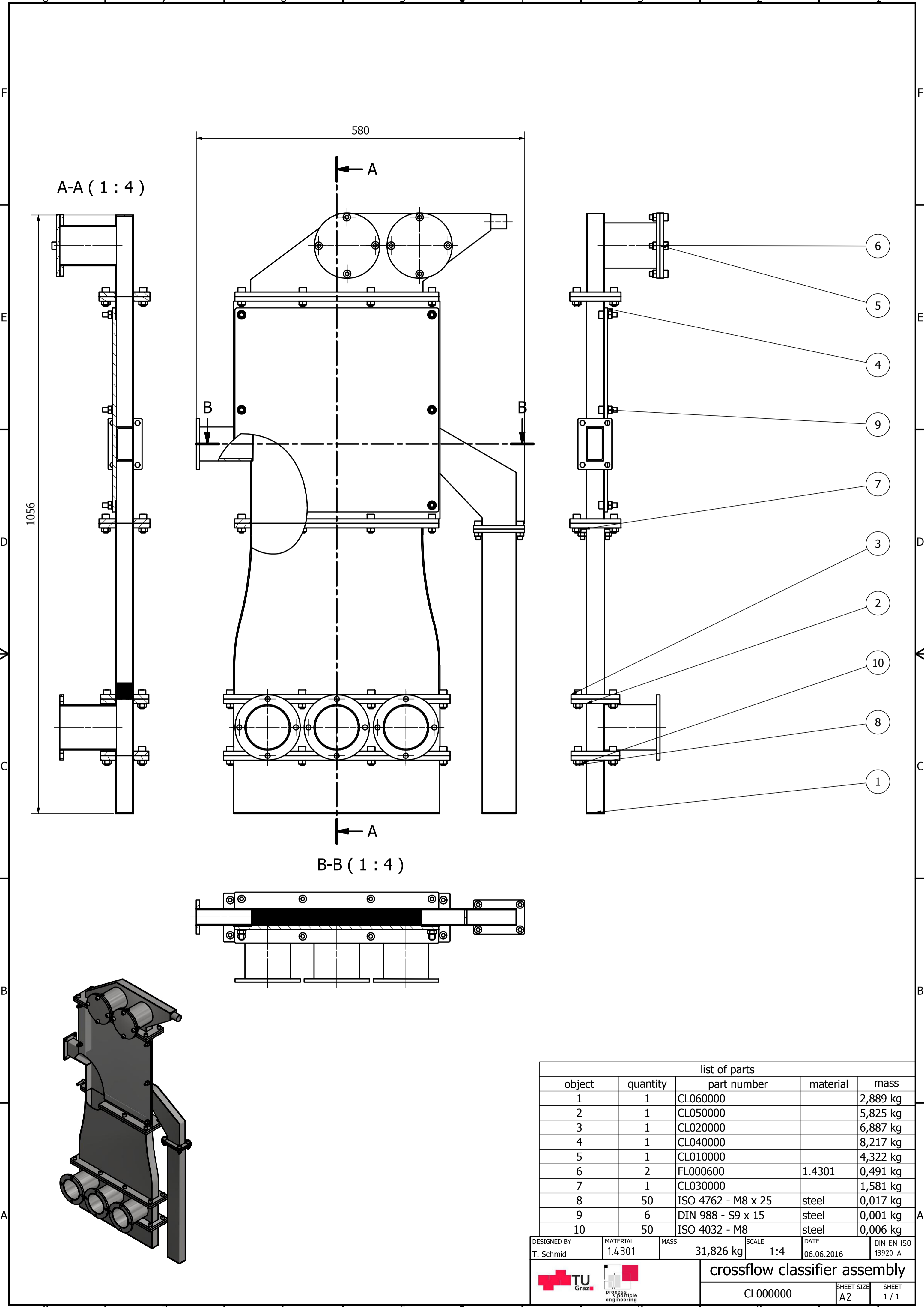
Table 11: structured list of assemblies and parts out of own construction

list of assemblies - layer 0		list of assemblies - layer 1		list of parts	
DRW No.	#	DRW No.	#	DRW No.	#
CL000000	1	CL010000	1	CL010100	1
CL000001	-			CL010200	1
				CL010300	1
				CL010400	1
		CL020000	1	CL020100	2
				CL020001	1
				CL020200	2
		CL030000	1	CL030100	1
		CL040000	1	CL040100	1
				CL040200	1
				CL040201	1
		CL050000	1	CL050100	2
				CL050200	1
		CL060000	1	CL060100	1
				CL060200	1
		CL070000	1	CL070100	2
				CL070200	1
				CL070300	1
		CL080000	1		
PC000000	1	PC010000	1		
		PC020000	1	PC020100	1
		PC030000	1	PC030100	2
				PC030200	1
BF000000	1	BF010001	1	BF000001	1
				BF010100	1
				BF010200	1
				BF010300	1
				BF010400	1
				BF010500	1
				BF010600	1
				BF010700	1
				BF010800	2
				BF010900	1
				BF011000	1
				BF011100	1
				BF011200	1
				BF011300	1
		BF020000	1	BF020100	1
				BF020200	1
				FL000100	4
				FL000200	11
				FL000300	3
				FL000400	5
				FL000500	5
				TB000100	5
				TB000200	1



list of parts			
object	quantity	part number	mass
1	1	CL000000	31,826 kg
2	1	PC000000	5,869 kg
3	1	BF000000	7,043 kg

DESIGNED BY T. Schmid	MATERIAL	MASS 44,738 kg	SCALE 1:5	DATE 07.06.2016
 		assembly		
00000000			SHEET SIZE A3	SHEET 1 / 1



A-A (1 : 4)

B-B (1 : 4)

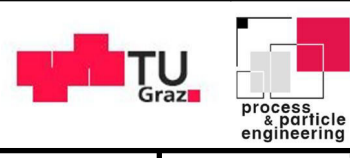
list of parts

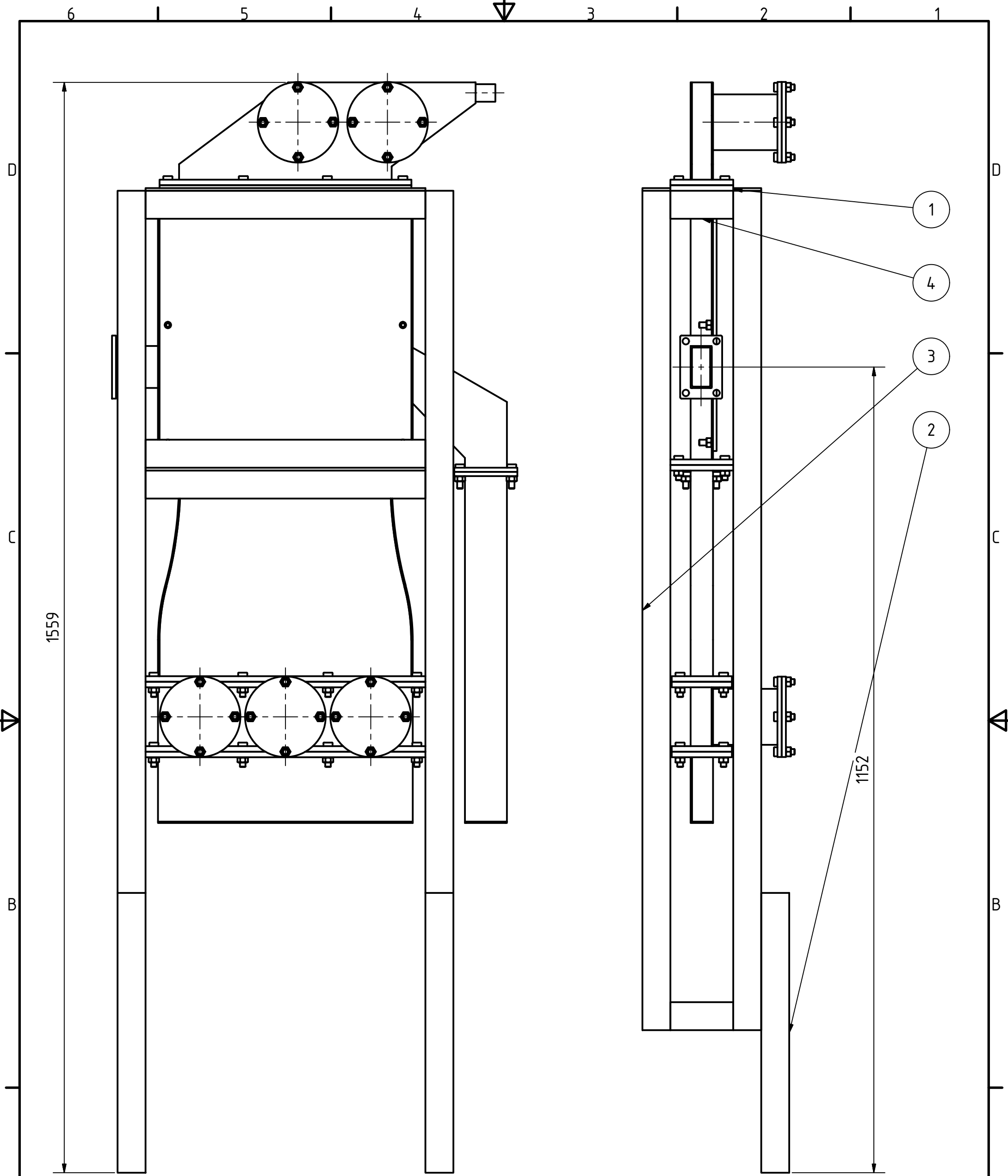
object	quantity	part number	material	mass
1	1	CL060000		2,889 kg
2	1	CL050000		5,825 kg
3	1	CL020000		6,887 kg
4	1	CL040000		8,217 kg
5	1	CL010000		4,322 kg
6	2	FL000600	1.4301	0,491 kg
7	1	CL030000		1,581 kg
8	50	ISO 4762 - M8 x 25	steel	0,017 kg
9	6	DIN 988 - S9 x 15	steel	0,001 kg
10	50	ISO 4032 - M8	steel	0,006 kg

DESIGNED BY T. Schmid	MATERIAL 1.4301	MASS 31,826 kg	SCALE 1:4	DATE 06.06.2016	DIN EN ISO 13920 A
--------------------------	--------------------	-------------------	--------------	--------------------	-----------------------

crossflow classifier assembly



CL000000	SHEET SIZE A2	SHEET 1 / 1
----------	------------------	----------------



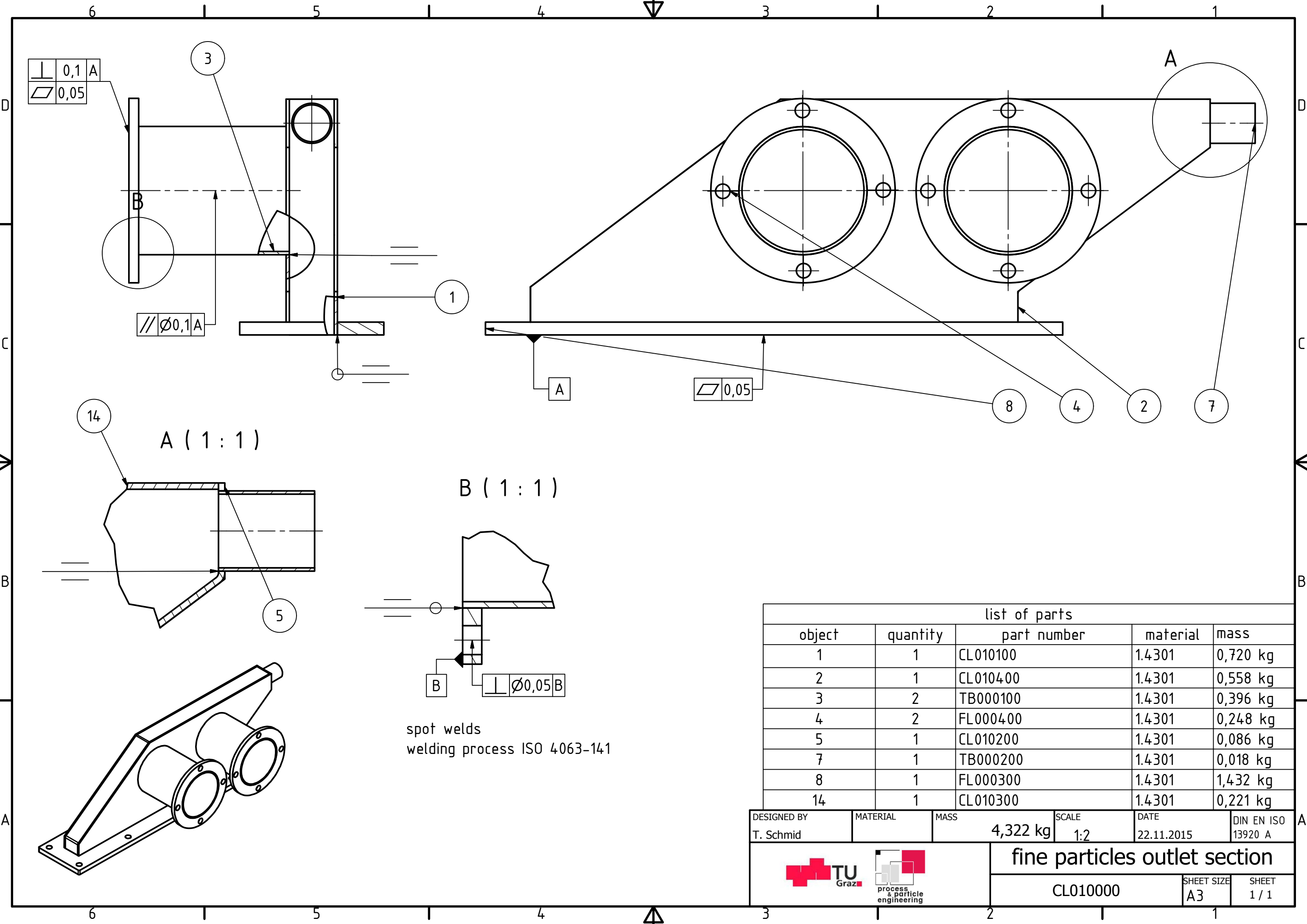


additional list of parts (only rack)			
object	quantity	part number	material
1	4	sheet 400x50x5	1.4301
2	8	item-profile 40x40x400	EN AW-1XXX
3	4	item-profile 40x40x1200	EN AW-1XXX
4	4	item-profile 40x40x90	EN AW-1XXX

DESIGNED BY T. Schmid	MATERIAL 1.4301	MASS	SCALE -	DATE 15.01.2016	DIN EN ISO 13920 A
--------------------------	--------------------	------	------------	--------------------	-----------------------

 	laboratory rack assembly	
	CL000001	SHEET SIZE A3

SHEET
1 / 1



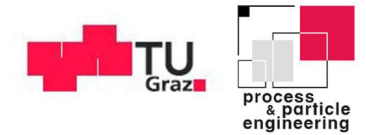
A (1:1)

B (1:1)

list of parts				
object	quantity	part number	material	mass
1	1	CL010100	1.4301	0,720 kg
2	1	CL010400	1.4301	0,558 kg
3	2	TB000100	1.4301	0,396 kg
4	2	FL000400	1.4301	0,248 kg
5	1	CL010200	1.4301	0,086 kg
7	1	TB000200	1.4301	0,018 kg
8	1	FL000300	1.4301	1,432 kg
14	1	CL010300	1.4301	0,221 kg

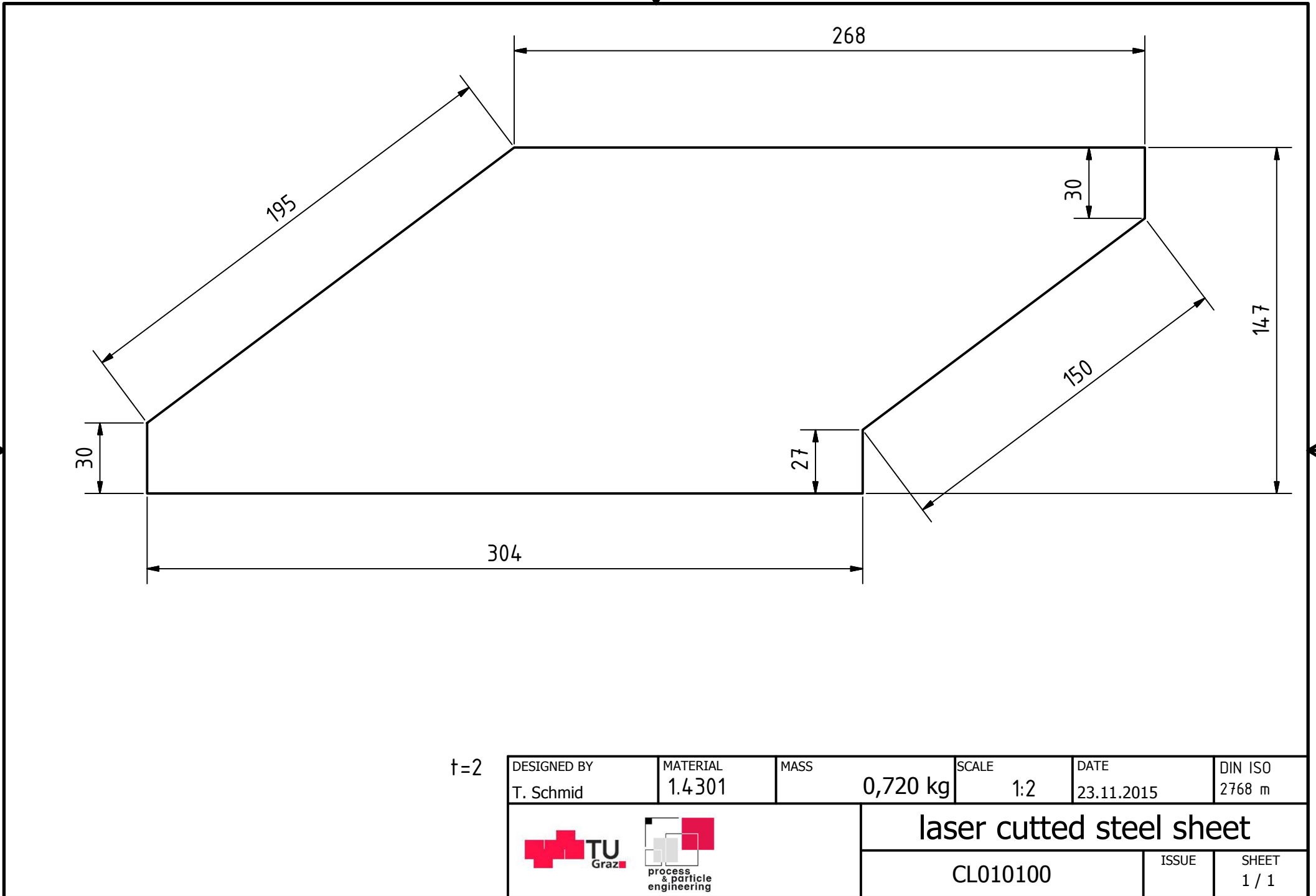
spot welds
welding process ISO 4063-141

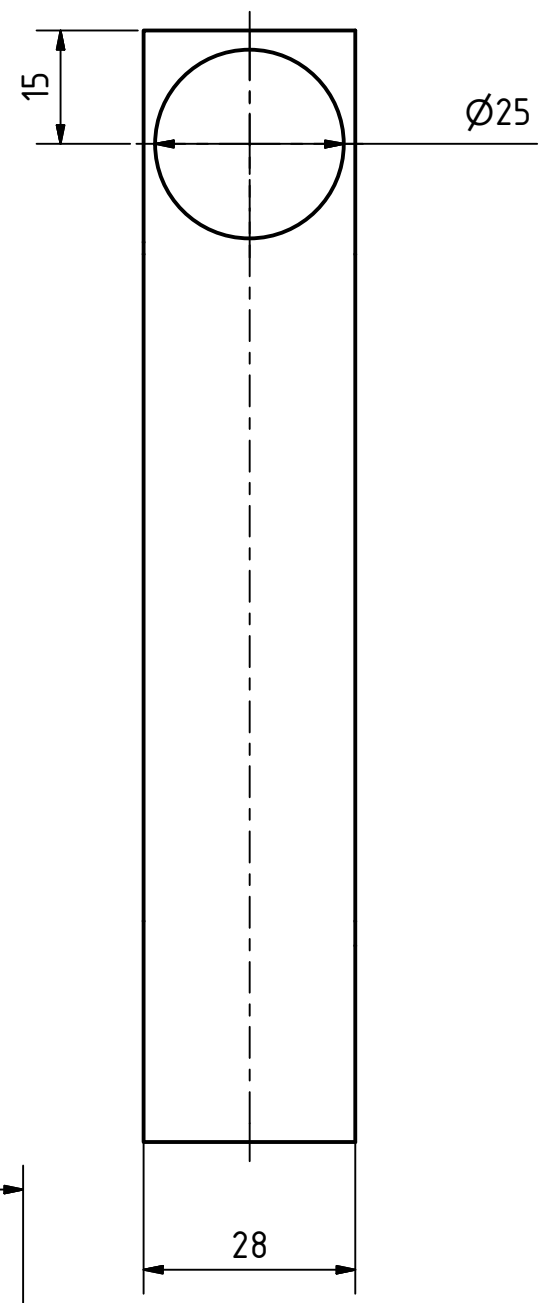
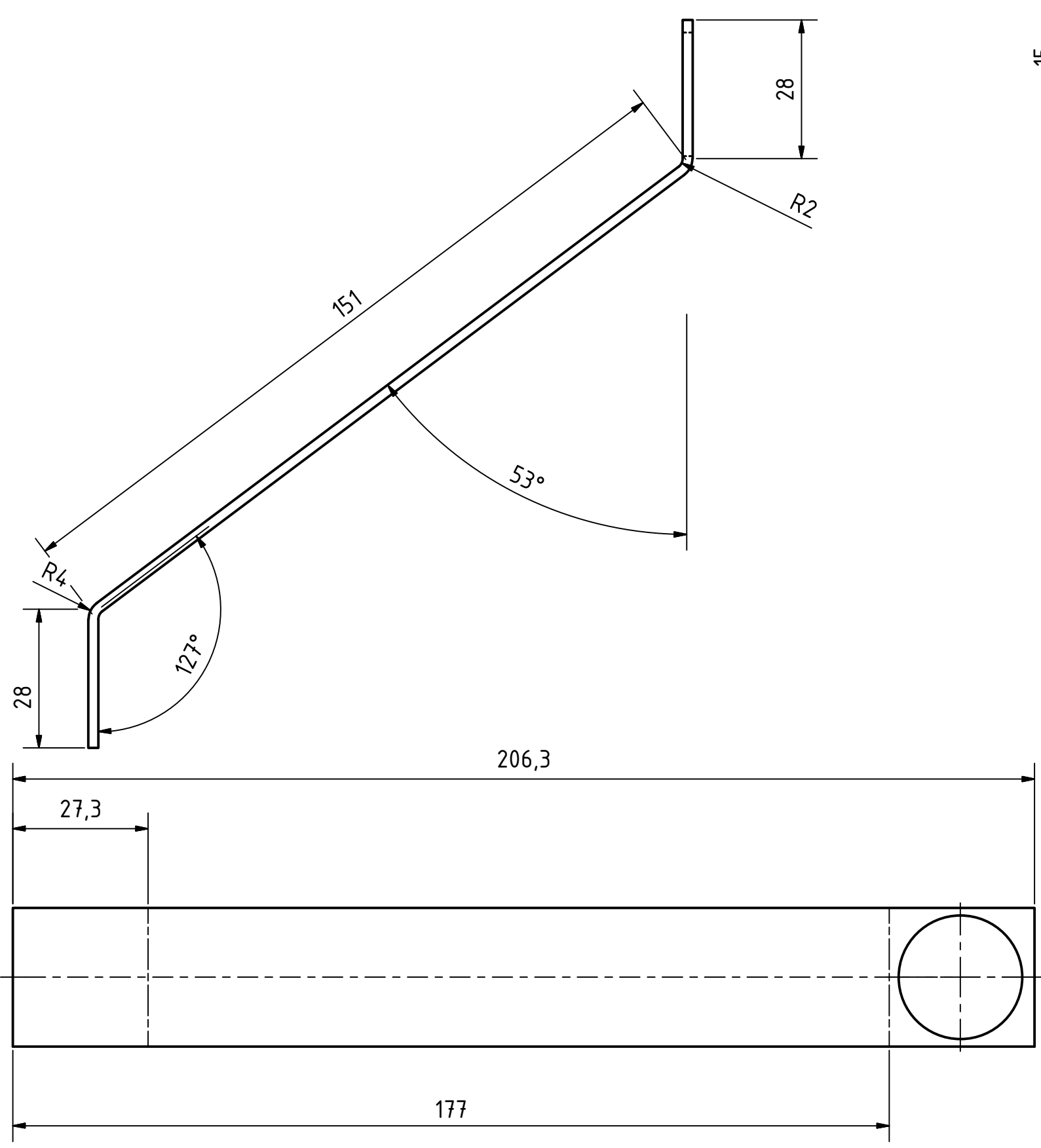
DESIGNED BY T. Schmid	MATERIAL	MASS 4,322 kg	SCALE 1:2	DATE 22.11.2015	DIN EN ISO 13920 A
--------------------------	----------	------------------	--------------	--------------------	-----------------------





fine particles outlet section

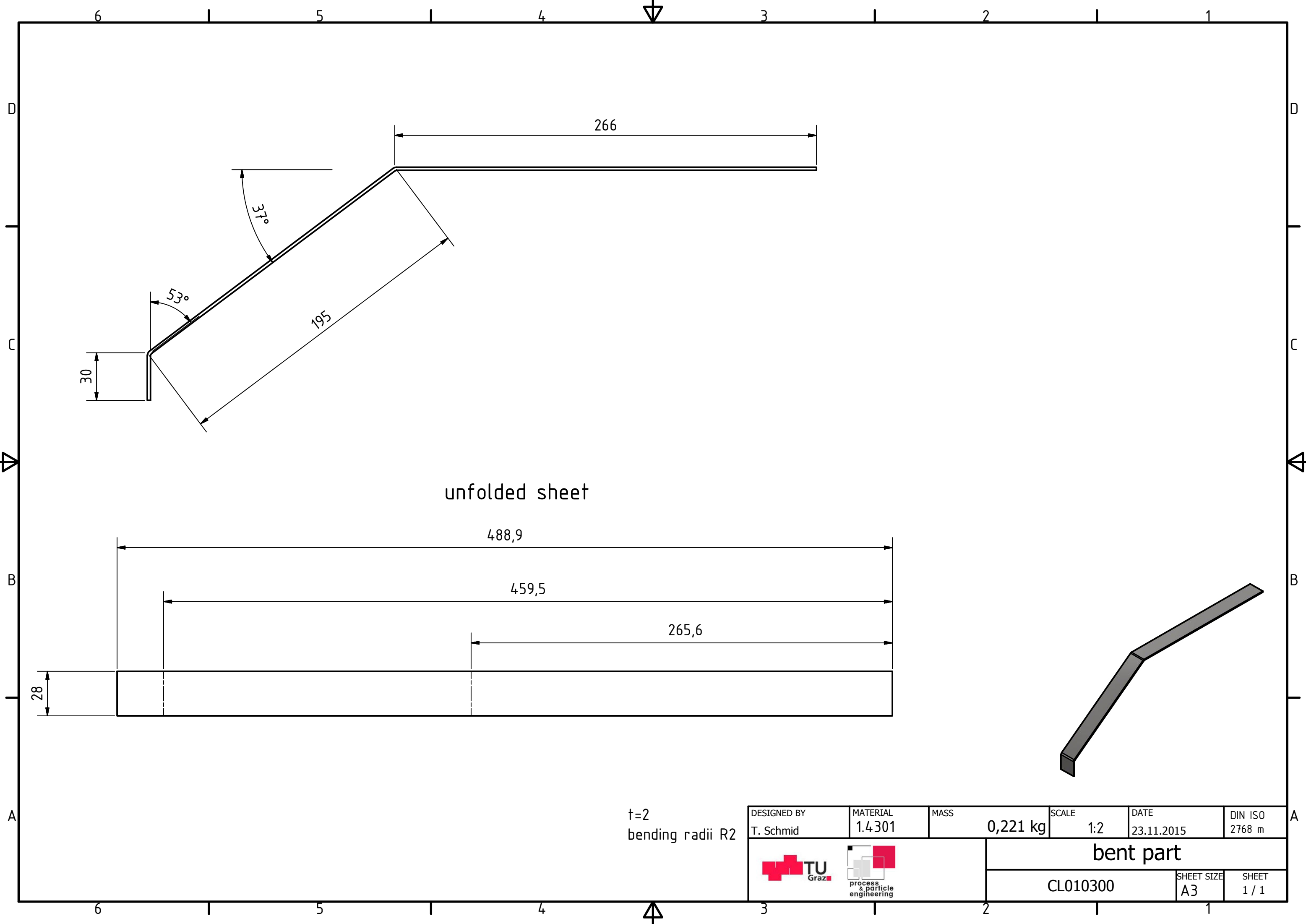
CL010000	SHEET SIZE A3	SHEET 1 / 1
----------	------------------	----------------





t=2
bending radii R2

DESIGNED BY T. Schmid	MATERIAL 1.4301	MASS 0,086 kg	SCALE 1:1	DATE 23.11.2015	DIN ISO 2768 m
 			bended metal sheet part		
			CL010200	SHEET SIZE A3	SHEET 1 / 1



unfolded sheet



488,9

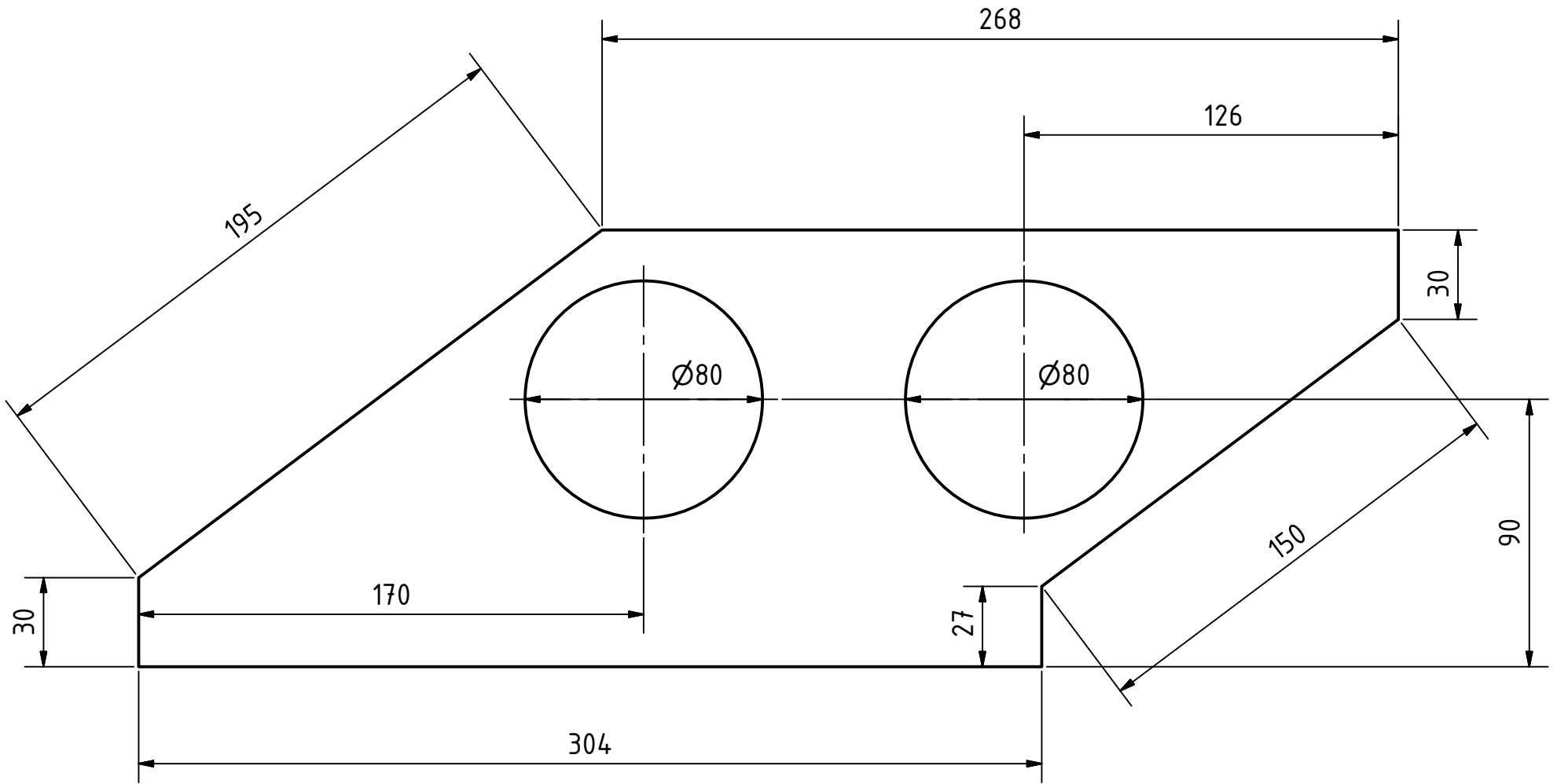
459,5

265,6



28

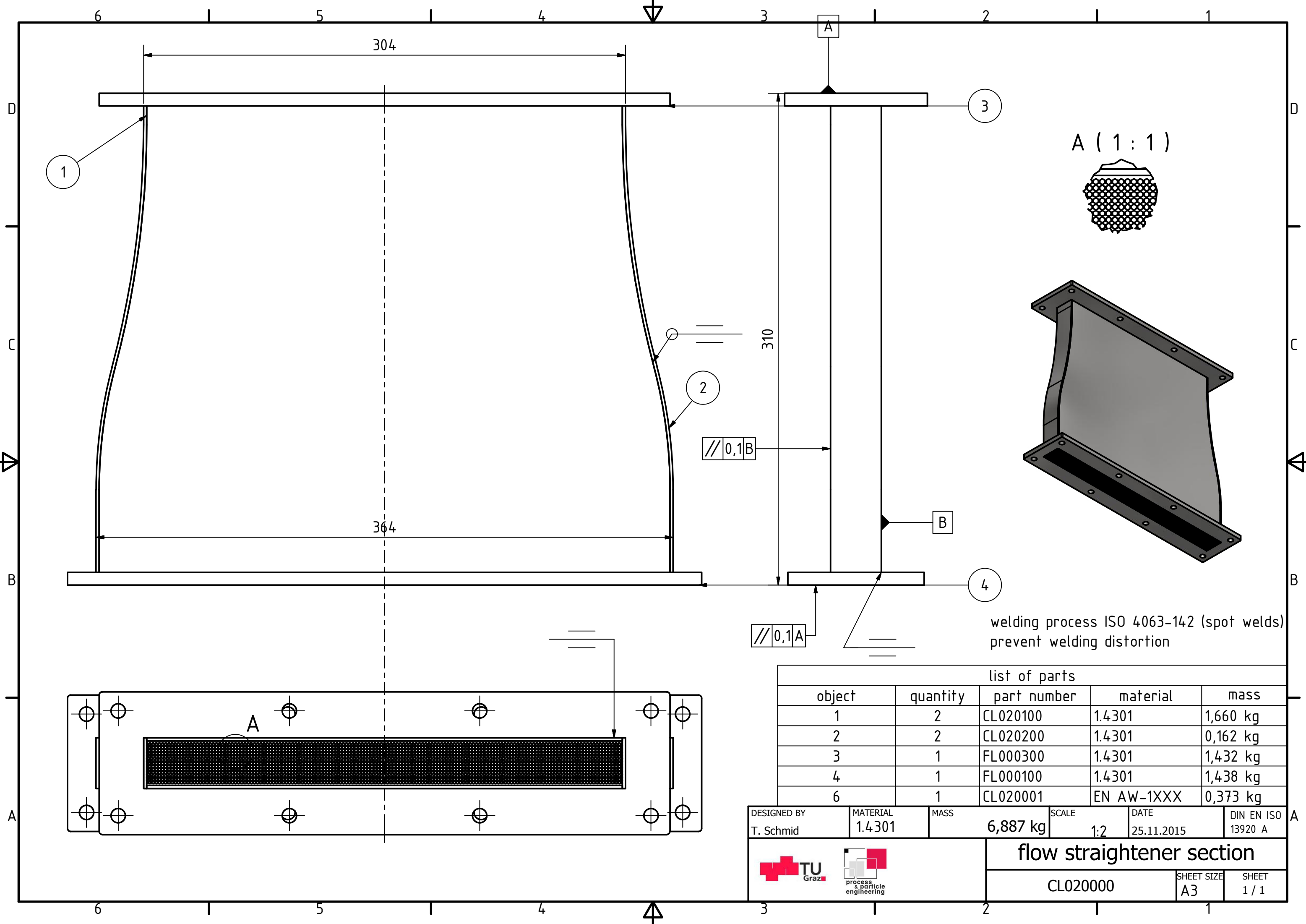
$t=2$
bending radii R2

DESIGNED BY T. Schmid	MATERIAL 1.4301	MASS 0,221 kg	SCALE 1:2	DATE 23.11.2015	DIN ISO 2768 m
 			bent part		
			CL010300	SHEET SIZE A3	SHEET 1 / 1



$t=2$



DESIGNED BY T. Schmid	MATERIAL 1.4301	MASS 0,558 kg	SCALE 1:2	DATE 25.11.2015	DIN ISO 2768 m
 		lasered metal sheet part			
CL010400			SHEET SIZE A4	SHEET 1 / 1	



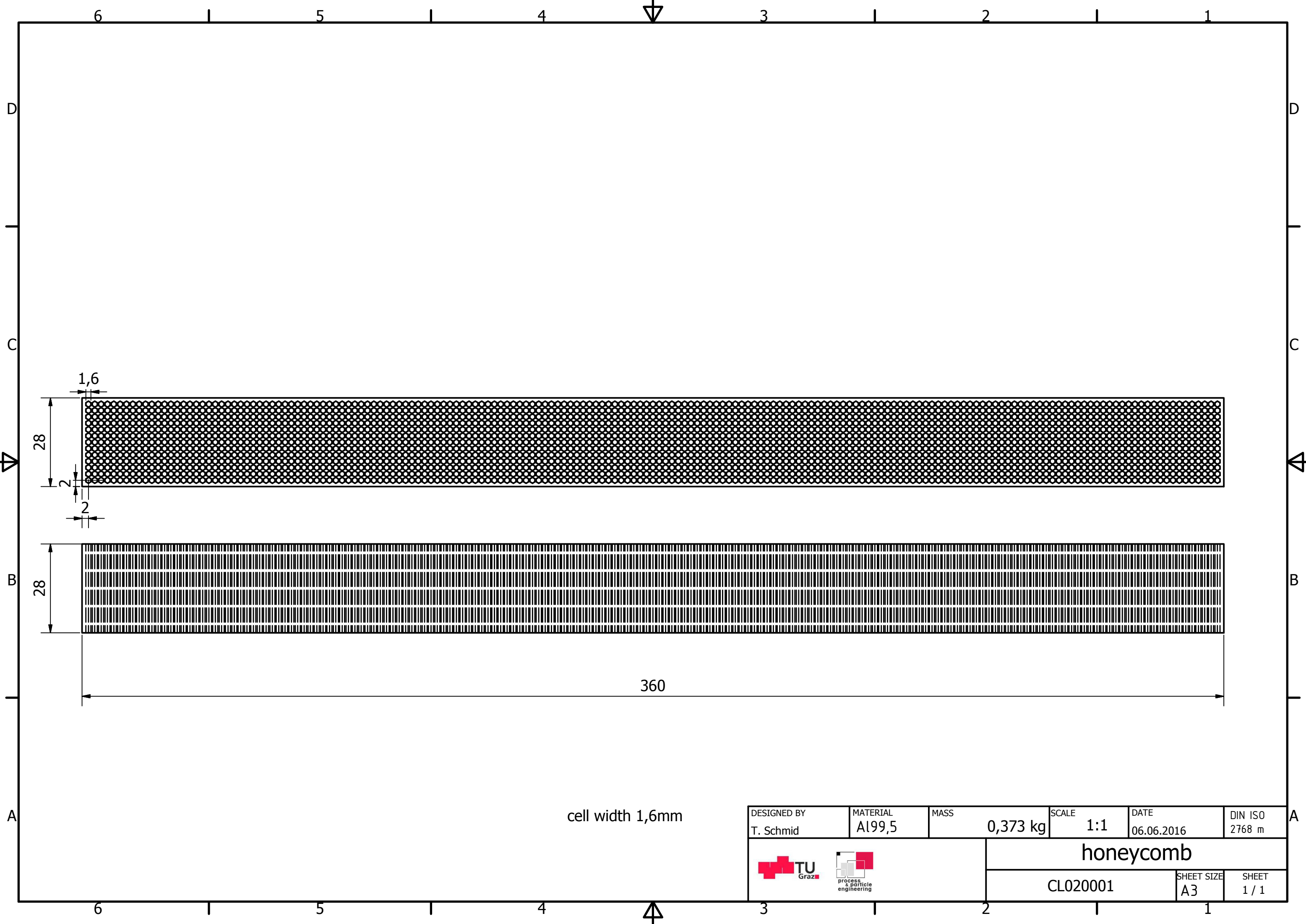
welding process ISO 4063-142 (spot welds)
prevent welding distortion

list of parts				
object	quantity	part number	material	mass
1	2	CL020100	1.4301	1,660 kg
2	2	CL020200	1.4301	0,162 kg
3	1	FL000300	1.4301	1,432 kg
4	1	FL000100	1.4301	1,438 kg
6	1	CL020001	EN AW-1XXX	0,373 kg



DESIGNED BY T. Schmid	MATERIAL 1.4301	MASS 6,887 kg	SCALE 1:2	DATE 25.11.2015	DIN EN ISO 13920 A
--------------------------	--------------------	------------------	--------------	--------------------	-----------------------

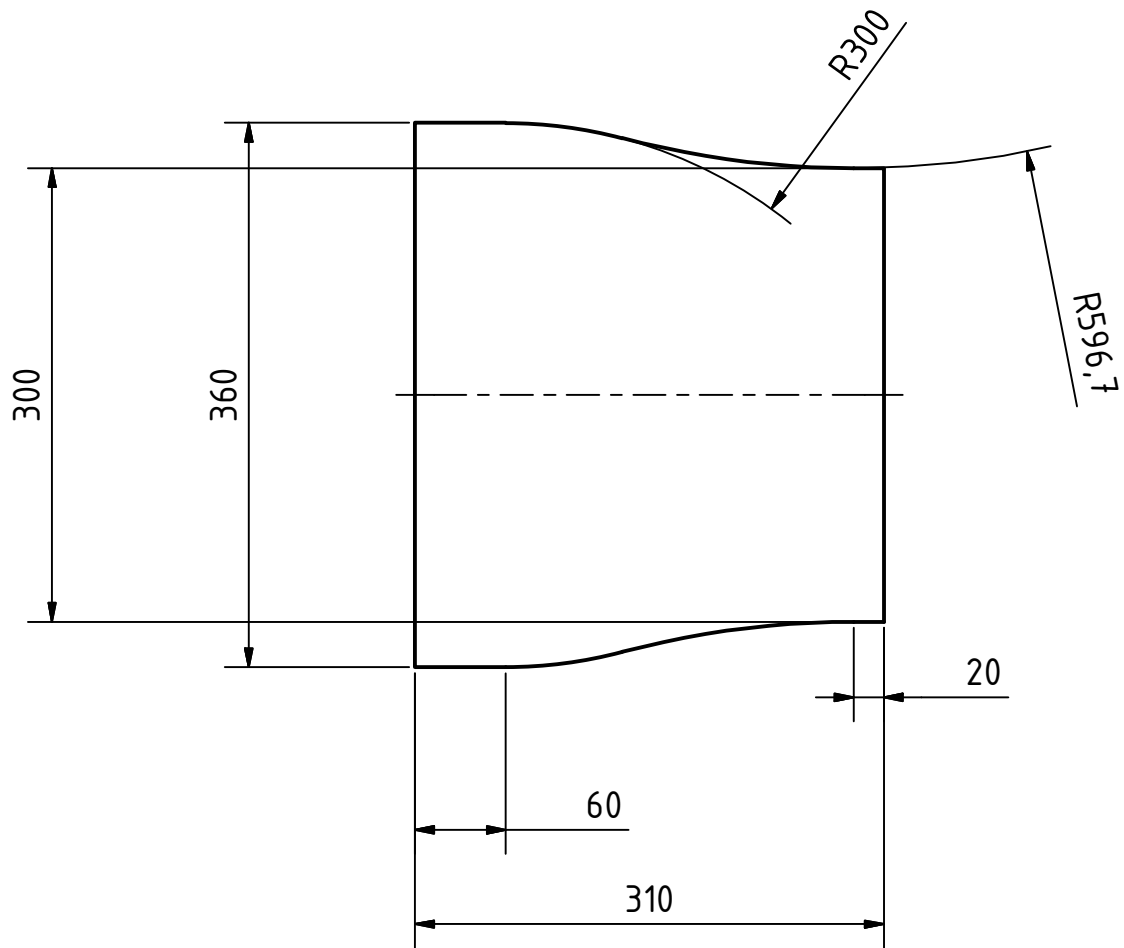
 	flow straightener section	
	CL020000	SHEET SIZE A3



SHEET
1 / 1

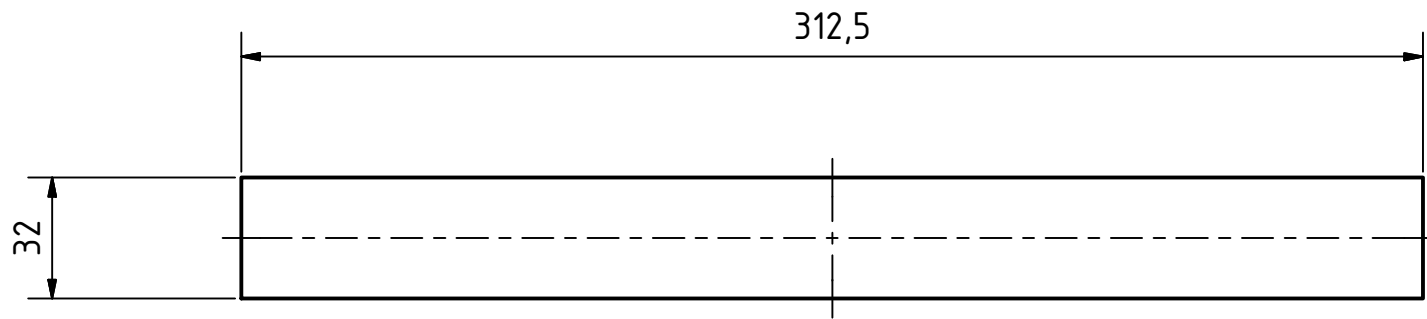


cell width 1,6mm



DESIGNED BY T. Schmid	MATERIAL Al99,5	MASS 0,373 kg	SCALE 1:1	DATE 06.06.2016	DIN ISO 2768 m
 			honeycomb		
			CL020001	SHEET SIZE A3	SHEET 1 / 1

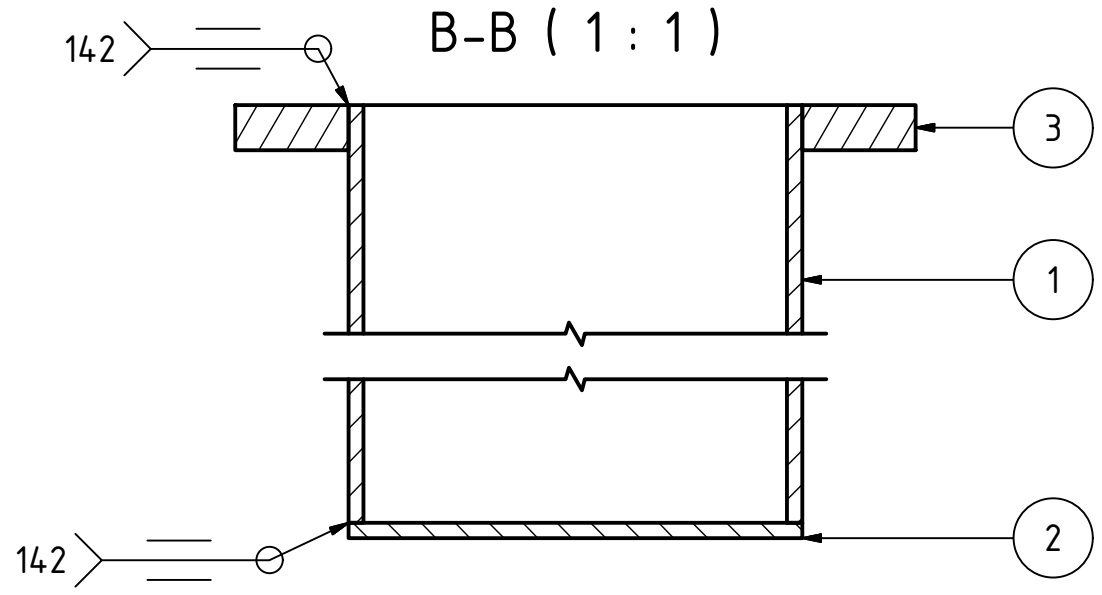
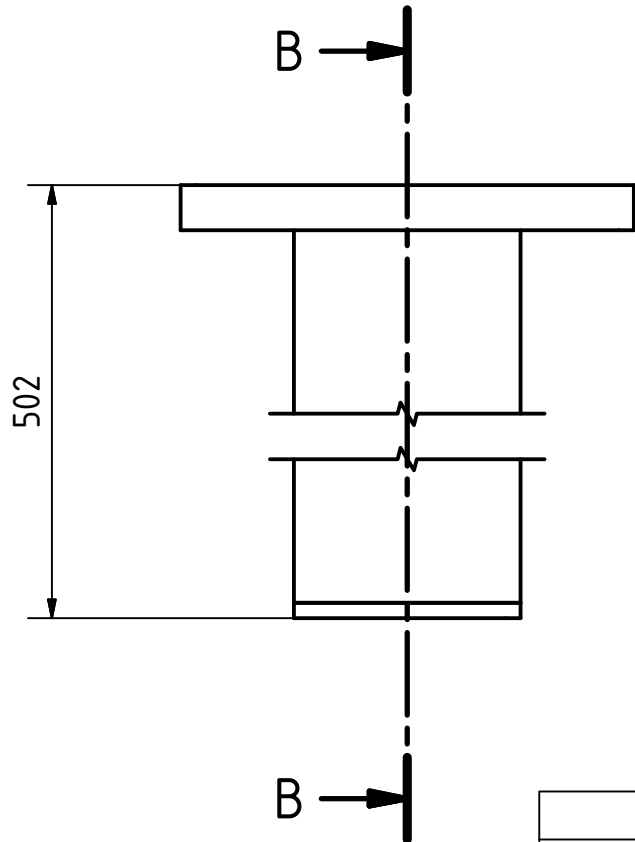


DESIGNED BY T. Schmid	MATERIAL 1.4301	MASS 1,660 kg	SCALE 1:5	DATE 24.11.2015	DIN ISO 2768 m
 			laser cut metal sheet		
			CL020100	SHEET SIZE A4	SHEET 1 / 1





t=2

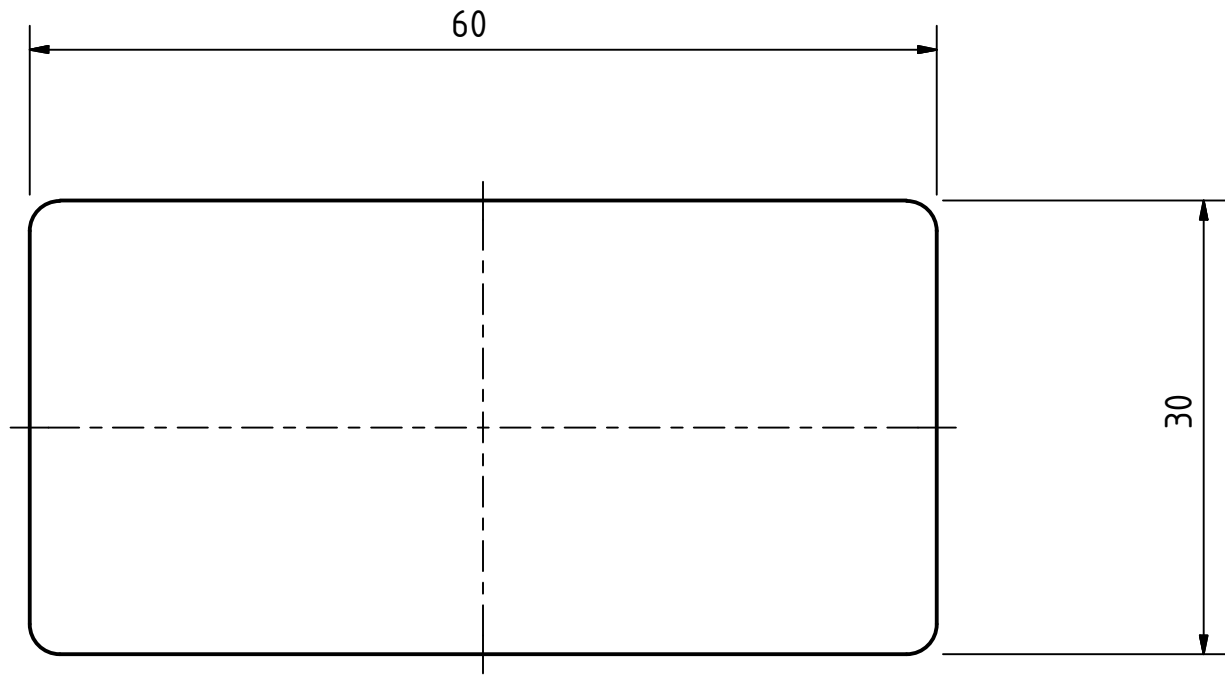
DESIGNED BY T. Schmid	MATERIAL 1.4301	MASS 0,162 kg	SCALE 1:2	DATE 24.11.2015	DIN ISO 2768 m
 		metal sheet			
CL020200			SHEET SIZE A4	SHEET 1 / 1	





list of parts				
object	quantity	part number	material	mass
1	1	hollow profile 60x30x2x500	1.4301	1,390 kg
2	1	CL030100	1.4301	0,029 kg
3	1	FL000200	1.4301	0,162 kg

DESIGNED BY T. Schmid	MATERIAL 1.4301	MASS 1,581 kg	SCALE 1:1	DATE 23.11.2015	DIN EN ISO 13920 A
--------------------------	--------------------	------------------	--------------	--------------------	-----------------------

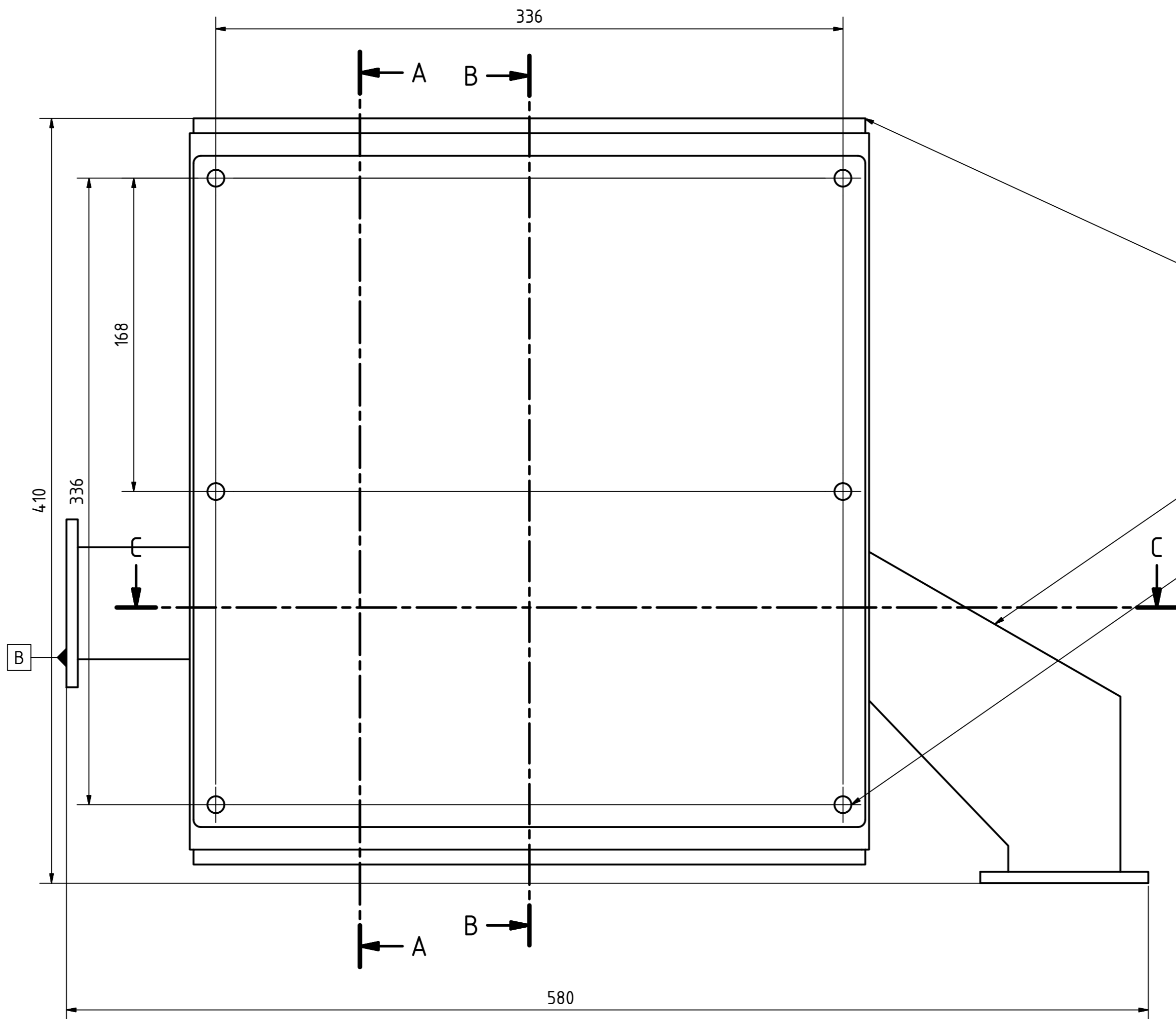
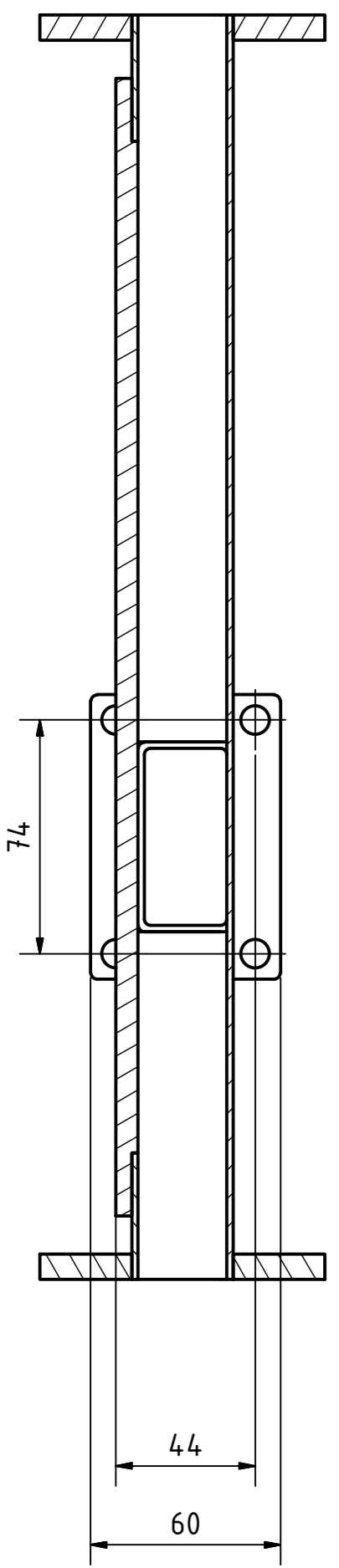
 	coarse particle container		
	CL030000	SHEET SIZE A4	SHEET 1 / 1



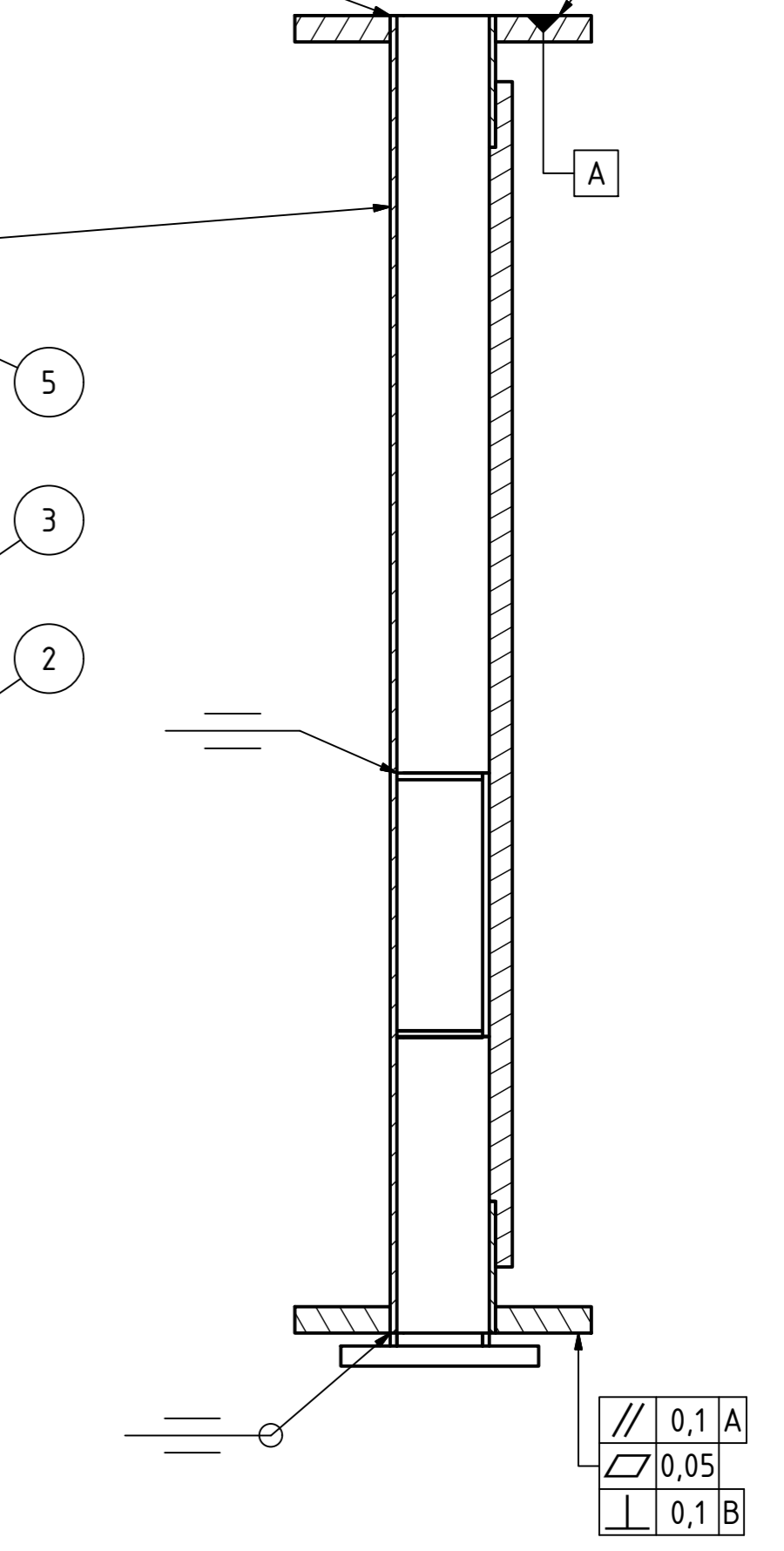
t=2

DESIGNED BY T. Schmid	MATERIAL 1.4301	MASS 0,029 kg	SCALE 2:1	DATE 23.11.2015	DIN ISO 2768 m
 		sheet metal			
CL030100			SHEET SIZE A4	SHEET 1 / 1	

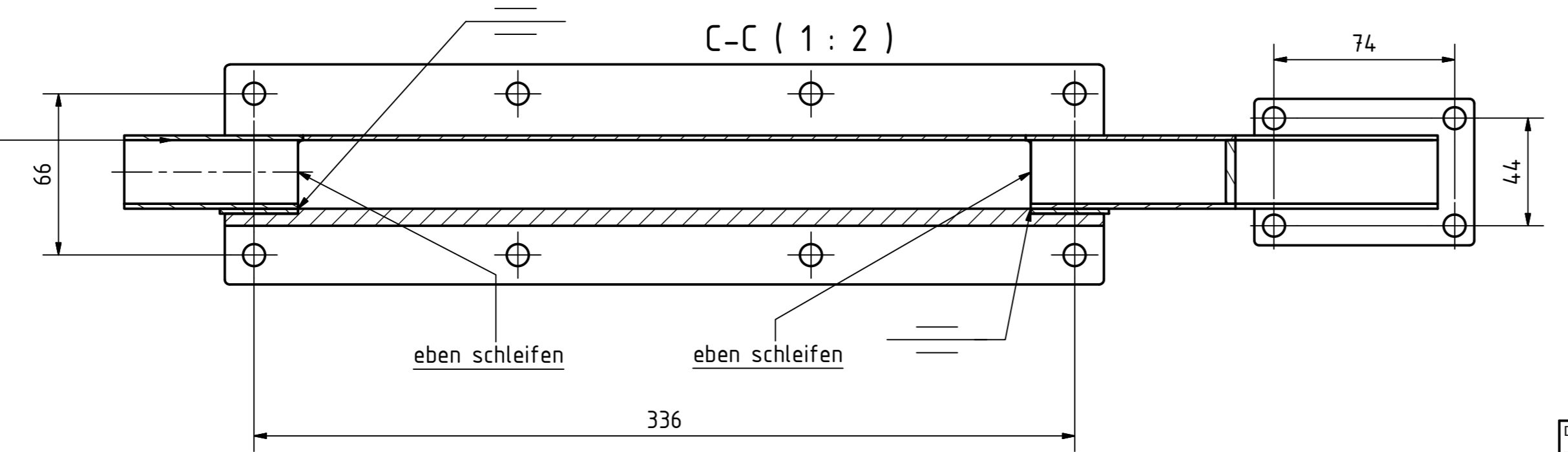
A-A (1:2)



B-B (1:2)



C-C (1:2)



list of parts				
object	quantity	part number	material	mass
1	1	CL040100	1.4301	2,241 kg
2	1	CL040200	1.4301	0,780 kg
3	1	CL070000		0,902 kg
4	1	CL080000		0,440 kg
5	2	FL000300	1.4301	1,432 kg
6	1	CL040201	acryl glass	0,997 kg

DESIGNED BY T. Schmid	MATERIAL 1.4301	MASS 8.217 kg	SCALE 1:2	DATE 24.11.2015	DIN EN ISO 13920 A
--------------------------	--------------------	------------------	--------------	--------------------	-----------------------

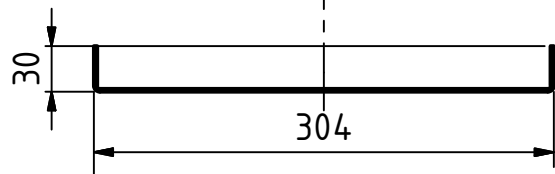
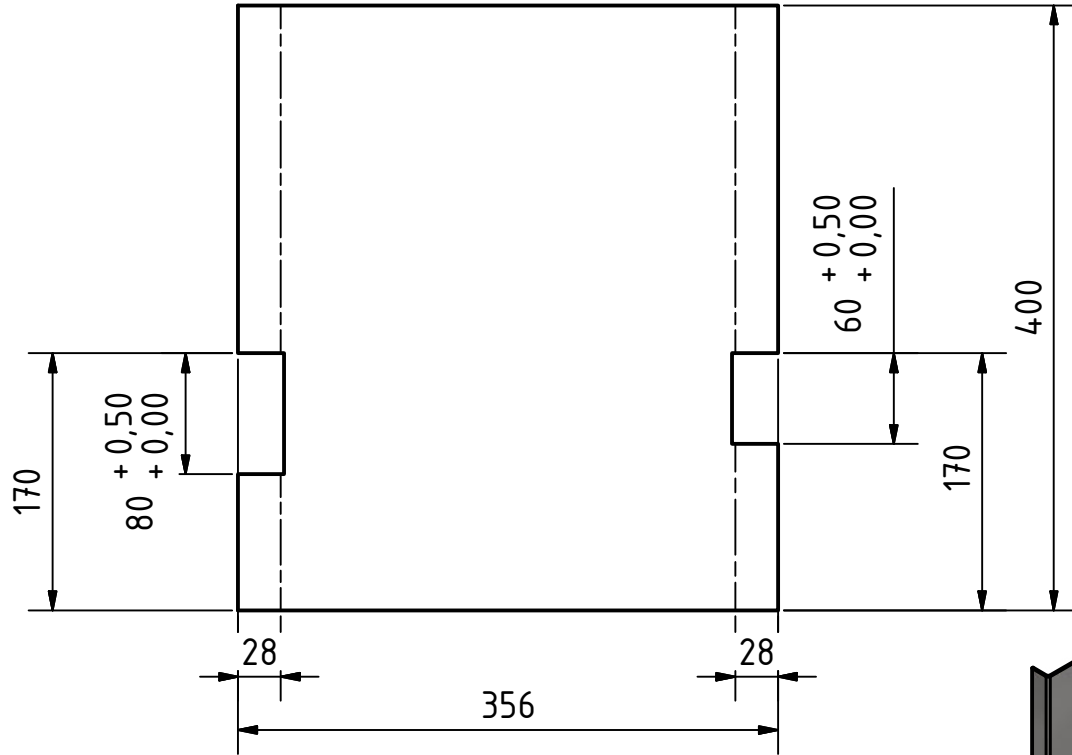
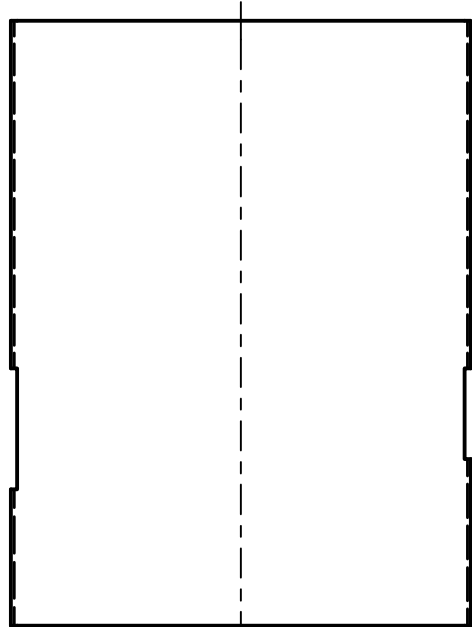
classifying section

CL040000	SHEET SIZE A2	SHEET 1 / 1
----------	------------------	----------------

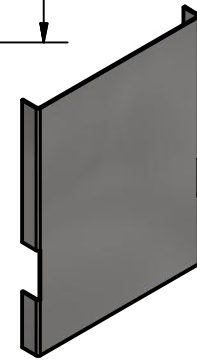
all not further defined welds are spot welds
welding process ISO 4063-141
all undefined bores Ø9





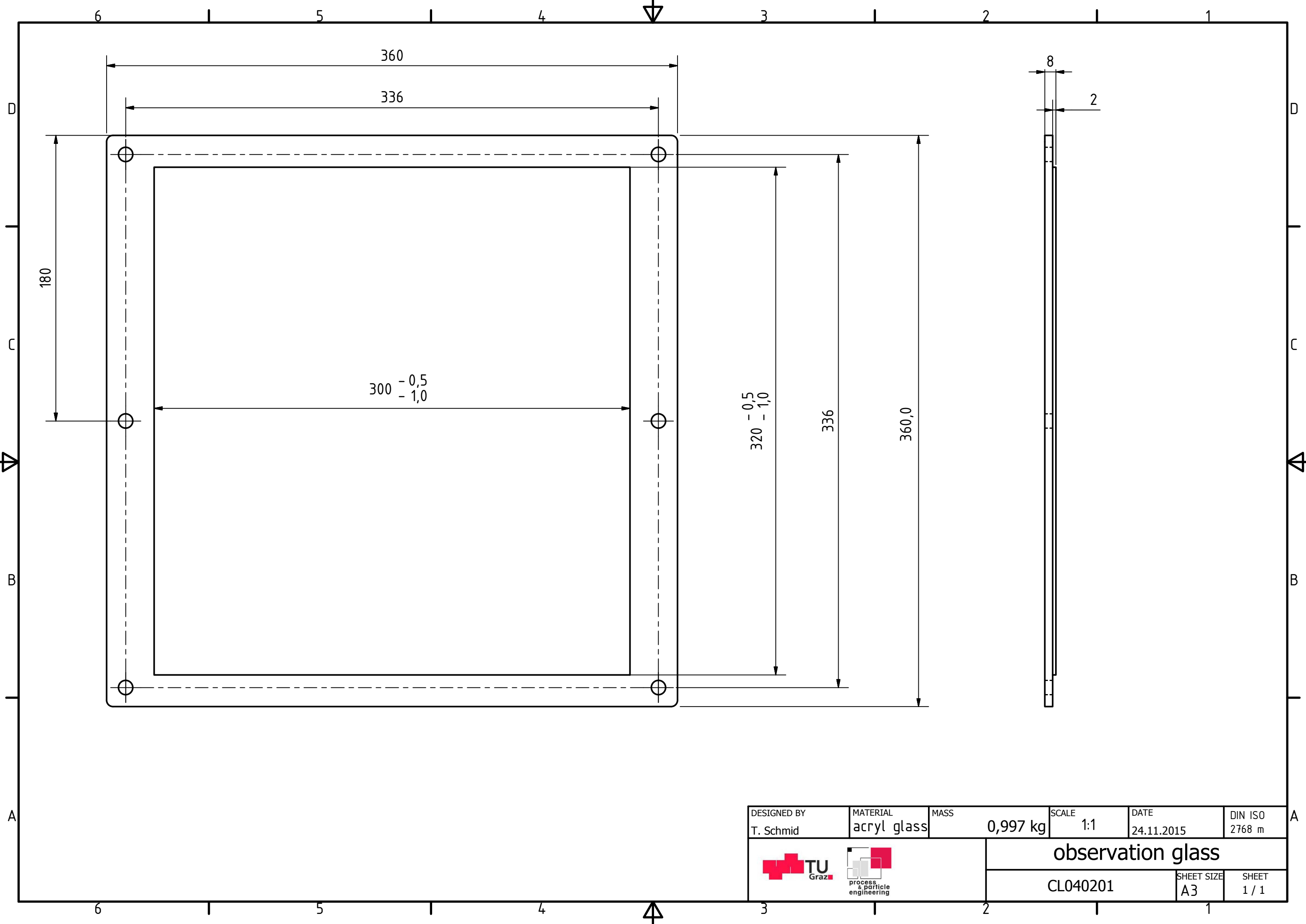
unfolded sheet





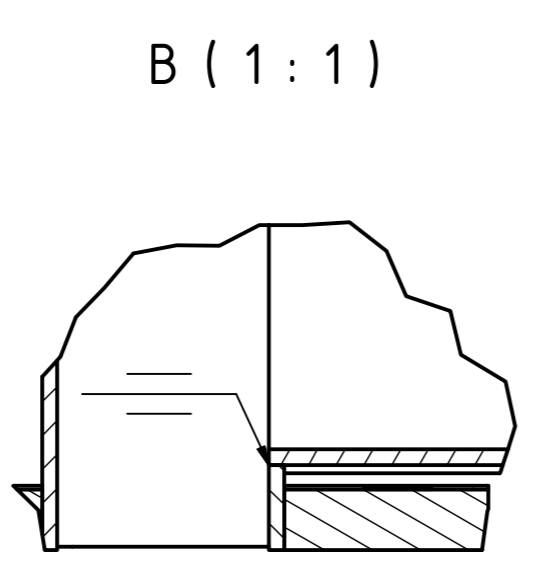
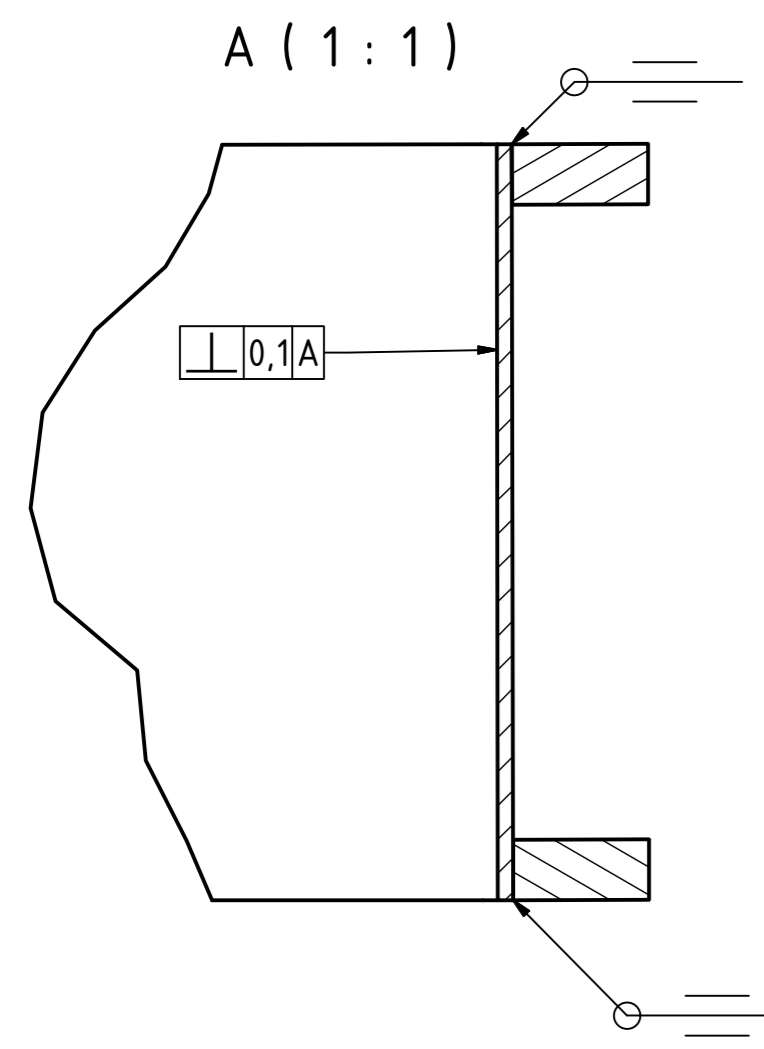
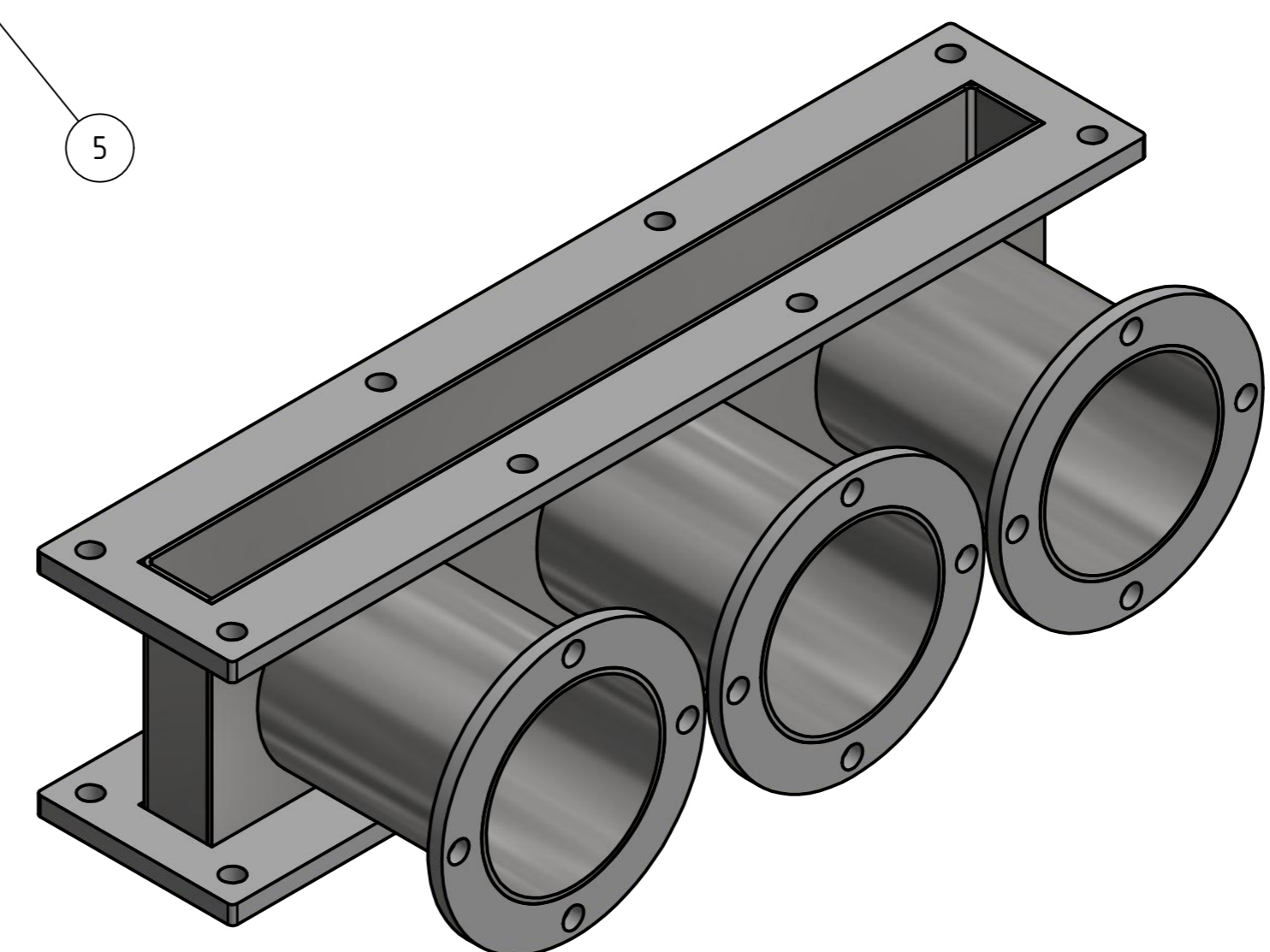
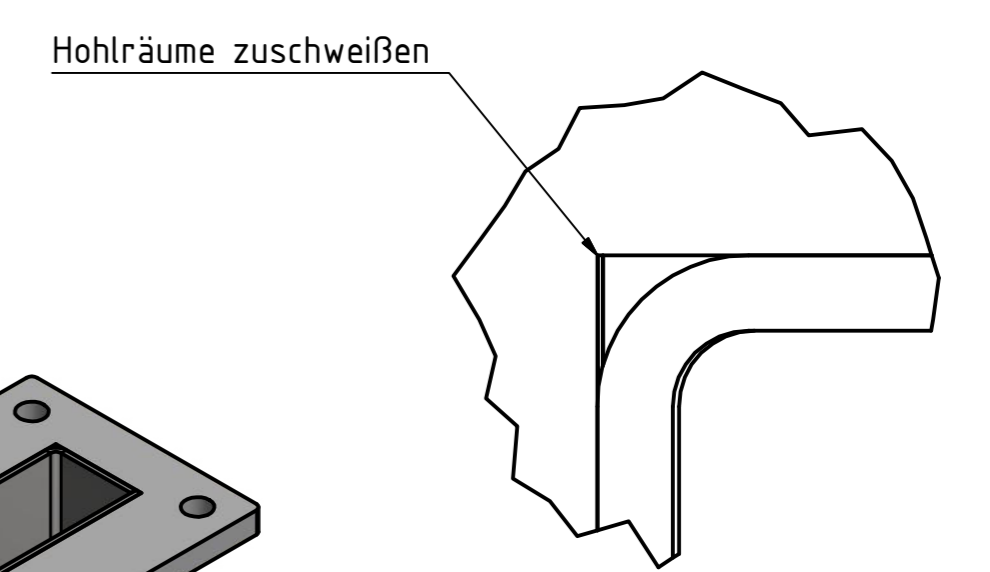
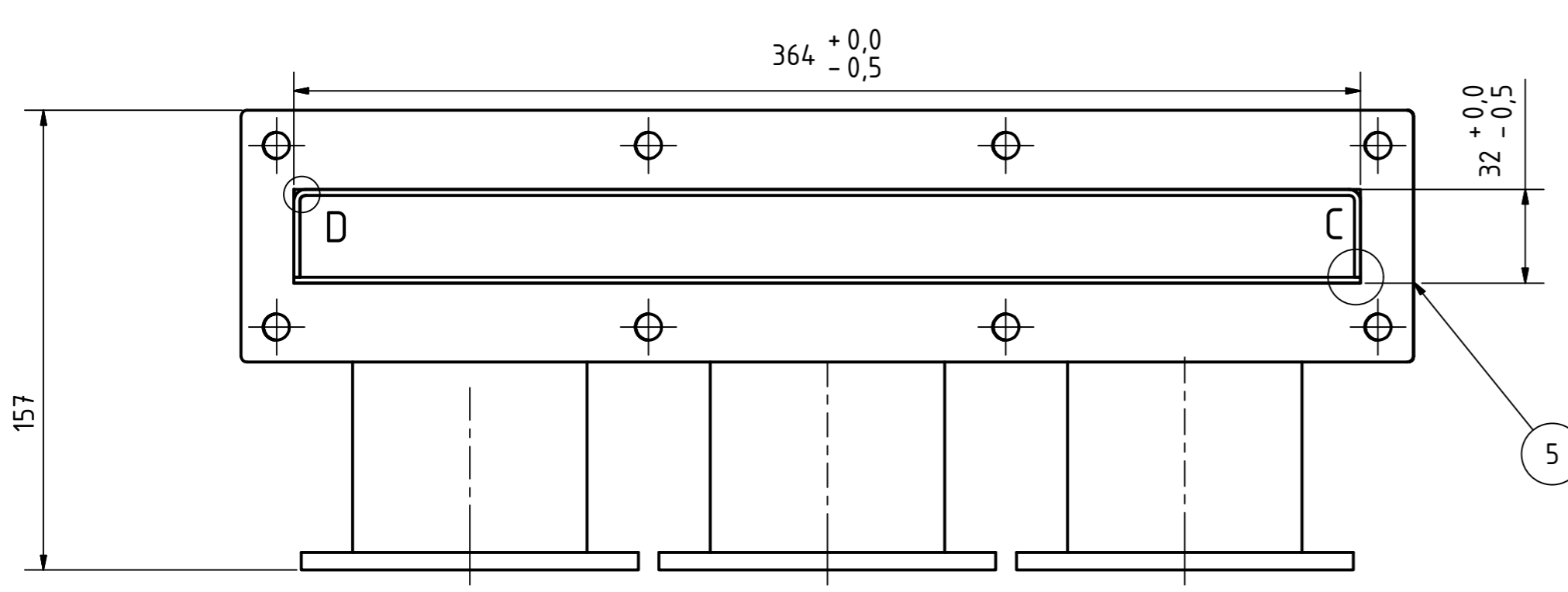
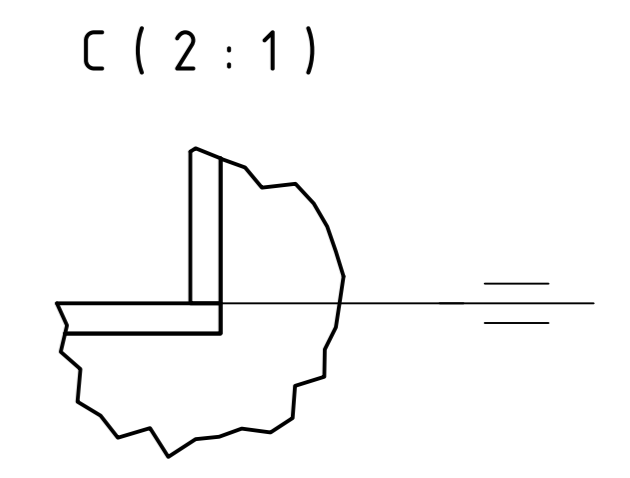
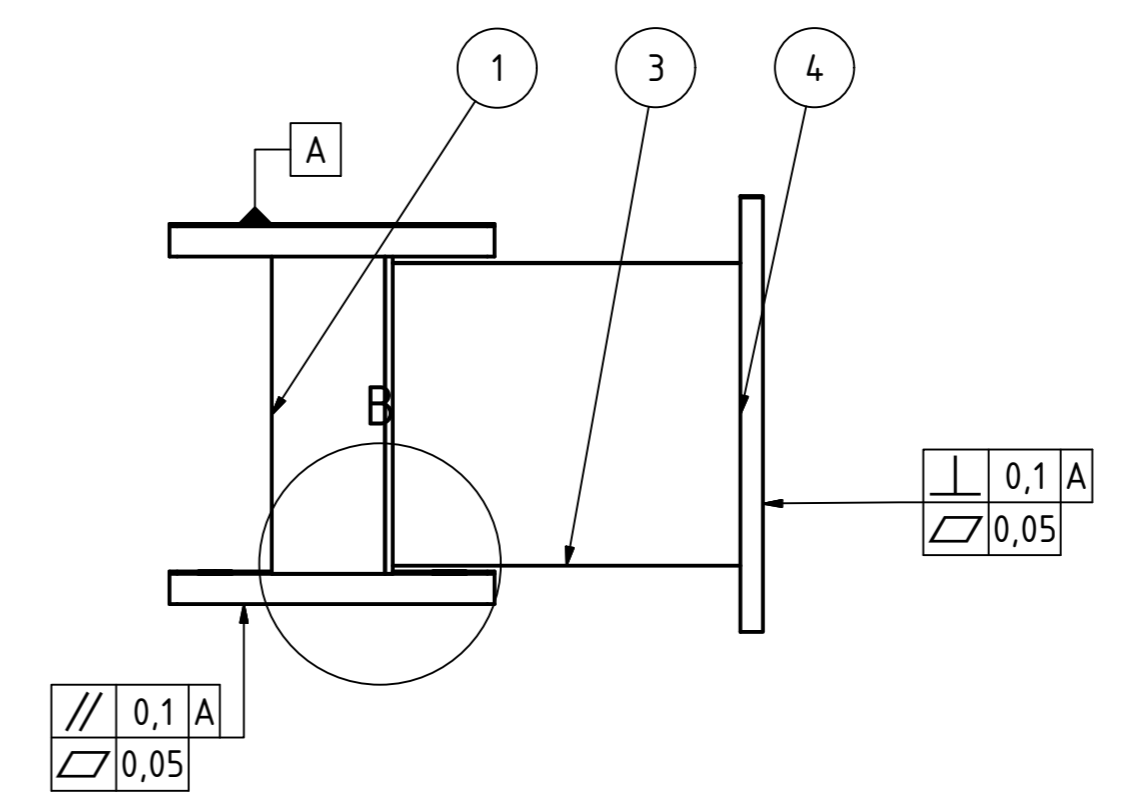
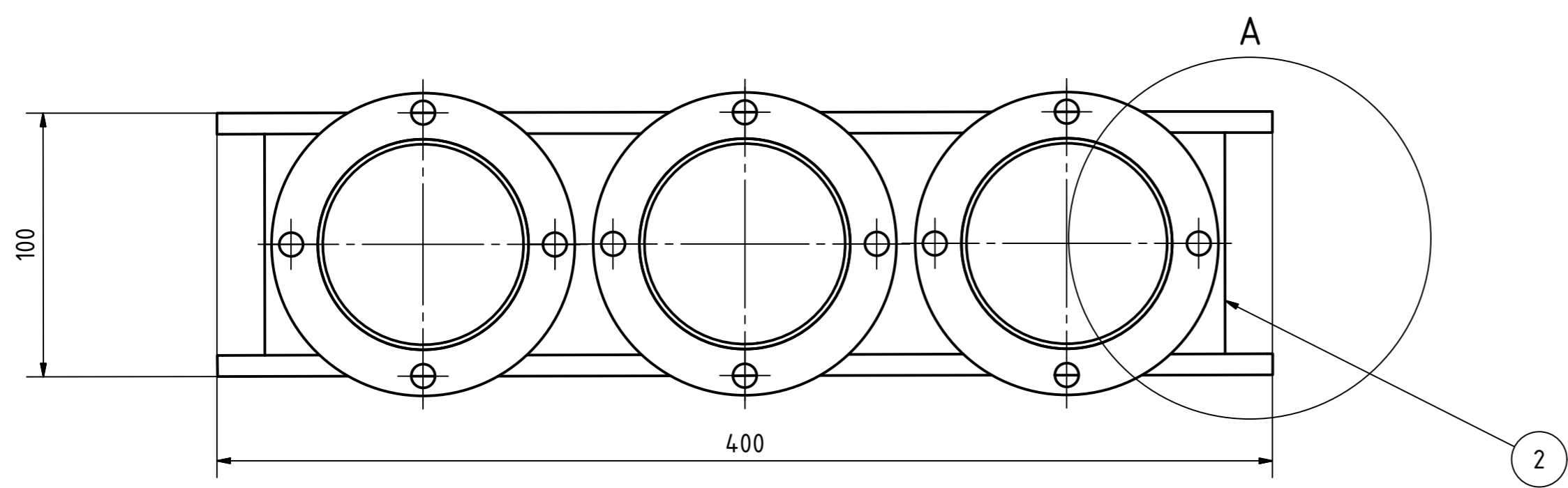
t=2
bending radii R2



DESIGNED BY T. Schmid	MATERIAL 1.4301	MASS 2,241 kg	SCALE 1:2	DATE 23.11.2015	DIN ISO 2768 m
 			bent part		
			CL040100		SHEET SIZE A4





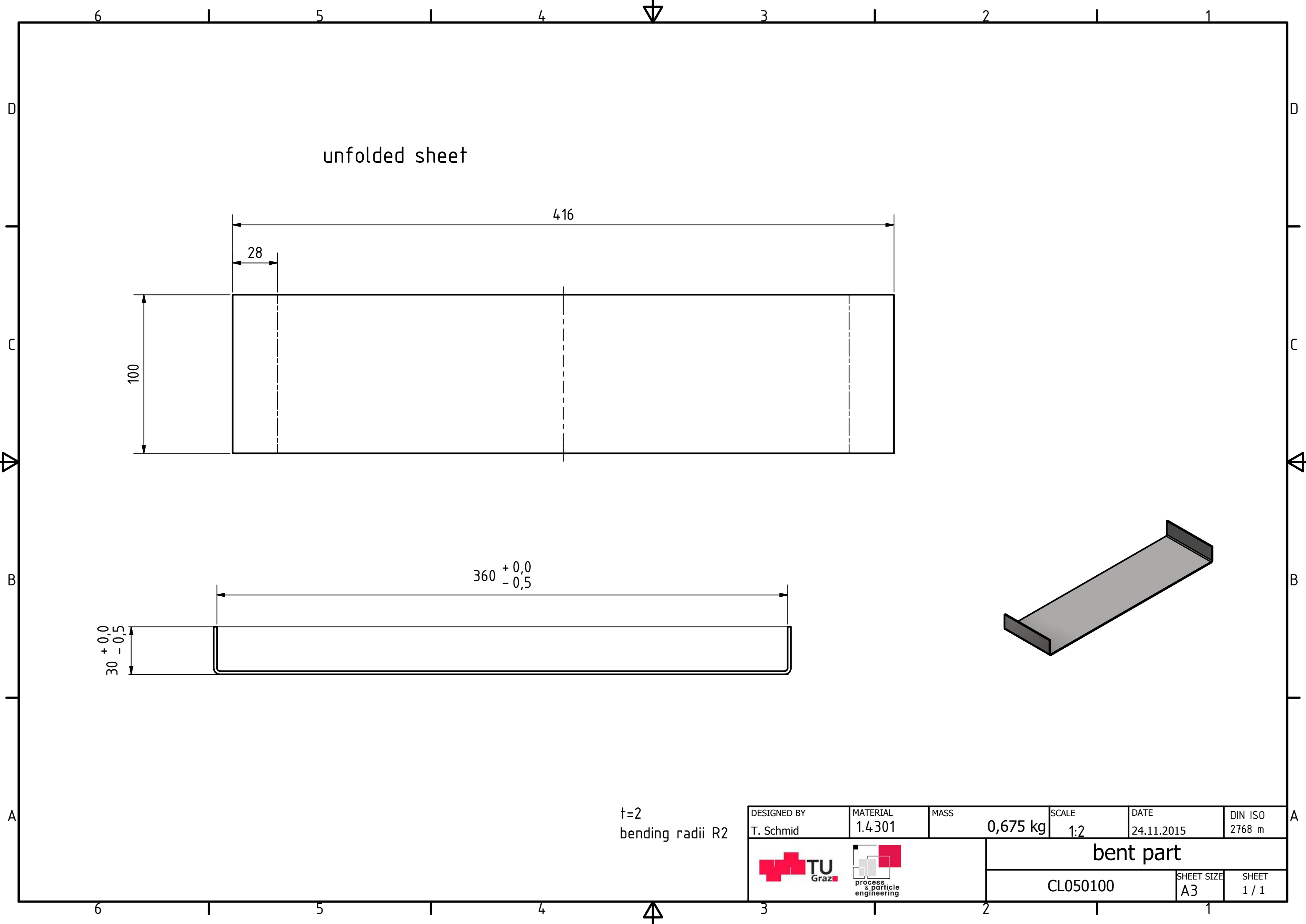
DESIGNED BY T. Schmid	MATERIAL acryl glass	MASS 0,997 kg	SCALE 1:1	DATE 24.11.2015	DIN ISO 2768 m
 			observation glass		
			CL040201	SHEET SIZE A3	SHEET 1 / 1



all not further defined welds spot welded (ISO 4063-142)
welding process ISO 4063-141

list of parts				
object	quantity	part number	material	mass
1	1	CL050100	1.4301	0,675 kg
2	1	CL050200	1.4301	0,345 kg
3	3	TB000100	1.4301	0,396 kg
4	3	FL000400	1.4301	0,248 kg
5	2	FL000100	1.4301	1,438 kg

DESIGNED BY T. Schmid	MATERIAL 1.4301	MASS 5,825 kg	SCALE 1:2	DATE 24.11.2015	DIN EN ISO 13920 A
 			air inlet section		
			CL050000	SHEET SIZE A2	SHEET 1 / 1



unfolded sheet

416



28

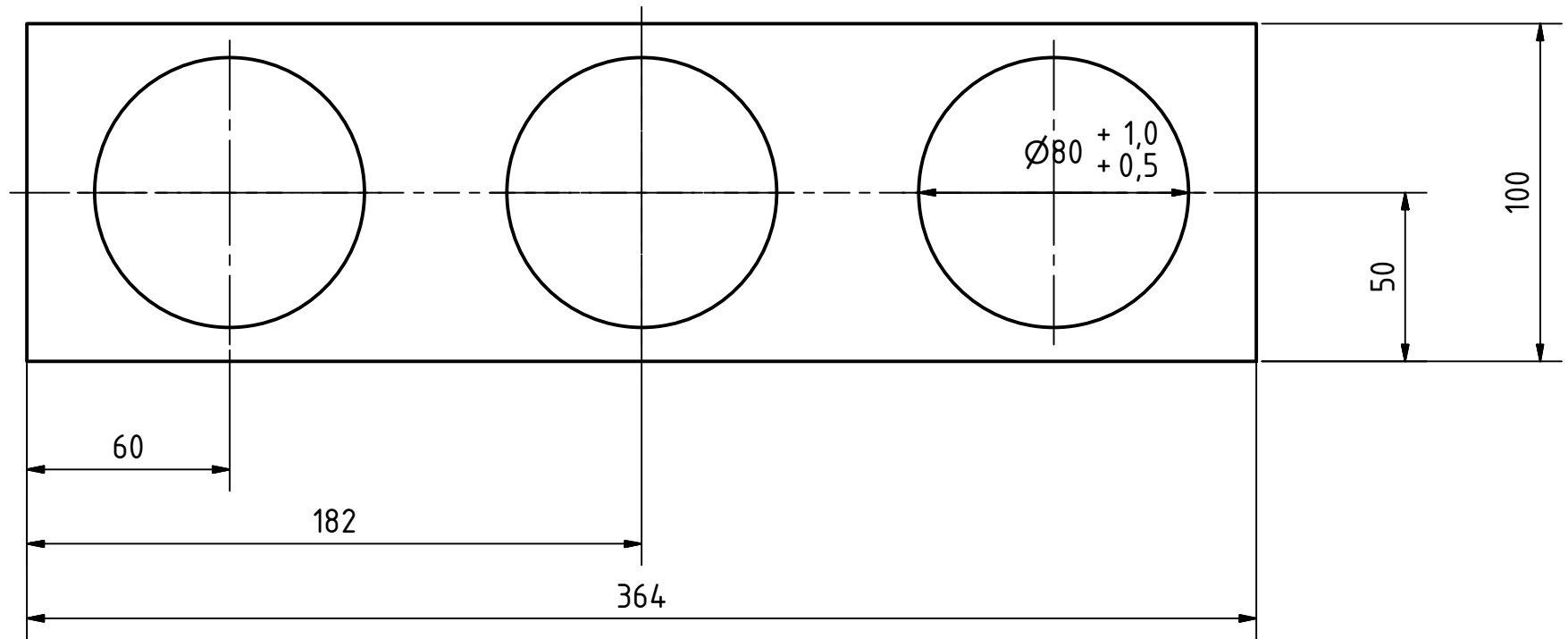
100

$360^{+0,0}_{-0,5}$



$30^{+0,0}_{-0,5}$

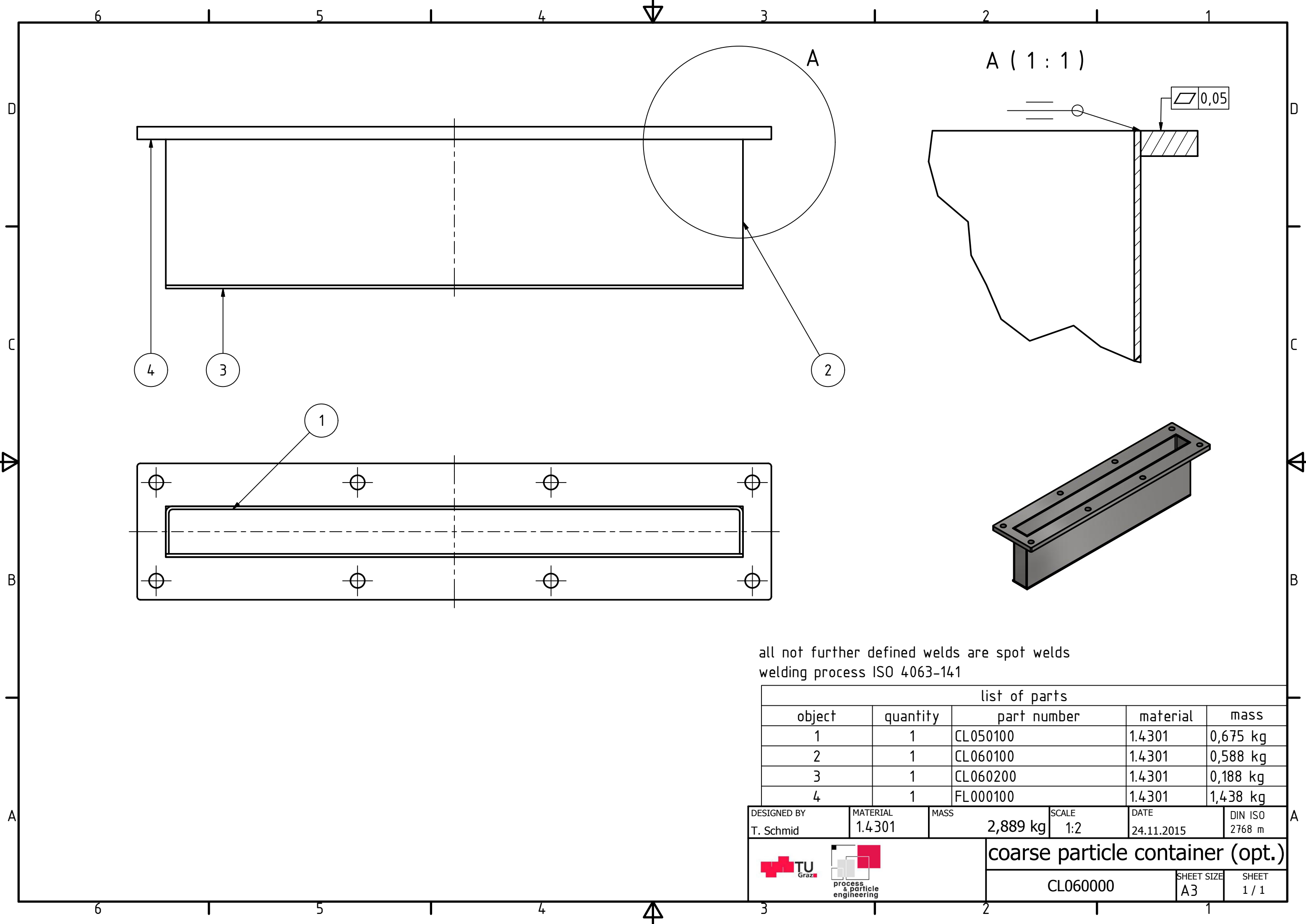
t=2
bending radii R2

DESIGNED BY T. Schmid	MATERIAL 1.4301	MASS 0,675 kg	SCALE 1:2	DATE 24.11.2015	DIN ISO 2768 m
 			bent part		
			CL050100	SHEET SIZE A3	SHEET 1 / 1





t=2

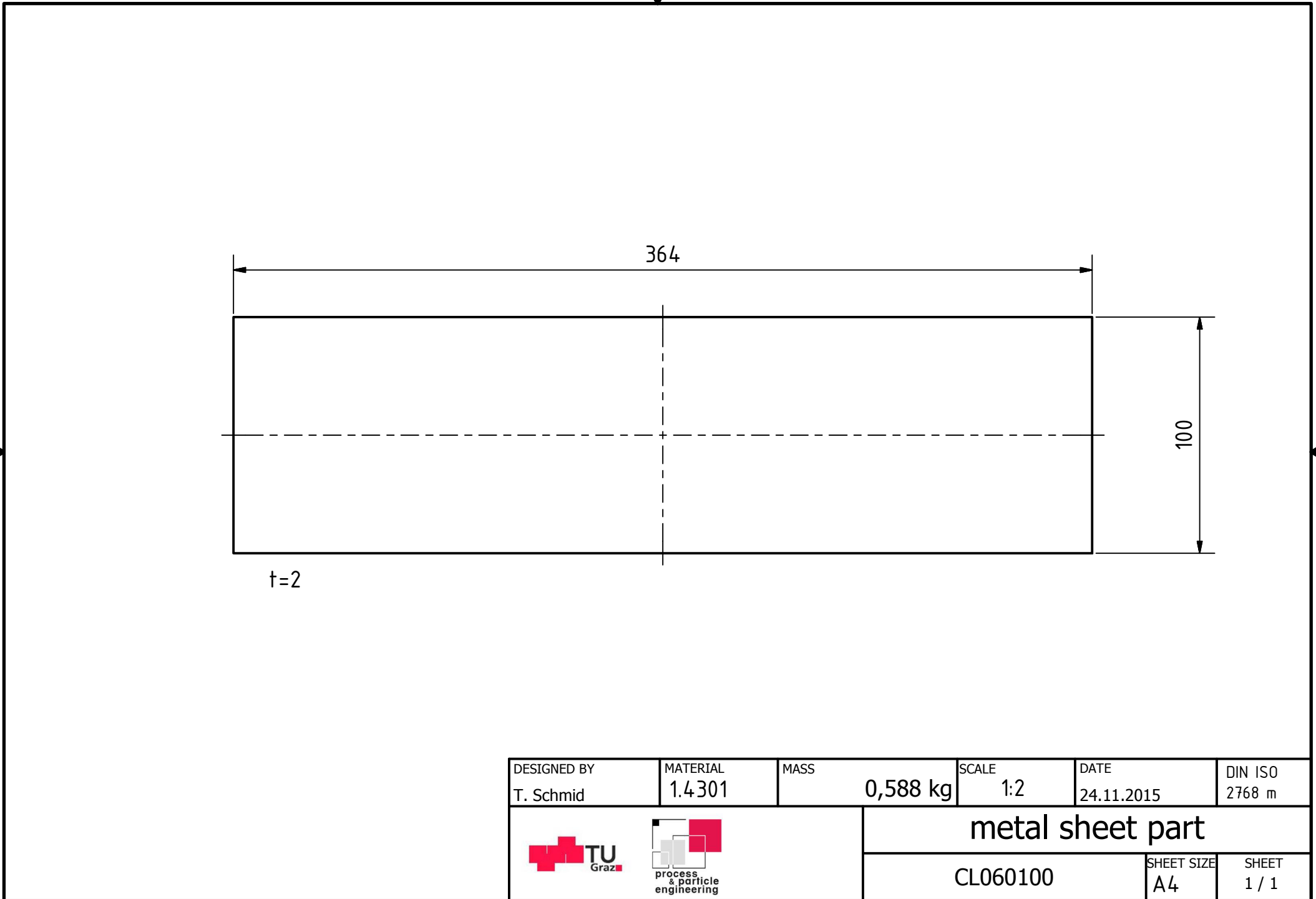
DESIGNED BY T. Schmid	MATERIAL 1.4301	MASS 0,345 kg	SCALE 1:2	DATE 24.11.2015	DIN ISO 2768 m
 			laser cutted metal sheet part		
CL050200			SHEET SIZE A4	SHEET 1 / 1	

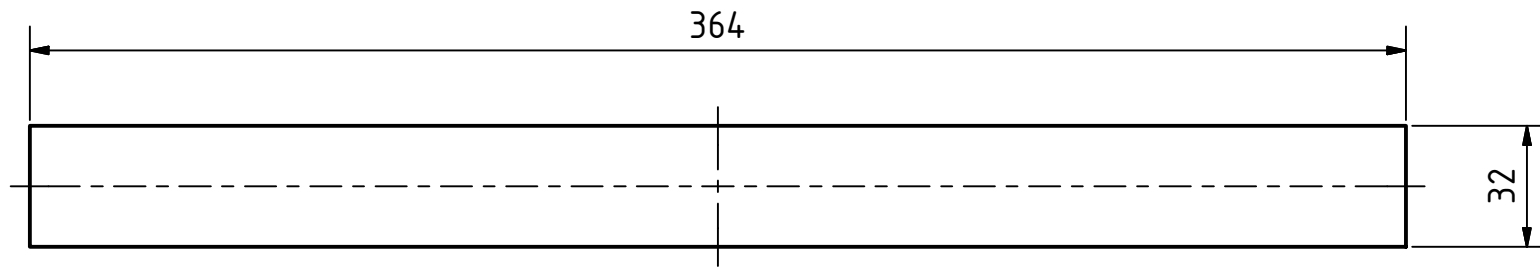


all not further defined welds are spot welds
welding process ISO 4063-141



list of parts				
object	quantity	part number	material	mass
1	1	CL050100	1.4301	0,675 kg
2	1	CL060100	1.4301	0,588 kg
3	1	CL060200	1.4301	0,188 kg
4	1	FL000100	1.4301	1,438 kg

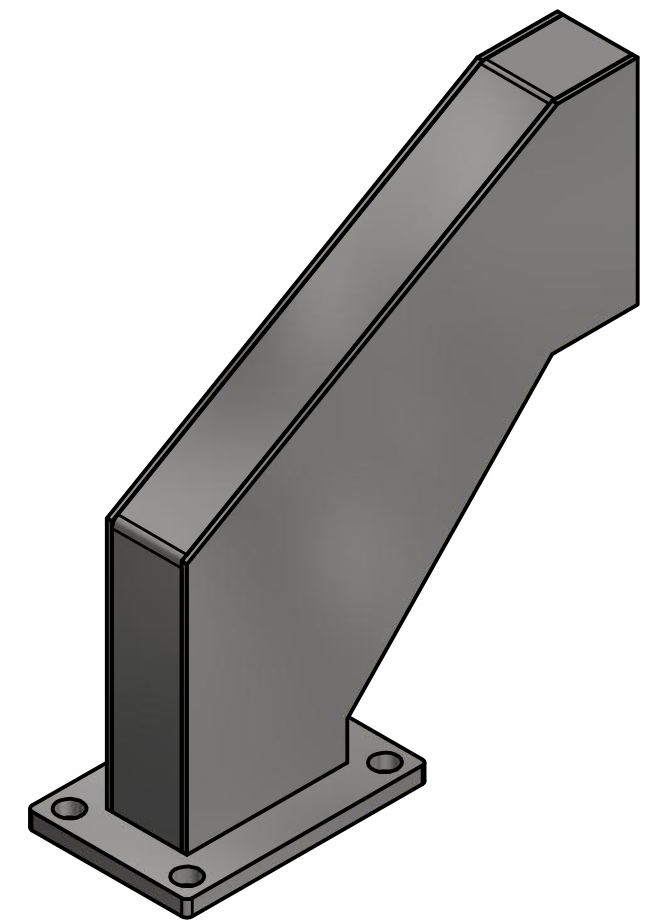
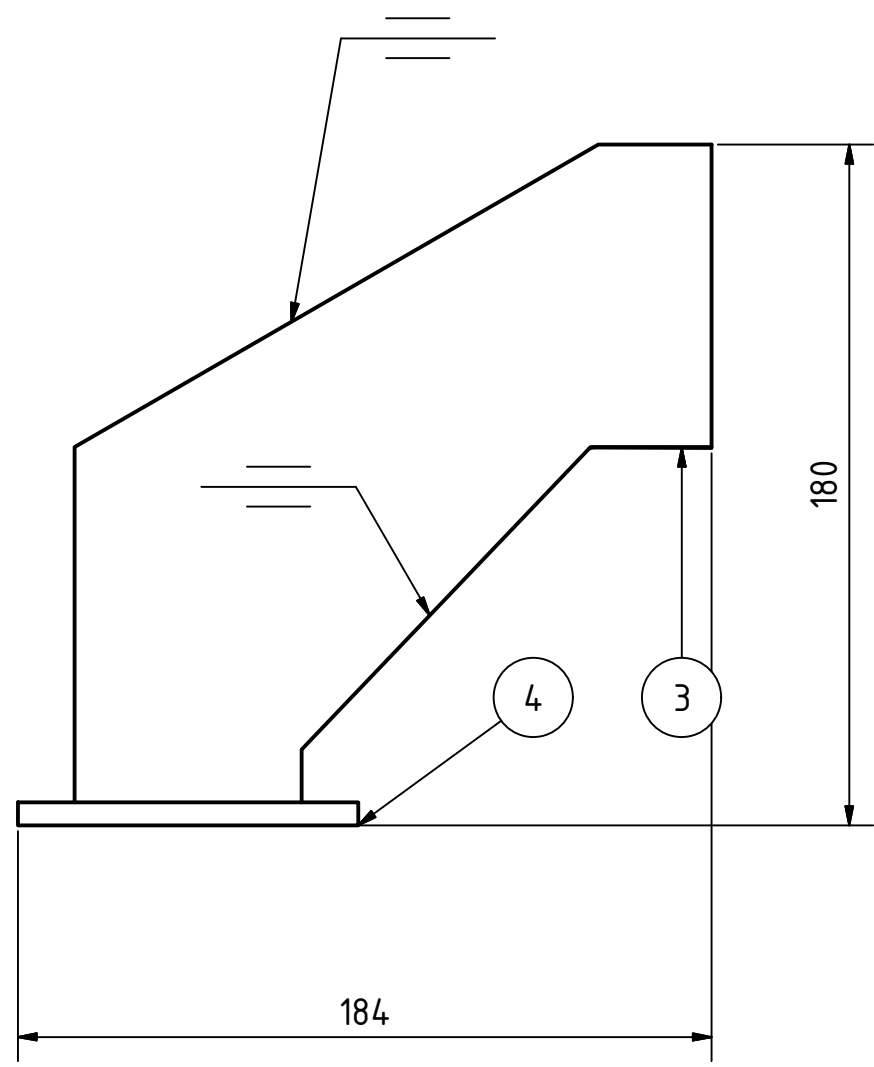
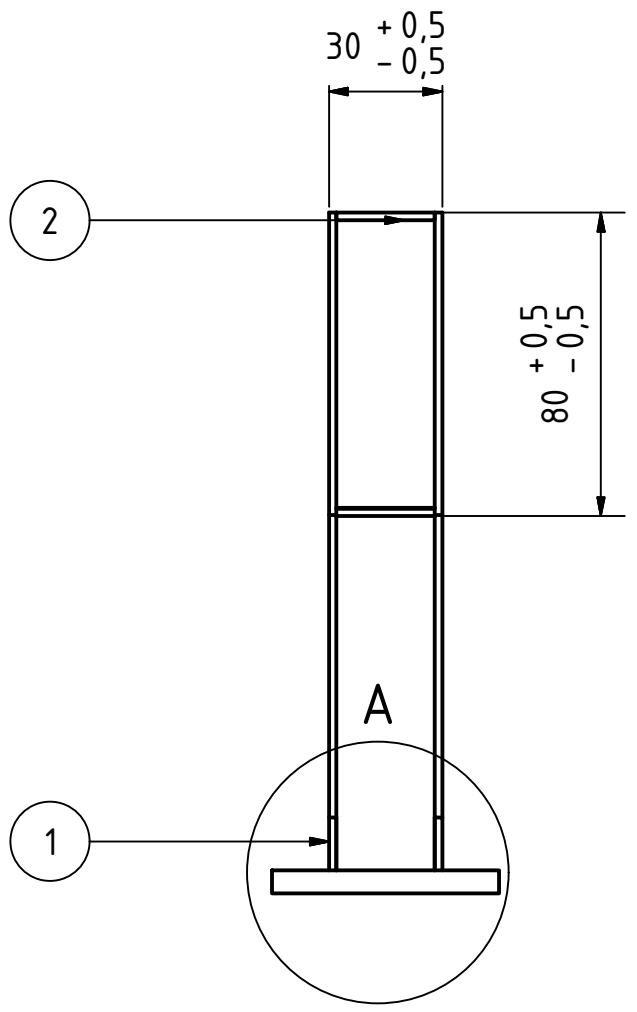
DESIGNED BY T. Schmid	MATERIAL 1.4301	MASS 2,889 kg	SCALE 1:2	DATE 24.11.2015	DIN ISO 2768 m
 			coarse particle container (opt.)		
CL060000			SHEET SIZE A3	SHEET 1 / 1	



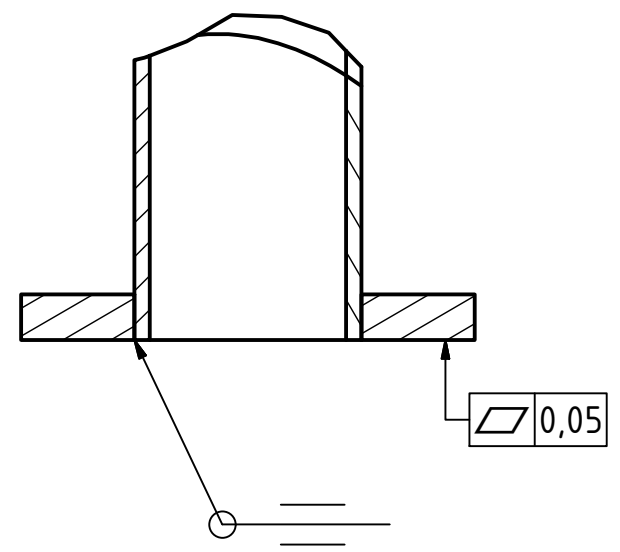


t=2

DESIGNED BY T. Schmid	MATERIAL 1.4301	MASS 0,188 kg	SCALE 1:2	DATE 24.11.2015	DIN ISO 2768 m
 			metal sheet		
			CL060200	SHEET SIZE A4	SHEET 1 / 1





A (1:1)

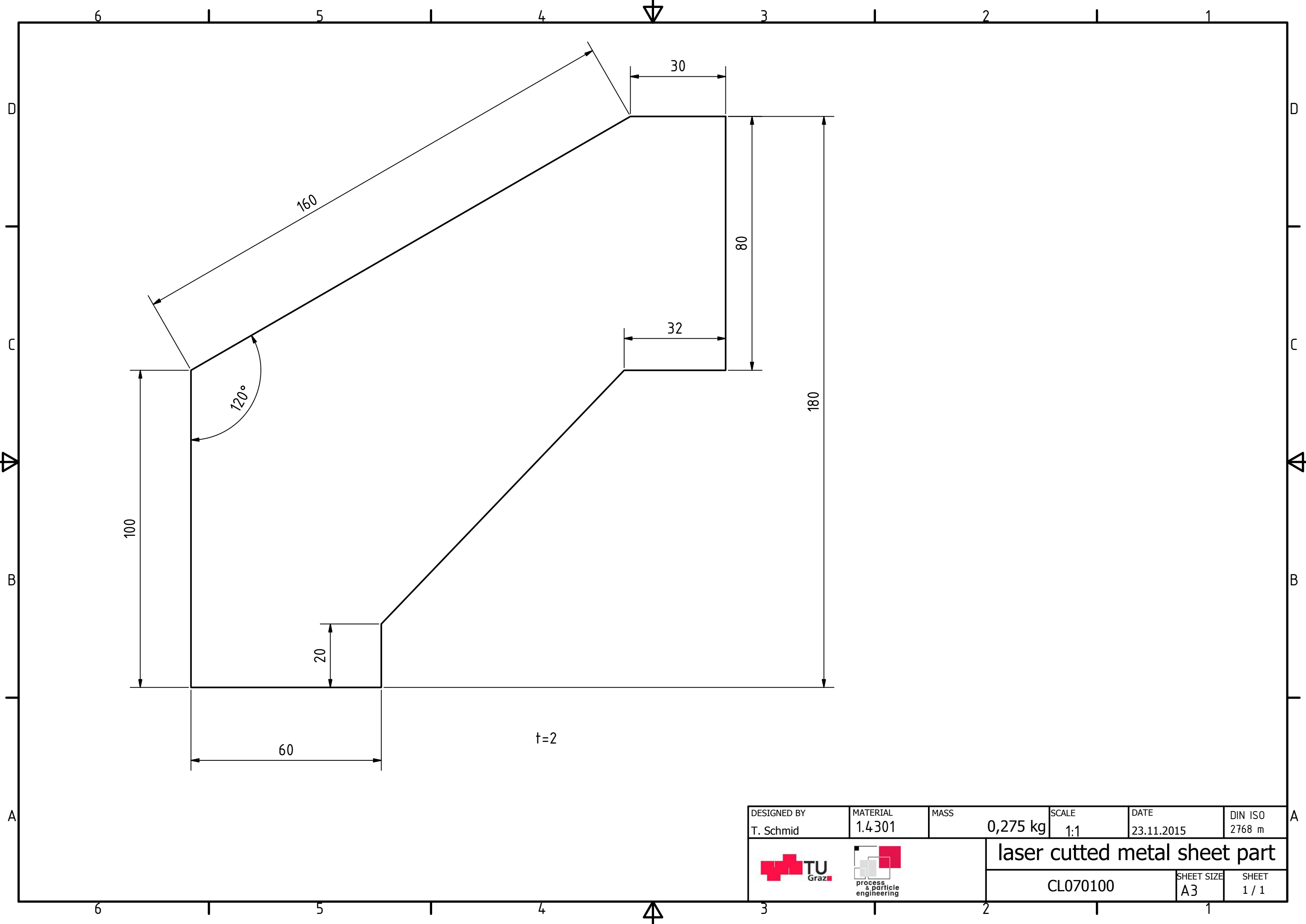




welding process ISO 4063-141
all undefined welds are spot welds

list of parts				
object	quantity	part number	material	mass
1	2	CL070100	1,4301	0,275 kg
2	1	CL070200	1,4301	0,121 kg
3	1	CL070300	1,4301	0,069 kg
4	1	FL000200	1,4301	0,162 kg

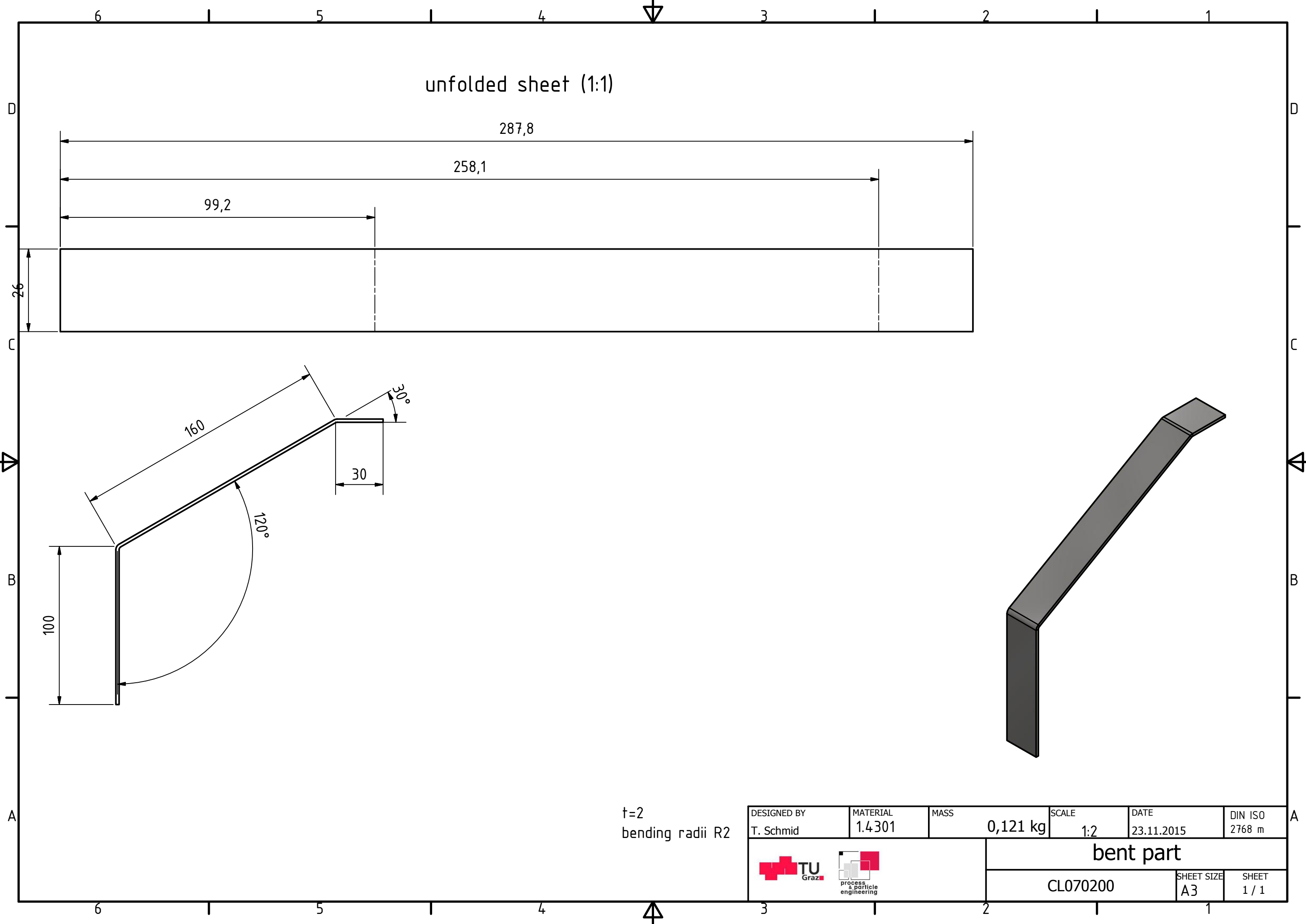
DESIGNED BY T. Schmid	MATERIAL 1.4301	MASS 0,902 kg	SCALE 1:2	DATE 23.11.2015	DIN EN ISO 13920 A
--------------------------	--------------------	------------------	--------------	--------------------	-----------------------

 	coarse particle outlet canal		
	CL070000	<table border="1"> <tr> <td>SHEET SIZE A3</td> <td>SHEET 1 / 1</td> </tr> </table>	SHEET SIZE A3
SHEET SIZE A3	SHEET 1 / 1		



DESIGNED BY T. Schmid	MATERIAL 1.4301	MASS 0,275 kg	SCALE 1:1	DATE 23.11.2015	DIN ISO 2768 m
 			laser cutted metal sheet part		

CL070100



unfolded sheet (1:1)

287,8

258,1

99,2

26

160



30°

30

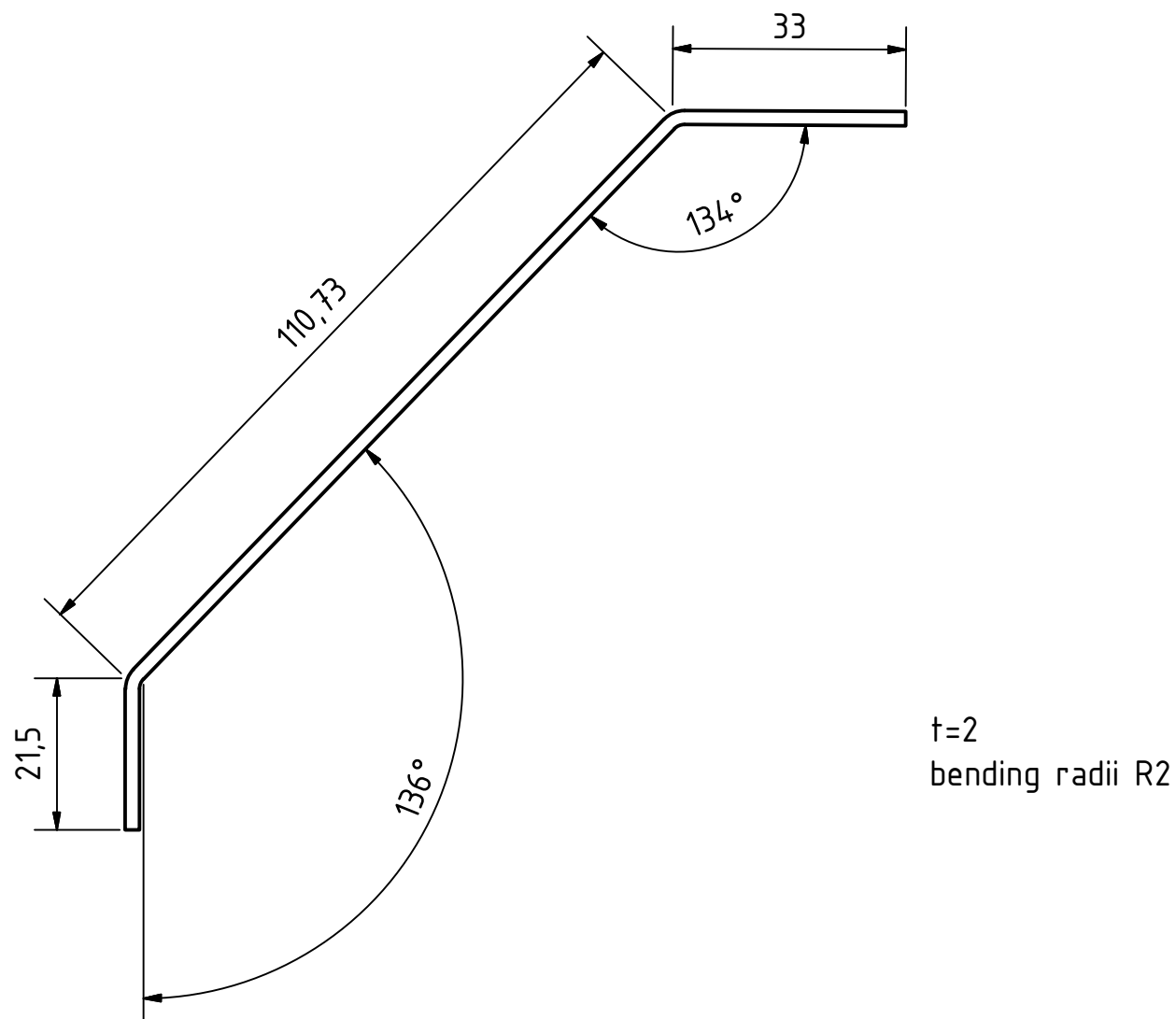
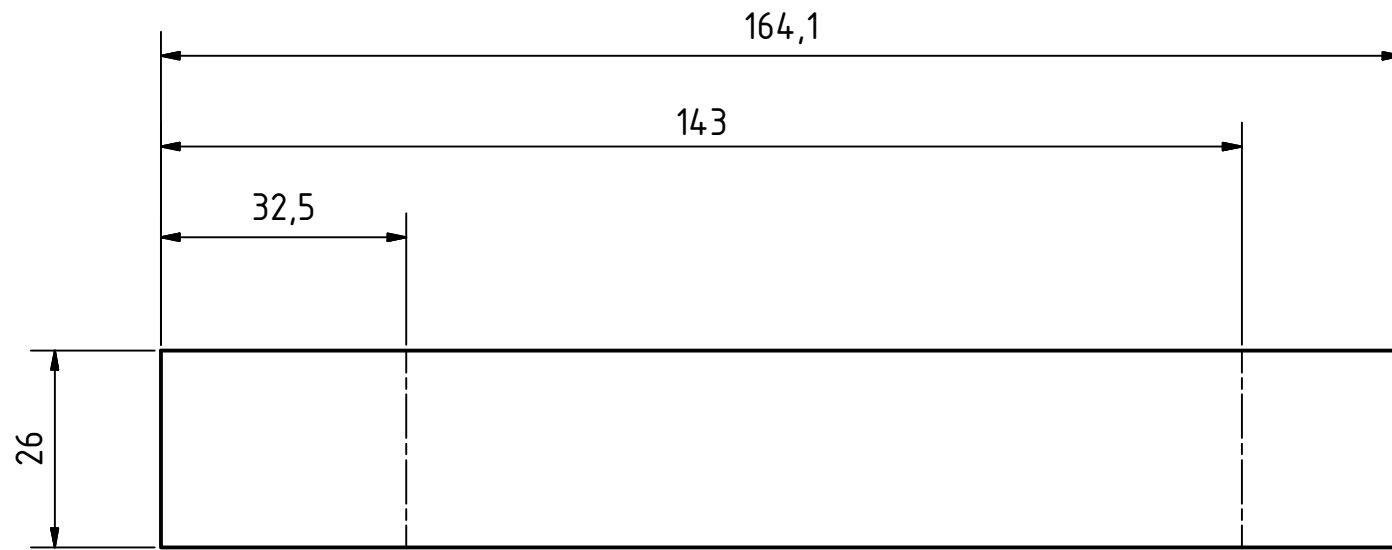
120°

100

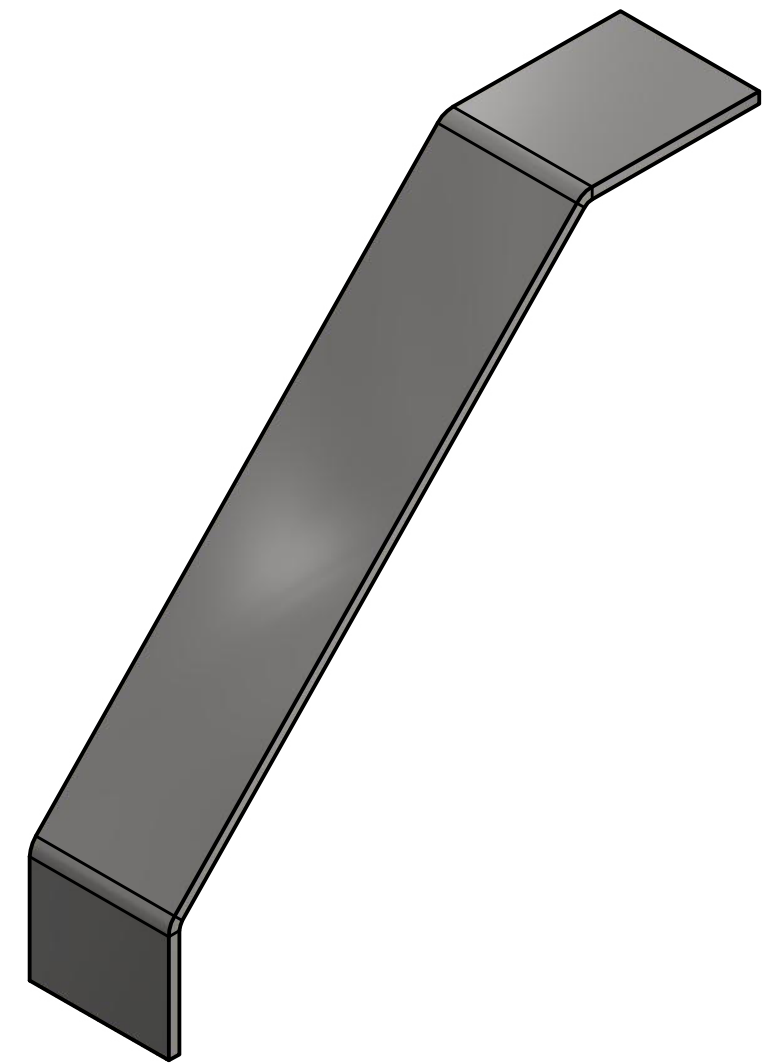
t=2
bending radii R2



DESIGNED BY T. Schmid	MATERIAL 1.4301	MASS 0,121 kg	SCALE 1:2	DATE 23.11.2015	DIN ISO 2768 m
 			bent part		
			CL070200	SHEET SIZE A3	SHEET 1 / 1

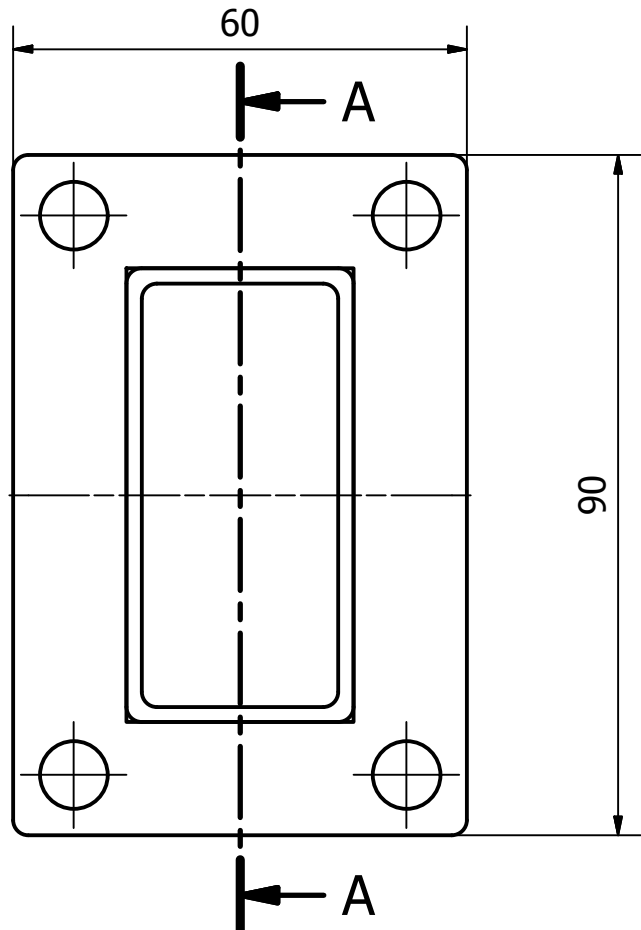
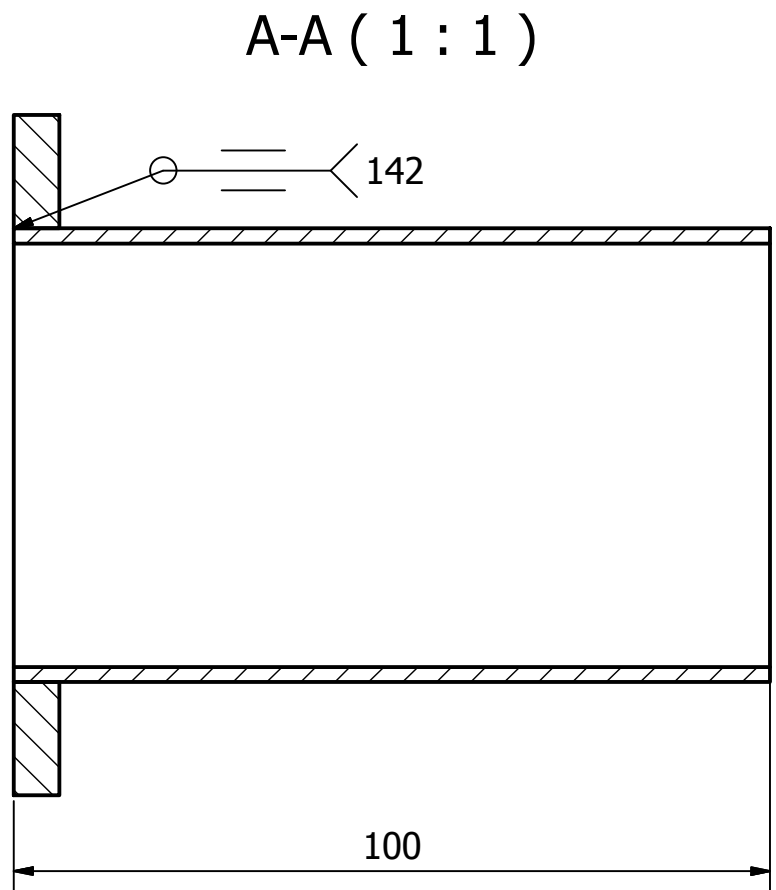
unfolded sheet (1:1)



t=2
bending radii R2





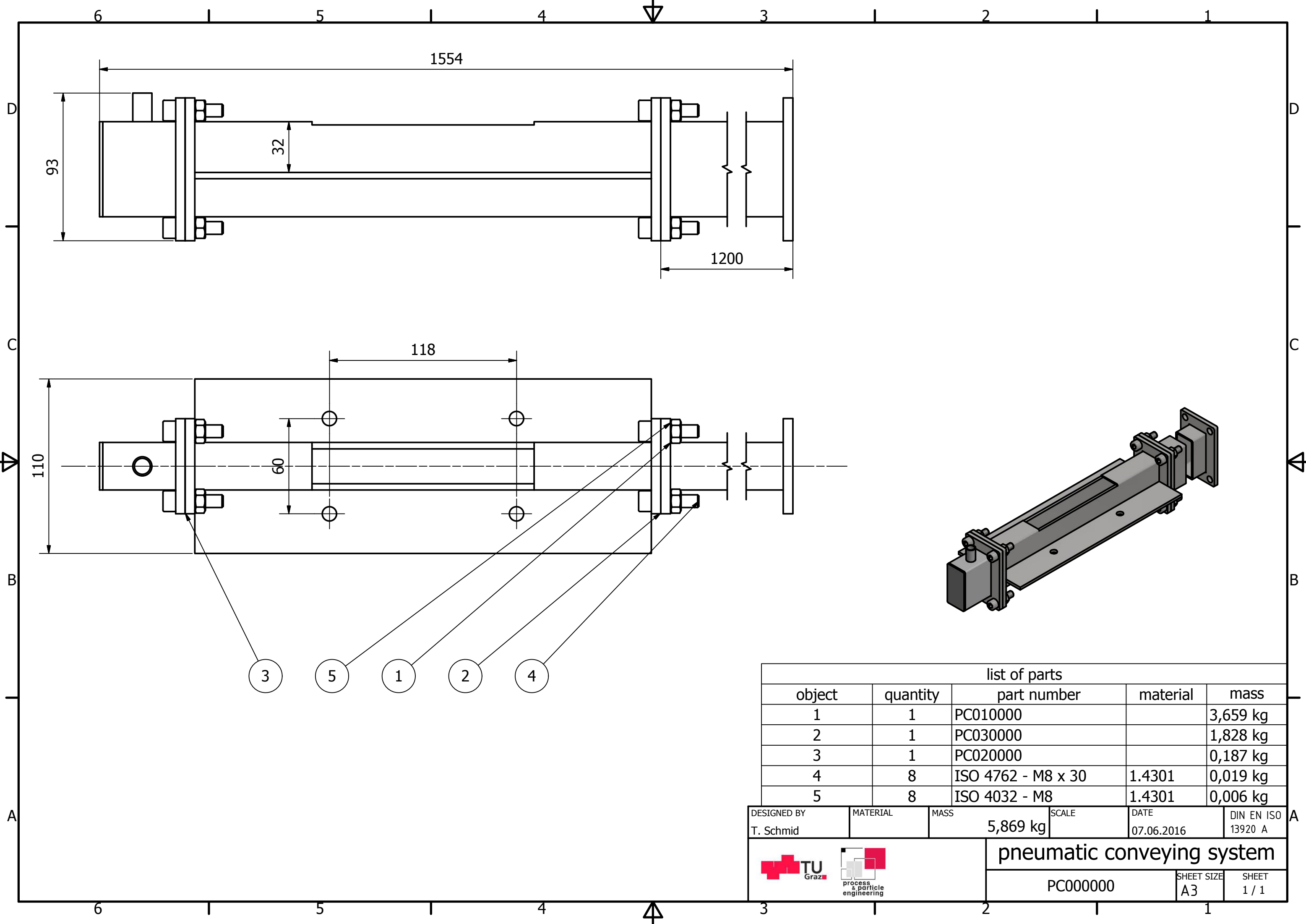
DESIGNED BY T. Schmid	MATERIAL 1.4301	MASS 0,069 kg	SCALE 1:1	DATE 23.11.2015	DIN ISO 2768 m
 			bent part		
			CL070300	SHEET SIZE A3	SHEET 1 / 1



list of parts				
object	quantity	part number	material	mass
1	1	hollow profile 60x30x2x100	1.4301	0,278 kg
2	1	FL000200	1.4301	0,162 kg



DESIGNED BY T. Schmid	MATERIAL 1.4301	MASS 0,440 kg	SCALE	DATE 06.06.2016	DIN ISO 2768 m
--------------------------	--------------------	------------------	-------	--------------------	-------------------

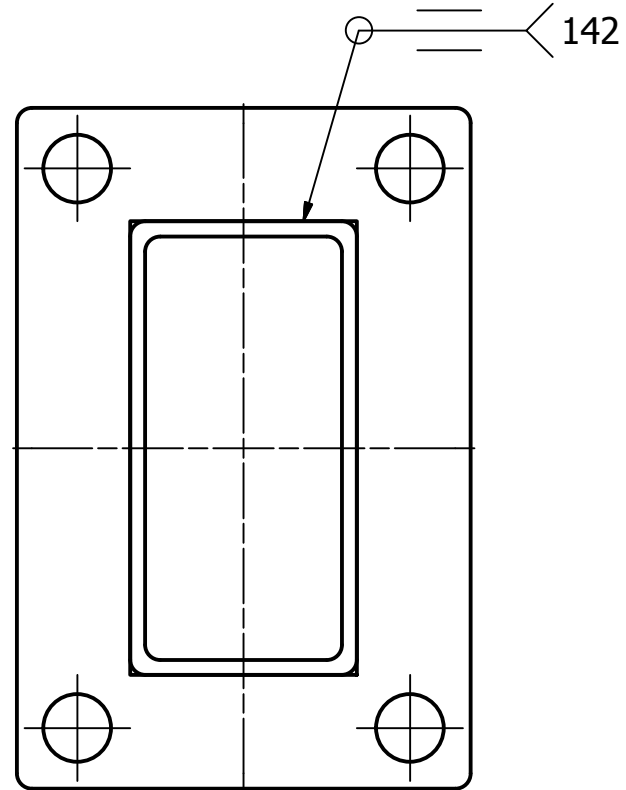
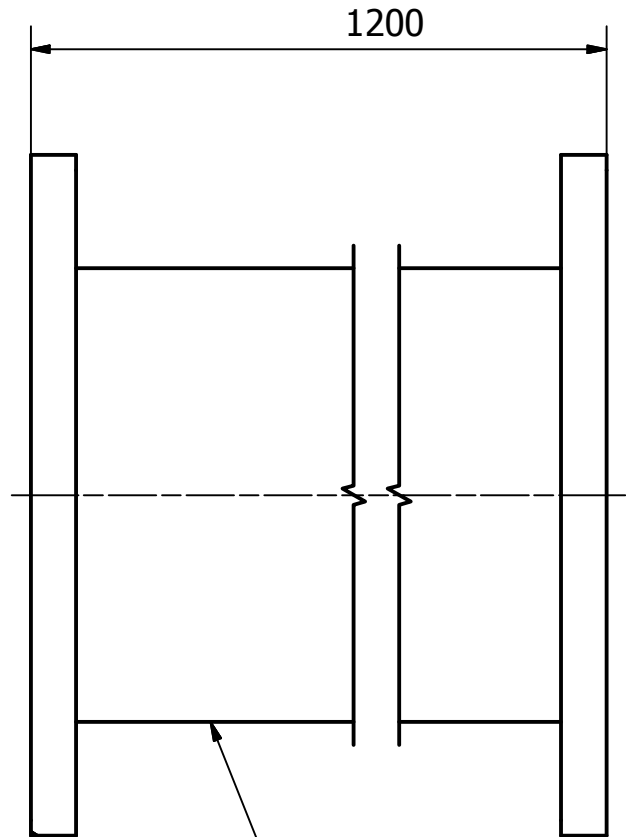
 	short feed pipe		
	CL080000	SHEET SIZE A4	SHEET 1 / 1



list of parts				
object	quantity	part number	material	mass
1	1	PC010000		3,659 kg
2	1	PC030000		1,828 kg
3	1	PC020000		0,187 kg
4	8	ISO 4762 - M8 x 30	1.4301	0,019 kg
5	8	ISO 4032 - M8	1.4301	0,006 kg

DESIGNED BY T. Schmid	MATERIAL	MASS 5,869 kg	SCALE	DATE 07.06.2016	DIN EN ISO 13920 A
--------------------------	----------	------------------	-------	--------------------	-----------------------

 	pneumatic conveying system		
	PC000000	<table border="1"> <tr> <td>SHEET SIZE A3</td> <td>SHEET 1 / 1</td> </tr> </table>	SHEET SIZE A3
SHEET SIZE A3	SHEET 1 / 1		

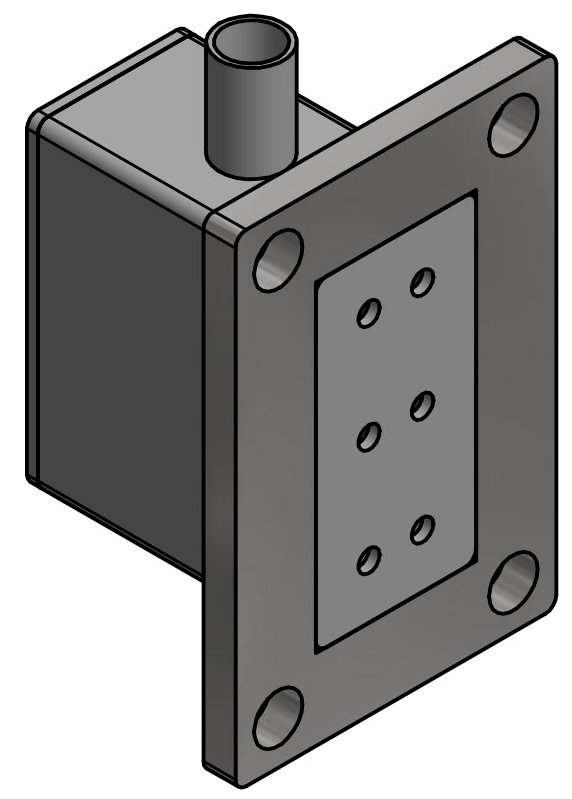
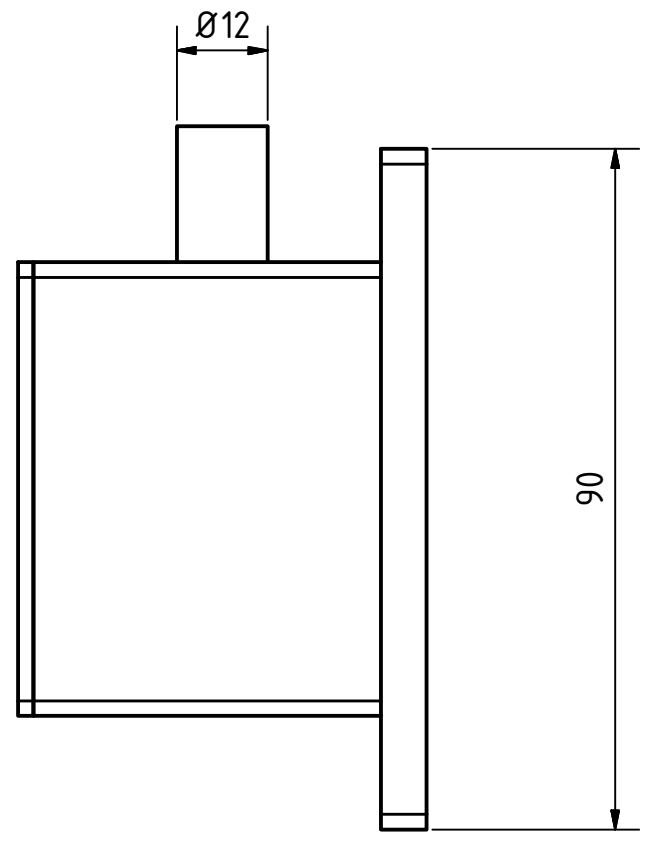
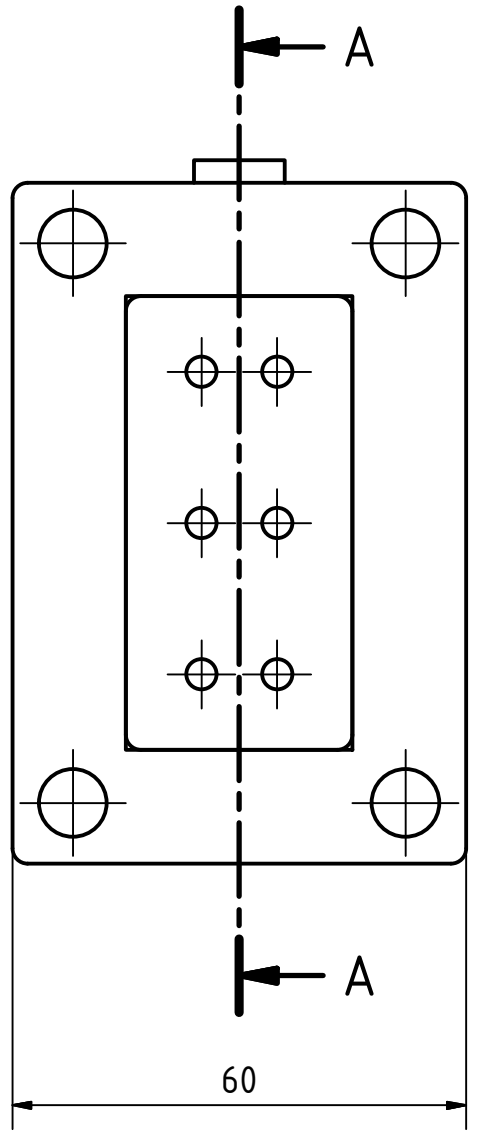
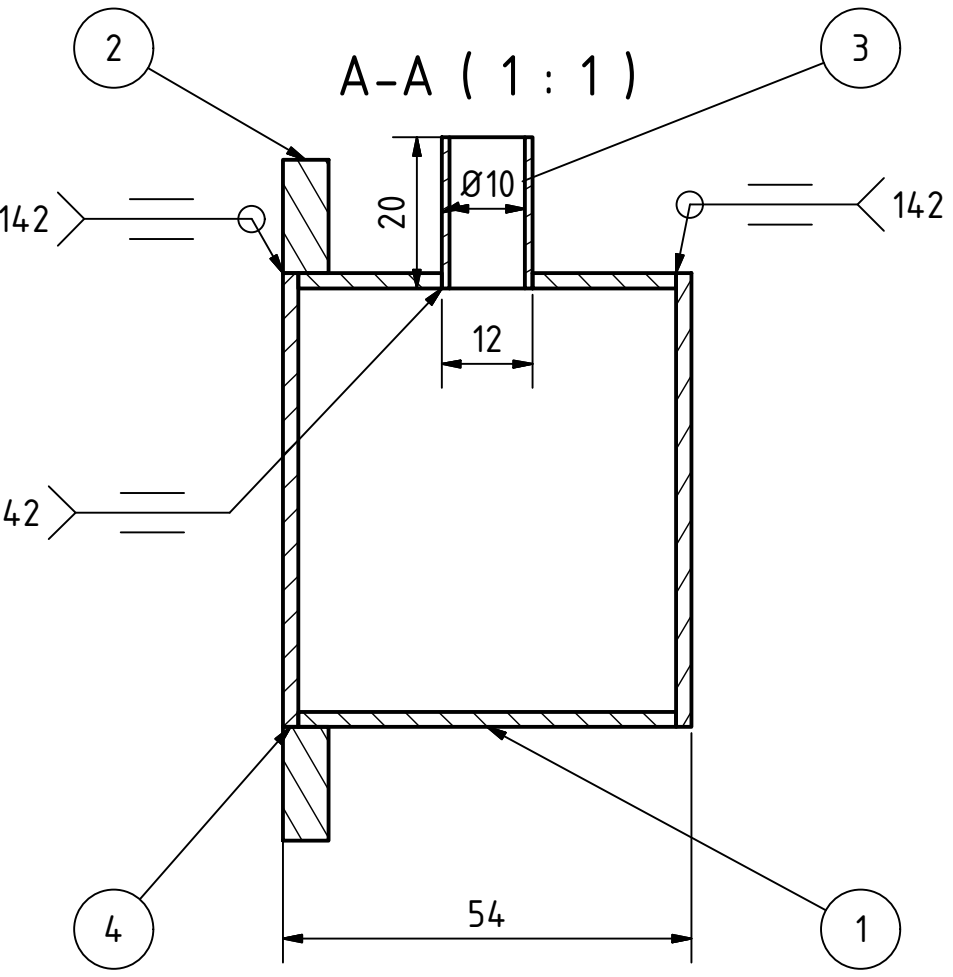
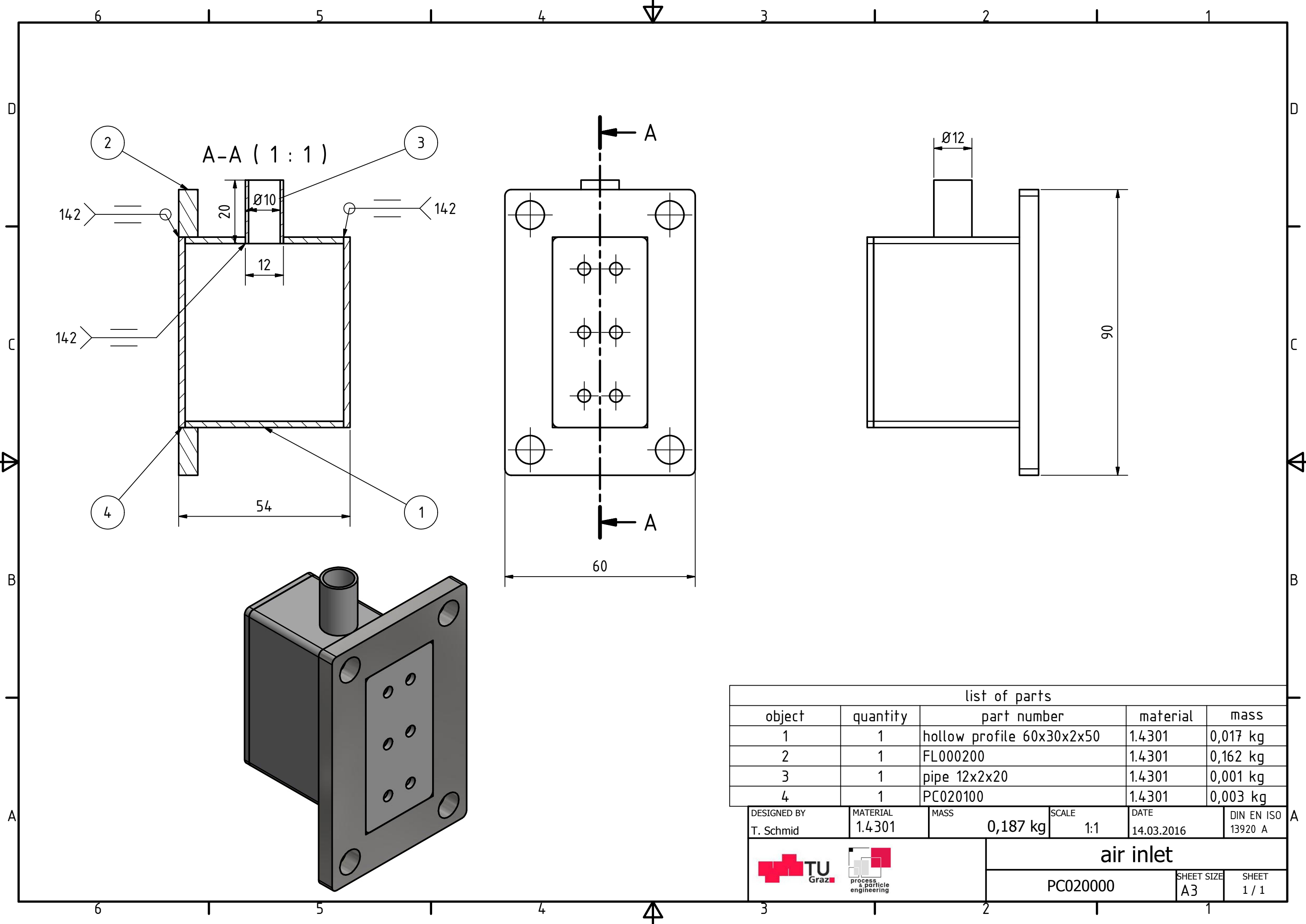


2 1



list of parts				
object	quantity	part number	material	mass
1	1	hollow profile 60x60x2x1500	1.4301	3,335 kg
2	2	FL000200	1.4301	0,162 kg

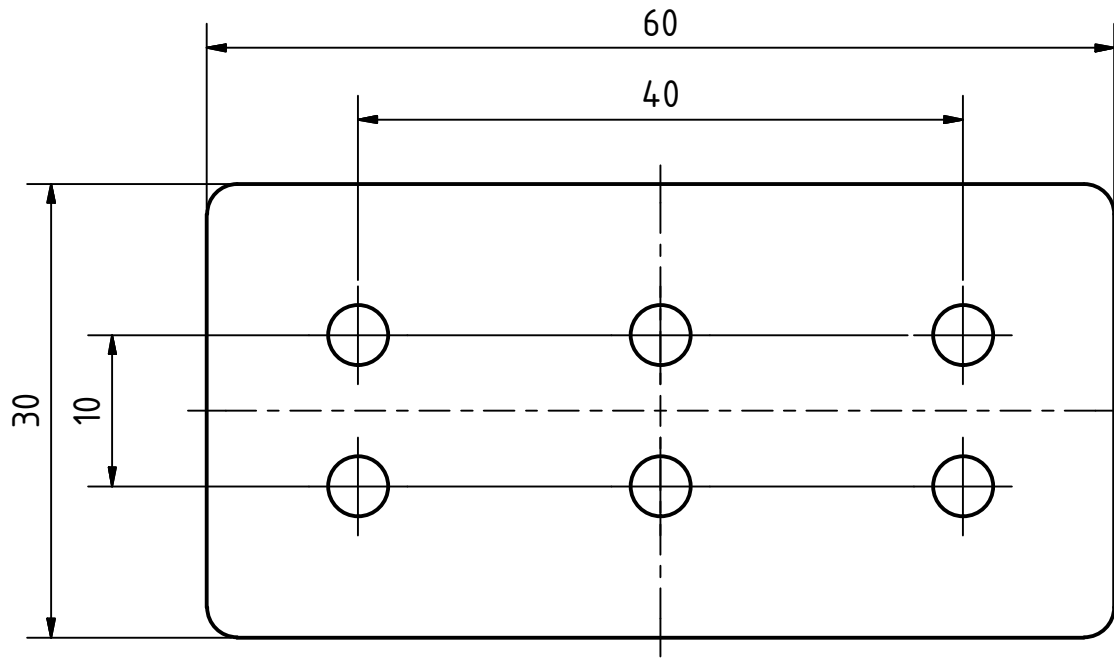
DESIGNED BY T. Schmid	MATERIAL	MASS 3,659 kg	SCALE	DATE 06.06.2016	DIN EN ISO 13920 A
--------------------------	----------	------------------	-------	--------------------	-----------------------

 	relaxation pipe		
	PC010000	SHEET SIZE A4	SHEET 1 / 1





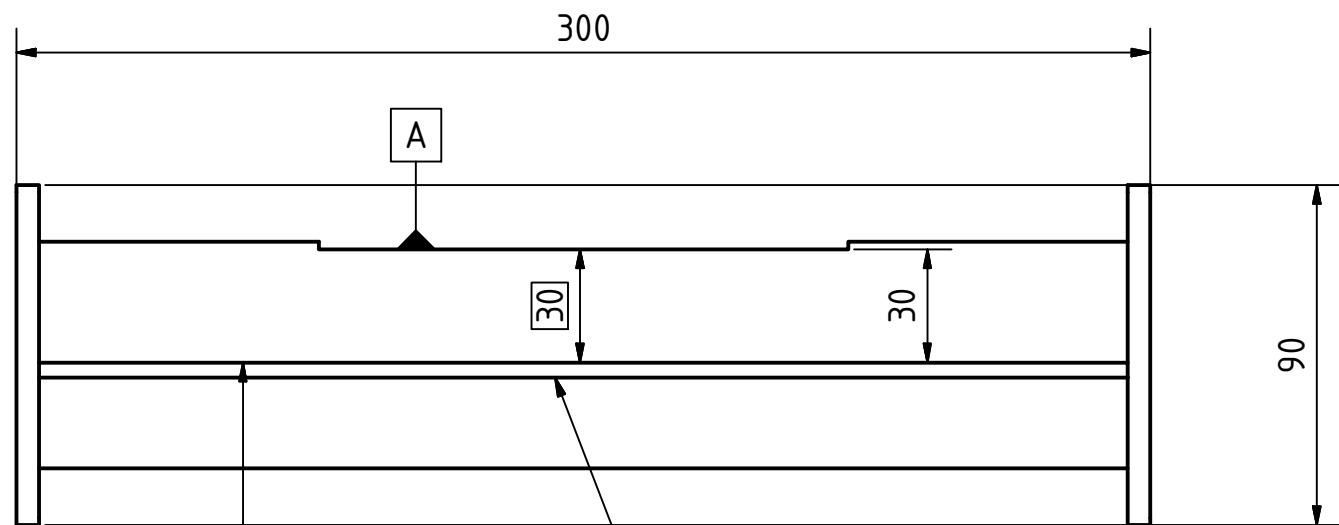
list of parts				
object	quantity	part number	material	mass
1	1	hollow profile 60x30x2x50	1.4301	0,017 kg
2	1	FL000200	1.4301	0,162 kg
3	1	pipe 12x2x20	1.4301	0,001 kg
4	1	PC020100	1.4301	0,003 kg

DESIGNED BY T. Schmid	MATERIAL 1.4301	MASS 0,187 kg	SCALE 1:1	DATE 14.03.2016	DIN EN ISO 13920 A
 			air inlet		
PC020000			SHEET SIZE A3	SHEET 1 / 1	

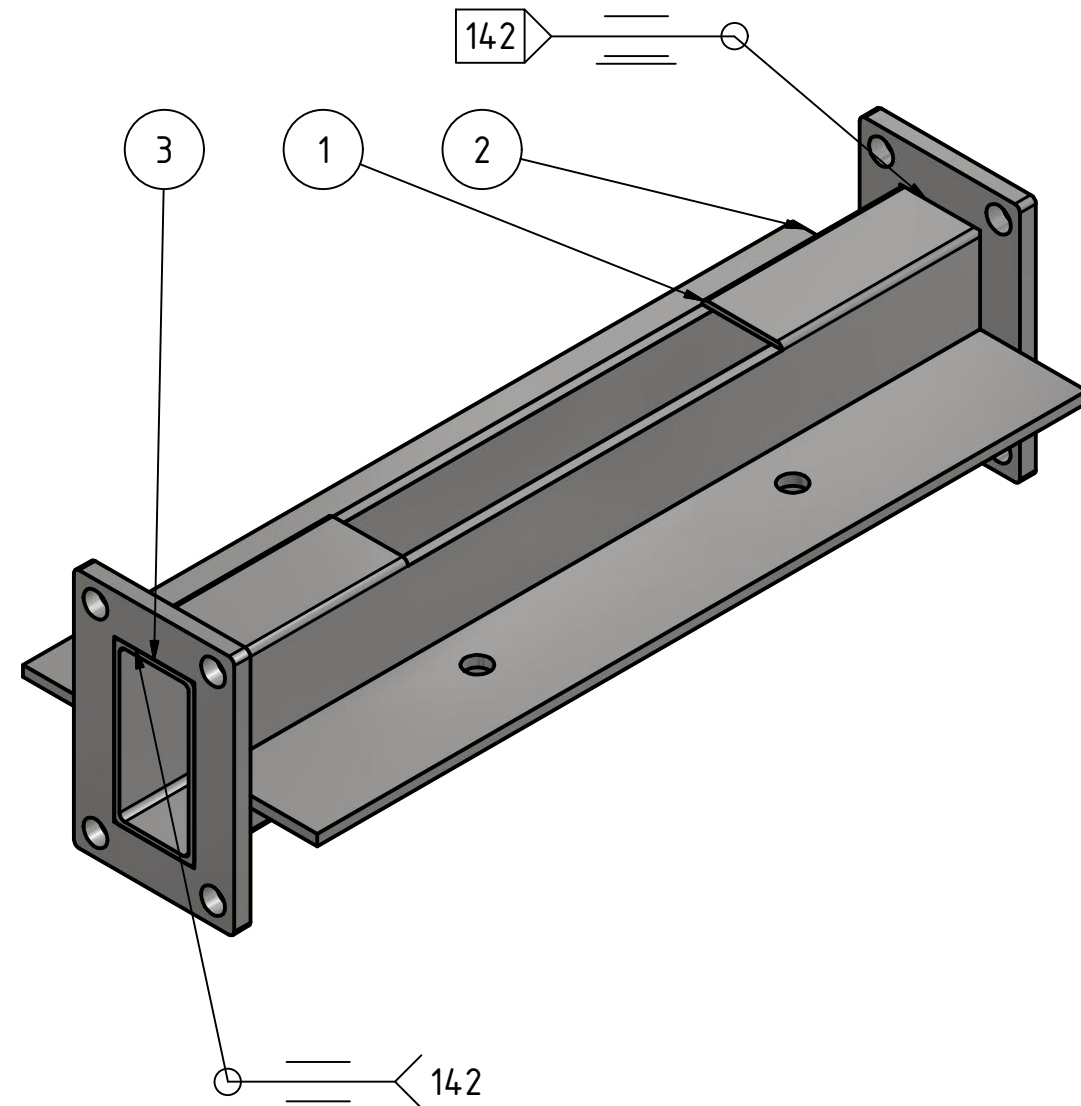
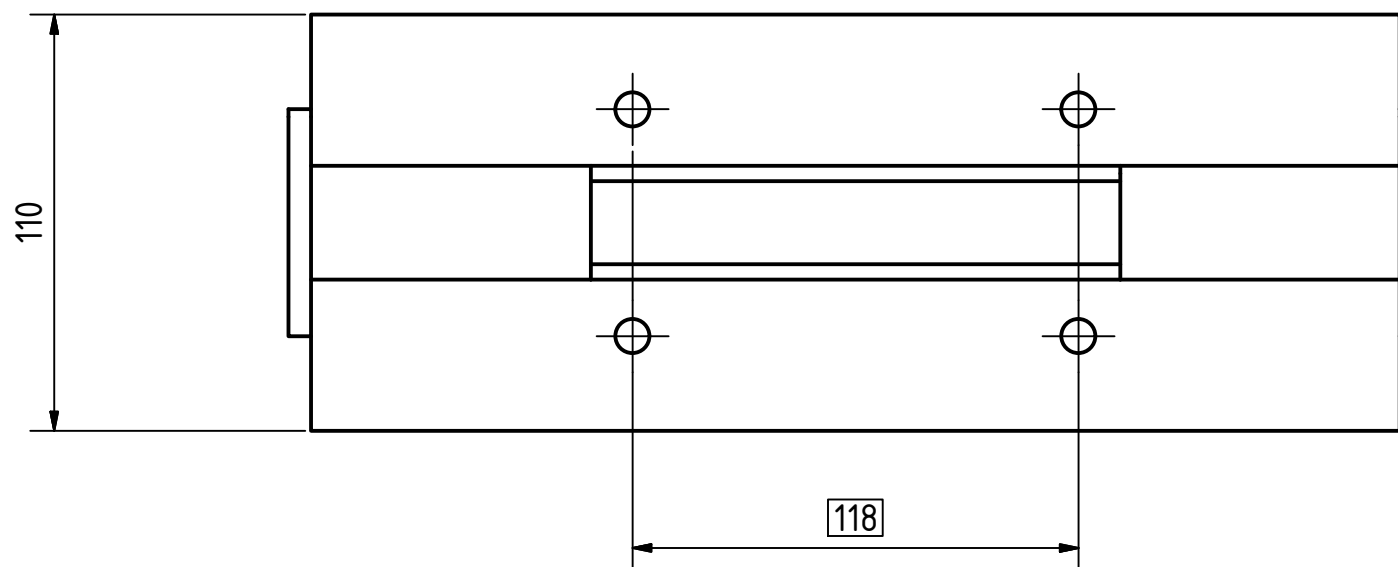
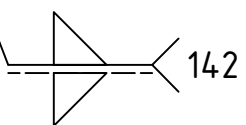


$t=2$
 all bores $\varnothing 4$
 all radii R2

DESIGNED BY T. Schmid	MATERIAL 1.4301	MASS 0,003 kg	SCALE 2:1	DATE 20.04.2016	DIN ISO 2768 m
 		perforated plate			
PC020100			SHEET SIZE A4	SHEET 1 / 1	



$\parallel 0,05 A$



align metal sheets during welding process

list of parts				
object	quantity	part number	material	mass
1	1	PC030200	1.4301	0,768 kg
2	2	PC030100	1.4301	0,368 kg
3	2	FL000200	1.4301	0,162 kg

DESIGNED BY T. Schmid	MATERIAL 1.4301	MASS 1,828 kg	SCALE 1:2	DATE 14.03.2016	DIN EN ISO 13920 A
--------------------------	--------------------	------------------	--------------	--------------------	-----------------------

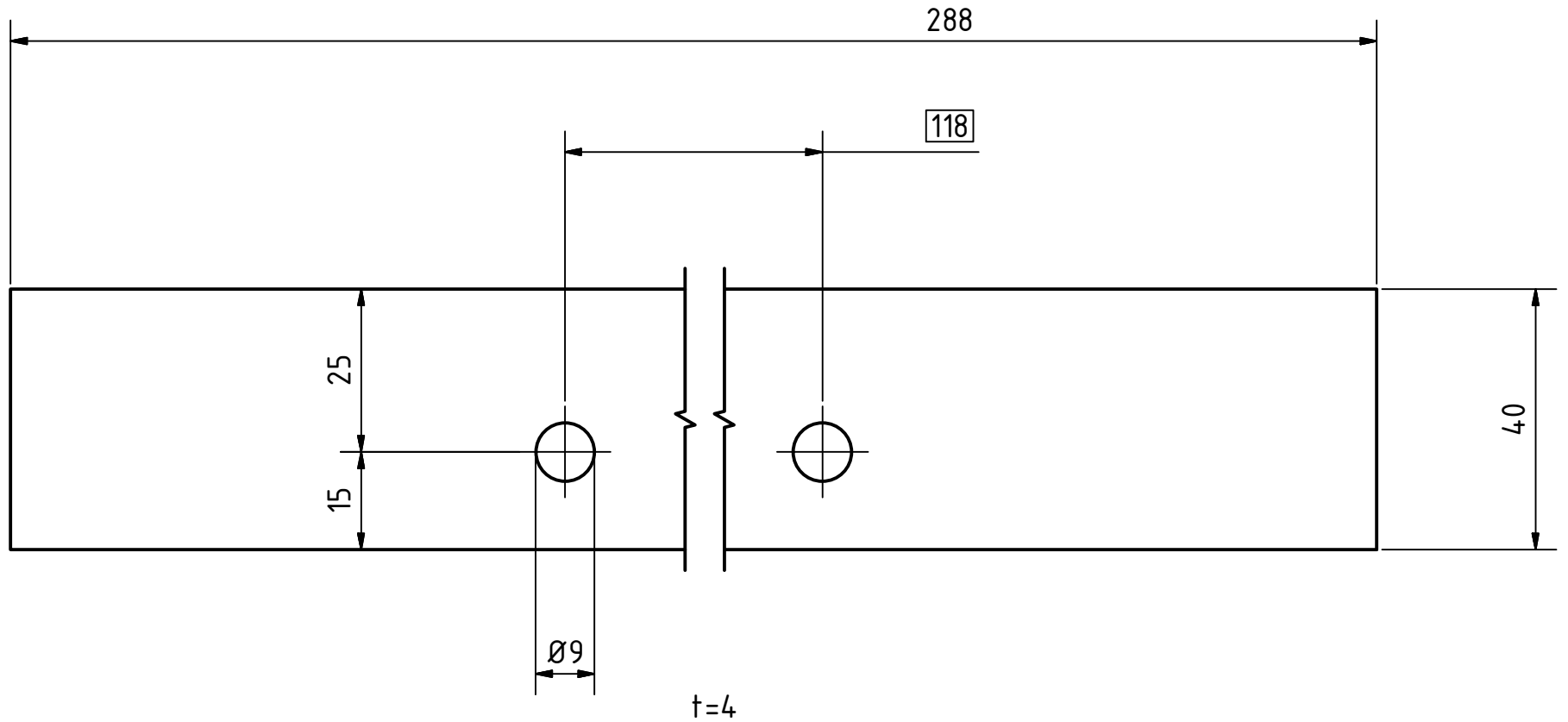




feeding canal

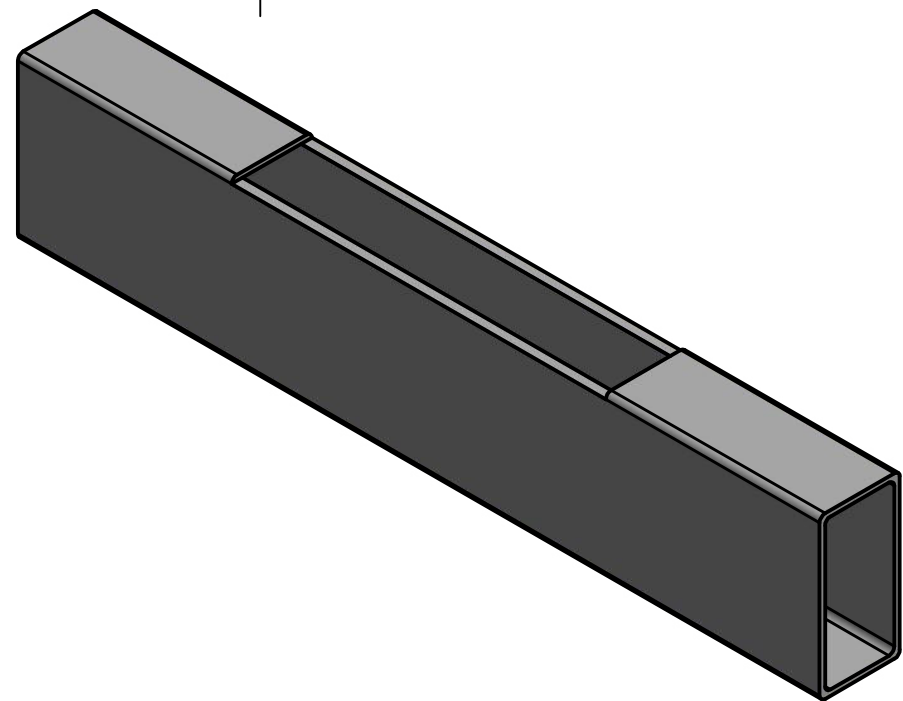
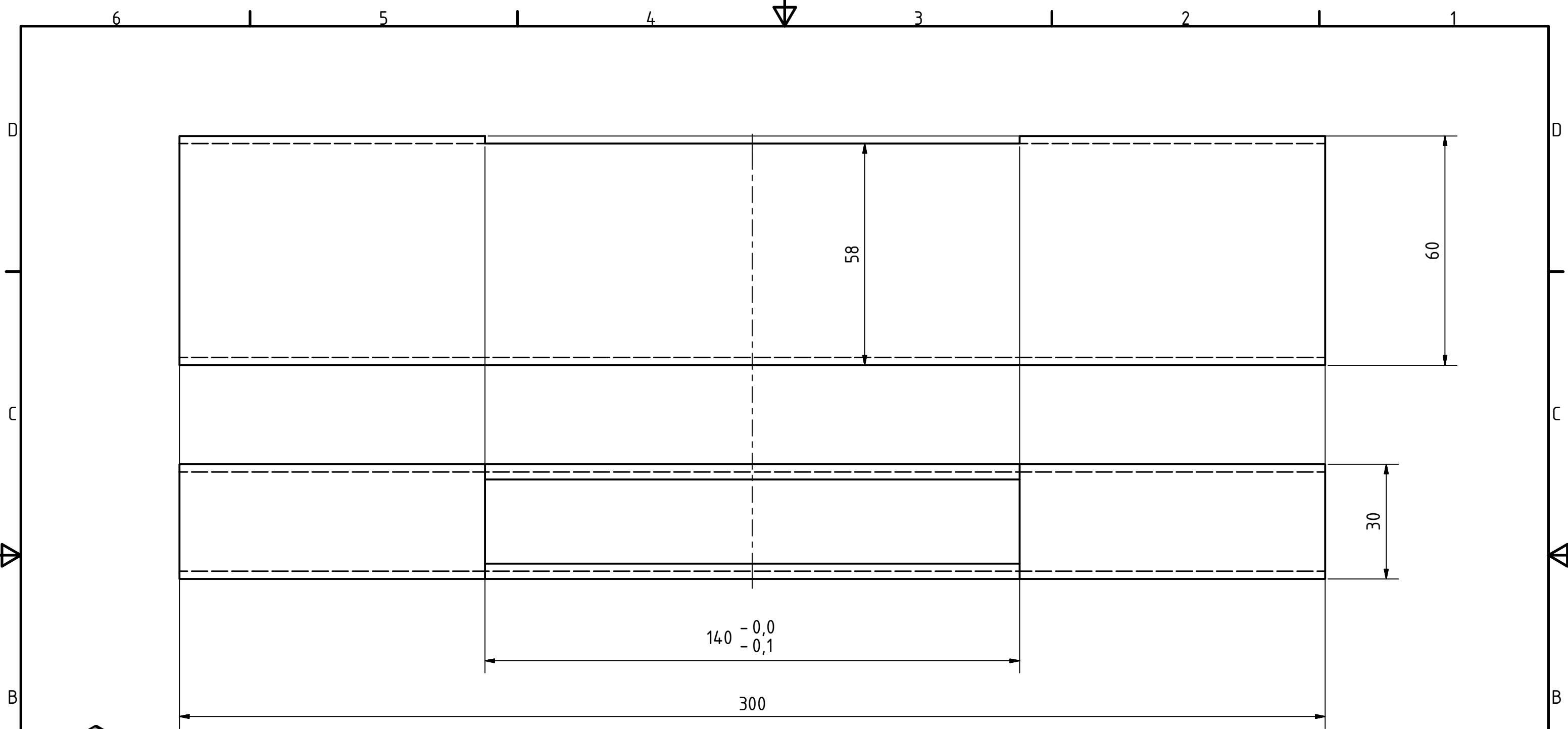
PC030000

SHEET SIZE
A3



SHEET
1 / 1

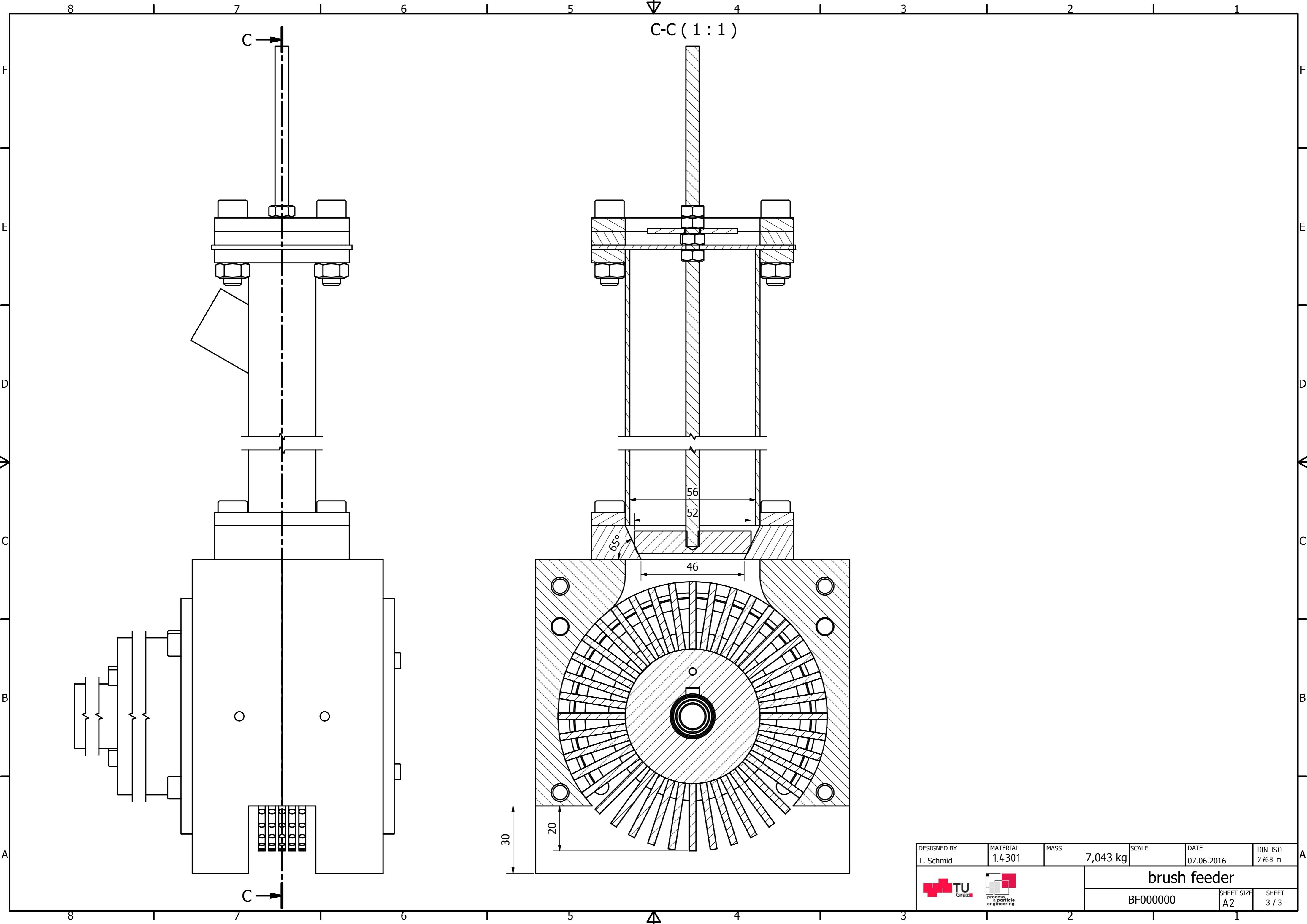




DESIGNED BY T. Schmid	MATERIAL 1.4301	MASS 0,046 kg	SCALE 1:1	DATE 14.03.2016	DIN ISO 2768 m
 		metal sheet			
PC030100			SHEET SIZE A4	SHEET 1 / 1	

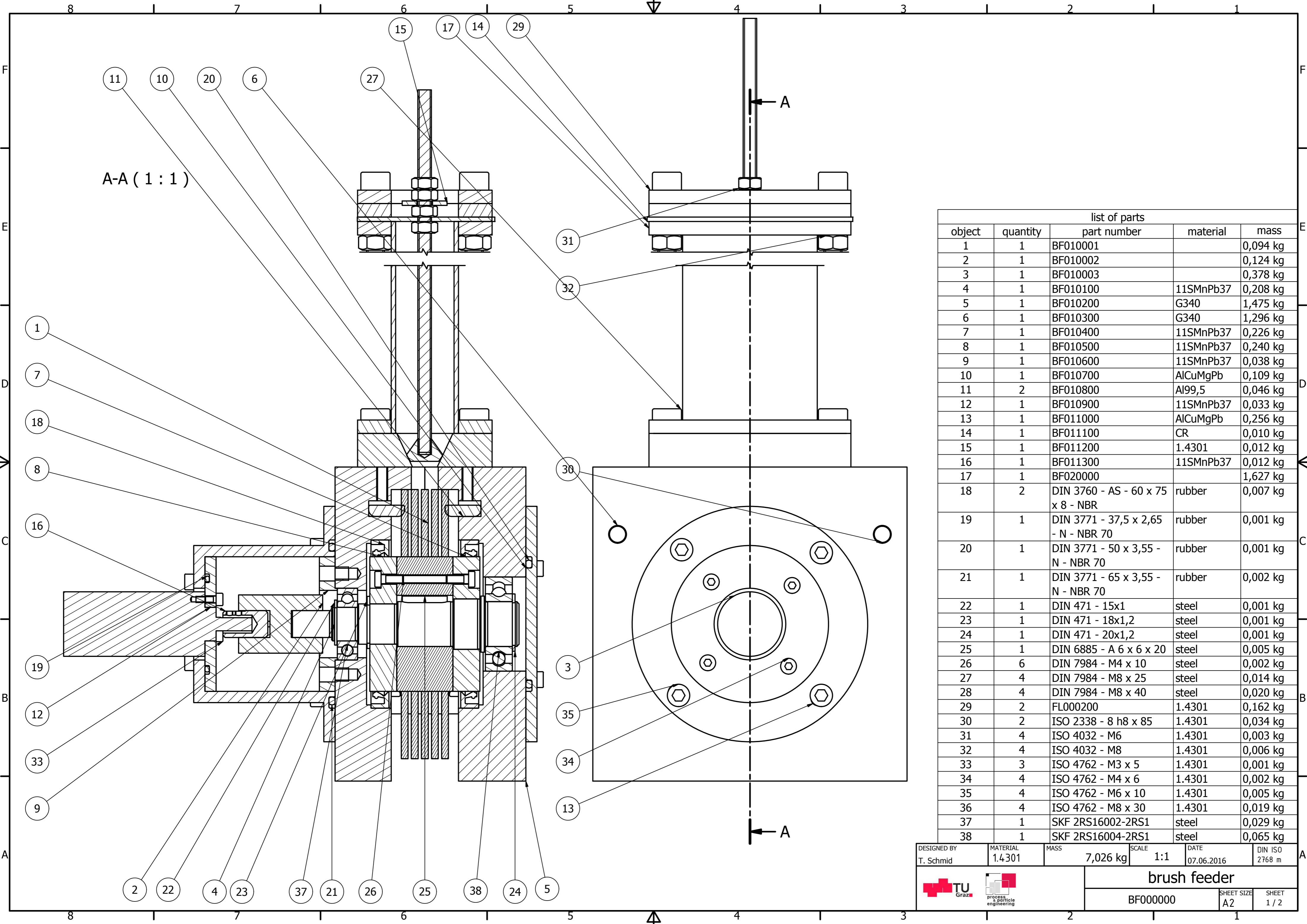


raw material: hollow profile 60x30x2x300



DESIGNED BY T. Schmid	MATERIAL 1.4301	MASS 0,095 kg	SCALE 1:1	DATE 14.03.2016	DIN ISO 2768 m
 			cut hollow profile		
PC030200			SHEET SIZE A3	SHEET 1 / 1	

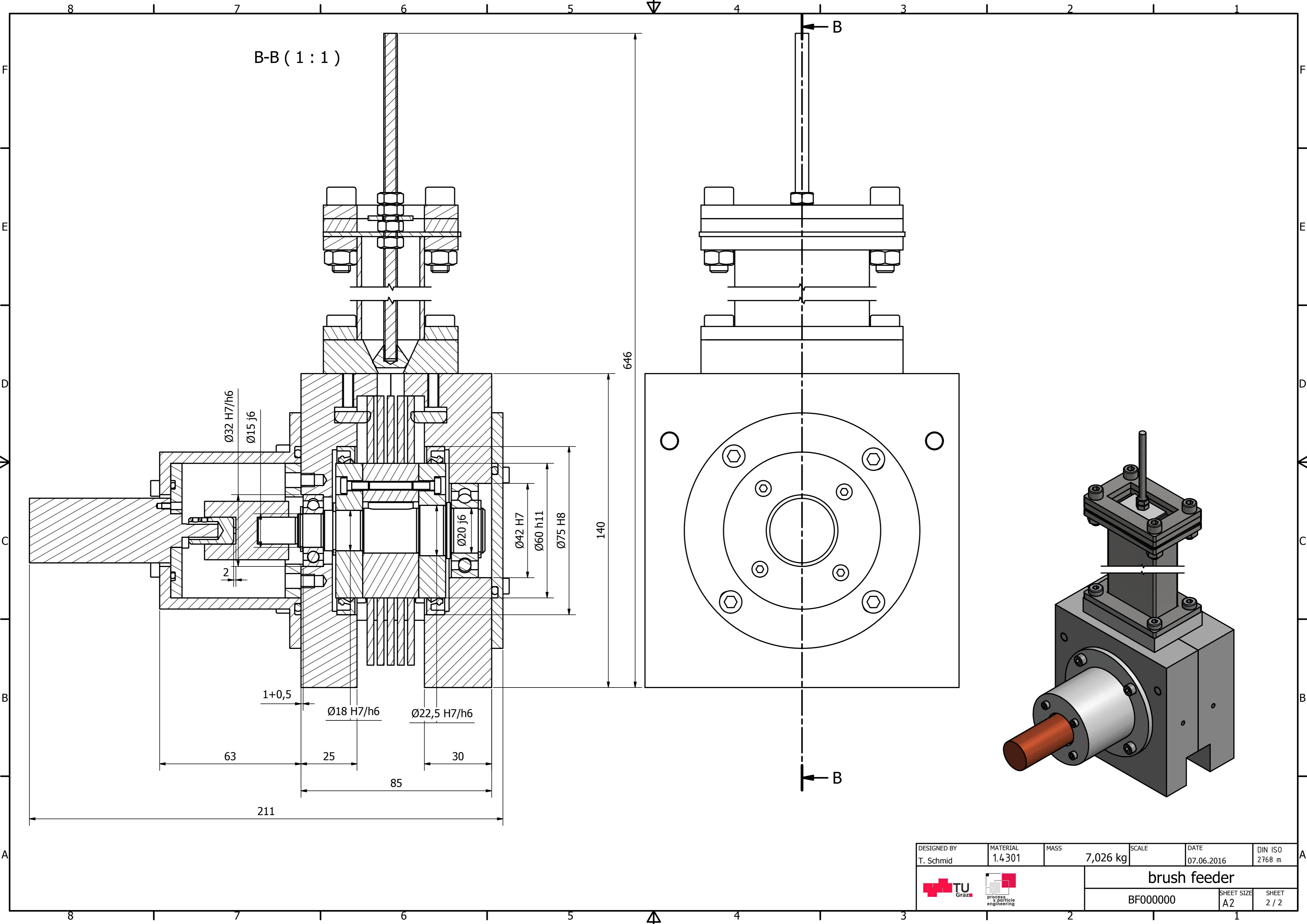


DESIGNED BY T. Schmid	MATERIAL 1.4301	MASS 7,043 kg	SCALE	DATE 07.06.2016	DIN ISO 2768 m
 			brush feeder		
			BF000000	SHEET SIZE A2	SHEET 3 / 3



list of parts				
object	quantity	part number	material	mass
1	1	BF010001		0,094 kg
2	1	BF010002		0,124 kg
3	1	BF010003		0,378 kg
4	1	BF010100	11SMnPb37	0,208 kg
5	1	BF010200	G340	1,475 kg
6	1	BF010300	G340	1,296 kg
7	1	BF010400	11SMnPb37	0,226 kg
8	1	BF010500	11SMnPb37	0,240 kg
9	1	BF010600	11SMnPb37	0,038 kg
10	1	BF010700	AlCuMgPb	0,109 kg
11	2	BF010800	Al99,5	0,046 kg
12	1	BF010900	11SMnPb37	0,033 kg
13	1	BF011000	AlCuMgPb	0,256 kg
14	1	BF011100	CR	0,010 kg
15	1	BF011200	1.4301	0,012 kg
16	1	BF011300	11SMnPb37	0,012 kg
17	1	BF020000		1,627 kg
18	2	DIN 3760 - AS - 60 x 75 x 8 - NBR	rubber	0,007 kg
19	1	DIN 3771 - 37,5 x 2,65 - N - NBR 70	rubber	0,001 kg
20	1	DIN 3771 - 50 x 3,55 - N - NBR 70	rubber	0,001 kg
21	1	DIN 3771 - 65 x 3,55 - N - NBR 70	rubber	0,002 kg
22	1	DIN 471 - 15x1	steel	0,001 kg
23	1	DIN 471 - 18x1,2	steel	0,001 kg
24	1	DIN 471 - 20x1,2	steel	0,001 kg
25	1	DIN 6885 - A 6 x 6 x 20	steel	0,005 kg
26	6	DIN 7984 - M4 x 10	steel	0,002 kg
27	4	DIN 7984 - M8 x 25	steel	0,014 kg
28	4	DIN 7984 - M8 x 40	steel	0,020 kg
29	2	FL000200	1.4301	0,162 kg
30	2	ISO 2338 - 8 h8 x 85	1.4301	0,034 kg
31	4	ISO 4032 - M6	1.4301	0,003 kg
32	4	ISO 4032 - M8	1.4301	0,006 kg
33	3	ISO 4762 - M3 x 5	1.4301	0,001 kg
34	4	ISO 4762 - M4 x 6	1.4301	0,002 kg
35	4	ISO 4762 - M6 x 10	1.4301	0,005 kg
36	4	ISO 4762 - M8 x 30	1.4301	0,019 kg
37	1	SKF 2RS16002-2RS1	steel	0,029 kg
38	1	SKF 2RS16004-2RS1	steel	0,065 kg

DESIGNED BY T. Schmid	MATERIAL 1.4301	MASS 7,026 kg	SCALE 1:1	DATE 07.06.2016	DIN ISO 2768 m
 			brush feeder		
			BF000000		SHEET SIZE A2



B-B (1 : 1)

Ø32 H7/h6
Ø15 j6

Ø20 j6

Ø42 H7

Ø60 h11

Ø75 H8

2

1+0,5

Ø18 H7/h6

Ø22,5 H7/h6

63

25



30

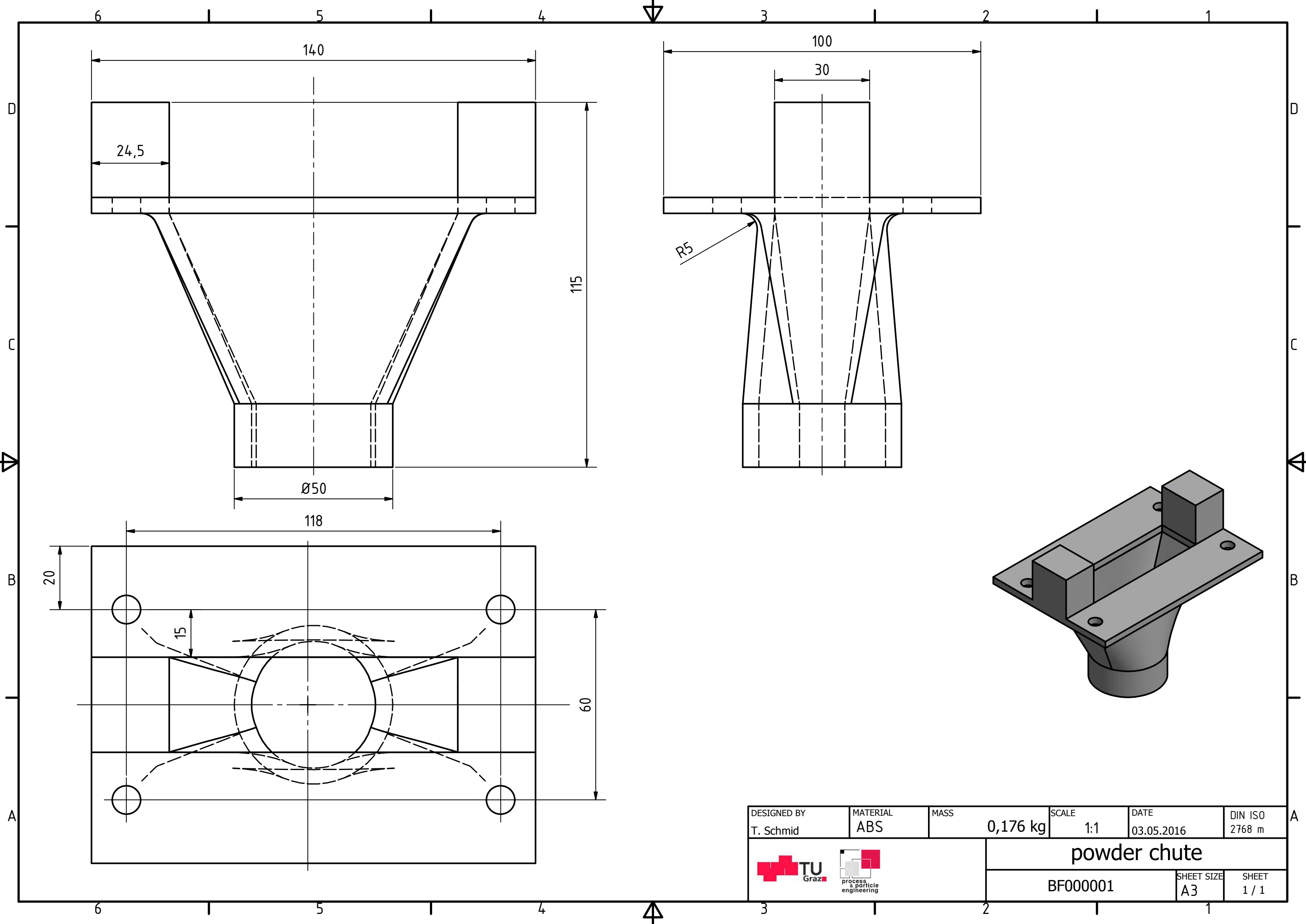
85



211

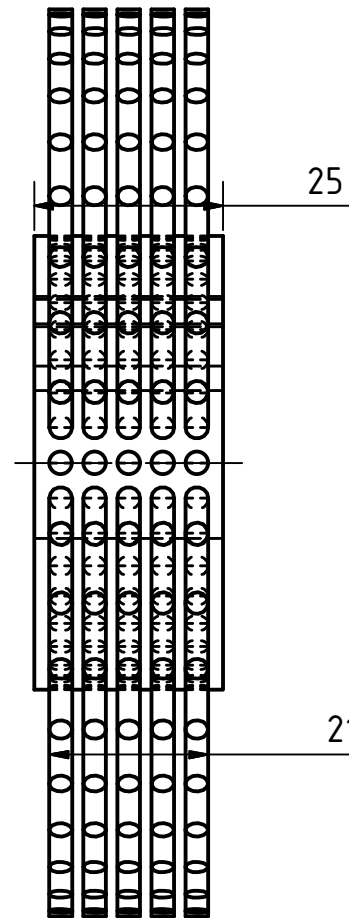
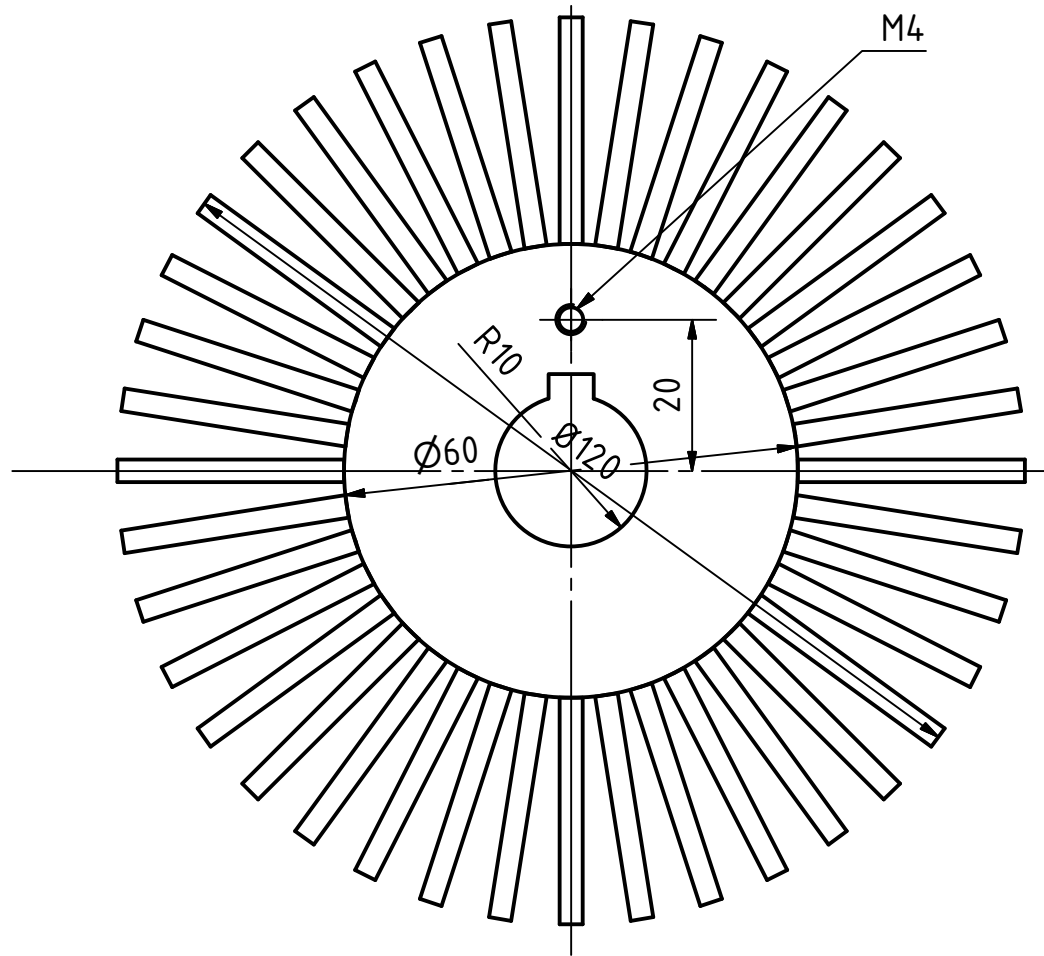
140

646



DESIGNED BY T. Schmid	MATERIAL 1.4301	MASS 7,026 kg	SCALE	DATE 07.06.2016	DIN ISO 2768 m
 		brush feeder			
BF000000			SHEET SIZE A2	SHEET 2 / 2	

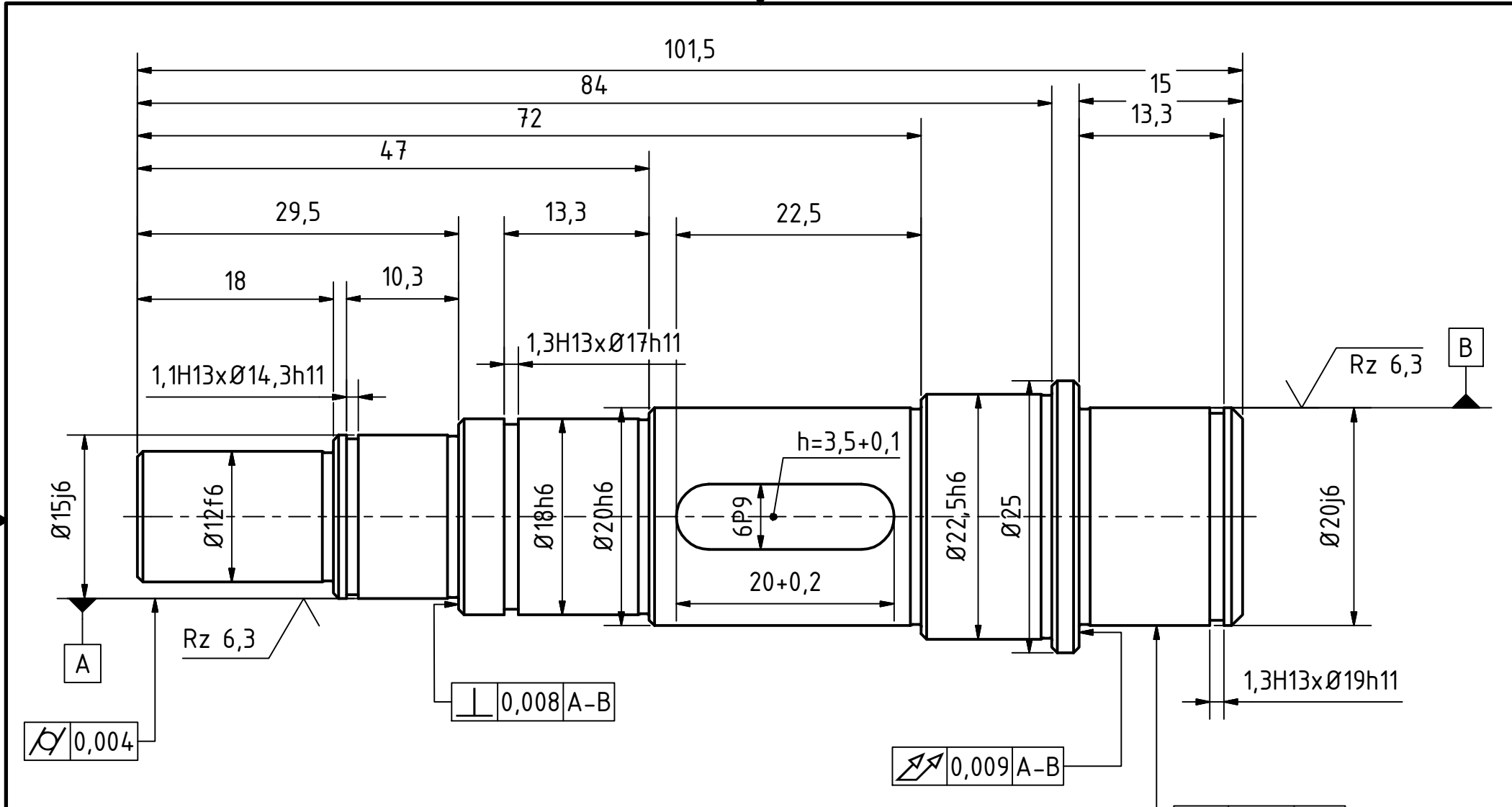


DESIGNED BY T. Schmid	MATERIAL ABS	MASS 0,176 kg	SCALE 1:1	DATE 03.05.2016	DIN ISO 2768 m
 		powder chute			
BF000001			SHEET SIZE A3	SHEET 1 / 1	

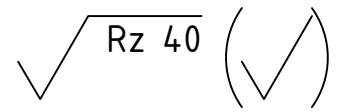



Bristles out of Nylon
 Bristles only symbolized
 Brush body out of ABS

DESIGNED BY T. Schmid	MATERIAL	MASS 0,094 kg	SCALE 1:1	DATE 02.03.2016	DIN ISO 2768 m
 			feeding brush		
			BF010001	SHEET SIZE A4	SHEET 1 / 1

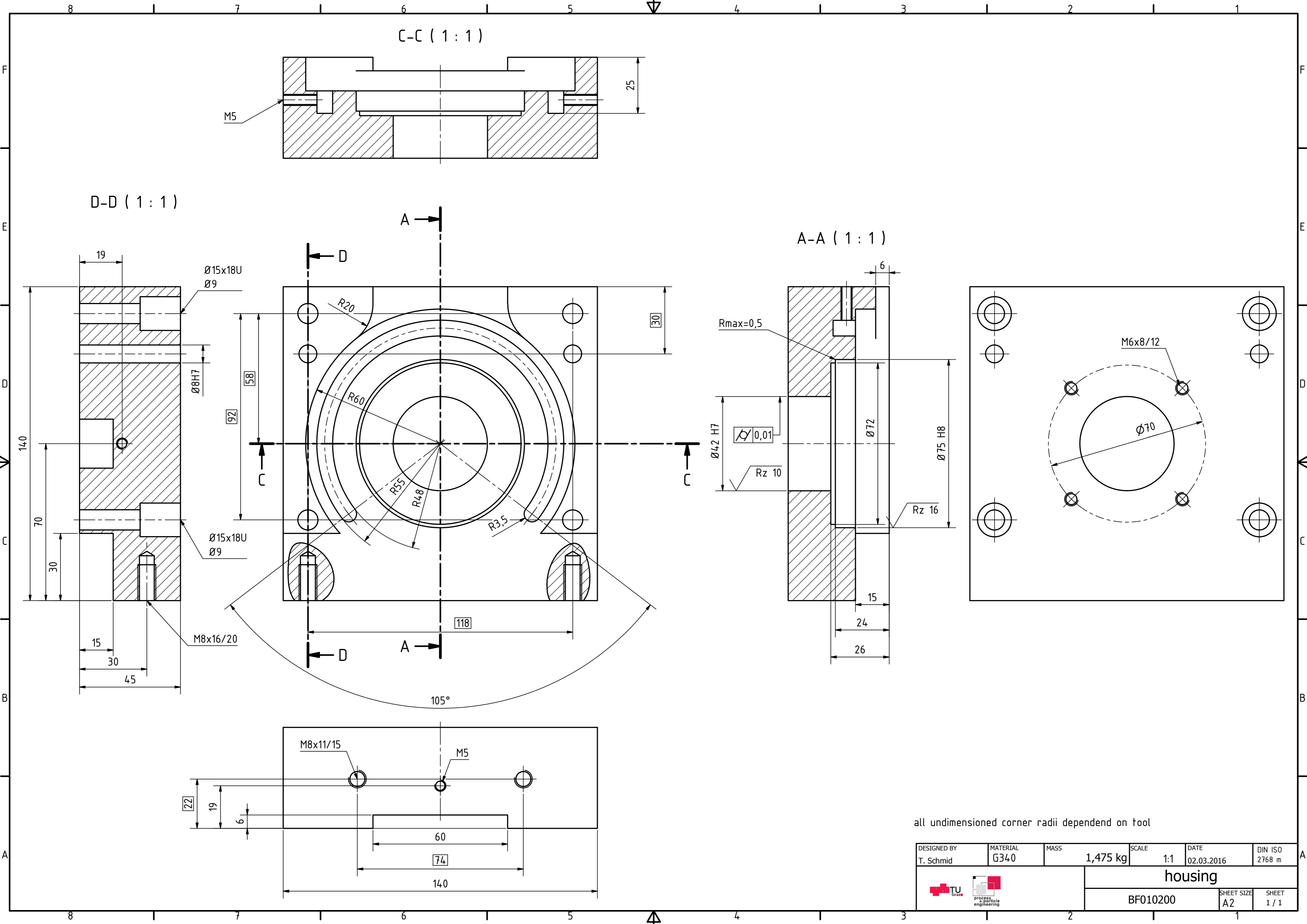


all undimensioned chamfers 0,5x45°
 all undimensioned undercuts DIN 509-F0,8x0,3





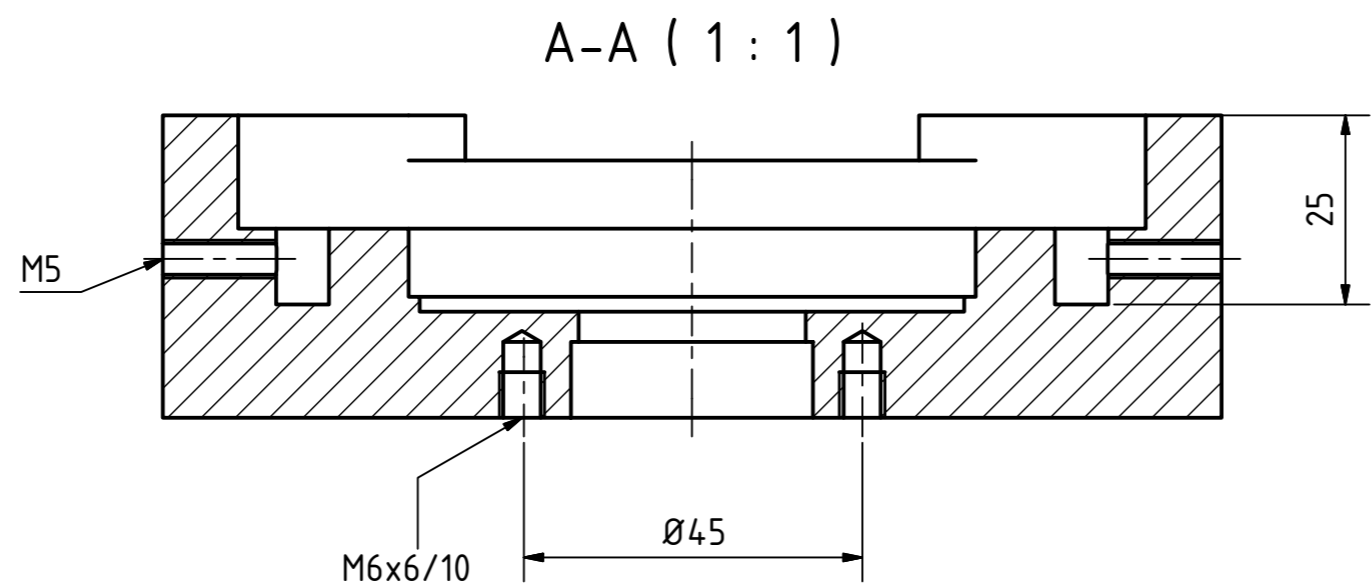
DESIGNED BY T. Schmid	MATERIAL 11SMnPb37	MASS 0,208 kg	SCALE 1:1	DATE 25.02.2016	DIN ISO 2768 f
			drive shaft		
			BF010100	SHEET SIZE A4	SHEET 1 / 1



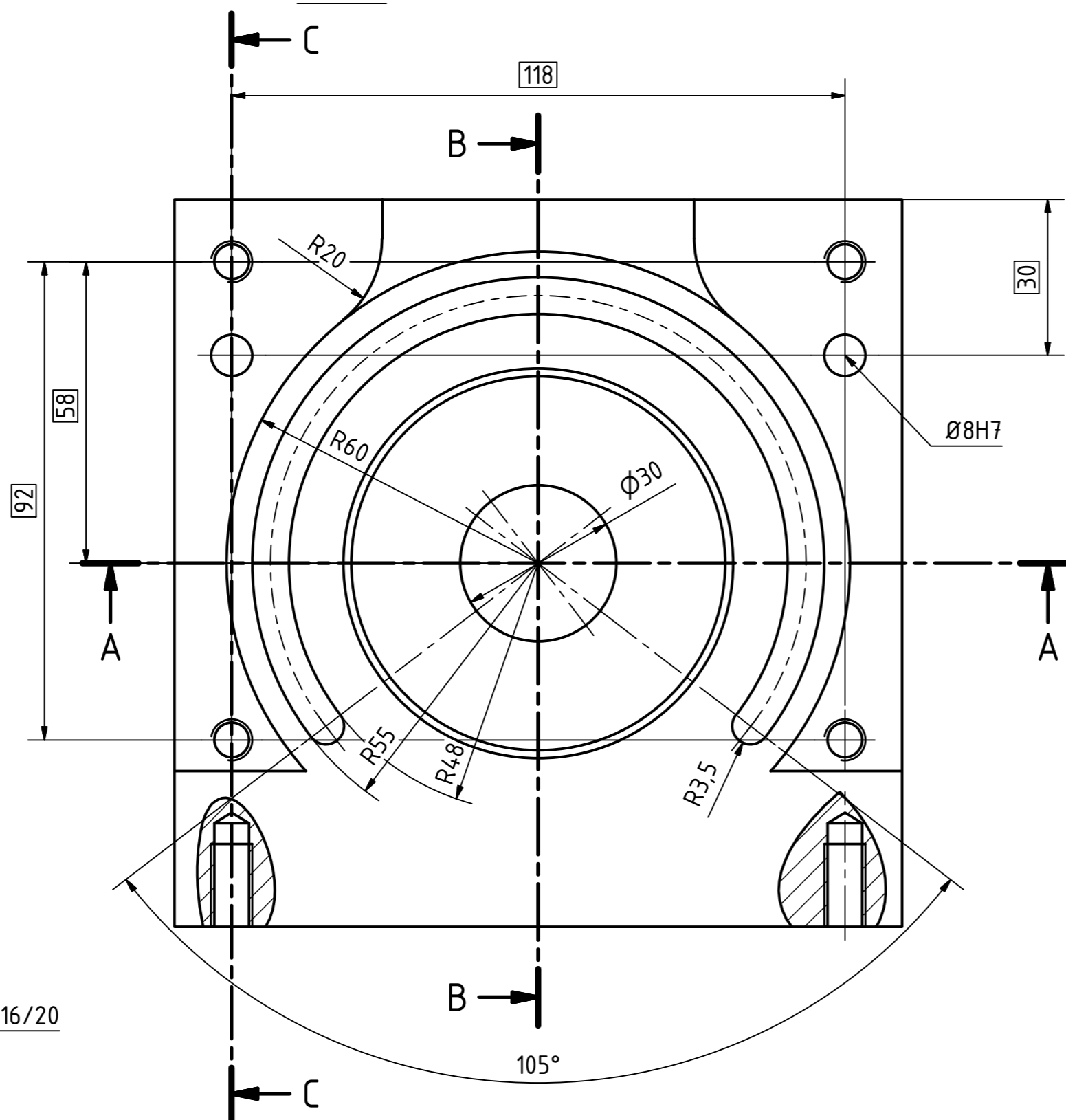
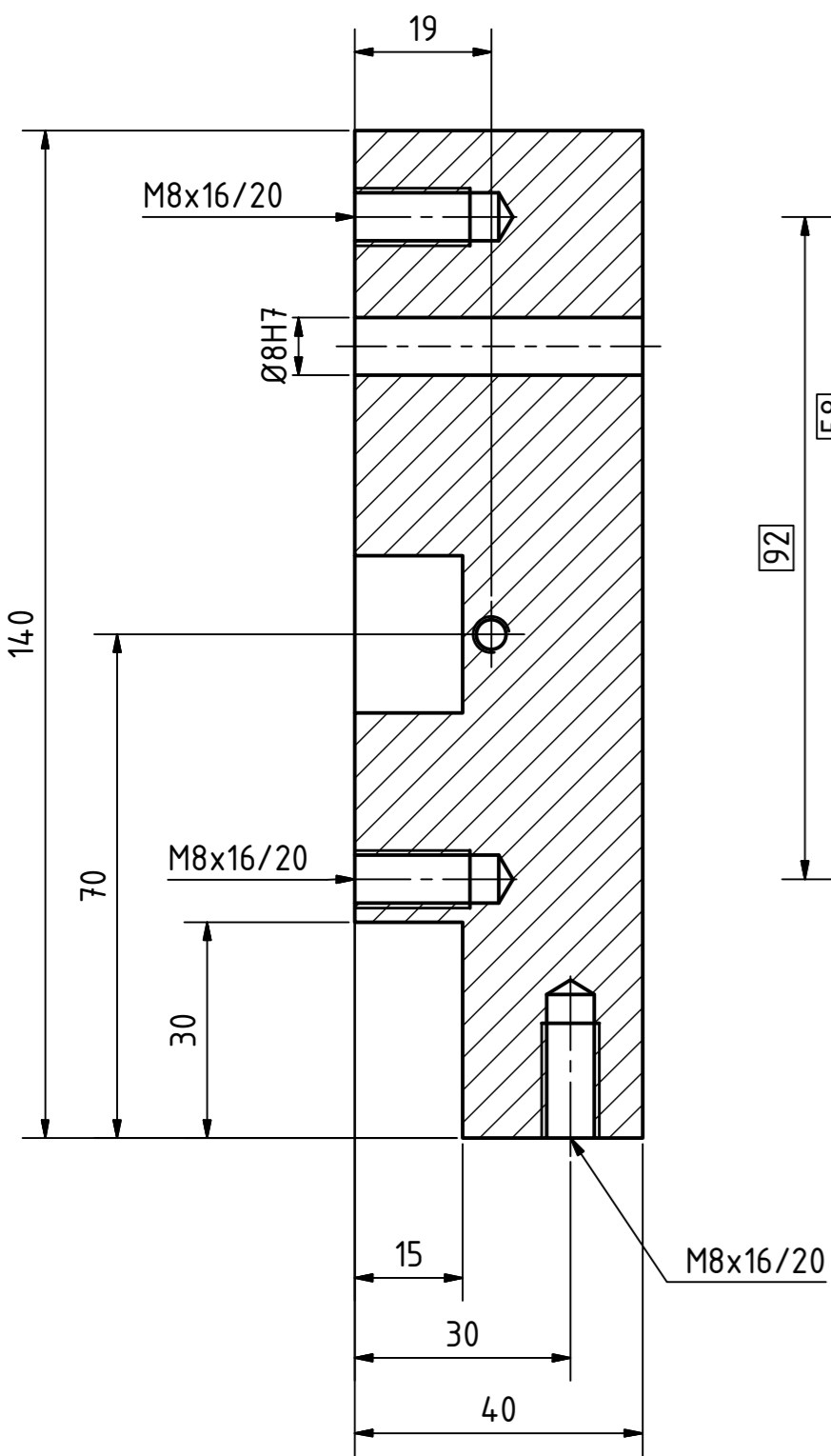


all undimensioned corner radii depend on tool

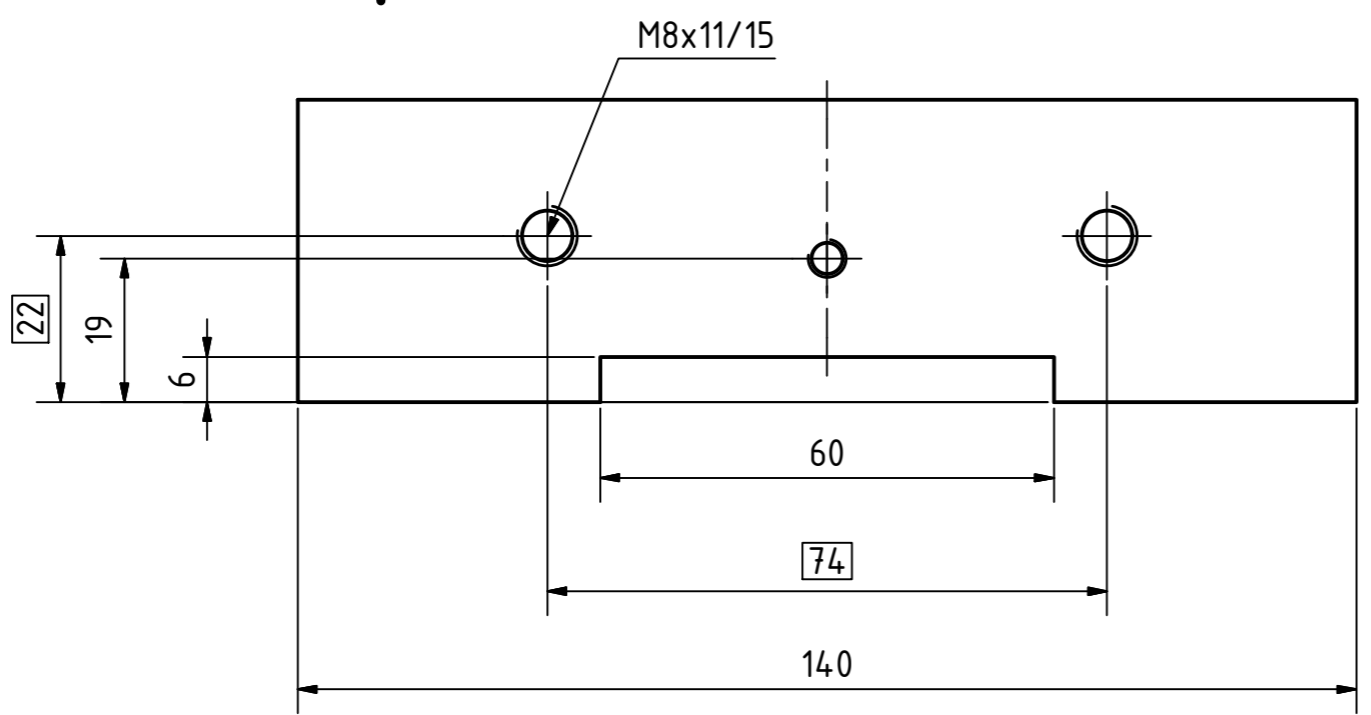
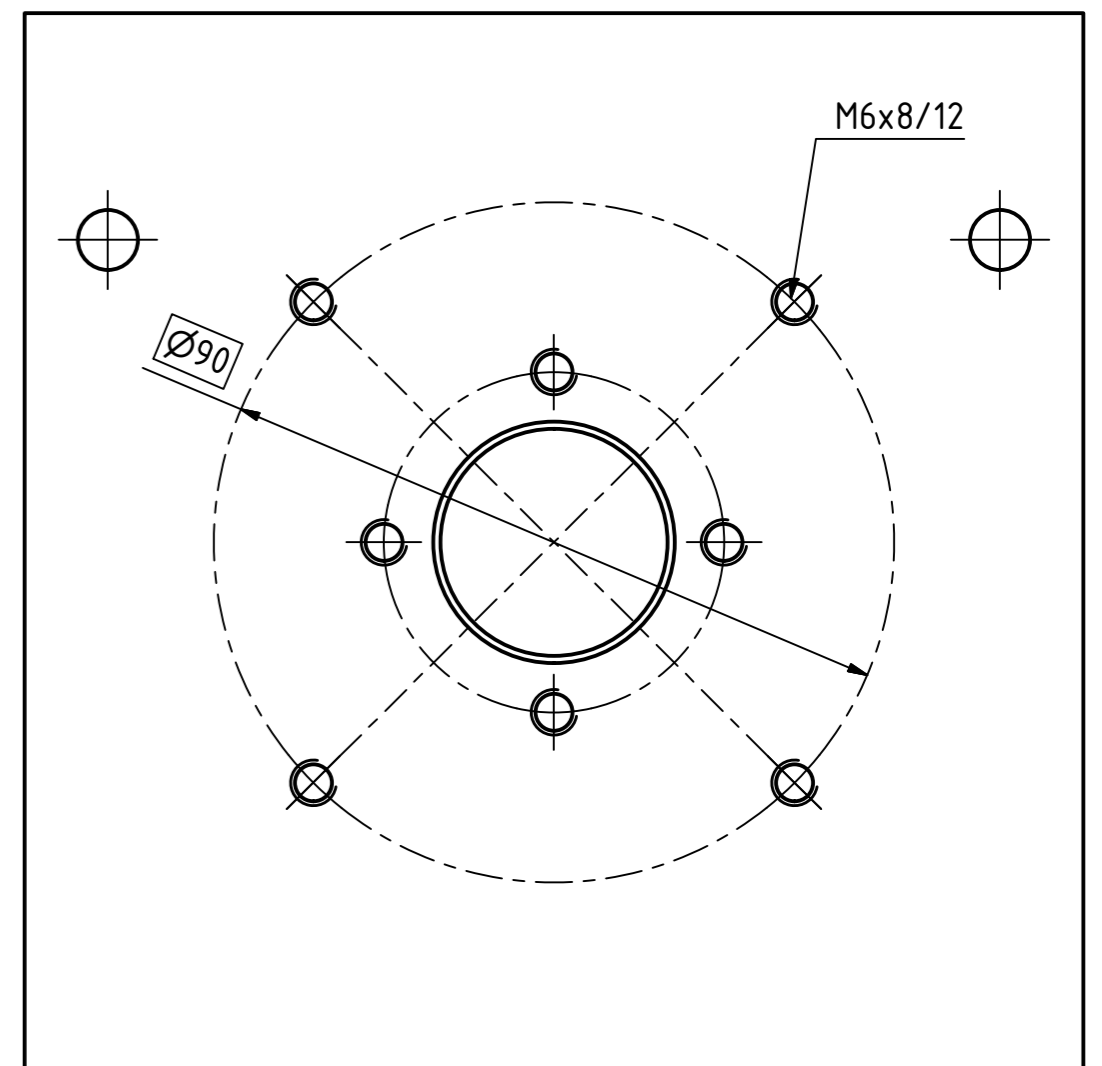
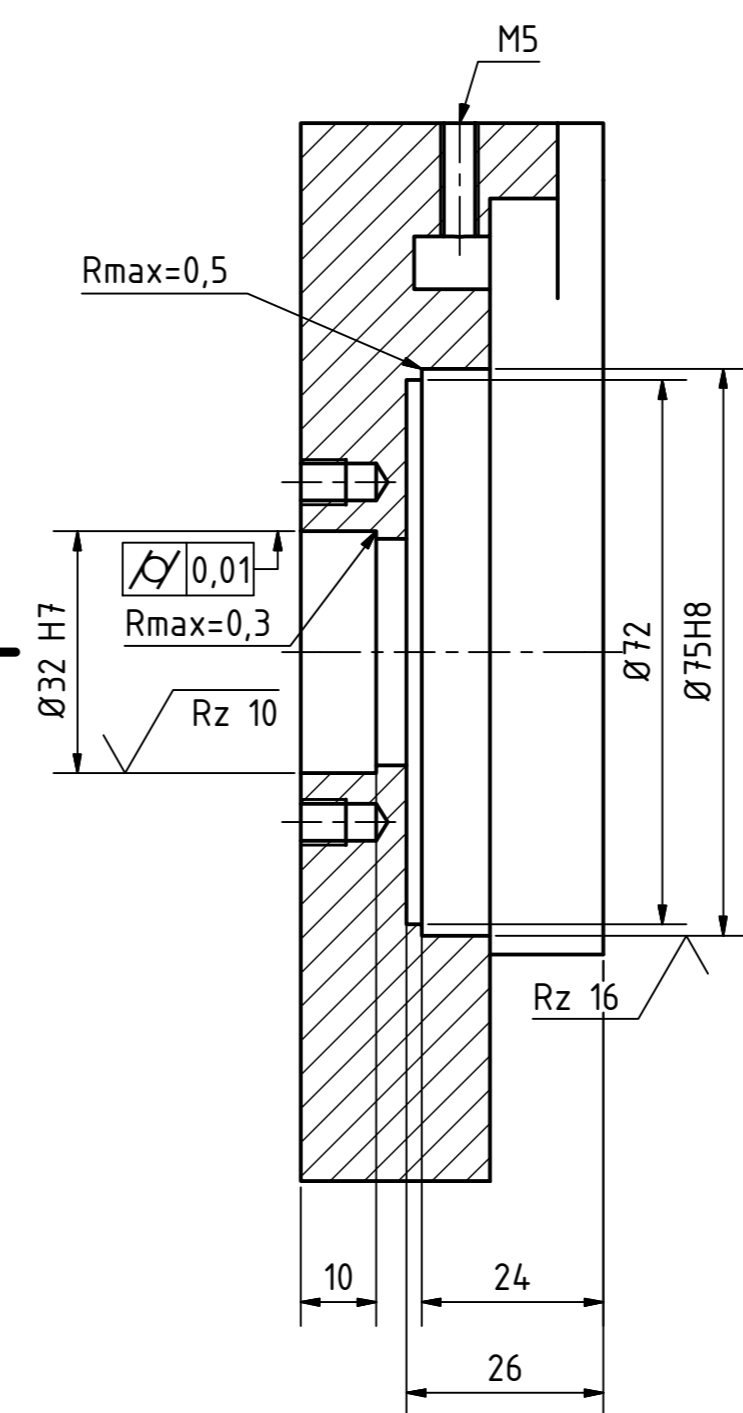
DESIGNED BY T. Schmid	MATERIAL G340	MASS 1,475 kg	SCALE 1:1	DATE 02.03.2016	DIN ISO 2768 m
 			housing		
			BF010200	SHEET SIZE A2	SHEET 1 / 1





C-C (1:1)



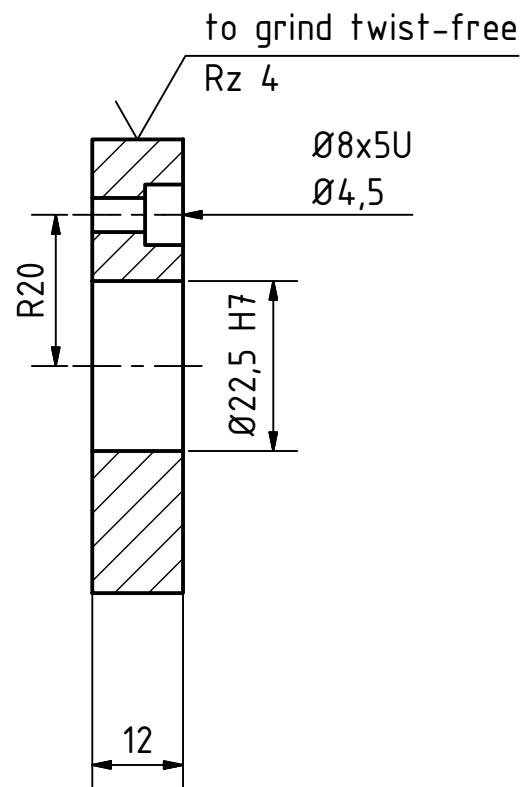
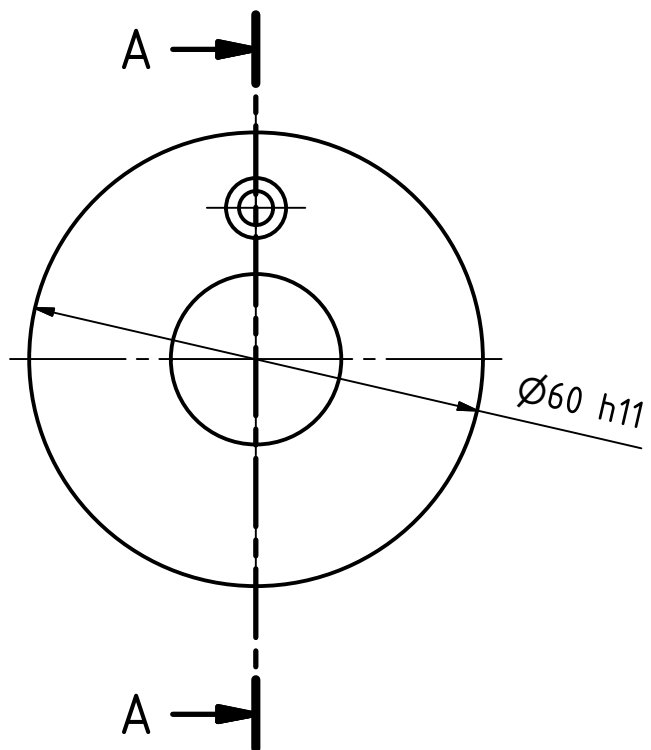
B-B (1:1)





alle undimensioned corner radii tool dependend

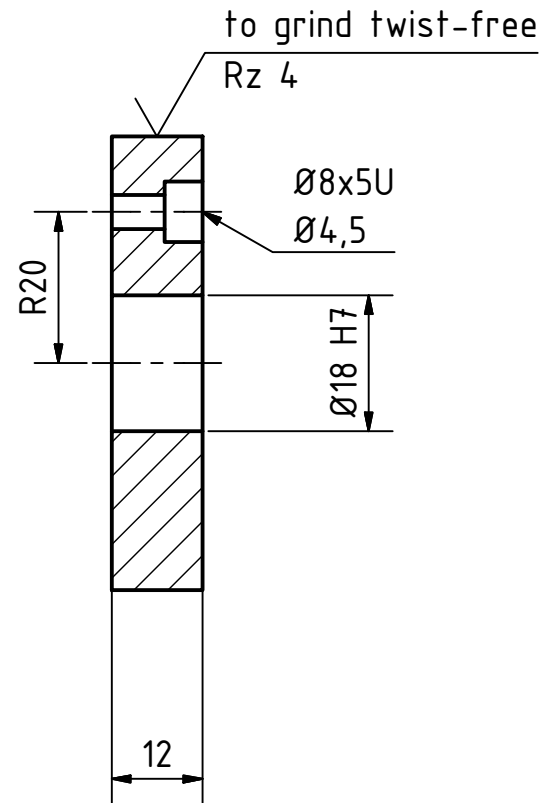
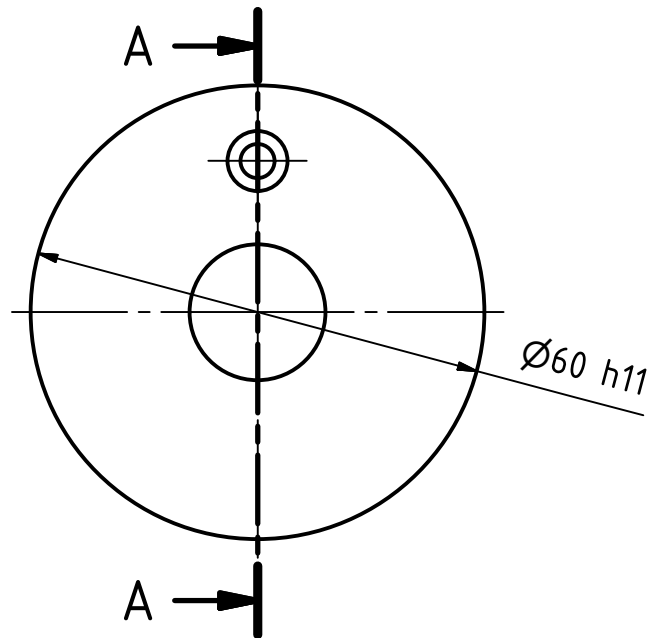
DESIGNED BY T. Schmid	MATERIAL G340	MASS 1,296 kg	SCALE 1:1	DATE 02.03.2016	DIN ISO 2768 f
 			housing		
			BF010300	SHEET SIZE A2	SHEET 1 / 1



A-A (1 : 1)

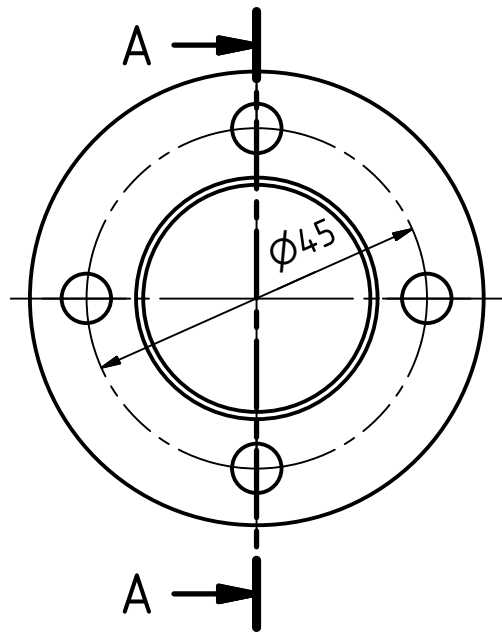


DESIGNED BY T. Schmid	MATERIAL 11SMnPb37	MASS 0,226 kg	SCALE 1:1	DATE 02.03.2016	DIN ISO 2768 m
 			disk		
			BF010400	SHEET SIZE A4	SHEET 1 / 1

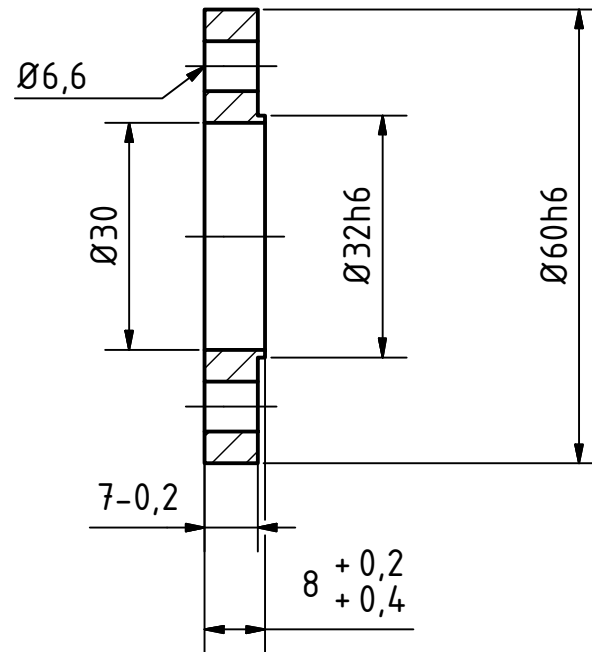
A-A (1 : 1)





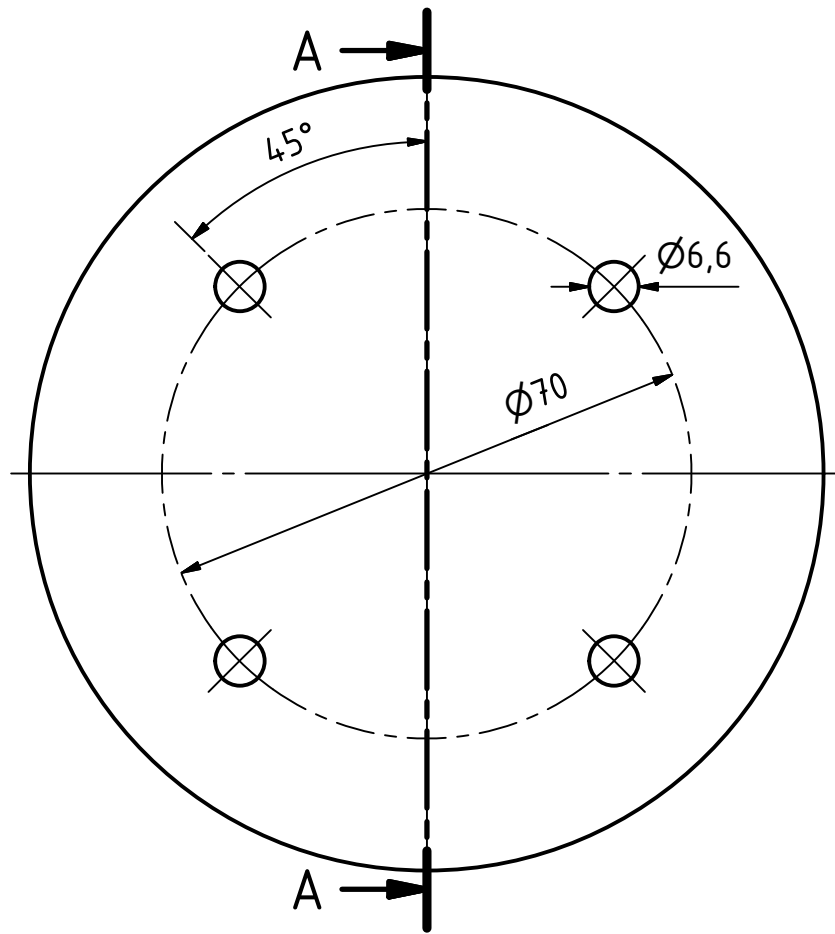
DESIGNED BY T. Schmid	MATERIAL 11SMnPb37	MASS 0,240 kg	SCALE 1:1	DATE 02.03.2016	DIN ISO 2768 m
 			disk		
			BF010500	SHEET SIZE A4	SHEET 1 / 1



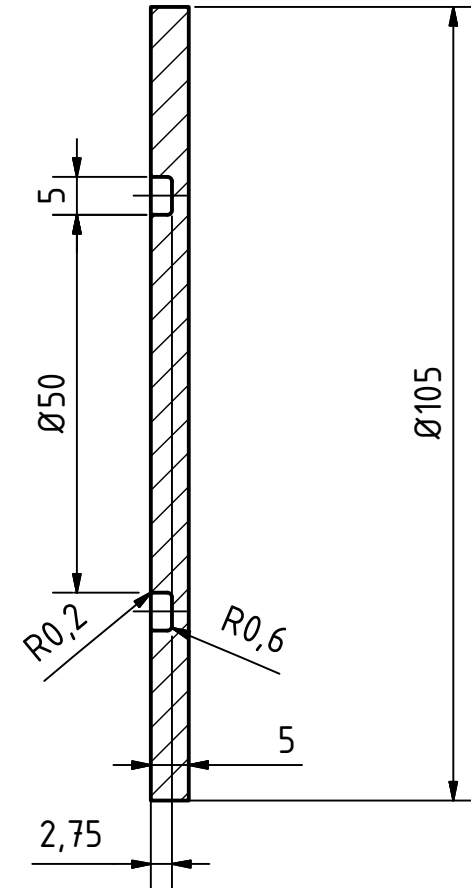
A-A (1 : 1)





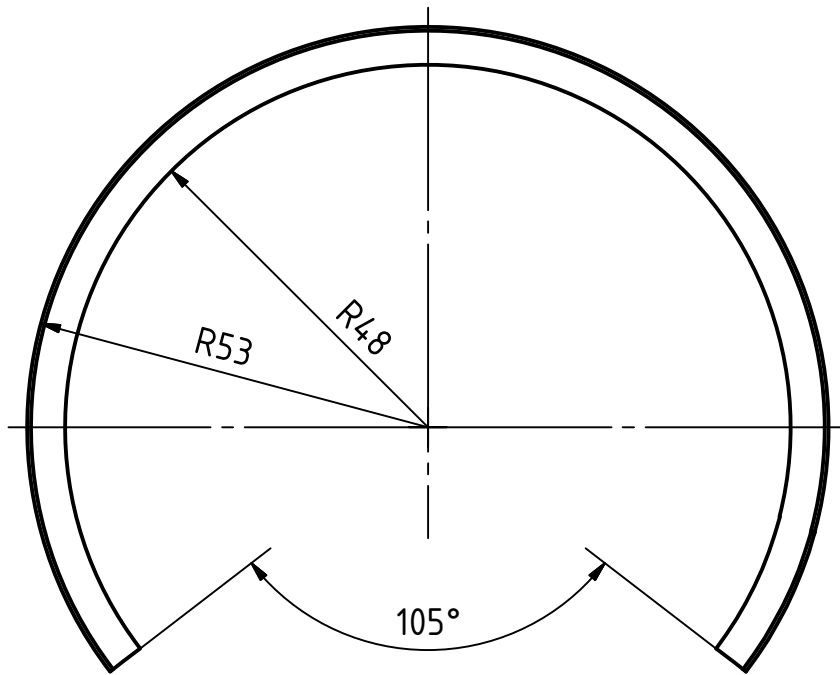
DESIGNED BY T. Schmid	MATERIAL 11SMnPb37	MASS 0,038 kg	SCALE 1:1	DATE 02.03.2016	DIN ISO 2768 m
 		housing cover			
BF010600			SHEET SIZE A4	SHEET 1 / 1	





A-A (1:1)

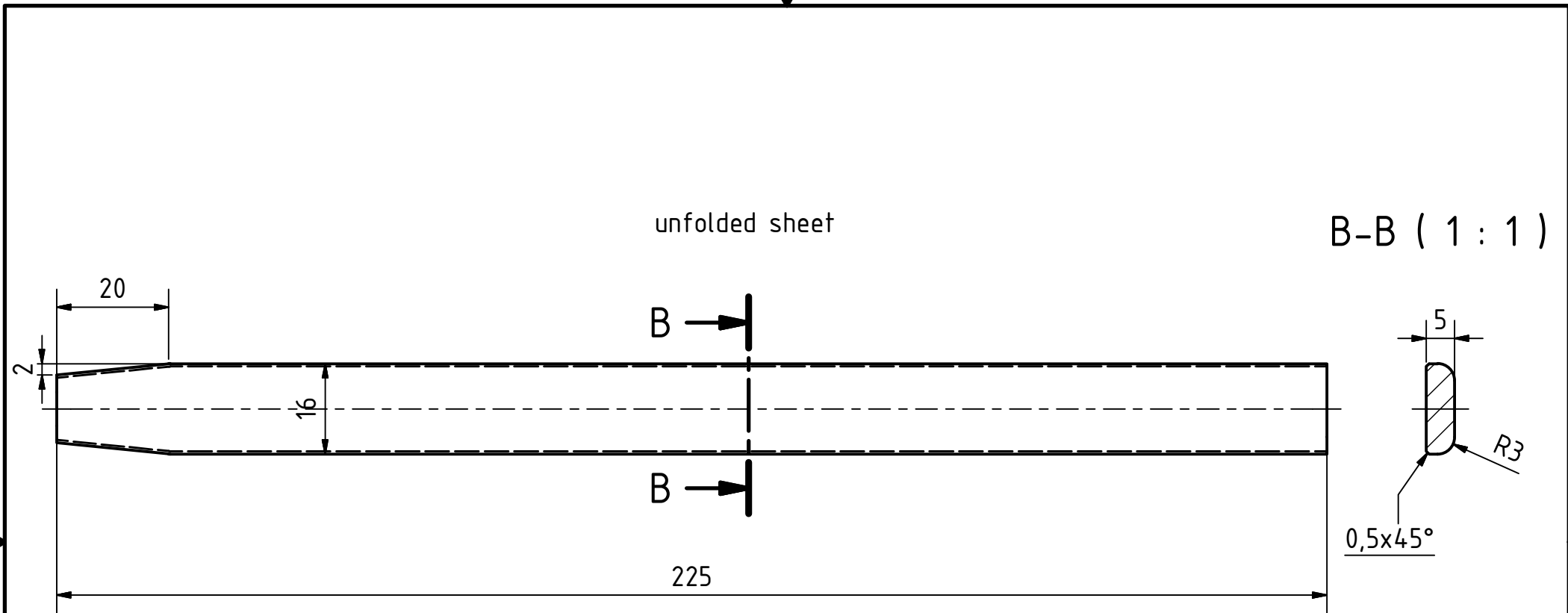




DESIGNED BY T. Schmid	MATERIAL AlCuMgPb	MASS 0,109 kg	SCALE 1:1	DATE 02.03.2016	DIN ISO 2768 m
 			housing cover		
BF010700			SHEET SIZE A4	SHEET 1 / 1	



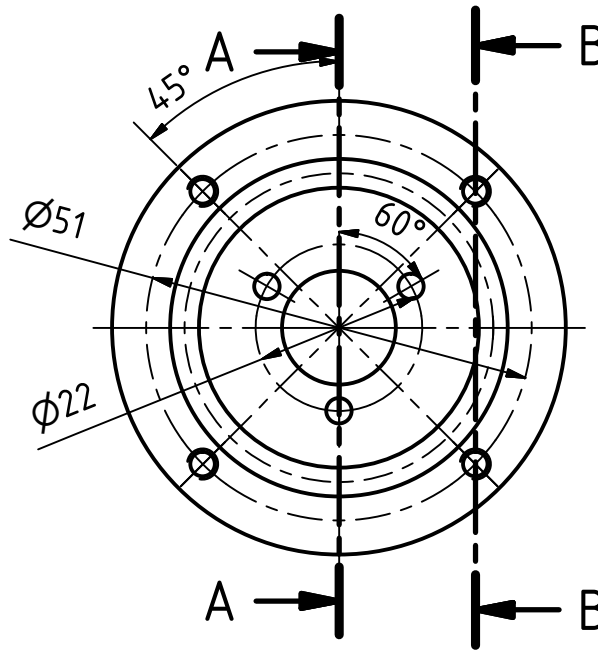
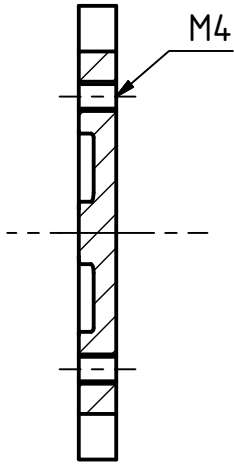
inner radius R3
 outer chamfer 0,5x45°

DESIGNED BY T. Schmid	MATERIAL Al99,5	MASS 0,017 kg	SCALE 1:1	DATE 16.03.2016	DIN ISO 2768 m
 		guide bar			
		BF010800	SHEET SIZE A4	SHEET 1 / 2	

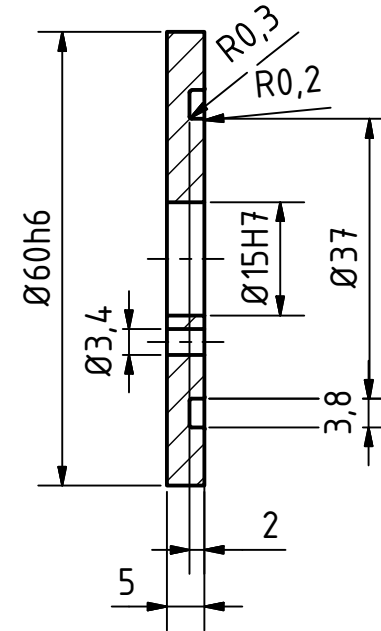




DESIGNED BY T. Schmid	MATERIAL Al99,5	MASS 0,017 kg	SCALE 1:1	DATE 16.03.2016	DIN ISO 2768 m
 			guide bar		
			BF010800	SHEET SIZE A4	SHEET 2 / 2

B-B (1 : 1)

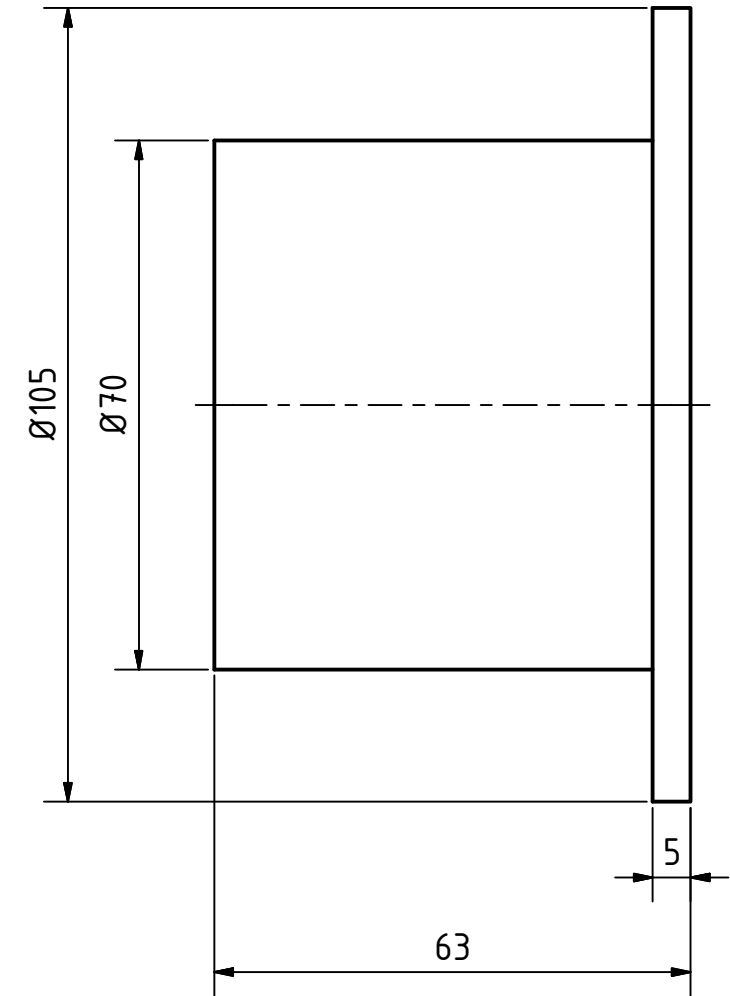
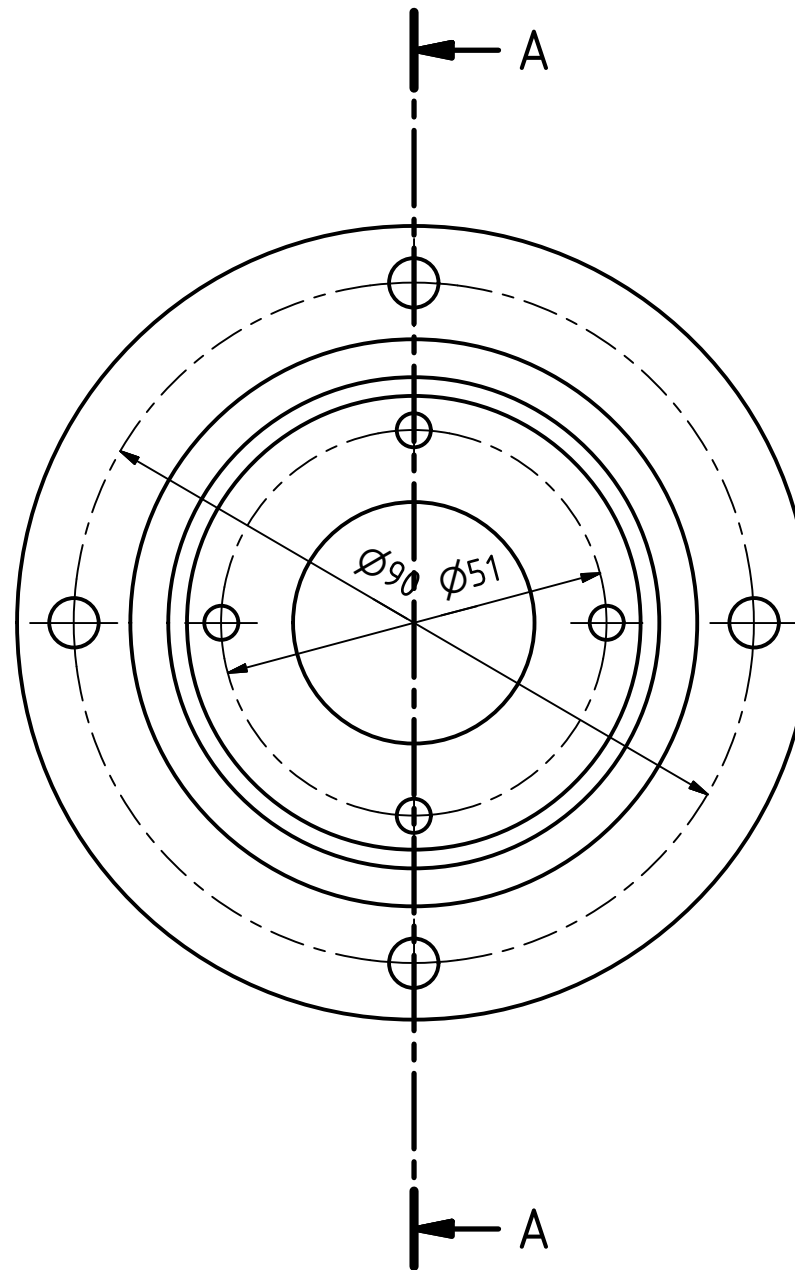
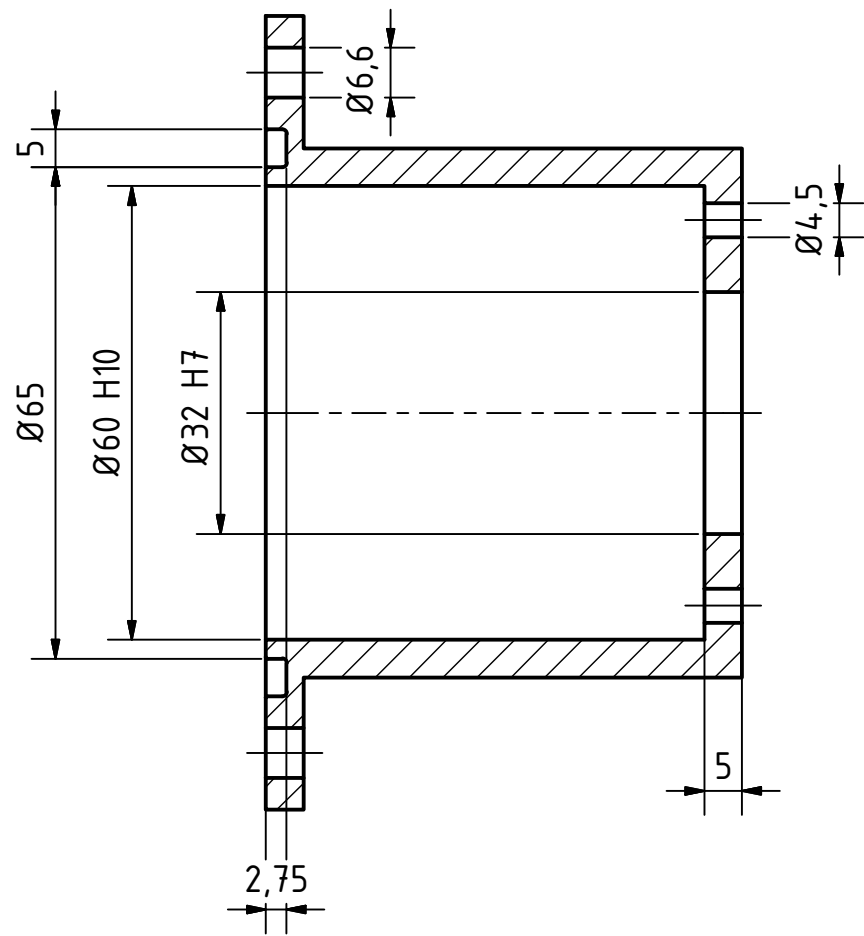




A-A (1 : 1)

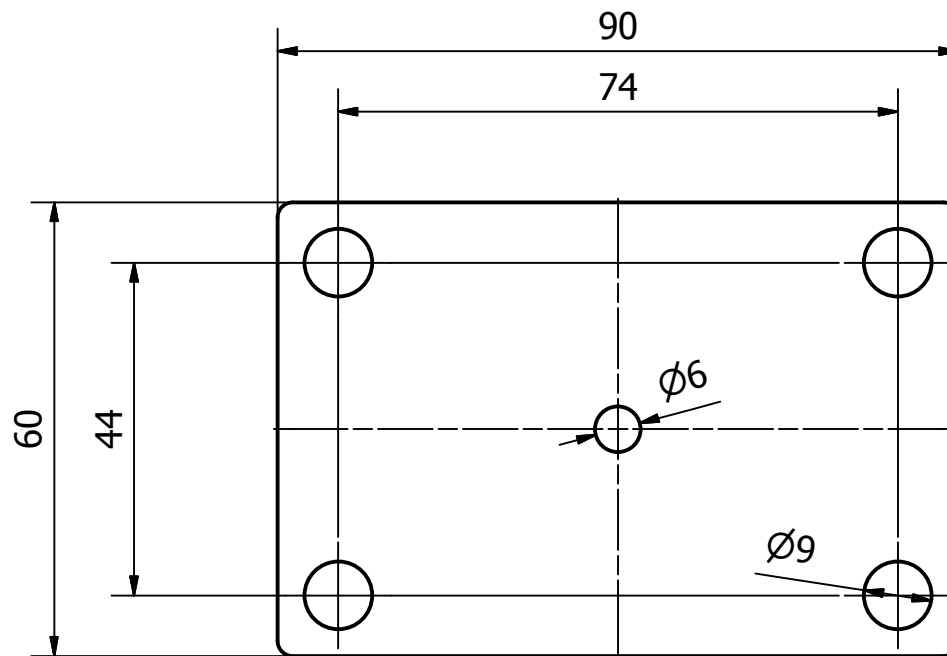




DESIGNED BY T. Schmid	MATERIAL 11SMnPb37	MASS 0,033 kg	SCALE 1:1	DATE 02.03.2016	DIN ISO 2768 m
 			cover		
			BF010900	SHEET SIZE A4	SHEET 1 / 1

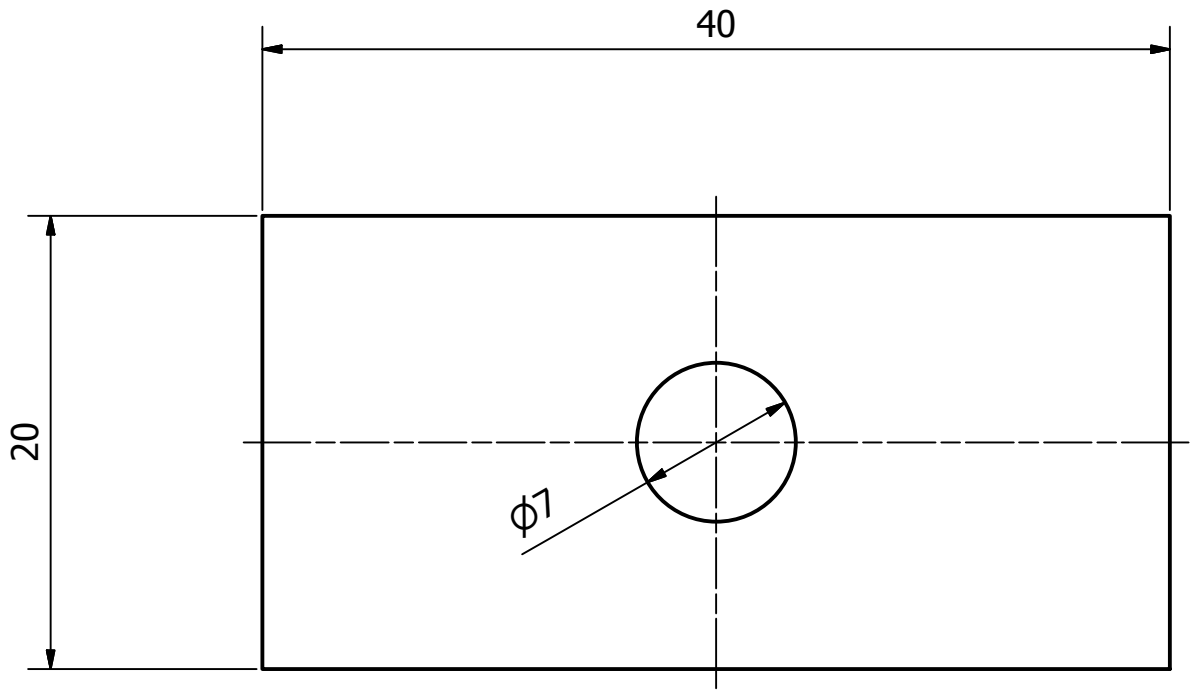
A-A (1 : 1)





DESIGNED BY T. Schmid	MATERIAL AlCuMgPb	MASS 0,256 kg	SCALE 1:1	DATE 02.03.2016	DIN ISO 2768 m
 		bell			
BF011000			SHEET SIZE A3	SHEET 1 / 1	

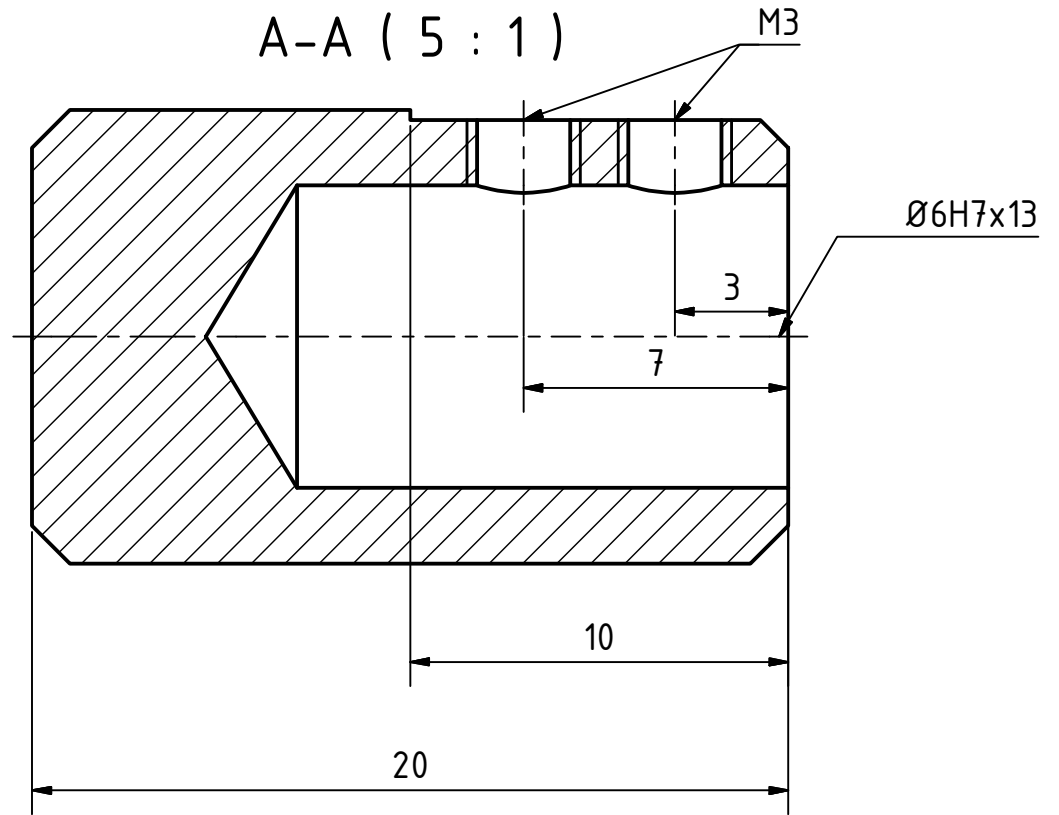
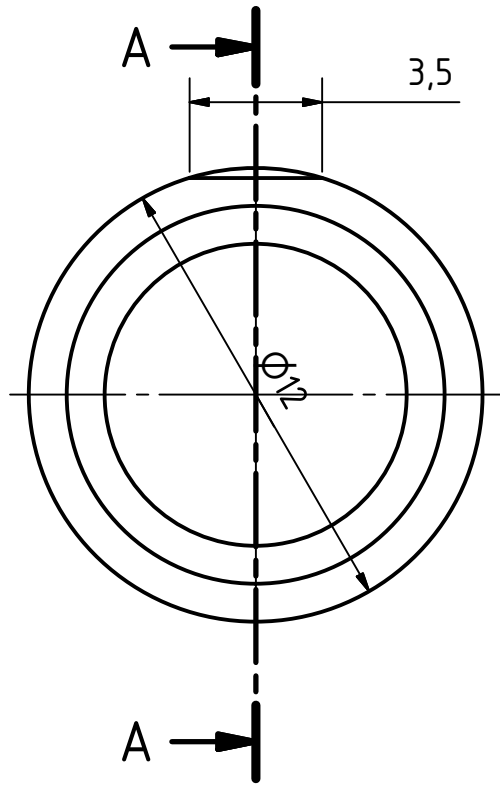


DESIGNED BY T. Schmid	MATERIAL CR	MASS 0,010 kg	SCALE 1:1	DATE 07.06.2016	DIN ISO 2768 m
 			polychloroprene plate		
BF011100			SHEET SIZE A4	SHEET 1 / 1	





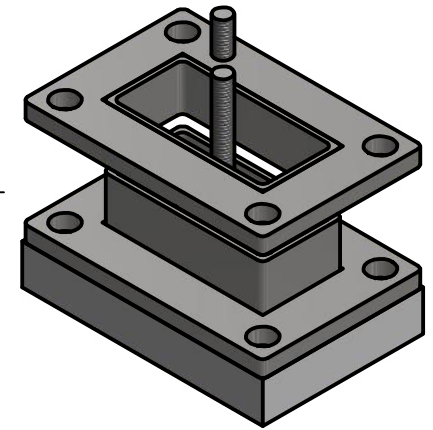
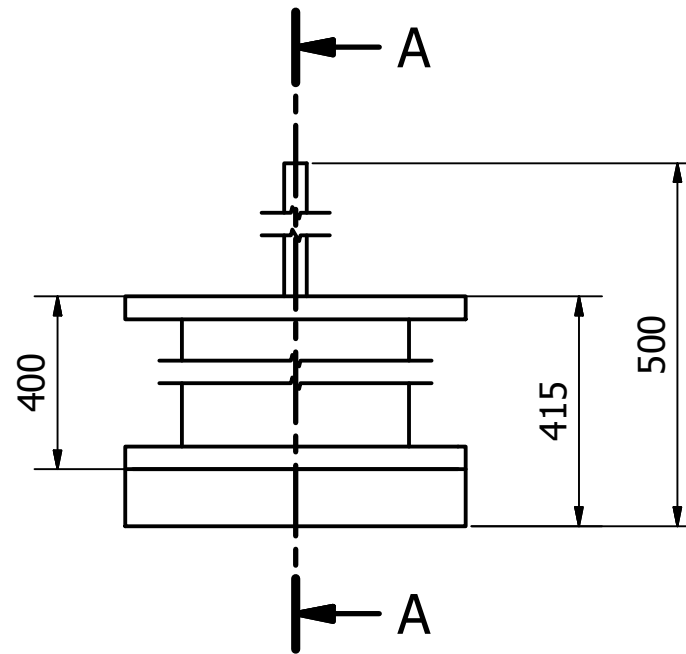
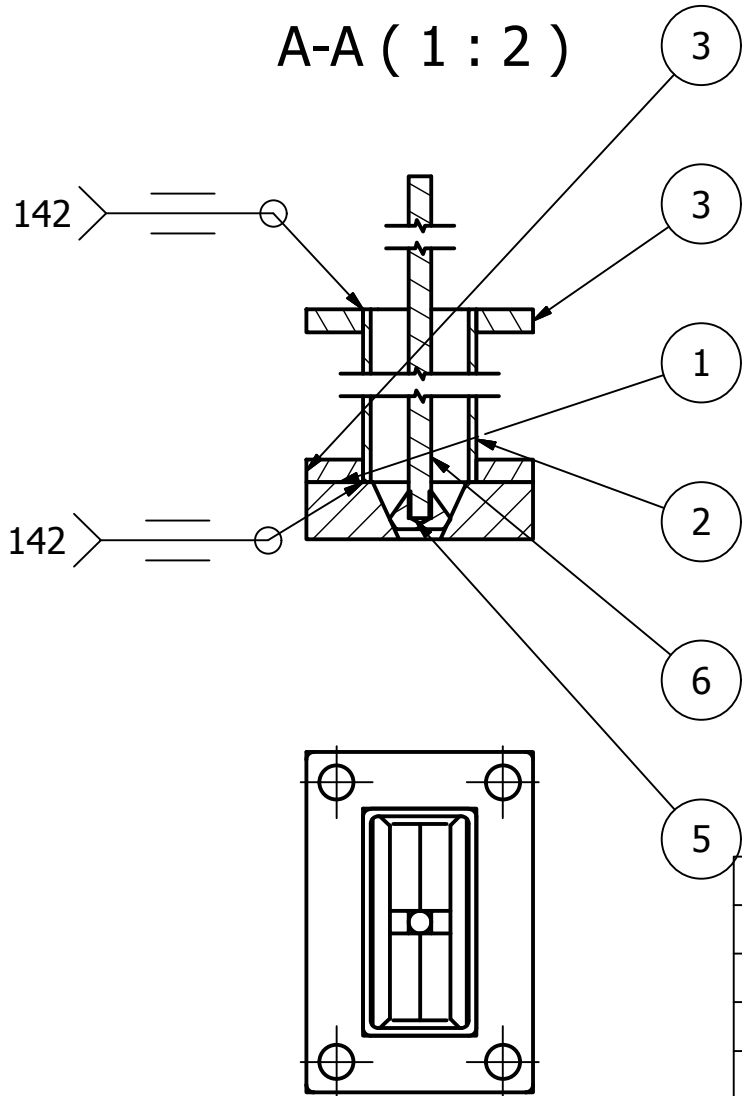
$t=2$

DESIGNED BY T. Schmid	MATERIAL 1.4301	MASS 0,002 kg	SCALE 3:1	DATE 07.06.2016	DIN ISO 2768 m
 			metal sheet		
			BF011200	SHEET SIZE A4	SHEET 1 / 1



all undimensioned chamfers $1 \times 45^\circ$

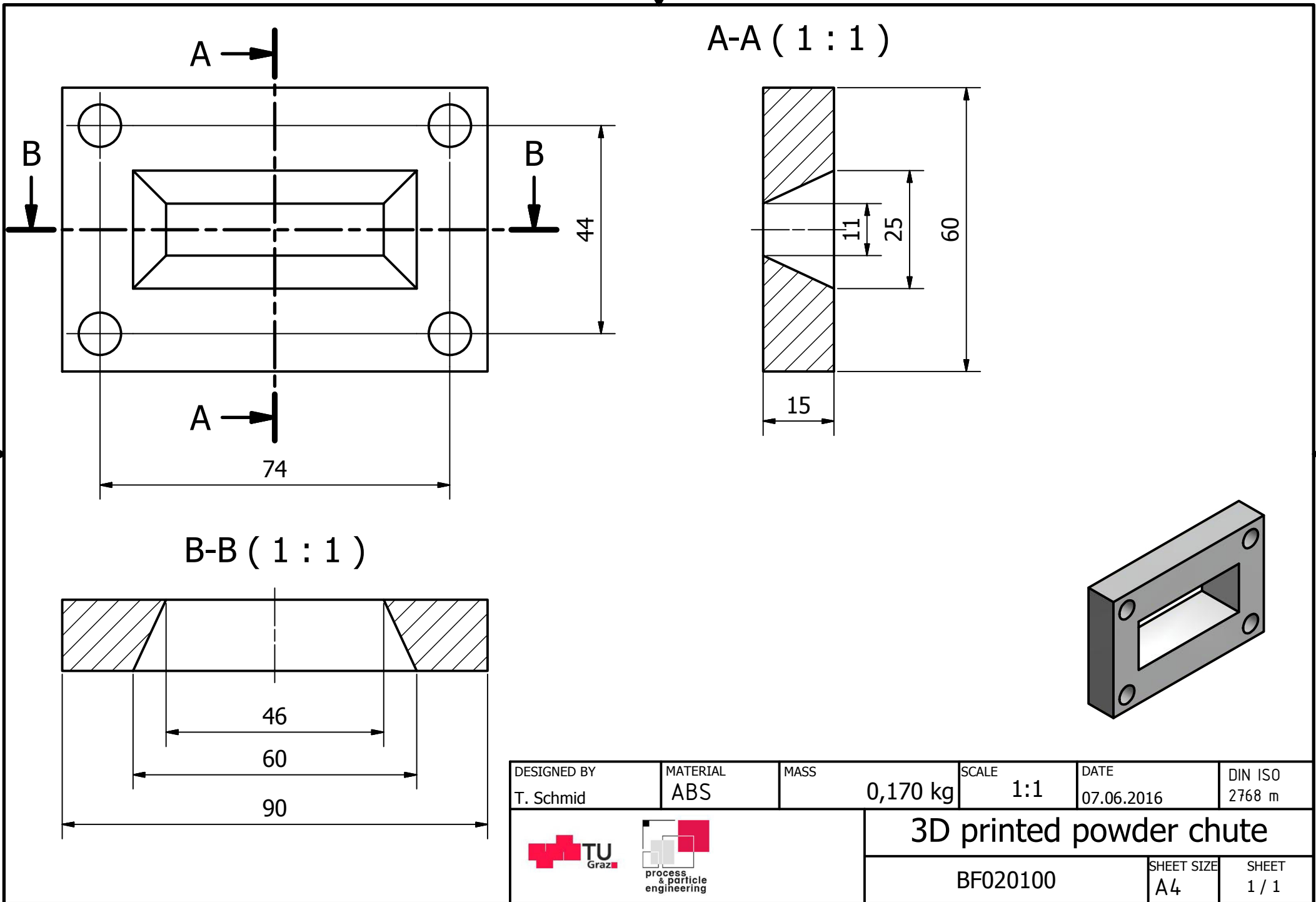
DESIGNED BY T. Schmid	MATERIAL 11SMnPb37	MASS 0,012 kg	SCALE 5:1	DATE 02.03.2016	DIN ISO 2768 m
 		adapter shaft			
BF011300			SHEET SIZE A4	SHEET 1 / 1	





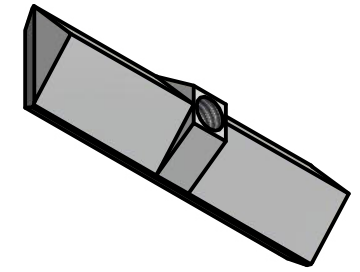
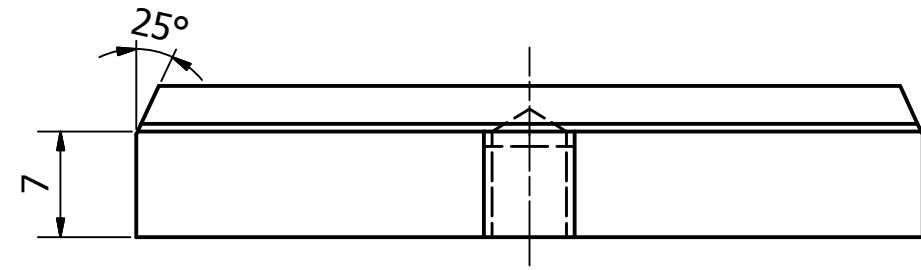
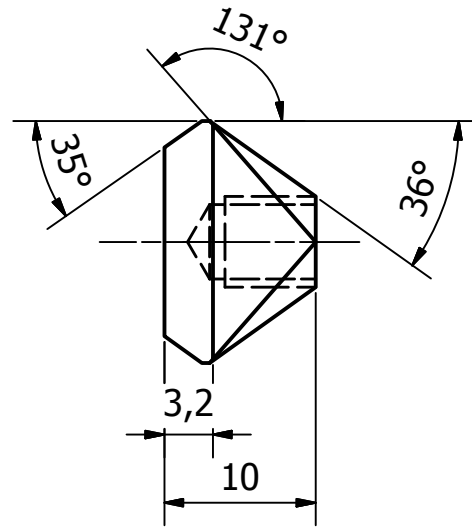
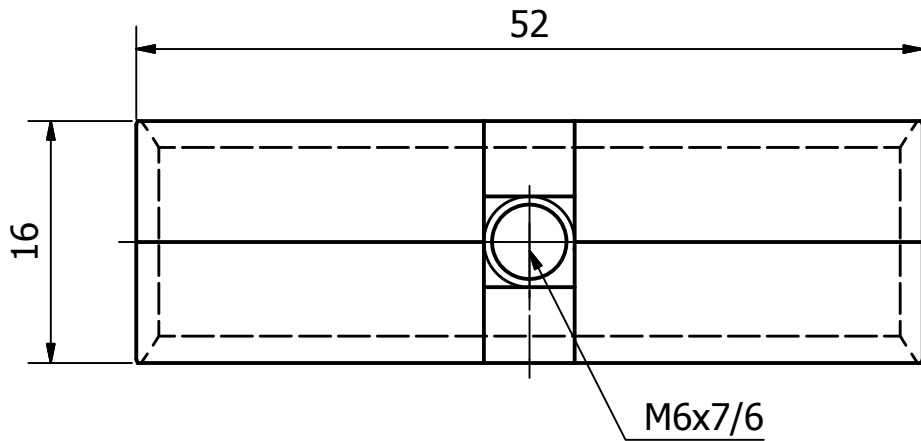
list of parts				
object	quantity	part number	material	mass
1	1	BF020100	ABS	0,066 kg
2	1	hollow profile 60x30x2x400	1.4301	1,112 kg
3	2	FL000200	1.4301	0,162 kg
5	1	BF020200	Al99,5	0,014 kg
6	1	thread bar M10x500	steel	0,014 kg



DESIGNED BY T. Schmid	MATERIAL	MASS 1,530 kg	SCALE 1:2	DATE 07.06.2016	DIN ISO 2768 m
--------------------------	----------	------------------	--------------	--------------------	-------------------

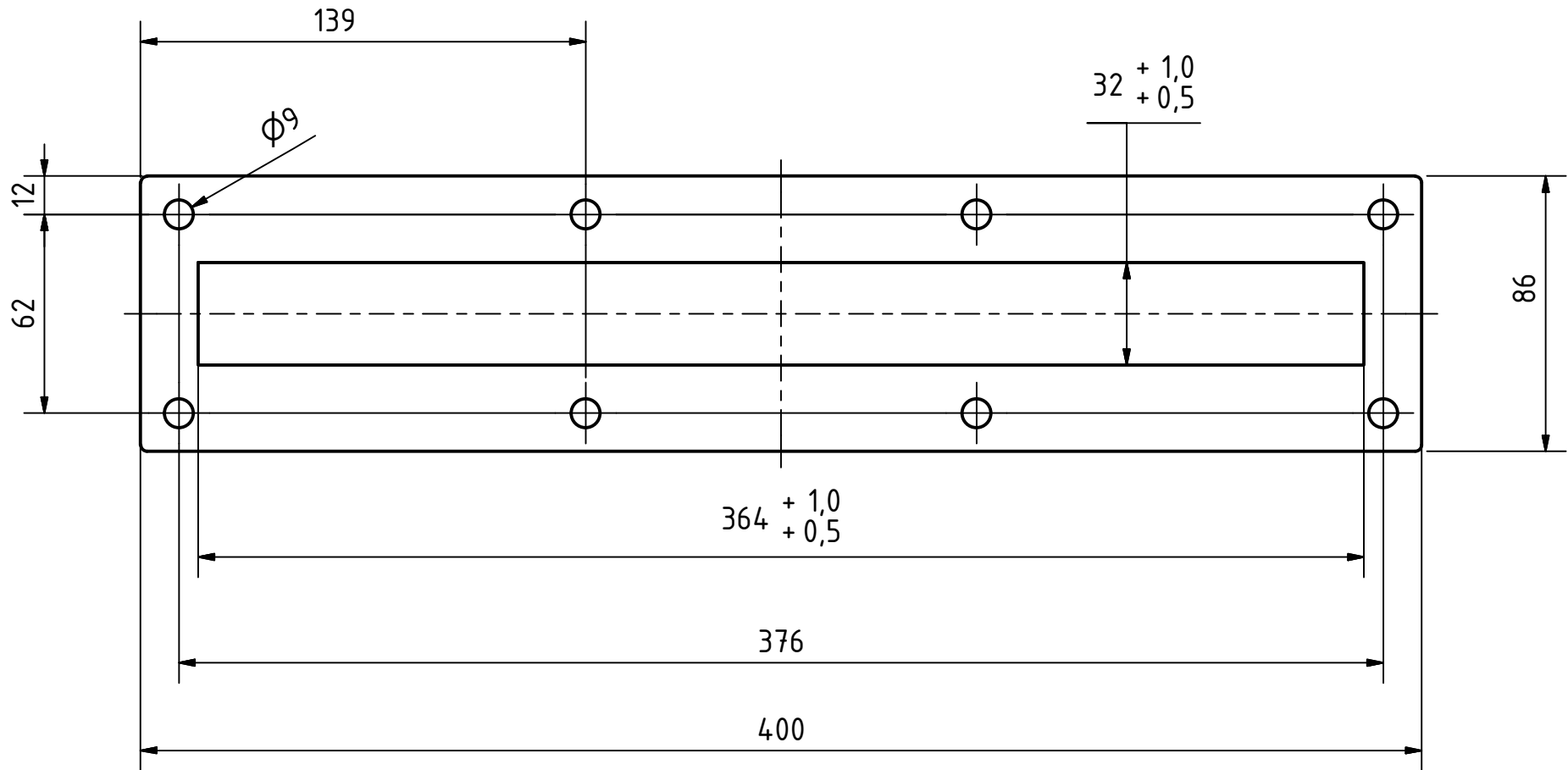
 	hopper		
	BF020000	SHEET SIZE A4	SHEET 1 / 1





DESIGNED BY T. Schmid	MATERIAL ABS	MASS 0,170 kg	SCALE 1:1	DATE 07.06.2016	DIN ISO 2768 m
 			3D printed powder chute		
			BF020100	SHEET SIZE A4	SHEET 1 / 1

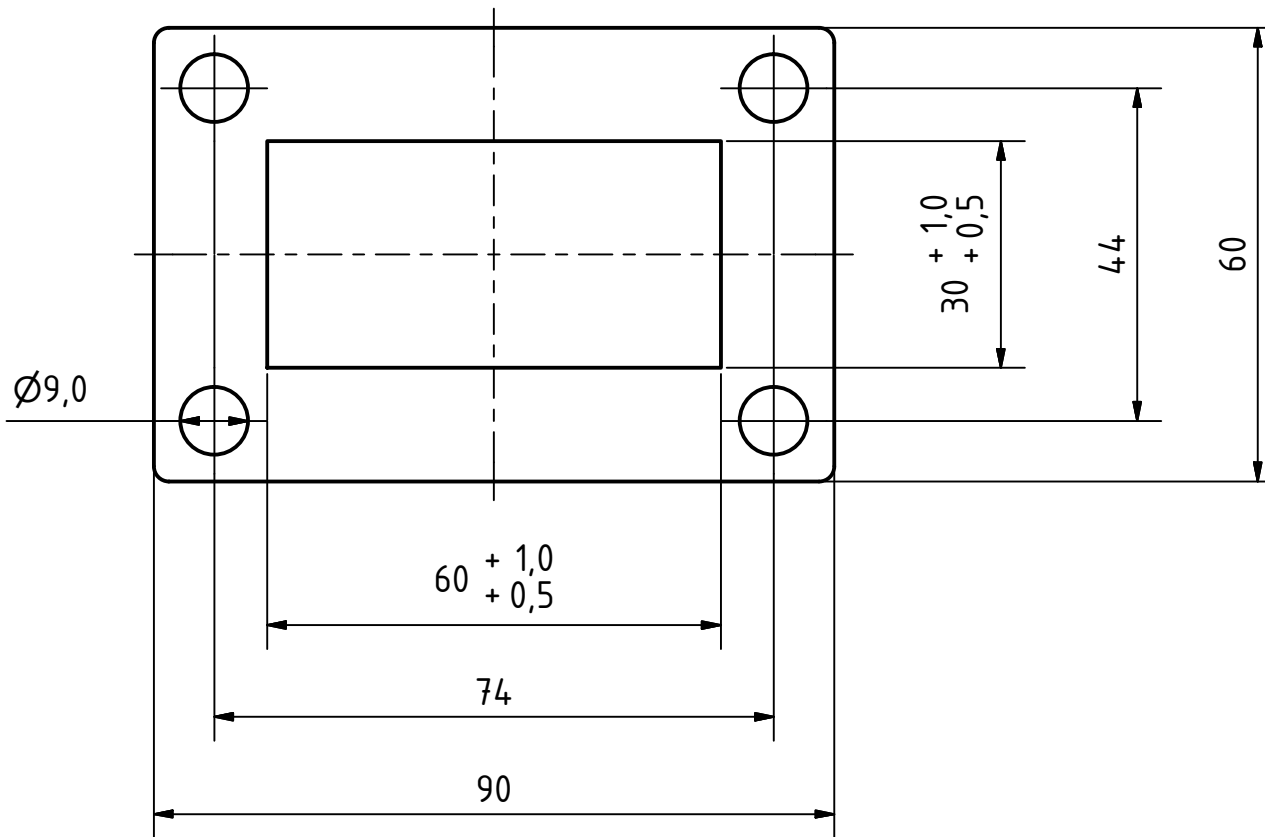


DESIGNED BY T. Schmid	MATERIAL Al99,5	MASS 0,014 kg	SCALE 2:1	DATE 07.06.2016	DIN ISO 2768 m
 		plug			
BF020200			SHEET SIZE A4	SHEET 1 / 1	





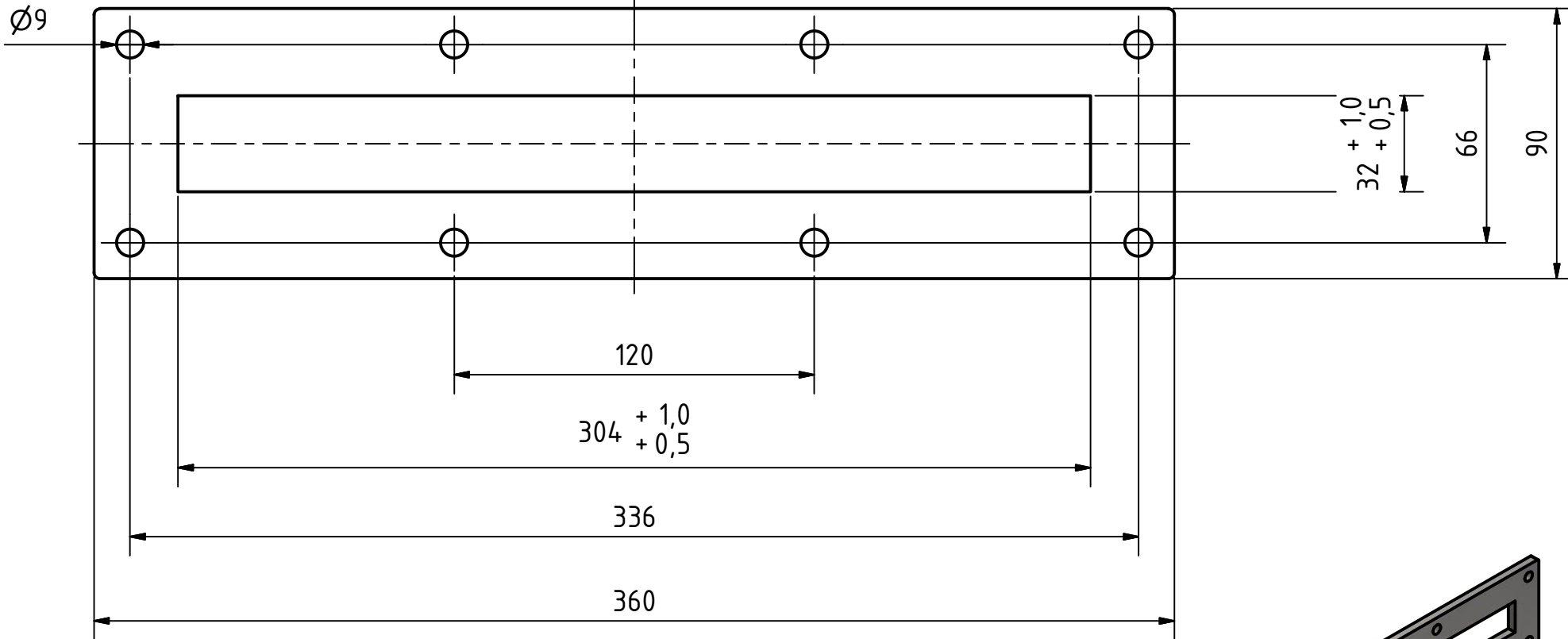
t=8
all undefined radii R2

DESIGNED BY T. Schmid	MATERIAL 1.4301	MASS 1,438 kg	SCALE 1:2	DATE 23.11.2015	DIN ISO 2768 f
 			flange		
FL000100				SHEET SIZE A4	SHEET 1 / 1





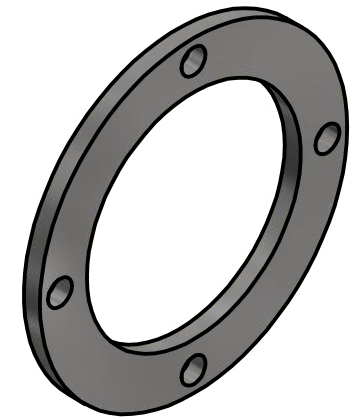
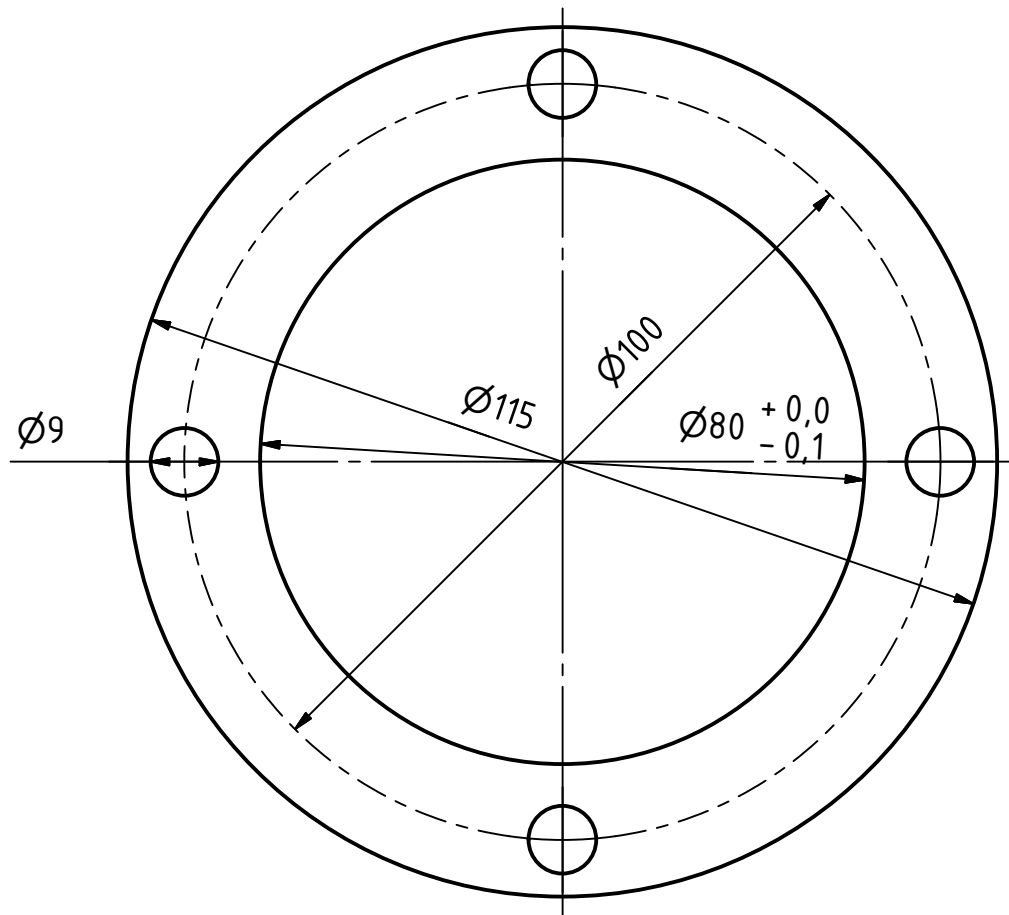
t=8
all undimensioned radii R2



DESIGNED BY T. Schmid	MATERIAL 1.4301	MASS 0,162 kg	SCALE 1:1	DATE 23.11.2015	DIN ISO 2768 f
 			flange		
FL000200				SHEET SIZE A4	SHEET 1 / 1

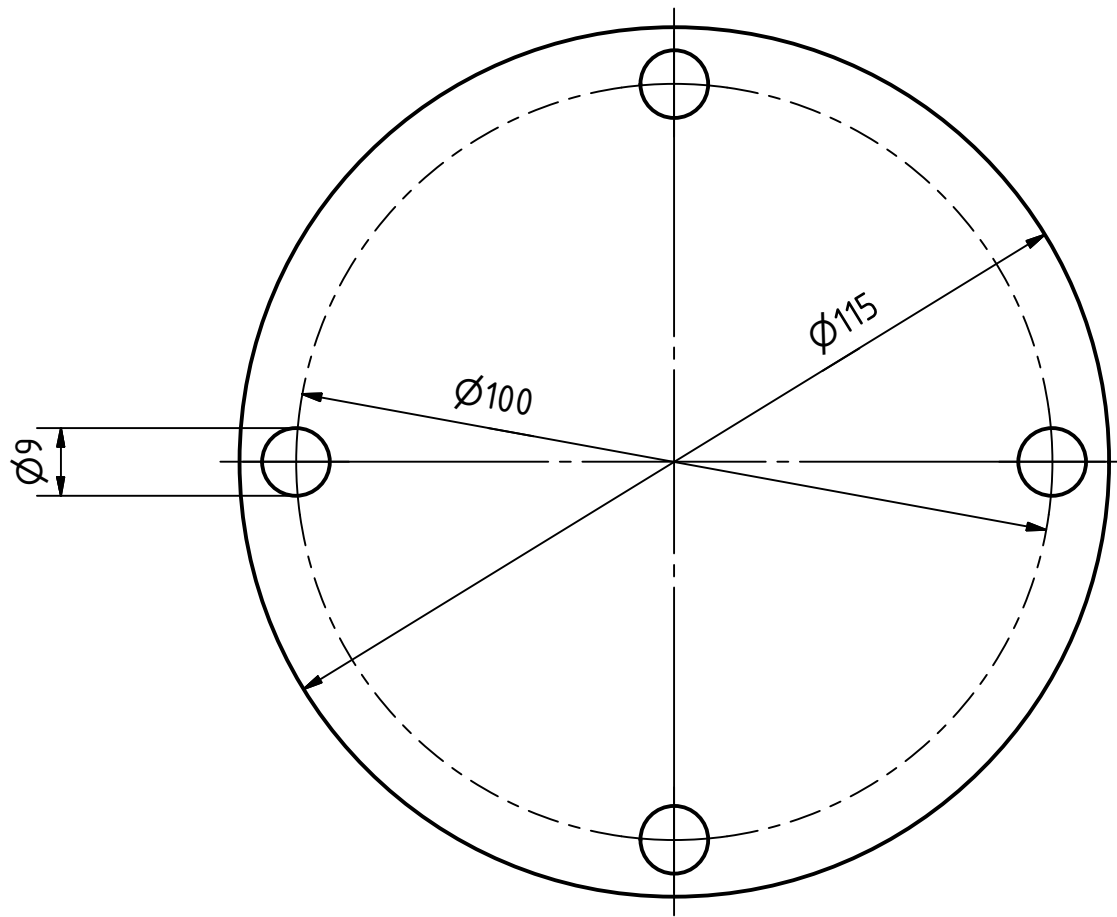


$t=8$
all undimensioned radii R2



DESIGNED BY T. Schmid	MATERIAL 1.4301	MASS 1,432 kg	SCALE 1:2	DATE 23.11.2015	DIN ISO 2768 f
 			flange		
			FL000300	SHEET SIZE A4	SHEET 1 / 1

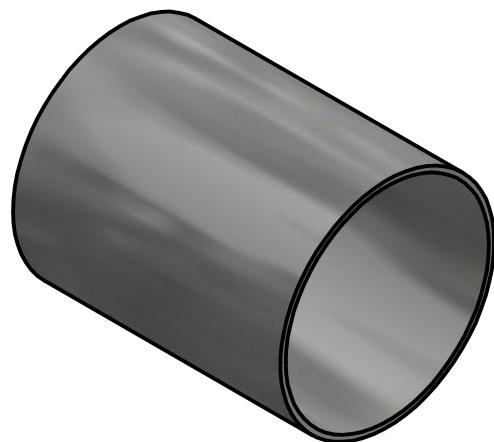
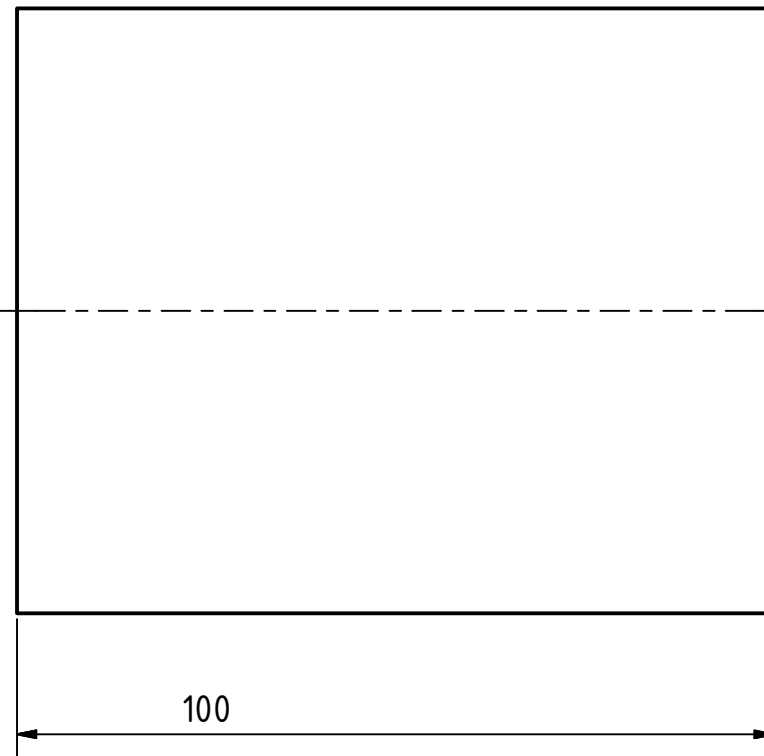
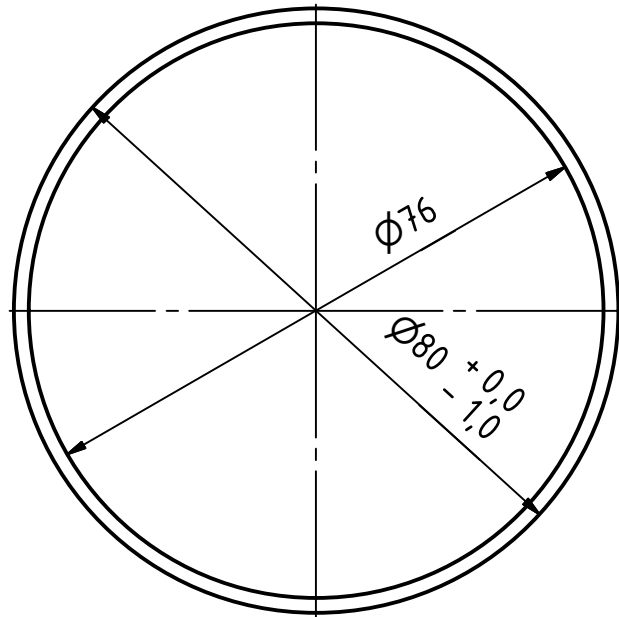




DESIGNED BY T. Schmid	MATERIAL 1.4301	MASS 0,248 kg	SCALE 1:1	DATE 24.11.2015	DIN ISO 2768 f
 			flange		
			FL000400	SHEET SIZE A4	SHEET 1 / 1

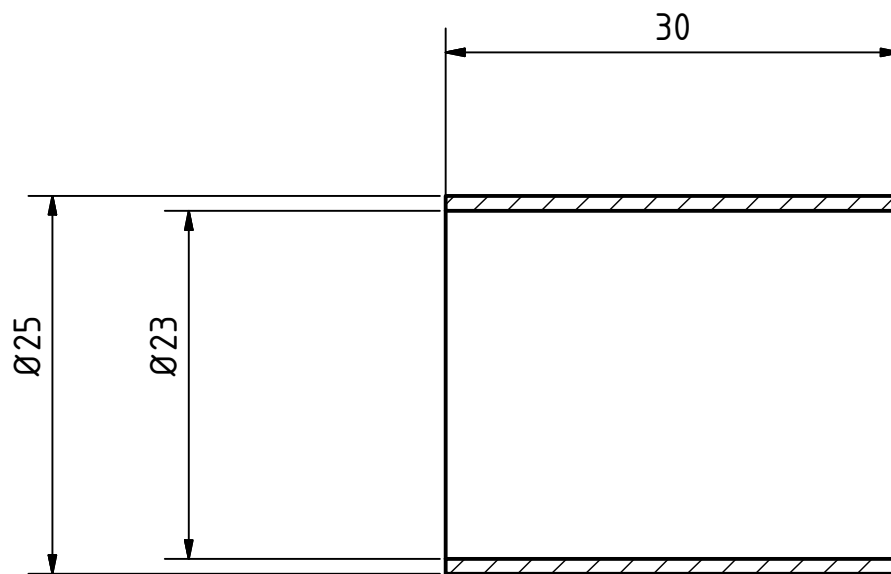


$t=6$



DESIGNED BY T. Schmid	MATERIAL 1.4301	MASS 0,491 kg	SCALE 1:1	DATE 25.11.2015	DIN ISO 2768 f
 			blind flange		
			FL000500	SHEET SIZE A4	SHEET 1 / 1



DESIGNED BY T. Schmid	MATERIAL 1.4301	MASS 0,396 kg	SCALE 1:1	DATE 24.11.2015	DIN ISO 2768 f
 		tube			
TB000100			SHEET SIZE A4	SHEET 1 / 1	



t=2

DESIGNED BY T. Schmid	MATERIAL 1.4301	MASS 0,018 kg	SCALE 2:1	DATE 24.11.2015	DIN ISO 2768 f
 			tube		
TB000200				SHEET SIZE A4	SHEET 1 / 1

Appendix C

C.1 Calculation of settling behaviour of particles in an air counter flow

Table 12: Calculation data sheet for calculating settling velocity v_s [m/s] numerically by using Microsoft Excel solver, dependent on particle diameter d_p [μm], drag coefficient C_d and Reynolds number Re .

$v_{s, guess}$ [m/s]	$v_{s, calc}$ [m/s]	residuals, squared	d_p [μm]	C_d	Re
1.56E-01	1.56E-01	1.74E-13	5.00E+01	5.10E+01	5.32E-01
2.17E-01	2.17E-01	6.04E-14	6.00E+01	3.17E+01	8.88E-01
2.85E-01	2.85E-01	2.76E-14	7.00E+01	2.15E+01	1.36E+00
3.58E-01	3.58E-01	2.24E-13	8.00E+01	1.56E+01	1.95E+00
4.35E-01	4.35E-01	8.14E-14	9.00E+01	1.19E+01	2.67E+00
5.16E-01	5.16E-01	1.07E-12	1.00E+02	9.37E+00	3.51E+00
6.00E-01	6.00E-01	1.24E-13	1.10E+02	7.63E+00	4.49E+00
6.85E-01	6.85E-01	1.65E-13	1.20E+02	6.38E+00	5.59E+00
7.72E-01	7.72E-01	2.48E-13	1.30E+02	5.45E+00	6.83E+00
8.60E-01	8.60E-01	2.96E-13	1.40E+02	4.73E+00	8.19E+00
9.48E-01	9.48E-01	3.38E-13	1.50E+02	4.17E+00	9.68E+00
1.04E+00	1.04E+00	4.62E-13	1.60E+02	3.72E+00	1.13E+01
1.12E+00	1.12E+00	5.64E-13	1.70E+02	3.35E+00	1.30E+01
1.21E+00	1.21E+00	6.18E-13	1.80E+02	3.05E+00	1.49E+01
1.30E+00	1.30E+00	7.74E-13	1.90E+02	2.80E+00	1.68E+01
1.39E+00	1.39E+00	8.52E-13	2.00E+02	2.59E+00	1.89E+01
1.47E+00	1.47E+00	9.88E-13	2.10E+02	2.41E+00	2.11E+01
1.56E+00	1.56E+00	1.12E-12	2.20E+02	2.25E+00	2.34E+01
1.65E+00	1.65E+00	1.43E-12	2.30E+02	2.12E+00	2.58E+01
1.73E+00	1.73E+00	1.19E-12	2.40E+02	2.00E+00	2.82E+01
1.81E+00	1.81E+00	1.42E-12	2.50E+02	1.90E+00	3.08E+01
1.89E+00	1.89E+00	1.81E-12	2.60E+02	1.81E+00	3.35E+01
1.98E+00	1.98E+00	1.97E-12	2.70E+02	1.72E+00	3.63E+01
2.06E+00	2.06E+00	2.24E-12	2.80E+02	1.65E+00	3.92E+01
2.14E+00	2.14E+00	2.39E-12	2.90E+02	1.59E+00	4.22E+01
2.22E+00	2.22E+00	2.26E-12	3.00E+02	1.53E+00	4.52E+01
2.29E+00	2.29E+00	2.83E-12	3.10E+02	1.47E+00	4.84E+01
2.37E+00	2.37E+00	3.07E-12	3.20E+02	1.42E+00	5.16E+01
2.45E+00	2.45E+00	3.28E-12	3.30E+02	1.38E+00	5.49E+01
2.52E+00	2.52E+00	3.54E-12	3.40E+02	1.34E+00	5.83E+01
2.59E+00	2.59E+00	3.81E-12	3.50E+02	1.30E+00	6.18E+01
2.67E+00	2.67E+00	4.08E-12	3.60E+02	1.26E+00	6.54E+01
2.74E+00	2.74E+00	4.25E-12	3.70E+02	1.23E+00	6.90E+01
2.81E+00	2.81E+00	4.63E-12	3.80E+02	1.20E+00	7.27E+01
2.88E+00	2.88E+00	4.87E-12	3.90E+02	1.17E+00	7.65E+01
2.95E+00	2.95E+00	5.35E-12	4.00E+02	1.14E+00	8.04E+01
3.02E+00	3.02E+00	5.49E-12	4.10E+02	1.12E+00	8.43E+01
3.09E+00	3.09E+00	5.84E-12	4.20E+02	1.10E+00	8.83E+01

3.16E+00	3.16E+00	6.03E-12	4.30E+02	1.08E+00	9.24E+01
3.22E+00	3.22E+00	6.17E-12	4.40E+02	1.06E+00	9.66E+01
3.29E+00	3.29E+00	6.78E-12	4.50E+02	1.04E+00	1.01E+02
3.36E+00	3.36E+00	7.06E-12	4.60E+02	1.02E+00	1.05E+02
3.42E+00	3.42E+00	7.42E-12	4.70E+02	1.00E+00	1.09E+02
3.49E+00	3.49E+00	7.79E-12	4.80E+02	9.86E-01	1.14E+02
3.55E+00	3.55E+00	8.08E-12	4.90E+02	9.70E-01	1.18E+02
3.61E+00	3.61E+00	8.42E-12	5.00E+02	9.56E-01	1.23E+02
sum of residuals		2.29E-11			

Table 13: Calculation data sheet for calculating the equivalent diameter d_{eq} [μm] of a particle in a counter flow by using Microsoft Excel solver, dependent on counter flow gas velocity v_g [m/s], drag coefficient C_d and Reynolds number.

$d_{eq, guess}$ [μm]	$d_{eq, calc}$ [μm]	residuals, squared	v_g [m/s]	C_d	Re
3.91E+01	3.91E+01	3.82E-08	1.00E-01	9.83E+01	2.66E-01
5.70E+01	5.70E+01	2.68E-08	2.00E-01	3.59E+01	7.76E-01
7.18E+01	7.18E+01	1.07E-07	3.00E-01	2.01E+01	1.47E+00
8.51E+01	8.51E+01	1.17E-07	4.00E-01	1.34E+01	2.32E+00
9.76E+01	9.76E+01	2.34E-08	5.00E-01	9.82E+00	3.32E+00
1.10E+02	1.10E+02	1.04E-07	6.00E-01	7.66E+00	4.47E+00
1.21E+02	1.21E+02	4.24E-08	7.00E-01	6.22E+00	5.77E+00
1.33E+02	1.33E+02	2.93E-08	8.00E-01	5.21E+00	7.22E+00
1.44E+02	1.44E+02	1.56E-10	9.00E-01	4.47E+00	8.82E+00
1.55E+02	1.55E+02	7.62E-08	1.00E+00	3.90E+00	1.06E+01
1.66E+02	1.66E+02	1.98E-07	1.10E+00	3.46E+00	1.25E+01
1.78E+02	1.78E+02	9.40E-08	1.20E+00	3.10E+00	1.45E+01
1.89E+02	1.89E+02	7.83E-08	1.30E+00	2.81E+00	1.67E+01
2.00E+02	2.00E+02	1.15E-08	1.40E+00	2.57E+00	1.91E+01
2.12E+02	2.12E+02	2.04E-09	1.50E+00	2.37E+00	2.16E+01
2.24E+02	2.24E+02	1.59E-07	1.60E+00	2.20E+00	2.43E+01
2.35E+02	2.35E+02	9.20E-09	1.70E+00	2.05E+00	2.72E+01
2.47E+02	2.47E+02	1.35E-08	1.80E+00	1.92E+00	3.03E+01
2.59E+02	2.59E+02	2.10E-07	1.90E+00	1.81E+00	3.35E+01
2.72E+02	2.72E+02	6.85E-08	2.00E+00	1.71E+00	3.70E+01
2.84E+02	2.84E+02	1.84E-07	2.10E+00	1.62E+00	4.06E+01
2.96E+02	2.96E+02	9.19E-10	2.20E+00	1.54E+00	4.44E+01
3.09E+02	3.09E+02	1.00E-07	2.30E+00	1.47E+00	4.84E+01
3.22E+02	3.22E+02	5.01E-07	2.40E+00	1.41E+00	5.26E+01
3.35E+02	3.35E+02	5.51E-08	2.50E+00	1.35E+00	5.71E+01
3.49E+02	3.49E+02	2.79E-07	2.60E+00	1.30E+00	6.17E+01
3.62E+02	3.62E+02	1.07E-08	2.70E+00	1.25E+00	6.66E+01
3.76E+02	3.76E+02	1.13E-07	2.80E+00	1.21E+00	7.17E+01
3.90E+02	3.90E+02	1.50E-07	2.90E+00	1.17E+00	7.70E+01
4.05E+02	4.05E+02	5.27E-07	3.00E+00	1.13E+00	8.26E+01
4.19E+02	4.19E+02	1.50E-07	3.10E+00	1.10E+00	8.84E+01

4.34E+02	4.34E+02	1.40E-07	3.20E+00	1.07E+00	9.45E+01
4.49E+02	4.49E+02	2.31E-07	3.30E+00	1.04E+00	1.01E+02
4.64E+02	4.64E+02	2.11E-07	3.40E+00	1.01E+00	1.07E+02
4.79E+02	4.79E+02	7.17E-08	3.50E+00	9.84E-01	1.14E+02
4.95E+02	4.95E+02	1.64E-08	3.60E+00	9.61E-01	1.21E+02
5.11E+02	5.11E+02	6.56E-10	3.70E+00	9.39E-01	1.29E+02
5.27E+02	5.27E+02	5.12E-12	3.80E+00	9.19E-01	1.36E+02
5.44E+02	5.44E+02	4.84E-13	3.90E+00	8.99E-01	1.44E+02
5.60E+02	5.60E+02	2.14E-14	4.00E+00	8.81E-01	1.53E+02
sum of residuals		4.15E-06			

C.2 Calculation of saltation velocity

Table 14: Calculation of saltation velocity for a solids mass flow $\dot{m}_p = 0,054$ [kg/s], a hydraulic pipe diameter $D_T = 0,0355$ [m] and a cross section of $A = 0,001456$ [m²] with air as gaseous phase, referring to the correlation of Rizk [45].

d_p [μm]	d	x	μ_{Ws} [kg/kg]	Fr_s	μ_{Fr} [kg/kg]	U_{salt} [m/s]	$(\mu_{Ws} - \mu_{Fr})^2$
1.00E+02	2.10E+00	2.61E+00	4.57E+00	1.15E+01	4.57E+00	6.76E+00	4,09E-08
1.20E+02	2.13E+00	2.63E+00	4.56E+00	1.15E+01	4.55E+00	6.78E+00	1,25E-07
1.40E+02	2.16E+00	2.65E+00	4.54E+00	1.15E+01	4.54E+00	6.81E+00	2,10E-07
1.60E+02	2.19E+00	2.68E+00	4.52E+00	1.16E+01	4.52E+00	6.83E+00	2,75E-07
1.80E+02	2.22E+00	2.70E+00	4.51E+00	1.16E+01	4.51E+00	6.85E+00	3,12E-07
2.00E+02	2.25E+00	2.72E+00	4.49E+00	1.17E+01	4.49E+00	6.88E+00	3,22E-07
2.20E+02	2.28E+00	2.74E+00	4.48E+00	1.17E+01	4.48E+00	6.90E+00	3,09E-07
2.40E+02	2.31E+00	2.76E+00	4.46E+00	1.17E+01	4.46E+00	6.92E+00	2,81E-07
2.60E+02	2.33E+00	2.79E+00	4.45E+00	1.18E+01	4.45E+00	6.94E+00	2,46E-07
2.80E+02	2.36E+00	2.81E+00	4.44E+00	1.18E+01	4.44E+00	6.97E+00	2,09E-07
3.00E+02	2.39E+00	2.83E+00	4.42E+00	1.18E+01	4.42E+00	6.99E+00	1,75E-07
3.20E+02	2.42E+00	2.85E+00	4.41E+00	1.19E+01	4.41E+00	7.01E+00	1,47E-07
3.40E+02	2.45E+00	2.87E+00	4.40E+00	1.19E+01	4.39E+00	7.03E+00	1,27E-07
3.60E+02	2.48E+00	2.90E+00	4.38E+00	1.19E+01	4.38E+00	7.05E+00	1,15E-07
3.80E+02	2.51E+00	2.92E+00	4.37E+00	1.20E+01	4.37E+00	7.07E+00	1,13E-07
4.00E+02	2.54E+00	2.94E+00	4.36E+00	1.20E+01	4.36E+00	7.10E+00	1,22E-07

4.20E+02	2.56E+00	2.96E+00	4.34E+00	1.21E+01	4.34E+00	7.12E+00	1,43E-07
4.40E+02	2.59E+00	2.98E+00	4.33E+00	1.21E+01	4.33E+00	7.14E+00	1,82E-07
4.60E+02	2.62E+00	3.01E+00	4.32E+00	1.21E+01	4.32E+00	7.16E+00	2,42E-07
4.80E+02	2.65E+00	3.03E+00	4.31E+00	1.22E+01	4.31E+00	7.18E+00	3,33E-07
5.00E+02	2.68E+00	3.05E+00	4.29E+00	1.22E+01	4.29E+00	7.20E+00	4,63E-07
1.00E+03	3.40E+00	3.60E+00	4.04E+00	1.30E+01	4.04E+00	7.65E+00	2,09E-08
2.00E+03	4.84E+00	4.70E+00	3.70E+00	1.41E+01	3.70E+00	8.35E+00	2,30E-06
3.00E+03	6.28E+00	5.80E+00	3.49E+00	1.50E+01	3.49E+00	8.86E+00	9,22E-07
5.00E+03	9.16E+00	8.00E+00	3.24E+00	1.62E+01	3.24E+00	9.55E+00	4,19E-07
1.00E+04	1.64E+01	1.35E+01	2.97E+00	1.77E+01	2.96E+00	1.04E+01	7,57E-06
sum of residuals							1.57E-05

Table 15: Calculation of saltation velocity for a solids mass flow $\dot{m}_p = 0,054$ [kg/s], a hydraulic pipe diameter $D_T = 0,0355$ [m] and a cross section of $A = 0,001456$ [m²] with air as gaseous phase, referring to the correlation of Matsumoto.

d_p [μm]	d_p [m]	d_p^* [m]	$d_p - d_p^*$ [m]	Fr_p	Fr_{ss}	$U_{g,ss}$ [m/s]	μ_s [kg/kg]	μ_s [kg/kg]	$\mu_s (W_s)$ [kg/kg]	residuals squared
1.00E+02	1.00E-04	1.63E-04	-6.32E-05	1.65E+01	8.42E+00	4.97E+00		6.22E+00	6.22E+00	1,08E-09
1.20E+02	1.20E-04	1.63E-04	-4.32E-05	2.00E+01	7.99E+00	4.72E+00		6.55E+00	6.55E+00	9,27E-10
1.40E+02	1.40E-04	1.63E-04	-2.32E-05	2.32E+01	7.64E+00	4.51E+00		6.85E+00	6.85E+00	1,78E-09
1.60E+02	1.60E-04	1.63E-04	-3.22E-06	2.62E+01	7.36E+00	4.34E+00		7.12E+00	7.12E+00	7,13E-10
1.80E+02	1.80E-04	1.63E-04	1.68E-05	2.89E+01	7.04E+00	4.16E+00	7.44E+00	7.06E+00	7.44E+00	2,75E-10
2.00E+02	2.00E-04	1.63E-04	3.68E-05	3.13E+01	7.52E+00	4.44E+00	6.96E+00		6.96E+00	1,24E-09
2.20E+02	2.20E-04	1.63E-04	5.68E-05	3.36E+01	7.95E+00	4.69E+00	6.59E+00		6.59E+00	9,34E-10

2.40E+02	2.40E-04	1.63E-04	7.68E-05	3.56E+01	8.34E+00	4.92E+00	6.28E+00	6.28E+00	1,27E-09
2.60E+02	2.60E-04	1.63E-04	9.68E-05	3.75E+01	8.69E+00	5.13E+00	6.03E+00	6.03E+00	7,26E-10
2.80E+02	2.80E-04	1.63E-04	1.17E-04	3.92E+01	9.01E+00	5.32E+00	5.81E+00	5.81E+00	5,50E-10
3.00E+02	3.00E-04	1.63E-04	1.37E-04	4.08E+01	9.30E+00	5.49E+00	5.63E+00	5.63E+00	6,57E-10
3.20E+02	3.20E-04	1.63E-04	1.57E-04	4.23E+01	9.57E+00	5.65E+00	5.47E+00	5.47E+00	6,24E-10
3.40E+02	3.40E-04	1.63E-04	1.77E-04	4.36E+01	9.81E+00	5.79E+00	5.34E+00	5.34E+00	4,74E-10
3.60E+02	3.60E-04	1.63E-04	1.97E-04	4.49E+01	1.00E+01	5.92E+00	5.22E+00	5.22E+00	3,94E-10
3.80E+02	3.80E-04	1.63E-04	2.17E-04	4.61E+01	1.02E+01	6.05E+00	5.11E+00	5.11E+00	4,32E-10
4.00E+02	4.00E-04	1.63E-04	2.37E-04	4.71E+01	1.04E+01	6.16E+00	5.02E+00	5.02E+00	5,36E-10
4.20E+02	4.20E-04	1.63E-04	2.57E-04	4.81E+01	1.06E+01	6.27E+00	4.93E+00	4.93E+00	6,14E-10
4.40E+02	4.40E-04	1.63E-04	2.77E-04	4.91E+01	1.08E+01	6.36E+00	4.86E+00	4.86E+00	5,94E-10
4.60E+02	4.60E-04	1.63E-04	2.97E-04	5.00E+01	1.09E+01	6.46E+00	4.79E+00	4.79E+00	5,07E-10
4.80E+02	4.80E-04	1.63E-04	3.17E-04	5.08E+01	1.11E+01	6.54E+00	4.73E+00	4.73E+00	4,67E-10
5.00E+02	5.00E-04	1.63E-04	3.37E-04	5.16E+01	1.12E+01	6.62E+00	4.67E+00	4.67E+00	6,52E-10
sum of residuals									1.54E-08

C.3 Calculation of penetration depth of particles into crossflow channel

Table 16: Calculation of penetration depth y [m] for different initial velocities and for different particle diameters d_p .

$u_{p0,1}$ [m/s]	$u_{p0,2}$ [m/s]	$u_{p0,3}$ [m/s]	w_{St} [m/s]	d_p [μm]	α	$F(\alpha)$	τ_v [s]	$y_{max,1}$ [m]	$y_{max,2}$ [m]	$y_{max,3}$ [m]
5.00E+00	6.00E+00	7.00E+00	4.22E-01	5.00E+01	1.08E+00	6.26E-01	1.82E-02	5.69E-02	6.83E-02	7.97E-02
5.00E+00	6.00E+00	7.00E+00	6.33E-01	7.50E+01	1.42E+00	5.66E-01	4.09E-02	1.16E-01	1.39E-01	1.62E-01
5.00E+00	6.00E+00	7.00E+00	8.44E-01	1.00E+02	1.72E+00	5.22E-01	7.27E-02	1.90E-01	2.28E-01	2.65E-01
5.00E+00	6.00E+00	7.00E+00	1.06E+00	1.25E+02	2.00E+00	4.87E-01	1.14E-01	2.77E-01	3.32E-01	3.87E-01
5.00E+00	6.00E+00	7.00E+00	1.27E+00	1.50E+02	2.25E+00	4.59E-01	1.64E-01	3.76E-01	4.51E-01	5.26E-01
5.00E+00	6.00E+00	7.00E+00	1.48E+00	1.75E+02	2.50E+00	4.36E-01	2.23E-01	4.86E-01	5.83E-01	6.80E-01
5.00E+00	6.00E+00	7.00E+00	1.69E+00	2.00E+02	2.73E+00	4.16E-01	2.91E-01	6.05E-01	7.26E-01	8.47E-01
5.00E+00	6.00E+00	7.00E+00	1.90E+00	2.25E+02	2.95E+00	3.99E-01	3.68E-01	7.34E-01	8.81E-01	1.03E+00
5.00E+00	6.00E+00	7.00E+00	2.11E+00	2.50E+02	3.17E+00	3.84E-01	4.54E-01	8.72E-01	1.05E+00	1.22E+00
5.00E+00	6.00E+00	7.00E+00	2.32E+00	2.75E+02	3.38E+00	3.70E-01	5.50E-01	1.02E+00	1.22E+00	1.42E+00
5.00E+00	6.00E+00	7.00E+00	2.53E+00	3.00E+02	3.58E+00	3.58E-01	6.54E-01	1.17E+00	1.40E+00	1.64E+00
5.00E+00	6.00E+00	7.00E+00	2.74E+00	3.25E+02	3.77E+00	3.47E-01	7.68E-01	1.33E+00	1.60E+00	1.86E+00
5.00E+00	6.00E+00	7.00E+00	2.96E+00	3.50E+02	3.96E+00	3.37E-01	8.91E-01	1.50E+00	1.80E+00	2.10E+00
5.00E+00	6.00E+00	7.00E+00	3.17E+00	3.75E+02	4.15E+00	3.27E-01	1.02E+00	1.67E+00	2.01E+00	2.34E+00
5.00E+00	6.00E+00	7.00E+00	3.38E+00	4.00E+02	4.33E+00	3.19E-01	1.16E+00	1.85E+00	2.23E+00	2.60E+00

C.4 Calculation of relaxation length in conveying pipe

Table 17: Calculation of relaxation length x_e [m] dependent on superficial gas velocity $U_g = 5$ [m/s], initial particle velocities $U_{p,0}$ (pre accelerated particles) for a step size of $(U_{p,0,calc,i} - U_{p,calc,i-1}) = 0,1$ [m/s]; the relaxation length from a certain $U_{p,0}$ to a certain percentage of U_g is calculated as the sum of relaxation lengths over the respective steps.

U_g [m/s]	U_p [m/s]	$U_{p,0,calc}$ [m/s]	x_e [m]	τ_p [s]	Re	$\phi(Re)$	U_p/U_g [%]	Σx_e	Σx_e	Σx_e	Σx_e
								$U_{p,0}=0$ [m]	$U_{p,0}=2$ [m/s] [m]	$U_{p,0}=3$ [m/s] [m]	$U_{p,0}=4$ [m/s] [m]
5.00E+00	0.00E+00	0.00E+00	0.00E+00	0.00E+00							
5.00E+00	1.00E-01	0.00E+00	1.63E-04	1.61E-01	9.33E+01	4.38E+00	2.00E+00	1.63E-04			
5.00E+00	2.00E-01	1.00E-01	5.05E-04	1.63E-01	9.14E+01	4.34E+00	4.00E+00	6.68E-04			
5.00E+00	3.00E-01	2.00E-01	8.68E-04	1.65E-01	8.95E+01	4.29E+00	6.00E+00	1.54E-03			
5.00E+00	4.00E-01	3.00E-01	1.25E-03	1.67E-01	8.76E+01	4.24E+00	8.00E+00	2.79E-03			
5.00E+00	5.00E-01	4.00E-01	1.67E-03	1.69E-01	8.58E+01	4.19E+00	1.00E+01	4.46E-03			
5.00E+00	6.00E-01	5.00E-01	2.11E-03	1.71E-01	8.39E+01	4.15E+00	1.20E+01	6.57E-03			
5.00E+00	7.00E-01	6.00E-01	2.58E-03	1.73E-01	8.20E+01	4.10E+00	1.40E+01	9.15E-03			
5.00E+00	8.00E-01	7.00E-01	3.08E-03	1.75E-01	8.01E+01	4.05E+00	1.60E+01	1.22E-02			
5.00E+00	9.00E-01	8.00E-01	3.62E-03	1.77E-01	7.82E+01	4.00E+00	1.80E+01	1.59E-02			
5.00E+00	1.00E+00	9.00E-01	4.20E-03	1.79E-01	7.63E+01	3.95E+00	2.00E+01	2.01E-02			
5.00E+00	1.10E+00	1.00E+00	4.82E-03	1.81E-01	7.45E+01	3.90E+00	2.20E+01	2.49E-02			
5.00E+00	1.20E+00	1.10E+00	5.49E-03	1.84E-01	7.26E+01	3.85E+00	2.40E+01	3.04E-02			
5.00E+00	1.30E+00	1.20E+00	6.21E-03	1.86E-01	7.07E+01	3.80E+00	2.60E+01	3.66E-02			
5.00E+00	1.40E+00	1.30E+00	6.98E-03	1.89E-01	6.88E+01	3.74E+00	2.80E+01	4.36E-02			

5.00E+00	1.50E+00	1.40E+00	7.82E-03	1.91E-01	6.69E+01	3.69E+00	3.00E+01	5.14E-02		
5.00E+00	1.60E+00	1.50E+00	8.72E-03	1.94E-01	6.50E+01	3.64E+00	3.20E+01	6.01E-02		
5.00E+00	1.70E+00	1.60E+00	9.71E-03	1.97E-01	6.31E+01	3.59E+00	3.40E+01	6.98E-02		
5.00E+00	1.80E+00	1.70E+00	1.08E-02	2.00E-01	6.13E+01	3.53E+00	3.60E+01	8.06E-02		
5.00E+00	1.90E+00	1.80E+00	1.19E-02	2.03E-01	5.94E+01	3.48E+00	3.80E+01	9.25E-02		
5.00E+00	2.00E+00	1.90E+00	1.32E-02	2.06E-01	5.75E+01	3.43E+00	4.00E+01	1.06E-01		
5.00E+00	2.10E+00	2.00E+00	1.46E-02	2.10E-01	5.56E+01	3.37E+00	4.20E+01	1.20E-01	1.46E-02	
5.00E+00	2.20E+00	2.10E+00	1.61E-02	2.13E-01	5.37E+01	3.32E+00	4.40E+01	1.36E-01	3.07E-02	
5.00E+00	2.30E+00	2.20E+00	1.77E-02	2.17E-01	5.18E+01	3.26E+00	4.60E+01	1.54E-01	4.84E-02	
5.00E+00	2.40E+00	2.30E+00	1.96E-02	2.21E-01	4.99E+01	3.20E+00	4.80E+01	1.74E-01	6.80E-02	
5.00E+00	2.50E+00	2.40E+00	2.16E-02	2.25E-01	4.81E+01	3.15E+00	5.00E+01	1.95E-01	8.96E-02	
5.00E+00	2.60E+00	2.50E+00	2.38E-02	2.29E-01	4.62E+01	3.09E+00	5.20E+01	2.19E-01	1.13E-01	
5.00E+00	2.70E+00	2.60E+00	2.63E-02	2.33E-01	4.43E+01	3.03E+00	5.40E+01	2.45E-01	1.40E-01	
5.00E+00	2.80E+00	2.70E+00	2.91E-02	2.38E-01	4.24E+01	2.97E+00	5.60E+01	2.75E-01	1.69E-01	
5.00E+00	2.90E+00	2.80E+00	3.22E-02	2.43E-01	4.05E+01	2.91E+00	5.80E+01	3.07E-01	2.01E-01	
5.00E+00	3.00E+00	2.90E+00	3.57E-02	2.48E-01	3.86E+01	2.85E+00	6.00E+01	3.43E-01	2.37E-01	
5.00E+00	3.10E+00	3.00E+00	3.97E-02	2.54E-01	3.68E+01	2.78E+00	6.20E+01	3.82E-01	2.77E-01	3.97E-02
5.00E+00	3.20E+00	3.10E+00	4.42E-02	2.60E-01	3.49E+01	2.72E+00	6.40E+01	4.26E-01	3.21E-01	8.40E-02
5.00E+00	3.30E+00	3.20E+00	4.94E-02	2.66E-01	3.30E+01	2.66E+00	6.60E+01	4.76E-01	3.70E-01	1.33E-01
5.00E+00	3.40E+00	3.30E+00	5.54E-02	2.73E-01	3.11E+01	2.59E+00	6.80E+01	5.31E-01	4.26E-01	1.89E-01
5.00E+00	3.50E+00	3.40E+00	6.24E-02	2.80E-01	2.92E+01	2.52E+00	7.00E+01	5.94E-01	4.88E-01	2.51E-01
5.00E+00	3.60E+00	3.50E+00	7.05E-02	2.88E-01	2.73E+01	2.46E+00	7.20E+01	6.64E-01	5.59E-01	3.22E-01

5.00E+00	3.70E+00	3.60E+00	8.01E-02	2.96E-01	2.54E+01	2.39E+00	7.40E+01	7.44E-01	6.39E-01	4.02E-01	
5.00E+00	3.80E+00	3.70E+00	9.17E-02	3.05E-01	2.36E+01	2.31E+00	7.60E+01	8.36E-01	7.30E-01	4.94E-01	
5.00E+00	3.90E+00	3.80E+00	1.06E-01	3.15E-01	2.17E+01	2.24E+00	7.80E+01	9.42E-01	8.36E-01	5.99E-01	
5.00E+00	4.00E+00	3.90E+00	1.23E-01	3.26E-01	1.98E+01	2.17E+00	8.00E+01	1.06E+00	9.59E-01	7.22E-01	
5.00E+00	4.10E+00	4.00E+00	1.44E-01	3.38E-01	1.79E+01	2.09E+00	8.20E+01	1.21E+00	1.10E+00	8.66E-01	1.44E-01
5.00E+00	4.20E+00	4.10E+00	1.72E-01	3.52E-01	1.60E+01	2.01E+00	8.40E+01	1.38E+00	1.28E+00	1.04E+00	3.16E-01
5.00E+00	4.30E+00	4.20E+00	2.08E-01	3.67E-01	1.41E+01	1.93E+00	8.60E+01	1.59E+00	1.48E+00	1.25E+00	5.25E-01
5.00E+00	4.40E+00	4.30E+00	2.58E-01	3.84E-01	1.23E+01	1.84E+00	8.80E+01	1.85E+00	1.74E+00	1.50E+00	7.83E-01
5.00E+00	4.50E+00	4.40E+00	3.28E-01	4.04E-01	1.04E+01	1.75E+00	9.00E+01	2.18E+00	2.07E+00	1.83E+00	1.11E+00
5.00E+00	4.60E+00	4.50E+00	4.35E-01	4.28E-01	8.48E+00	1.65E+00	9.20E+01	2.61E+00	2.50E+00	2.27E+00	1.55E+00
5.00E+00	4.70E+00	4.60E+00	6.11E-01	4.57E-01	6.60E+00	1.55E+00	9.40E+01	3.22E+00	3.12E+00	2.88E+00	2.16E+00
5.00E+00	4.80E+00	4.70E+00	9.49E-01	4.93E-01	4.71E+00	1.44E+00	9.60E+01	4.17E+00	4.06E+00	3.83E+00	3.11E+00
5.00E+00	4.90E+00	4.80E+00	1.82E+00	5.41E-01	2.83E+00	1.31E+00	9.80E+01	5.99E+00	5.89E+00	5.65E+00	4.93E+00

Table 18: Calculation of relaxation length x_e [m] dependent on superficial gas velocity $U_g = 6$ [m/s], initial particle velocities $U_{p,0}$ (pre accelerated particles) for a step size of $(U_{p,0,calc,i} - U_{p,calc,i-1}) = 0,1$ [m/s]; the relaxation length from a certain $U_{p,0}$ to a certain percentage of U_g is calculated as the sum of relaxation lengths over the respective steps.

U_g [m/s]	U_p [m/s]	$U_{p,0,calc}$ [m/s]	x_e [m]	τ_p [s]	Re	$\varphi(Re)$	U_p/U_g [%]	Σx_e					
								$U_{p,0}=0$ [m]	$U_{p,0}=2$ [m/s] [m]	$U_{p,0}=3$ [m/s] [m]	$U_{p,0}=4$ [m/s] [m]		
6.00E+00	0.00E+00	0.00E+00	0.00E+00	0.00E+00									
6.00E+00	1.00E-01	0.00E+00	1.23E-04	1.46E-01	1.12E+02	4.84E+00	1.67E+00	1.23E-04					
6.00E+00	2.00E-01	1.00E-01	3.78E-04	1.47E-01	1.10E+02	4.80E+00	3.33E+00	5.01E-04					
6.00E+00	3.00E-01	2.00E-01	6.47E-04	1.49E-01	1.08E+02	4.75E+00	5.00E+00	1.15E-03					
6.00E+00	4.00E-01	3.00E-01	9.31E-04	1.50E-01	1.06E+02	4.71E+00	6.67E+00	2.08E-03					
6.00E+00	5.00E-01	4.00E-01	1.23E-03	1.52E-01	1.05E+02	4.66E+00	8.33E+00	3.31E-03					
6.00E+00	6.00E-01	5.00E-01	1.55E-03	1.53E-01	1.03E+02	4.61E+00	1.00E+01	4.86E-03					
6.00E+00	7.00E-01	6.00E-01	1.88E-03	1.55E-01	1.01E+02	4.57E+00	1.17E+01	6.74E-03					
6.00E+00	8.00E-01	7.00E-01	2.23E-03	1.56E-01	9.90E+01	4.52E+00	1.33E+01	8.97E-03					
6.00E+00	9.00E-01	8.00E-01	2.61E-03	1.58E-01	9.71E+01	4.48E+00	1.50E+01	1.16E-02					
6.00E+00	1.00E+00	9.00E-01	3.00E-03	1.60E-01	9.52E+01	4.43E+00	1.67E+01	1.46E-02					
6.00E+00	1.10E+00	1.00E+00	3.42E-03	1.61E-01	9.33E+01	4.38E+00	1.83E+01	1.80E-02					
6.00E+00	1.20E+00	1.10E+00	3.87E-03	1.63E-01	9.14E+01	4.34E+00	2.00E+01	2.19E-02					
6.00E+00	1.30E+00	1.20E+00	4.34E-03	1.65E-01	8.95E+01	4.29E+00	2.17E+01	2.62E-02					
6.00E+00	1.40E+00	1.30E+00	4.84E-03	1.67E-01	8.76E+01	4.24E+00	2.33E+01	3.10E-02					
6.00E+00	1.50E+00	1.40E+00	5.37E-03	1.69E-01	8.58E+01	4.19E+00	2.50E+01	3.64E-02					
6.00E+00	1.60E+00	1.50E+00	5.94E-03	1.71E-01	8.39E+01	4.15E+00	2.67E+01	4.24E-02					

6.00E+00	1.70E+00	1.60E+00	6.55E-03	1.73E-01	8.20E+01	4.10E+00	2.83E+01	4.89E-02		
6.00E+00	1.80E+00	1.70E+00	7.19E-03	1.75E-01	8.01E+01	4.05E+00	3.00E+01	5.61E-02		
6.00E+00	1.90E+00	1.80E+00	7.88E-03	1.77E-01	7.82E+01	4.00E+00	3.17E+01	6.40E-02		
6.00E+00	2.00E+00	1.90E+00	8.62E-03	1.79E-01	7.63E+01	3.95E+00	3.33E+01	7.26E-02		
6.00E+00	2.10E+00	2.00E+00	9.41E-03	1.81E-01	7.45E+01	3.90E+00	3.50E+01	8.20E-02	9.41E-03	
6.00E+00	2.20E+00	2.10E+00	1.03E-02	1.84E-01	7.26E+01	3.85E+00	3.67E+01	9.23E-02	1.97E-02	
6.00E+00	2.30E+00	2.20E+00	1.12E-02	1.86E-01	7.07E+01	3.80E+00	3.83E+01	1.03E-01	3.08E-02	
6.00E+00	2.40E+00	2.30E+00	1.22E-02	1.89E-01	6.88E+01	3.74E+00	4.00E+01	1.16E-01	4.30E-02	
6.00E+00	2.50E+00	2.40E+00	1.32E-02	1.91E-01	6.69E+01	3.69E+00	4.17E+01	1.29E-01	5.62E-02	
6.00E+00	2.60E+00	2.50E+00	1.44E-02	1.94E-01	6.50E+01	3.64E+00	4.33E+01	1.43E-01	7.06E-02	
6.00E+00	2.70E+00	2.60E+00	1.56E-02	1.97E-01	6.31E+01	3.59E+00	4.50E+01	1.59E-01	8.62E-02	
6.00E+00	2.80E+00	2.70E+00	1.69E-02	2.00E-01	6.13E+01	3.53E+00	4.67E+01	1.76E-01	1.03E-01	
6.00E+00	2.90E+00	2.80E+00	1.84E-02	2.03E-01	5.94E+01	3.48E+00	4.83E+01	1.94E-01	1.21E-01	
6.00E+00	3.00E+00	2.90E+00	2.00E-02	2.06E-01	5.75E+01	3.43E+00	5.00E+01	2.14E-01	1.41E-01	
6.00E+00	3.10E+00	3.00E+00	2.17E-02	2.10E-01	5.56E+01	3.37E+00	5.17E+01	2.36E-01	1.63E-01	2.17E-02
6.00E+00	3.20E+00	3.10E+00	2.36E-02	2.13E-01	5.37E+01	3.32E+00	5.33E+01	2.59E-01	1.87E-01	4.52E-02
6.00E+00	3.30E+00	3.20E+00	2.56E-02	2.17E-01	5.18E+01	3.26E+00	5.50E+01	2.85E-01	2.12E-01	7.09E-02
6.00E+00	3.40E+00	3.30E+00	2.79E-02	2.21E-01	4.99E+01	3.20E+00	5.67E+01	3.13E-01	2.40E-01	9.88E-02
6.00E+00	3.50E+00	3.40E+00	3.04E-02	2.25E-01	4.81E+01	3.15E+00	5.83E+01	3.43E-01	2.71E-01	1.29E-01
6.00E+00	3.60E+00	3.50E+00	3.32E-02	2.29E-01	4.62E+01	3.09E+00	6.00E+01	3.76E-01	3.04E-01	1.62E-01
6.00E+00	3.70E+00	3.60E+00	3.63E-02	2.33E-01	4.43E+01	3.03E+00	6.17E+01	4.13E-01	3.40E-01	1.99E-01
6.00E+00	3.80E+00	3.70E+00	3.97E-02	2.38E-01	4.24E+01	2.97E+00	6.33E+01	4.52E-01	3.80E-01	2.38E-01

6.00E+00	3.90E+00	3.80E+00	4.35E-02	2.43E-01	4.05E+01	2.91E+00	6.50E+01	4.96E-01	4.23E-01	2.82E-01	
6.00E+00	4.00E+00	3.90E+00	4.79E-02	2.48E-01	3.86E+01	2.85E+00	6.67E+01	5.44E-01	4.71E-01	3.30E-01	
6.00E+00	4.10E+00	4.00E+00	5.27E-02	2.54E-01	3.68E+01	2.78E+00	6.83E+01	5.96E-01	5.24E-01	3.82E-01	5.27E-02
6.00E+00	4.20E+00	4.10E+00	5.83E-02	2.60E-01	3.49E+01	2.72E+00	7.00E+01	6.55E-01	5.82E-01	4.41E-01	1.11E-01
6.00E+00	4.30E+00	4.20E+00	6.46E-02	2.66E-01	3.30E+01	2.66E+00	7.17E+01	7.19E-01	6.47E-01	5.05E-01	1.76E-01
6.00E+00	4.40E+00	4.30E+00	7.20E-02	2.73E-01	3.11E+01	2.59E+00	7.33E+01	7.91E-01	7.19E-01	5.77E-01	2.48E-01
6.00E+00	4.50E+00	4.40E+00	8.04E-02	2.80E-01	2.92E+01	2.52E+00	7.50E+01	8.72E-01	7.99E-01	6.58E-01	3.28E-01
6.00E+00	4.60E+00	4.50E+00	9.04E-02	2.88E-01	2.73E+01	2.46E+00	7.67E+01	9.62E-01	8.90E-01	7.48E-01	4.18E-01
6.00E+00	4.70E+00	4.60E+00	1.02E-01	2.96E-01	2.54E+01	2.39E+00	7.83E+01	1.06E+00	9.92E-01	8.50E-01	5.21E-01
6.00E+00	4.80E+00	4.70E+00	1.16E-01	3.05E-01	2.36E+01	2.31E+00	8.00E+01	1.18E+00	1.11E+00	9.66E-01	6.37E-01
6.00E+00	4.90E+00	4.80E+00	1.33E-01	3.15E-01	2.17E+01	2.24E+00	8.17E+01	1.31E+00	1.24E+00	1.10E+00	7.70E-01
6.00E+00	5.00E+00	4.90E+00	1.54E-01	3.26E-01	1.98E+01	2.17E+00	8.33E+01	1.47E+00	1.39E+00	1.25E+00	9.24E-01
6.00E+00	5.10E+00	5.00E+00	1.80E-01	3.38E-01	1.79E+01	2.09E+00	8.50E+01	1.65E+00	1.57E+00	1.43E+00	1.10E+00
6.00E+00	5.20E+00	5.10E+00	2.13E-01	3.52E-01	1.60E+01	2.01E+00	8.67E+01	1.86E+00	1.79E+00	1.65E+00	1.32E+00
6.00E+00	5.30E+00	5.20E+00	2.57E-01	3.67E-01	1.41E+01	1.93E+00	8.83E+01	2.12E+00	2.05E+00	1.90E+00	1.57E+00
6.00E+00	5.40E+00	5.30E+00	3.17E-01	3.84E-01	1.23E+01	1.84E+00	9.00E+01	2.44E+00	2.36E+00	2.22E+00	1.89E+00
6.00E+00	5.50E+00	5.40E+00	4.02E-01	4.04E-01	1.04E+01	1.75E+00	9.17E+01	2.84E+00	2.76E+00	2.62E+00	2.29E+00
6.00E+00	5.60E+00	5.50E+00	5.30E-01	4.28E-01	8.48E+00	1.65E+00	9.33E+01	3.37E+00	3.30E+00	3.15E+00	2.82E+00
6.00E+00	5.70E+00	5.60E+00	7.42E-01	4.57E-01	6.60E+00	1.55E+00	9.50E+01	4.11E+00	4.04E+00	3.90E+00	3.57E+00
6.00E+00	5.80E+00	5.70E+00	1.15E+00	4.93E-01	4.71E+00	1.44E+00	9.67E+01	5.26E+00	5.19E+00	5.04E+00	4.72E+00
6.00E+00	5.90E+00	5.80E+00	2.20E+00	5.41E-01	2.83E+00	1.31E+00	9.83E+01	7.46E+00	7.38E+00	7.24E+00	6.91E+00

Table 19: Calculation of relaxation length x_e [m] dependent on superficial gas velocity $U_g = 7$ [m/s], initial particle velocities $U_{p,0}$ (pre accelerated particles) for a step size of $(U_{p,0,calc,i} - U_{p,calc,i-1}) = 0,1$ [m/s]; the relaxation length from a certain $U_{p,0}$ to a certain percentage of U_g is calculated as the sum of relaxation lengths over the respective steps.

U_g [m/s]	U_p [m/s]	$U_{p,0,calc}$ [m/s]	x_e [m]	τ_p [s]	Re	$\varphi(Re)$	U_p/U_g [%]	Σx_e	Σx_e	Σx_e	Σx_e
								$U_{p,0}=0$ [m]	$U_{p,0}=2$ [m/s] [m]	$U_{p,0}=3$ [m/s] [m]	$U_{p,0}=4$ [m/s] [m]
7.00E+00	0.00E+00	0.00E+00	0.00E+00	0.00E+00							
7.00E+00	1.00E-01	0.00E+00	9.67E-05	1.34E-01	1.31E+02	5.27E+00	1.43E+00	9.67E-05			
7.00E+00	2.00E-01	1.00E-01	2.96E-04	1.35E-01	1.29E+02	5.23E+00	2.86E+00	3.93E-04			
7.00E+00	3.00E-01	2.00E-01	5.05E-04	1.36E-01	1.27E+02	5.19E+00	4.29E+00	8.98E-04			
7.00E+00	4.00E-01	3.00E-01	7.23E-04	1.37E-01	1.25E+02	5.14E+00	5.71E+00	1.62E-03			
7.00E+00	5.00E-01	4.00E-01	9.52E-04	1.39E-01	1.23E+02	5.10E+00	7.14E+00	2.57E-03			
7.00E+00	6.00E-01	5.00E-01	1.19E-03	1.40E-01	1.22E+02	5.06E+00	8.57E+00	3.77E-03			
7.00E+00	7.00E-01	6.00E-01	1.44E-03	1.41E-01	1.20E+02	5.02E+00	1.00E+01	5.21E-03			
7.00E+00	8.00E-01	7.00E-01	1.71E-03	1.42E-01	1.18E+02	4.97E+00	1.14E+01	6.91E-03			
7.00E+00	9.00E-01	8.00E-01	1.98E-03	1.43E-01	1.16E+02	4.93E+00	1.29E+01	8.90E-03			
7.00E+00	1.00E+00	9.00E-01	2.27E-03	1.45E-01	1.14E+02	4.88E+00	1.43E+01	1.12E-02			
7.00E+00	1.10E+00	1.00E+00	2.58E-03	1.46E-01	1.12E+02	4.84E+00	1.57E+01	1.37E-02			
7.00E+00	1.20E+00	1.10E+00	2.90E-03	1.47E-01	1.10E+02	4.80E+00	1.71E+01	1.66E-02			
7.00E+00	1.30E+00	1.20E+00	3.23E-03	1.49E-01	1.08E+02	4.75E+00	1.86E+01	1.99E-02			
7.00E+00	1.40E+00	1.30E+00	3.59E-03	1.50E-01	1.06E+02	4.71E+00	2.00E+01	2.35E-02			
7.00E+00	1.50E+00	1.40E+00	3.96E-03	1.52E-01	1.05E+02	4.66E+00	2.14E+01	2.74E-02			
7.00E+00	1.60E+00	1.50E+00	4.36E-03	1.53E-01	1.03E+02	4.61E+00	2.29E+01	3.18E-02			

7.00E+00	1.70E+00	1.60E+00	4.77E-03	1.55E-01	1.01E+02	4.57E+00	2.43E+01	3.66E-02		
7.00E+00	1.80E+00	1.70E+00	5.21E-03	1.56E-01	9.90E+01	4.52E+00	2.57E+01	4.18E-02		
7.00E+00	1.90E+00	1.80E+00	5.67E-03	1.58E-01	9.71E+01	4.48E+00	2.71E+01	4.74E-02		
7.00E+00	2.00E+00	1.90E+00	6.16E-03	1.60E-01	9.52E+01	4.43E+00	2.86E+01	5.36E-02		
7.00E+00	2.10E+00	2.00E+00	6.68E-03	1.61E-01	9.33E+01	4.38E+00	3.00E+01	6.03E-02	6.68E-03	
7.00E+00	2.20E+00	2.10E+00	7.23E-03	1.63E-01	9.14E+01	4.34E+00	3.14E+01	6.75E-02	1.39E-02	
7.00E+00	2.30E+00	2.20E+00	7.81E-03	1.65E-01	8.95E+01	4.29E+00	3.29E+01	7.53E-02	2.17E-02	
7.00E+00	2.40E+00	2.30E+00	8.42E-03	1.67E-01	8.76E+01	4.24E+00	3.43E+01	8.37E-02	3.01E-02	
7.00E+00	2.50E+00	2.40E+00	9.08E-03	1.69E-01	8.58E+01	4.19E+00	3.57E+01	9.28E-02	3.92E-02	
7.00E+00	2.60E+00	2.50E+00	9.77E-03	1.71E-01	8.39E+01	4.15E+00	3.71E+01	1.03E-01	4.90E-02	
7.00E+00	2.70E+00	2.60E+00	1.05E-02	1.73E-01	8.20E+01	4.10E+00	3.86E+01	1.13E-01	5.95E-02	
7.00E+00	2.80E+00	2.70E+00	1.13E-02	1.75E-01	8.01E+01	4.05E+00	4.00E+01	1.24E-01	7.08E-02	
7.00E+00	2.90E+00	2.80E+00	1.21E-02	1.77E-01	7.82E+01	4.00E+00	4.14E+01	1.37E-01	8.29E-02	
7.00E+00	3.00E+00	2.90E+00	1.30E-02	1.79E-01	7.63E+01	3.95E+00	4.29E+01	1.50E-01	9.60E-02	
7.00E+00	3.10E+00	3.00E+00	1.40E-02	1.81E-01	7.45E+01	3.90E+00	4.43E+01	1.64E-01	1.10E-01	1.40E-02
7.00E+00	3.20E+00	3.10E+00	1.50E-02	1.84E-01	7.26E+01	3.85E+00	4.57E+01	1.79E-01	1.25E-01	2.90E-02
7.00E+00	3.30E+00	3.20E+00	1.61E-02	1.86E-01	7.07E+01	3.80E+00	4.71E+01	1.95E-01	1.41E-01	4.52E-02
7.00E+00	3.40E+00	3.30E+00	1.73E-02	1.89E-01	6.88E+01	3.74E+00	4.86E+01	2.12E-01	1.58E-01	6.25E-02
7.00E+00	3.50E+00	3.40E+00	1.86E-02	1.91E-01	6.69E+01	3.69E+00	5.00E+01	2.31E-01	1.77E-01	8.11E-02
7.00E+00	3.60E+00	3.50E+00	2.00E-02	1.94E-01	6.50E+01	3.64E+00	5.14E+01	2.51E-01	1.97E-01	1.01E-01
7.00E+00	3.70E+00	3.60E+00	2.15E-02	1.97E-01	6.31E+01	3.59E+00	5.29E+01	2.72E-01	2.19E-01	1.23E-01
7.00E+00	3.80E+00	3.70E+00	2.31E-02	2.00E-01	6.13E+01	3.53E+00	5.43E+01	2.95E-01	2.42E-01	1.46E-01

7.00E+00	3.90E+00	3.80E+00	2.48E-02	2.03E-01	5.94E+01	3.48E+00	5.57E+01	3.20E-01	2.66E-01	1.70E-01	
7.00E+00	4.00E+00	3.90E+00	2.67E-02	2.06E-01	5.75E+01	3.43E+00	5.71E+01	3.47E-01	2.93E-01	1.97E-01	
7.00E+00	4.10E+00	4.00E+00	2.88E-02	2.10E-01	5.56E+01	3.37E+00	5.86E+01	3.76E-01	3.22E-01	2.26E-01	2.88E-02
7.00E+00	4.20E+00	4.10E+00	3.10E-02	2.13E-01	5.37E+01	3.32E+00	6.00E+01	4.07E-01	3.53E-01	2.57E-01	5.98E-02
7.00E+00	4.30E+00	4.20E+00	3.35E-02	2.17E-01	5.18E+01	3.26E+00	6.14E+01	4.40E-01	3.87E-01	2.91E-01	9.34E-02
7.00E+00	4.40E+00	4.30E+00	3.62E-02	2.21E-01	4.99E+01	3.20E+00	6.29E+01	4.76E-01	4.23E-01	3.27E-01	1.30E-01
7.00E+00	4.50E+00	4.40E+00	3.92E-02	2.25E-01	4.81E+01	3.15E+00	6.43E+01	5.16E-01	4.62E-01	3.66E-01	1.69E-01
7.00E+00	4.60E+00	4.50E+00	4.25E-02	2.29E-01	4.62E+01	3.09E+00	6.57E+01	5.58E-01	5.04E-01	4.09E-01	2.11E-01
7.00E+00	4.70E+00	4.60E+00	4.62E-02	2.33E-01	4.43E+01	3.03E+00	6.71E+01	6.04E-01	5.51E-01	4.55E-01	2.58E-01
7.00E+00	4.80E+00	4.70E+00	5.03E-02	2.38E-01	4.24E+01	2.97E+00	6.86E+01	6.55E-01	6.01E-01	5.05E-01	3.08E-01
7.00E+00	4.90E+00	4.80E+00	5.48E-02	2.43E-01	4.05E+01	2.91E+00	7.00E+01	7.09E-01	6.56E-01	5.60E-01	3.63E-01
7.00E+00	5.00E+00	4.90E+00	6.00E-02	2.48E-01	3.86E+01	2.85E+00	7.14E+01	7.69E-01	7.16E-01	6.20E-01	4.23E-01
7.00E+00	5.10E+00	5.00E+00	6.58E-02	2.54E-01	3.68E+01	2.78E+00	7.29E+01	8.35E-01	7.82E-01	6.86E-01	4.88E-01
7.00E+00	5.20E+00	5.10E+00	7.23E-02	2.60E-01	3.49E+01	2.72E+00	7.43E+01	9.07E-01	8.54E-01	7.58E-01	5.61E-01
7.00E+00	5.30E+00	5.20E+00	7.99E-02	2.66E-01	3.30E+01	2.66E+00	7.57E+01	9.87E-01	9.34E-01	8.38E-01	6.41E-01
7.00E+00	5.40E+00	5.30E+00	8.85E-02	2.73E-01	3.11E+01	2.59E+00	7.71E+01	1.08E+00	1.02E+00	9.26E-01	7.29E-01
7.00E+00	5.50E+00	5.40E+00	9.85E-02	2.80E-01	2.92E+01	2.52E+00	7.86E+01	1.17E+00	1.12E+00	1.02E+00	8.28E-01
7.00E+00	5.60E+00	5.50E+00	1.10E-01	2.88E-01	2.73E+01	2.46E+00	8.00E+01	1.28E+00	1.23E+00	1.13E+00	9.38E-01
7.00E+00	5.70E+00	5.60E+00	1.24E-01	2.96E-01	2.54E+01	2.39E+00	8.14E+01	1.41E+00	1.36E+00	1.26E+00	1.06E+00
7.00E+00	5.80E+00	5.70E+00	1.41E-01	3.05E-01	2.36E+01	2.31E+00	8.29E+01	1.55E+00	1.50E+00	1.40E+00	1.20E+00
7.00E+00	5.90E+00	5.80E+00	1.61E-01	3.15E-01	2.17E+01	2.24E+00	8.43E+01	1.71E+00	1.66E+00	1.56E+00	1.36E+00
7.00E+00	6.00E+00	5.90E+00	1.85E-01	3.26E-01	1.98E+01	2.17E+00	8.57E+01	1.89E+00	1.84E+00	1.75E+00	1.55E+00

7.00E+00	6.10E+00	6.00E+00	2.16E-01	3.38E-01	1.79E+01	2.09E+00	8.71E+01	2.11E+00	2.06E+00	1.96E+00	1.76E+00
7.00E+00	6.20E+00	6.10E+00	2.55E-01	3.52E-01	1.60E+01	2.01E+00	8.86E+01	2.37E+00	2.31E+00	2.22E+00	2.02E+00
7.00E+00	6.30E+00	6.20E+00	3.06E-01	3.67E-01	1.41E+01	1.93E+00	9.00E+01	2.67E+00	2.62E+00	2.52E+00	2.33E+00
7.00E+00	6.40E+00	6.30E+00	3.76E-01	3.84E-01	1.23E+01	1.84E+00	9.14E+01	3.05E+00	2.99E+00	2.90E+00	2.70E+00
7.00E+00	6.50E+00	6.40E+00	4.76E-01	4.04E-01	1.04E+01	1.75E+00	9.29E+01	3.52E+00	3.47E+00	3.37E+00	3.18E+00
7.00E+00	6.60E+00	6.50E+00	6.26E-01	4.28E-01	8.48E+00	1.65E+00	9.43E+01	4.15E+00	4.10E+00	4.00E+00	3.80E+00
7.00E+00	6.70E+00	6.60E+00	8.74E-01	4.57E-01	6.60E+00	1.55E+00	9.57E+01	5.02E+00	4.97E+00	4.87E+00	4.68E+00
7.00E+00	6.80E+00	6.70E+00	1.35E+00	4.93E-01	4.71E+00	1.44E+00	9.71E+01	6.37E+00	6.32E+00	6.22E+00	6.03E+00
7.00E+00	6.90E+00	6.80E+00	2.57E+00	5.41E-01	2.83E+00	1.31E+00	9.86E+01	8.94E+00	8.89E+00	8.79E+00	8.60E+00

C.5 Calculation of separation efficiency

Table 20: Calculation of separation efficiency $T(x)$ based on QICPIC results $Q_{3, Fi}(x)$ and $Q_{3, C}(x)$ dependent on given x_3 [μm] and basing on measured masses m_{Fi} of the fines and $m_{F, C}$ of the coarse particle fraction.

x_3 [μm]	$Q_{3, Fi}$ [%]	$\Delta Q_{3, Fi}(x)$	$q_{3, Fi}(x)$	$m_{Fi}(x)$	$Q_{3, C}$ [%]	$\Delta Q_{3, C}(x)$	$q_C(x)$	$q_F(x)$	$m_C(x)$	$m_{Fe}(x)$	$T(x)$
2.00E+01	0.00E+00	0.00E+00		0.00E+00	0.00E+00	0.00E+00		0.00E+00	0.00E+00	0.00E+00	0.00E+00
2.43E+01	2.00E-02	2.00E-02	4.66E-03	1.47E+00	0.00E+00	0.00E+00	0.00E+00	1.73E-03	0.00E+00	1.47E+00	0.00E+00
2.95E+01	3.00E-02	1.00E-02	1.92E-03	6.05E-01	0.00E+00	0.00E+00	0.00E+00	7.12E-04	0.00E+00	6.05E-01	0.00E+00
3.58E+01	6.00E-02	3.00E-02	4.73E-03	1.49E+00	0.00E+00	0.00E+00	0.00E+00	1.76E-03	0.00E+00	1.49E+00	0.00E+00
4.35E+01	1.40E-01	8.00E-02	1.04E-02	3.28E+00	1.00E-02	1.00E-02	1.30E-03	4.68E-03	6.95E-01	3.98E+00	1.75E-01
5.29E+01	2.80E-01	1.40E-01	1.50E-02	4.72E+00	1.00E-02	0.00E+00	0.00E+00	5.56E-03	0.00E+00	4.72E+00	0.00E+00
6.42E+01	5.90E-01	3.10E-01	2.73E-02	8.60E+00	2.00E-02	1.00E-02	8.81E-04	1.07E-02	4.70E-01	9.07E+00	5.18E-02
7.80E+01	1.09E+00	5.00E-01	3.63E-02	1.14E+01	4.00E-02	2.00E-02	1.45E-03	1.44E-02	7.76E-01	1.22E+01	6.35E-02
9.47E+01	1.86E+00	7.70E-01	4.60E-02	1.45E+01	7.00E-02	3.00E-02	1.79E-03	1.82E-02	9.57E-01	1.54E+01	6.20E-02
1.15E+02	3.74E+00	1.88E+00	9.25E-02	2.91E+01	1.10E-01	4.00E-02	1.97E-03	3.56E-02	1.05E+00	3.02E+01	3.48E-02
1.40E+02	8.98E+00	5.24E+00	2.12E-01	6.69E+01	2.40E-01	1.30E-01	5.27E-03	8.21E-02	2.81E+00	6.97E+01	4.04E-02
1.70E+02	2.08E+01	1.18E+01	3.93E-01	1.24E+02	8.70E-01	6.30E-01	2.10E-02	1.59E-01	1.12E+01	1.35E+02	8.31E-02
2.06E+02	4.08E+01	2.01E+01	5.51E-01	1.74E+02	4.42E+00	3.55E+00	9.75E-02	2.66E-01	5.21E+01	2.26E+02	2.31E-01
2.50E+02	7.02E+01	2.94E+01	6.64E-01	2.09E+02	2.40E+01	1.96E+01	4.43E-01	5.25E-01	2.37E+02	4.46E+02	5.31E-01
3.04E+02	9.28E+01	2.26E+01	4.21E-01	1.33E+02	6.33E+01	3.93E+01	7.32E-01	6.16E-01	3.91E+02	5.23E+02	7.47E-01
3.69E+02	9.91E+01	6.32E+00	9.69E-02	3.05E+01	8.77E+01	2.44E+01	3.73E-01	2.71E-01	1.99E+02	2.30E+02	8.67E-01
4.49E+02	9.99E+01	8.20E-01	1.03E-02	3.26E+00	9.66E+01	8.93E+00	1.13E-01	7.47E-02	6.02E+01	6.34E+01	9.49E-01
5.45E+02	1.00E+02	6.00E-02	6.23E-04	1.96E-01	9.93E+01	2.71E+00	2.82E-02	1.79E-02	1.50E+01	1.52E+01	9.87E-01
6.62E+02	1.00E+02	1.00E-02	8.55E-05	2.69E-02	9.99E+01	5.80E-01	4.96E-03	3.15E-03	2.65E+00	2.68E+00	9.90E-01
8.04E+02	1.00E+02	0.00E+00	0.00E+00	0.00E+00	1.00E+02	7.00E-02	4.93E-04	3.10E-04	2.63E-01	2.63E-01	1.00E+00
9.76E+02	1.00E+02	0.00E+00	0.00E+00	0.00E+00	1.00E+02	3.00E-02	1.74E-04	1.09E-04	9.29E-02	9.29E-02	1.00E+00
1.19E+03	1.00E+02	0.00E+00	0.00E+00		1.00E+02	0.00E+00	0.00E+00	0.00E+00			

C.6 Mass flow rate vs. brush speed – raw data

Table 21: Time averaged mass flow rate of feeder \dot{m} [g/s], rotational speed of brush n [rpm], circumferential speed of brush u_0 [m/s], current consumption of drive motor I [A], electrical power P [W] and estimated mechanical torque M [Nm] dependent on voltage signal of power supply tested with glass powder, sized between 100 to 200 [μm].

exp #	d_p [μm]	U [V]	I [A]	n [rpm]	n [1/s]	u_0 [m/s]	P [W]	M [Nm]	\dot{m} [g/s]
V1.1	100 - 200	5.90	3.2	95	1.58	0.60	18.88	11.92	52.3
V2.19	100 - 200	6.00	2.9	111	1.85	0.70	17.4	9.41	50.6
V1.2	100 - 200	7.00	3.25	160	2.67	1.01	22.75	8.53	51.4
V2.18	100 - 200	7.00	2.92	164	2.73	1.03	20.44	7.48	46
V2.17	100 - 200	8.00	2.9	242	4.03	1.52	23.2	5.75	38.9
V3.1	100 - 200	8.00	3.06	240	4.00	1.51	24.48	6.12	49.1
V5.1	100 - 200	8.00	2.9	258	4.30	1.62	23.2	5.40	49.2
V5.2	100 - 200	8.00	2.96	256	4.27	1.61	23.68	5.55	44.8
V5.3	100 - 200	8.00	2.96	256	4.27	1.61	23.68	5.55	41.7
V1.3	100 - 200	8.10	3.3	220	3.67	1.38	26.73	7.29	46.1
V1.4	100 - 200	9.00	3.35	270	4.50	1.70	30.15	6.70	43.1
V2.16	100 - 200	9.00	2.88	310	5.17	1.95	25.92	5.02	39.8
V3.2	100 - 200	9.90	3.2	345	5.75	2.17	31.68	5.51	39.7
V1.5	100 - 200	10.00	3.36	330	5.50	2.07	33.6	6.11	39.5
V2.15	100 - 200	10.00	2.87	375	6.25	2.36	28.7	4.59	32.7
V5.4	100 - 200	10.00	3.13	365	6.08	2.29	31.3	5.15	38.3
V5.5	100 - 200	10.00	3.11	366	6.10	2.30	31.1	5.10	35.1
V5.6	100 - 200	10.00	3.13	362	6.03	2.27	31.3	5.19	36.7
V5.7	100 - 200	10.00	3.15	354	5.90	2.22	31.5	5.34	39.1
V1.6	100 - 200	11.00	3.4	390	6.50	2.45	37.4	5.75	37
V2.14	100 - 200	11.00	2.9	443	7.38	2.78	31.9	4.32	30.2

V2.13	100 - 200	11.90	2.88	495	8.25	3.11	34.272	4.15	28.9
V1.7	100 - 200	12.00	3.45	450	7.50	2.83	41.4	5.52	33
V3.3	100 - 200	12.00	3.36	465	7.75	2.92	40.32	5.20	35
V5.8	100 - 200	12.00	3.28	465	7.75	2.92	39.36	5.08	36.1
V5.9	100 - 200	12.00	3.3	475	7.92	2.98	39.6	5.00	32.9
V5.10	100 - 200	12.00	3.3	478	7.97	3.00	39.6	4.97	32.5
V6.1	100 - 200	12.00	3.2	479	7.99	3.01	38.4	4.81	29
V2.12	100 - 200	12.90	2.9	560	9.33	3.52	37.41	4.01	27.5
V1.8	100 - 200	13.00	3.51	512	8.53	3.22	45.63	5.35	33.2
V2.11	100 - 200	13.90	2.93	630	10.50	3.96	40.727	3.88	24.6
V1.9	100 - 200	14.00	3.56	571	9.52	3.59	49.84	5.24	30.8
V3.4	100 - 200	14.00	3.5	578	9.63	3.63	49	5.09	26
V5.11	100 - 200	14.00	3.4	600	10.00	3.77	47.6	4.76	29.5
V5.12	100 - 200	14.00	3.42	602	10.03	3.78	47.88	4.77	29.5
V5.13	100 - 200	14.00	3.4	604	10.07	3.80	47.6	4.73	28.5
V5.14	100 - 200	14.00	3.45	603	10.05	3.79	48.3	4.81	27.8
V6.2	100 - 200	14.00	3.3	602	10.03	3.78	46.2	4.60	25
V1.10	100 - 200	15.00	3.55	644	10.73	4.05	53.25	4.96	28
V2.10	100 - 200	15.00	2.92	696	11.60	4.37	43.8	3.78	23.5
V1.11	100 - 200	15.90	3.5	700	11.67	4.40	55.65	4.77	25.6
V2.9	100 - 200	16.00	2.91	760	12.67	4.78	46.56	3.68	23.9
V3.5	100 - 200	16.00	3.6	695	11.58	4.37	57.6	4.97	25.3
V5.15	100 - 200	16.00	3.55	712	11.87	4.47	56.8	4.79	26.1
V5.16	100 - 200	16.00	3.56	714	11.90	4.49	56.96	4.79	25.6
V5.17	100 - 200	16.00	3.55	720	12.00	4.52	56.8	4.73	23.9

V5.18	100 - 200	16.00	3.51	722	12.03	4.54	56.16	4.67	24.6
V6.3	100 - 200	16.00	3.4	725	12.08	4.55	54.4	4.50	22.5
V1.12	100 - 200	17.00	3.48	766	12.77	4.81	59.16	4.63	25.3
V2.8	100 - 200	17.00	2.95	828	13.80	5.20	50.15	3.63	22.8
V1.13	100 - 200	18.00	3.43	837	13.95	5.26	61.74	4.43	23.9
V2.7	100 - 200	18.00	3.4	890	14.83	5.59	61.2	4.13	21.2
V3.6	100 - 200	18.00	3.6	835	13.92	5.25	64.8	4.66	22.6
V5.19	100 - 200	18.00	3.6	840	14.00	5.28	64.8	4.63	21.2
V5.20	100 - 200	18.00	3.58	841	14.02	5.28	64.44	4.60	22.5
V5.21	100 - 200	18.00	3.52	847	14.12	5.32	63.36	4.49	21
V5.22	100 - 200	18.00	3.45	854	14.23	5.37	62.1	4.36	20.8
V6.4	100 - 200	18.00	3.5	848	14.13	5.33	63	4.46	20.5
V1.14	100 - 200	19.00	3.45	906	15.10	5.69	65.55	4.34	22.2
V2.6	100 - 200	19.00	3.05	943	15.72	5.93	57.95	3.69	18.6
V1.15	100 - 200	20.00	3.48	970	16.17	6.09	69.6	4.31	20.7
V2.5	100 - 200	20.00	3.13	996	16.60	6.26	62.6	3.77	18.5
V3.7	100 - 200	20.00	3.6	962	16.03	6.04	72	4.49	20.2
V5.23	100 - 200	20.00	3.5	976	16.27	6.13	70	4.30	18.9
V5.24	100 - 200	20.00	3.5	980	16.33	6.16	70	4.29	20.2
V5.25	100 - 200	20.00	3.45	982	16.37	6.17	69	4.22	18.8
V5.26	100 - 200	20.00	3.42	988	16.47	6.21	68.4	4.15	20.1
V6.5	100 - 200	20.00	3.6	971	16.18	6.10	72	4.45	19.1
V1.16	100 - 200	21.00	3.6	1018	16.97	6.40	75.6	4.46	20
V2.4	100 - 200	21.00	3.17	1047	17.45	6.58	66.57	3.81	17.9
V1.17	100 - 200	22.00	3.7	1065	17.75	6.69	81.4	4.59	19.2

V2.3	100 - 200	22.00	3.25	1104	18.40	6.94	71.5	3.89	17.5
V3.8	100 - 200	22.00	3.8	1071	17.85	6.73	83.6	4.68	19.2
V5.27	100 - 200	22.00	3.8	1080	18.00	6.79	83.6	4.64	18
V5.28	100 - 200	22.00	3.78	1085	18.08	6.82	83.16	4.60	17.7
V5.29	100 - 200	22.00	3.7	1089	18.15	6.84	81.4	4.48	17.6
V5.30	100 - 200	22.00	3.65	1093	18.22	6.87	80.3	4.41	17.3
V6.6	100 - 200	22.00	3.9	1093	18.22	6.87	85.8	4.71	17.5
V1.18	100 - 200	23.00	3.55	1150	19.17	7.23	81.65	4.26	18.6
V2.2	100 - 200	23.00	3.43	1153	19.22	7.24	78.89	4.11	18
V1.19	100 - 200	24.00	3.5	1224	20.40	7.69	84	4.12	17.6
V2.1	100 - 200	24.00	3.5	1200	20.00	7.54	84	4.20	18.8
V3.9	100 - 200	24.00	3.7	1210	20.17	7.60	88.8	4.40	18.6
V5.31	100 - 200	24.00	3.8	1208	20.13	7.59	91.2	4.53	18.4
V5.32	100 - 200	24.00	3.7	1220	20.33	7.67	88.8	4.37	18.6
V5.33	100 - 200	24.00	3.6	1230	20.50	7.73	86.4	4.21	18.2
V5.34	100 - 200	24.00	3.5	1235	20.58	7.76	84	4.08	17.8
V6.7	100 - 200	24.00	4	1216	20.27	7.64	96	4.74	17

Table 22: Time averaged mass flow rate of feeder \dot{m} [g/s], rotational speed of brush n [rpm], circumferential speed of brush u_0 [m/s], current consumption of drive motor I [A], electrical power P [W] and estimated mechanical torque M [Nm] dependent on voltage signal of power for glass bead powder sized between 400 to 600 [μm].

exp #	d_p [μm]	U [V]	I [A]	n [rpm]	n [1/s]	u_0 [m/s]	P [W]	M [Nm]	\dot{m} [g/s]
V7.1	400 - 600	12.00	3.1	479	8.0	3.0	37	4.66	30.7
V8.1	400 - 600	12.00	3.2	479	8.0	3.0	38	4.81	31.9
V7.2	400 - 600	14.00	3.1	602	10.0	3.8	43	4.33	28.9
V8.2	400 - 600	14.00	3.3	602	10.0	3.8	46	4.60	29.1

V7.3	400 - 600	15.90	3.2	719	12.0	4.5	51	4.25	27.4
v8.3	400 - 600	16.00	3.4	725	12.1	4.6	54	4.50	27.5
V7.4	400 - 600	18.00	3.3	848	14.1	5.3	59	4.20	27.3
V8.4	400 - 600	18.00	3.6	848	14.1	5.3	65	4.59	26.5
V7.5	400 - 600	20.00	3.9	971	16.2	6.1	78	4.82	25
V8.5	400 - 600	20.00	3.7	971	16.2	6.1	74	4.57	25
v7.6	400 - 600	22.00	4	1093	18.2	6.9	88	4.83	23.3
V8.6	400 - 600	22.00	3.9	1093	18.2	6.9	86	4.71	23.5
V7.7	400 - 600	24.00	4.2	1216	20.3	7.6	101	4.97	24
V8.7	400 - 600	24.00	4	1216	20.3	7.6	96	4.74	24.4

Table 23: Time averaged mass flow rate of feeder \dot{m} [g/s], current consumption of drive motor I [A], electrical power P [W] dependent on voltage signal of power for glass bead powder sized between 400 to 600 [μm] and a brush guiding bar pinch of 4 [mm] each side.

exp #	U [V]	I [A]	d_p [μm]	P [W]	\dot{m} [g/s]
V10.1		12	3.2 400 - 600	38.4	23.5
V10.8		12	3.1 400 - 600	37.2	22.2
V10.2		14	3.2 400 - 600	44.8	22.8
V10.9		14	3.15 400 - 600	44.1	23.8
V10.3		16	3.3 400 - 600	52.8	21.9
V10.10		16	3.3 400 - 600	52.8	21.6
V10.4		18	3.45 400 - 600	62.1	19.9
V10.11		18	3.4 400 - 600	61.2	22.3
V10.5		20	3.6 400 - 600	72	19.6
V10.12		20	3.55 400 - 600	71	19.7
V10.6		22	3.9 400 - 600	85.8	18
V10.13		22	3.8 400 - 600	83.6	15.7
V10.7		24	4.3 400 - 600	103.2	18
V10.14		24	4.1 400 - 600	98.4	17.5

Table 24: Time averaged mass flow rate of feeder \dot{m} [g/s], current consumption of drive motor I [A], electrical power P [W] dependent on voltage signal of power for glass bead powder sized between 100 to 200 [μm] and a brush guiding bar pinch of 4 [mm] each side.

exp #	U [V]	I [A]	d_p [μm]	P [W]	\dot{m} [g/s]
V11.1	12	2.85	100 - 200	34.2	21.9
V11.8	12	2.84	100 - 200	34.08	17.4
V11.2	14	2.93	100 - 200	41.02	21
V11.9	14	2.92	100 - 200	40.88	17.8
V11.3	16	3.05	100 - 200	48.8	21.7
V11.10	16	3	100 - 200	48	16.5
V11.4	18	3.15	100 - 200	56.7	17.7
V11.11	18.1	3.1	100 - 200	56.11	16
V11.12	20	3.33	100 - 200	66.6	14
V11.5	20.1	3.35	100 - 200	67.335	14.8
V11.6	22	3.73	100 - 200	82.06	13.5
V11.13	22	3.7	100 - 200	81.4	13
V11.14	24	3.8	100 - 200	91.2	12.4
V11.7	24.1	3.95	100 - 200	95.195	13.5

Table 25: Time averaged mass flow rate of feeder \dot{m} [g/s], current consumption of drive motor I [A], electrical power P [W] dependent on voltage signal of power for glass bead powder sized between 100 to 200 [μm] and a brush guiding bar pinch of 5 [mm] each side.

exp #	U [V]	I [A]	d_p [μm]	P [W]	\dot{m} [g/s]
V12.1	12	3.2	100 - 200	38.4	17.5
V12.8	12	3.1	100 - 200	37.2	17.3
V12.2	14	3.2	100 - 200	44.8	17.3
V12.9	14.1	3.15	100 - 200	44.415	16.9
V12.3	16	3.3	100 - 200	52.8	16
V12.10	16	3.2	100 - 200	51.2	17.7
V12.4	18	3.4	100 - 200	61.2	16.3
V12.11	18	3.4	100 - 200	61.2	16.6
V12.5	20	3.45	100 - 200	69	15.5
V12.12	20	3.5	100 - 200	70	16.3
V12.6	22	3.75	100 - 200	82.5	15
V12.13	22	3.85	100 - 200	84.7	16
V12.14	24	4.15	100 - 200	99.6	15.3
V12.7	24.1	4	100 - 200	96.4	15

Table 26: Time averaged mass flow rate of feeder \dot{m} [g/s], current consumption of drive motor I [A], electrical power P [W] dependent on voltage signal of power for glass bead powder sized between 400 to 600 [μm] and a brush guiding bar pinch of 5 [mm] each side.

exp #	U [V]	I [A]	d_p [μm]	P [W]	\dot{m} [g/s]
V13.1	12	3	400 - 600	36	25.1
V13.8	12	3.15	400 - 600	37.8	28.1
V13.2	14	3.15	400 - 600	44.1	21.7
V13.9	14.1	3.15	400 - 600	44.415	25.3
V13.3	16	3.3	400 - 600	52.8	23
V13.10	16.1	3.3	400 - 600	53.13	25.5
V13.4	18	3.5	400 - 600	63	21.5
V13.11	18	3.42	400 - 600	61.56	24.3
V13.5	20	3.65	400 - 600	73	21.6
V13.12	20	3.55	400 - 600	71	21.8
V13.13	22	3.9	400 - 600	85.8	19.6
V13.6	22.1	3.95	400 - 600	87.295	20.8
V13.14	24	4.2	400 - 600	100.8	19.5
V13.7	24.1	4.25	400 - 600	102.425	20.3

Table 27: Time- and number averaged mass flow values $\dot{m}_{averaged}$ [g/s] including their number averaged standard deviations σ , absolute and in percent, and the corresponding number of experiments i in relation to the adjusted power supply voltage U [V] for glass powder sized between 100 to 200 [μm] and without using brush guiding bars.

U [V]	$\dot{m}_{averaged}$ [g/s]	σ [g/s]	σ [%]	i
8	45	3.73	8.3	6
10	37.3	2.43	6.5	7
12	32.5	2.53	7.8	7
14	27.7	2.14	7.7	8
16	24.7	1.12	4.5	8
18	21.7	1.09	5.0	8
20	19.6	0.77	3.9	8
22	18	0.72	4.0	8
24	18.1	0.41	2.3	8

Table 28: Time- and number averaged mass flow values $\dot{m}_{averaged}$ [g/s] including their number averaged standard deviations σ , absolute and in percent, and the corresponding number of experiments i in relation to the adjusted power supply voltage U [V] for glass powder sized between 400 to 600 [μm] and without using brush guiding bars.

U [V]	$\dot{m}_{averaged}$ [g/s]	σ [g/s]	σ [%]	i
12	31.3	0.6	1.9	2
14	29	0.1	0.3	2
16	27.5	0.05	0.2	2
18	26.9	0.4	1.5	2
20	25	0	0	2
22	23.4	0.1	0.4	2
24	24.2	0.2	0.8	2

Table 29: Time- and number averaged mass flow values $\dot{m}_{averaged}$ [g/s] including their number averaged standard deviations σ , absolute and in percent, and the corresponding number of experiments i in relation to the adjusted power supply voltage U [V] for glass powder sized between 400 to 600 [μm] and with using brush guiding bar pinch of 4 [mm].

U [V]	$\dot{m}_{averaged}$ [g/s]	σ [g/s]	σ [%]	i
12	22,9	0,65	2,8	2
14	23,3	0,5	2,1	2
16	21,8	0,15	0,7	2
18	21,1	1,2	5,7	2
20	19,7	0,05	0,3	2
22	16,9	1,15	6,8	2
24	17,8	0,25	1,4	2

Table 30: Time- and number averaged mass flow values $\dot{m}_{averaged}$ [g/s] including their number averaged standard deviations σ , absolute and in percent, and the corresponding number of experiments i in relation to the adjusted power supply voltage U [V] for glass powder sized between 100 to 200 [μm] and with an applied brush pinch of 4 [mm].

U [V]	$\dot{m}_{averaged}$ [g/s]	σ [g/s]	σ [%]	i
12	19,7	2,25	11,4	2
14	19,4	1,6	8,2	2
16	19,1	2,6	13,6	2
18	16,9	0,85	5,0	2
20	14,4	0,4	2,8	2
22	13,3	0,25	1,9	2
24	13	0,55	4,2	2

Table 31: Time- and number averaged mass flow values $\dot{m}_{averaged}$ [g/s] including their number averaged standard deviations σ , absolute and in percent, and the corresponding number of experiments i in relation to the adjusted power supply voltage U [V] for glass powder sized between 100 to 200 [μm] and with an applied brush pinch of 5 [mm].

U [V]	$\dot{m}_{averaged}$ [g/s]	σ [g/s]	σ [%]	i
12	17.4	0.1	0.6	2
14	17.1	0.2	1.2	2
16	16.9	0.85	5.0	2
18	16.5	0.15	0.9	2
20	15.9	0.4	2.5	2
22	15.5	0.5	3.2	2
24	15.2	0.15	1.0	2

Table 32: Time- and number averaged mass flow values $\dot{m}_{averaged}$ [g/s] including their number averaged standard deviations σ , absolute and in percent, and the corresponding number of experiments i in relation to the adjusted power supply voltage U [V] for glass powder sized between 400 to 600 [μm] and with an applied brush pinch of 5 [mm].

U [V]	$\dot{m}_{averaged}$ [g/s]	σ [g/s]	σ [%]	i
12	26.6	1.5	5.6	2
14	23.5	1.8	7.7	2
16	24.3	1.25	5.1	2
18	22.9	1.4	6.1	2
20	21.7	0.1	0.5	2
22	20.2	0.6	3.0	2
24	19.9	0.4	2.0	2

Appendix D

D.1 Mass flow diagrams

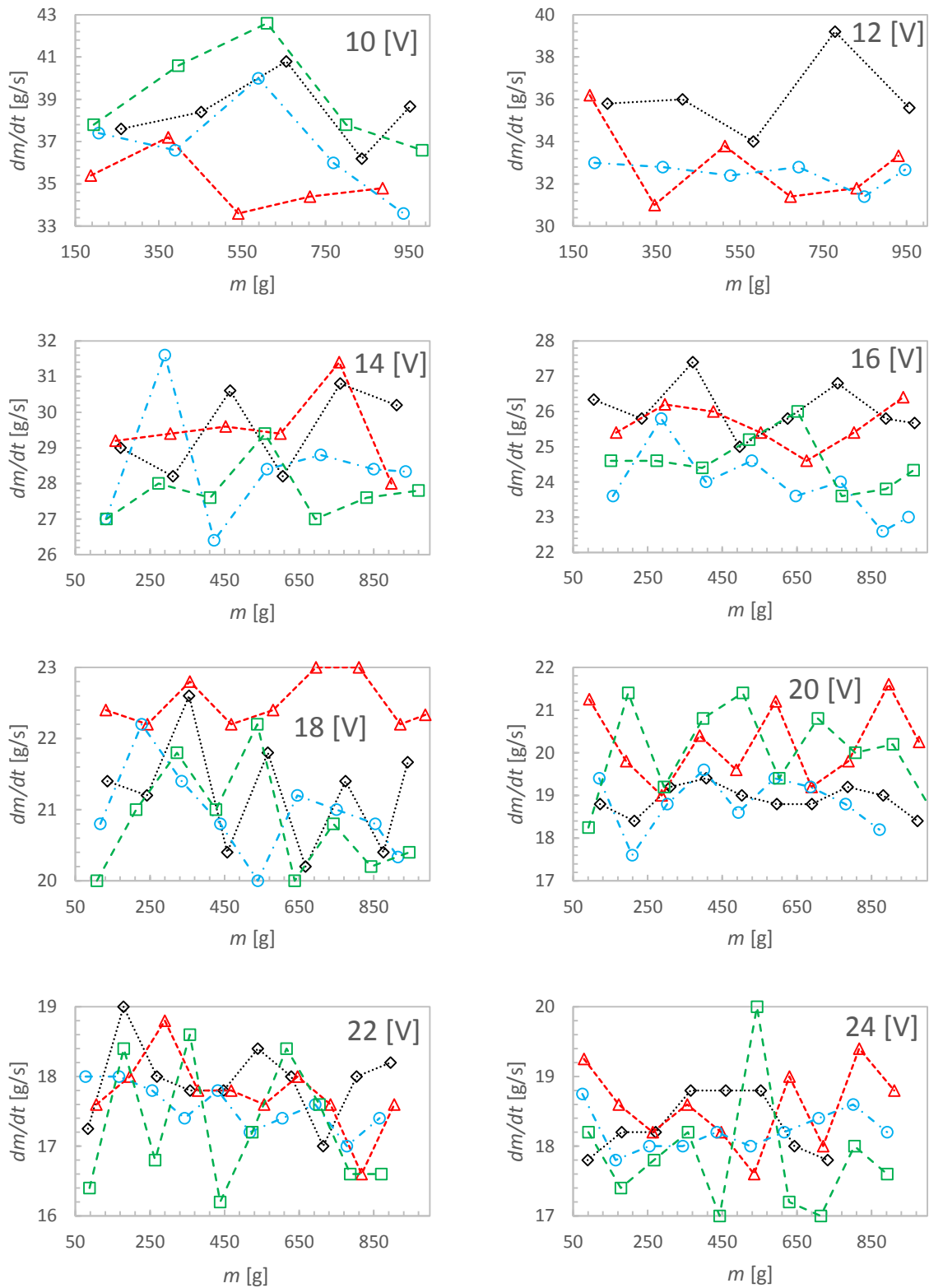


Figure A 1: Mass flow of particles \dot{m} [g/s] versus fed mass m [g] from the hopper. Symbols represent different experimental runs (glass bead diameter: 100 to 200 μm), without using brush guiding bars.

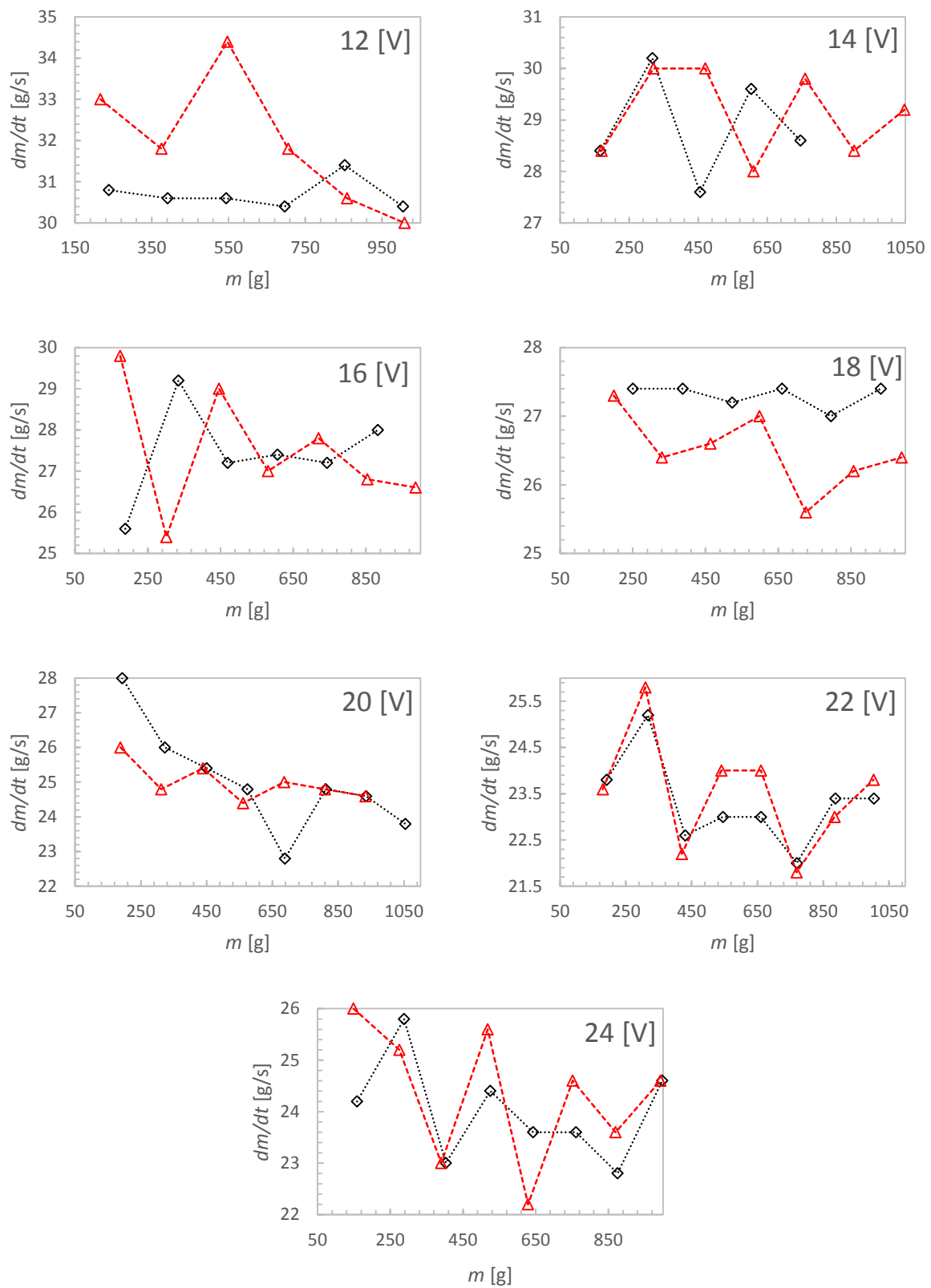


Figure A 2: Mass flow of particles \dot{m} [g/s] versus fed mass m [g] from the hopper. Symbols represent different experimental runs (glass bead diameter: 400 to 600 [μm], without using brush guiding bars).

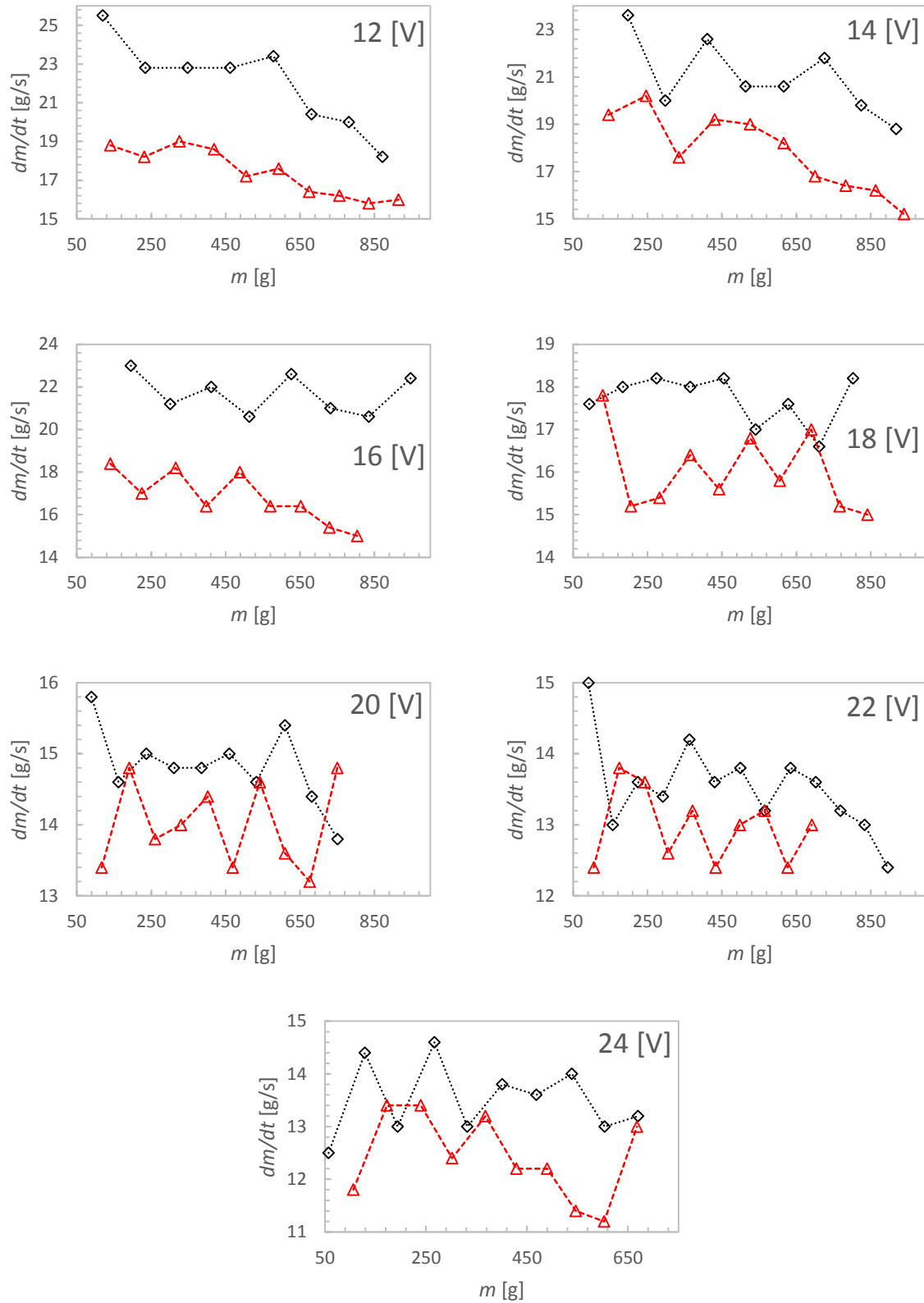


Figure A 3: Mass flow of particles \dot{m} [g/s] versus fed mass m [g] from the hopper. Symbols represent different experimental runs (glass bead diameter: 100 to 200 μm ; brush pinch: $\xi = 4$ [mm] each side).

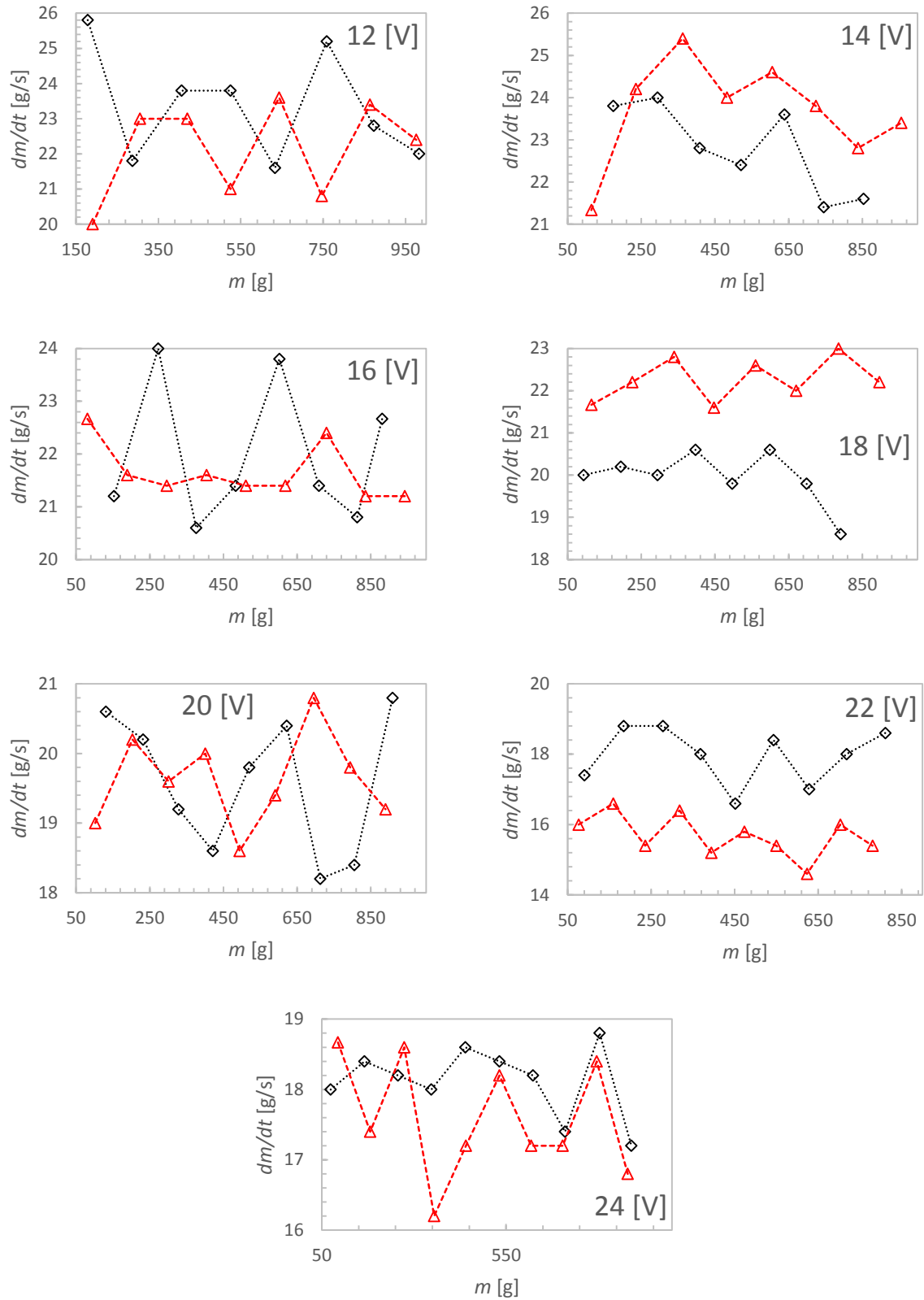


Figure A 4: Mass flow of particles \dot{m} [g/s] versus fed mass m [g] from the hopper. Symbols represent different experimental runs (glass bead diameter: 400 to 600 μm ; brush pinch: $\xi = 4$ [mm] each side).

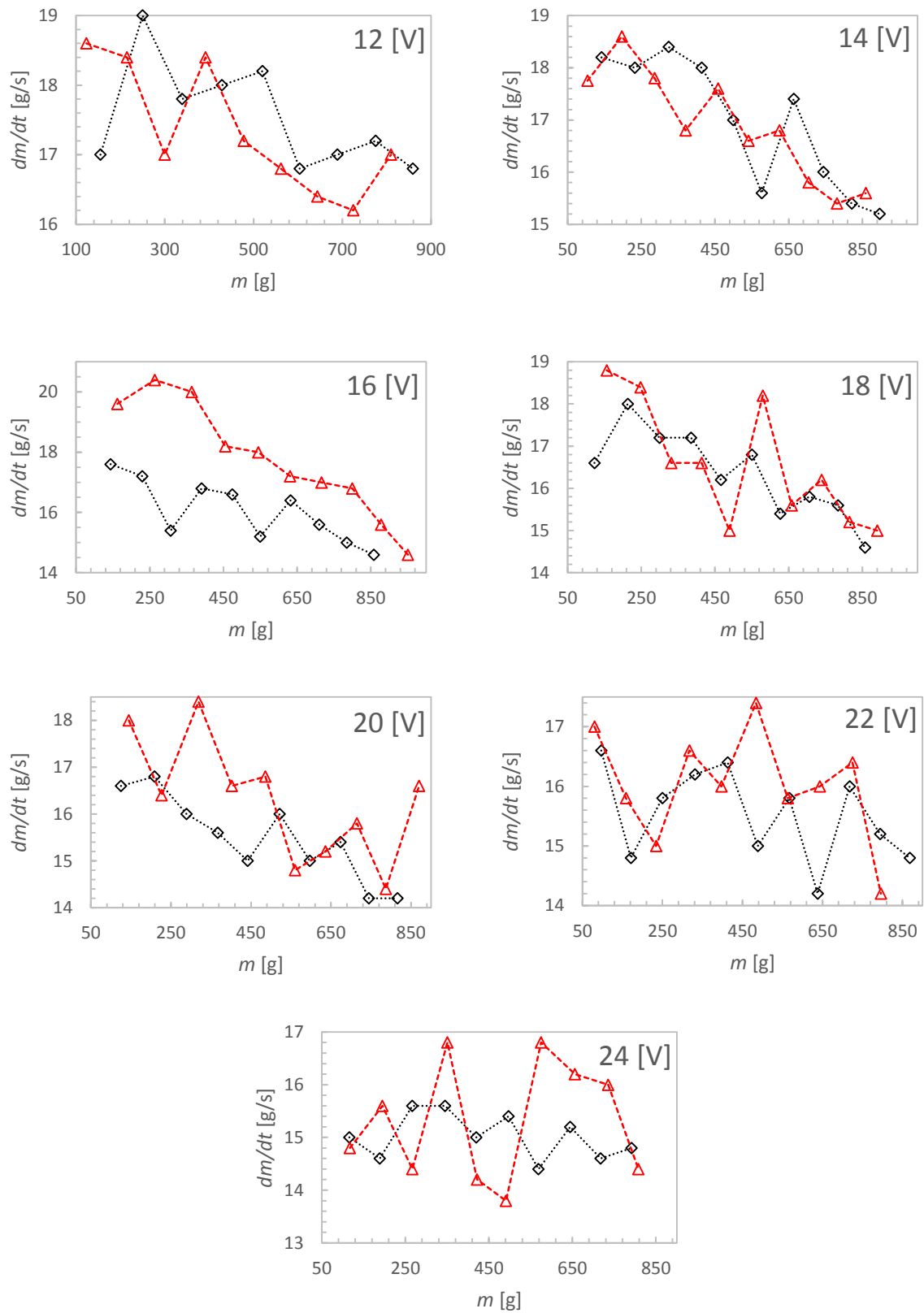


Figure A 5: Mass flow of particles \dot{m} [g/s] versus fed mass m [g] from the hopper. Symbols represent different experimental runs (glass bead diameter: 100 to 200 [μm] brush pinch: $\xi = 5$ [mm] each side).

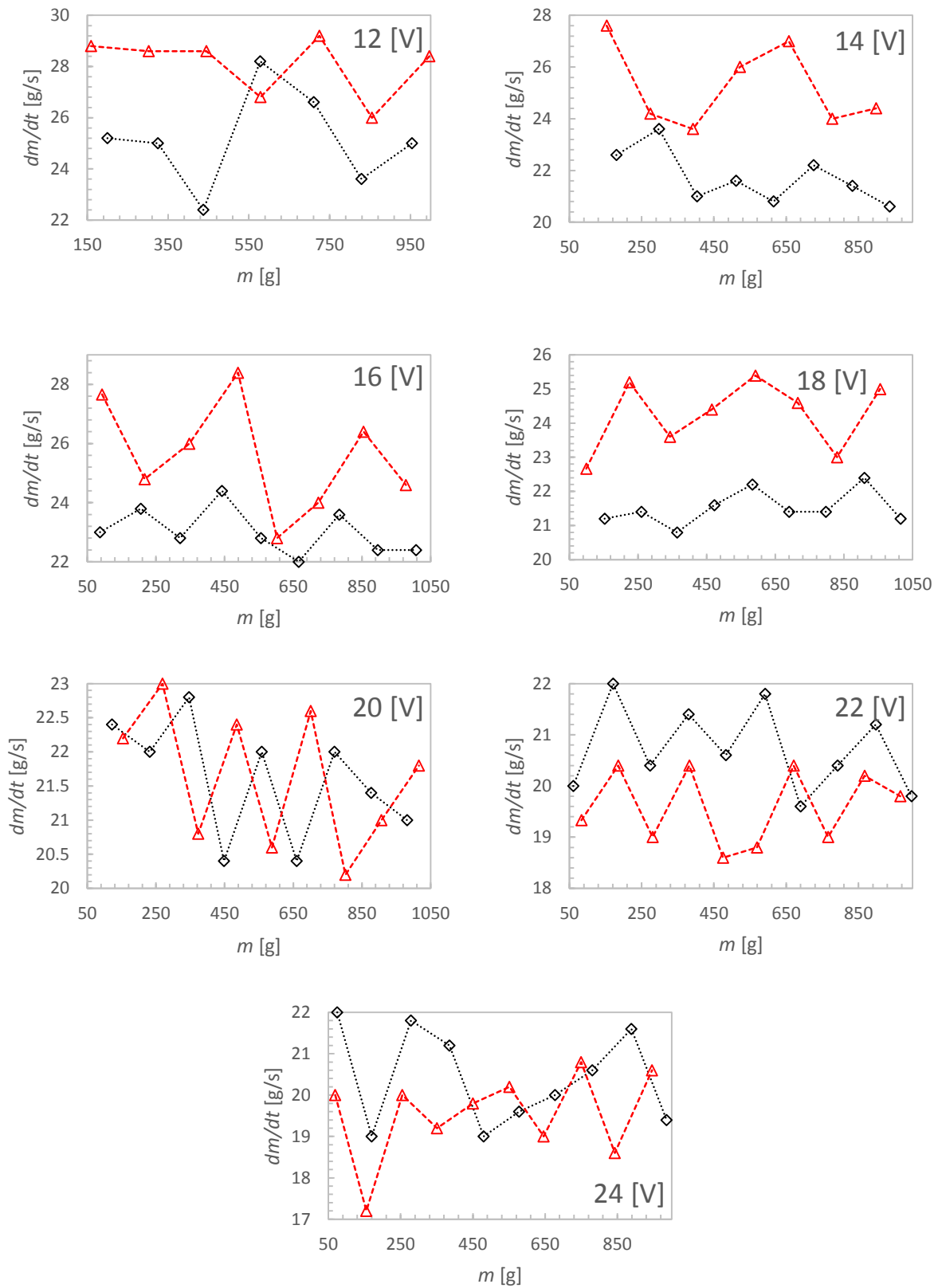


Figure A 6: Mass flow of particles \dot{m} [g/s] versus fed mass m [g] from the hopper. Symbols represent different experimental runs (glass bead diameter: 400 to 600 [μm] brush pinch: $\xi = 5$ [mm] each side).

Appendix E

E.1 Temporal velocity distributions measured by PIV

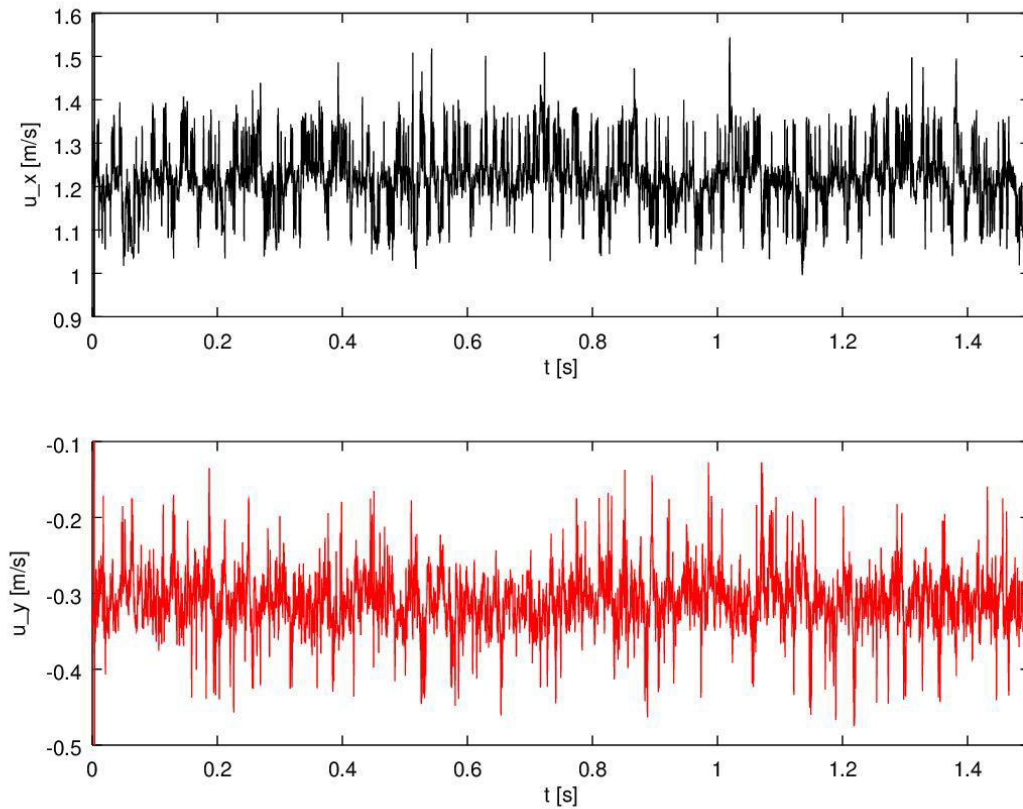


Figure A 7: Temporal velocity distributions in horizontal direction (u_x) and in vertical direction (u_y) for the 20th row and the 10th column of the residual matrices of experiment #1, i.e., for 3000 matrices generated for the observation time of 1.5 [s].

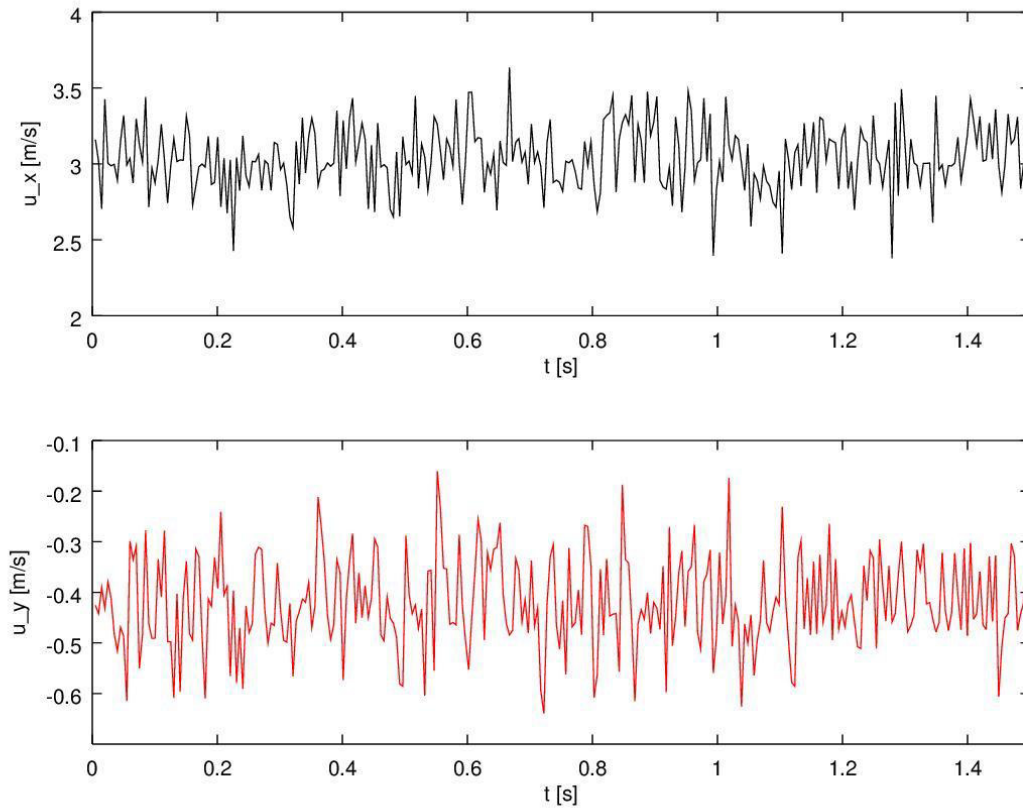


Figure A 8: Temporal velocity distributions in horizontal (x) direction (left panel) and in vertical (y) direction (right panel) for the 20th row and the 10th column of the residual matrices of experiment #2, i.e., for 300 matrices generated for the observation time of 1.5 [s].

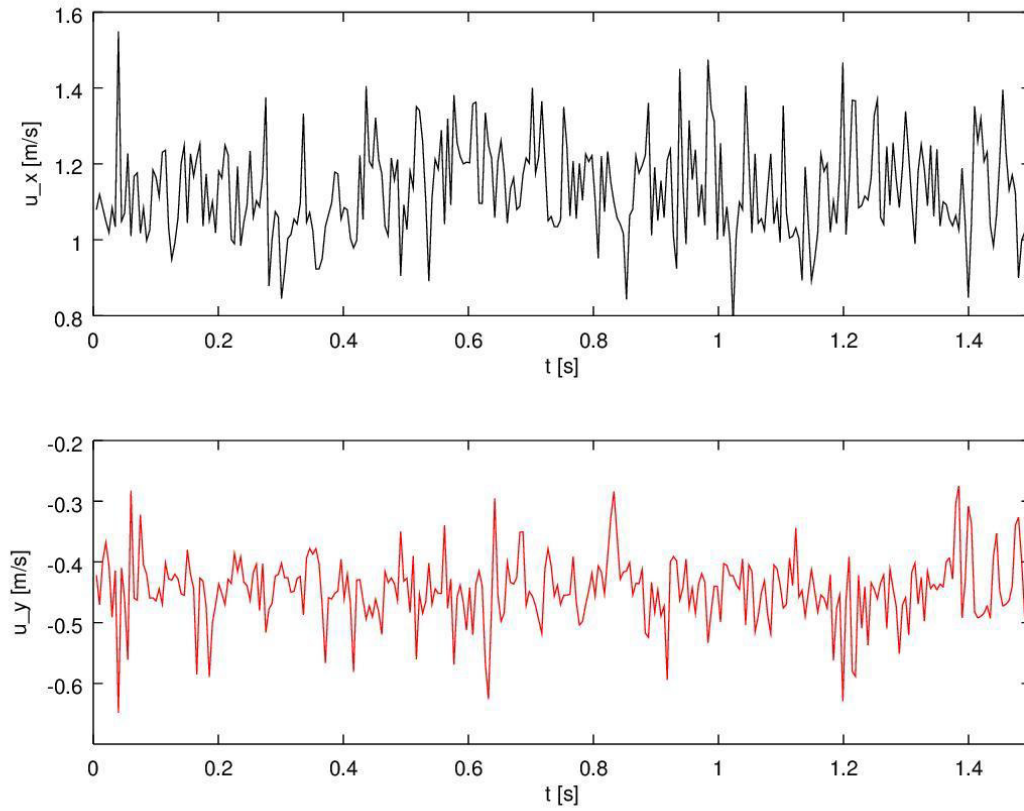


Figure A 9: Temporal velocity distributions in horizontal (x) direction (left panel) and in vertical (y) direction (right panel) for the 20th row and the 10th column of the residual matrices of experiment #3, i.e., for 300 matrices generated for the observation time of 1.5 [s].

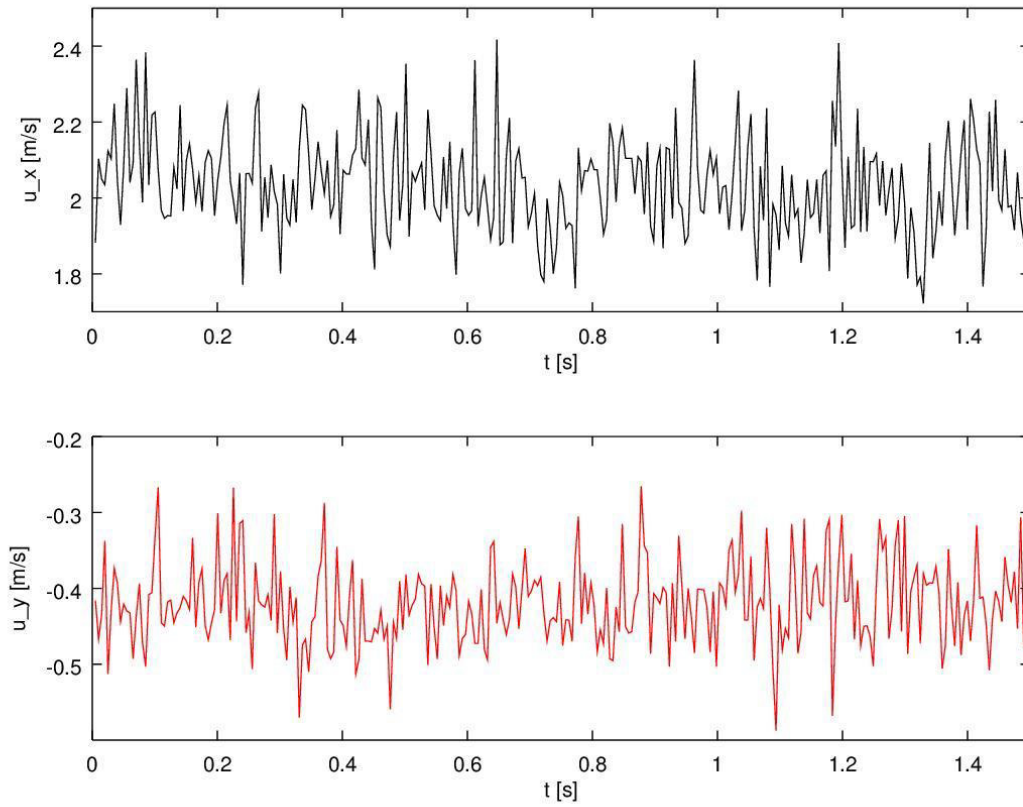


Figure A 10: Temporal velocity distributions in horizontal (x) direction (left panel) and in vertical (y) direction (right panel) for the 20th row and the 10th column of the residual matrices of experiment #4, i.e., for 300 matrices generated for the observation time of 1.5 [s].

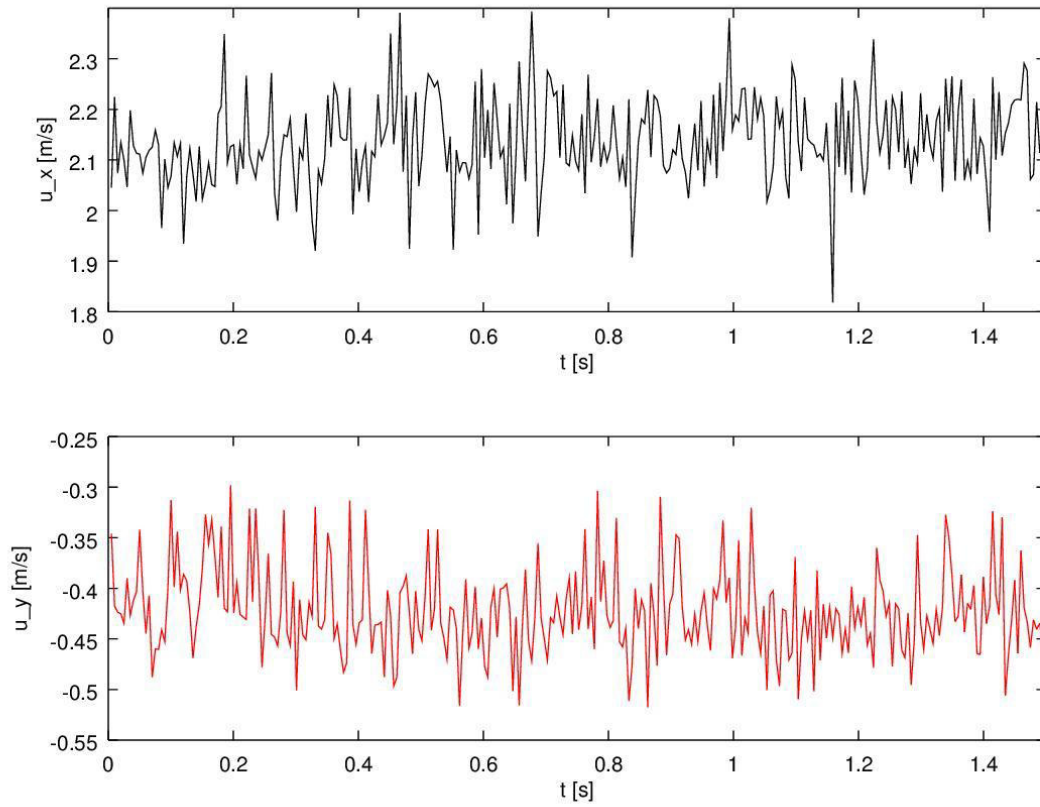


Figure A 11: Temporal velocity distributions in horizontal (x) direction (left panel) and in vertical (y) direction (right panel) for the 20th row and the 10th column of the residual matrices of experiment #5, i.e., for 300 matrices generated for the observation time of 1.5 [s].

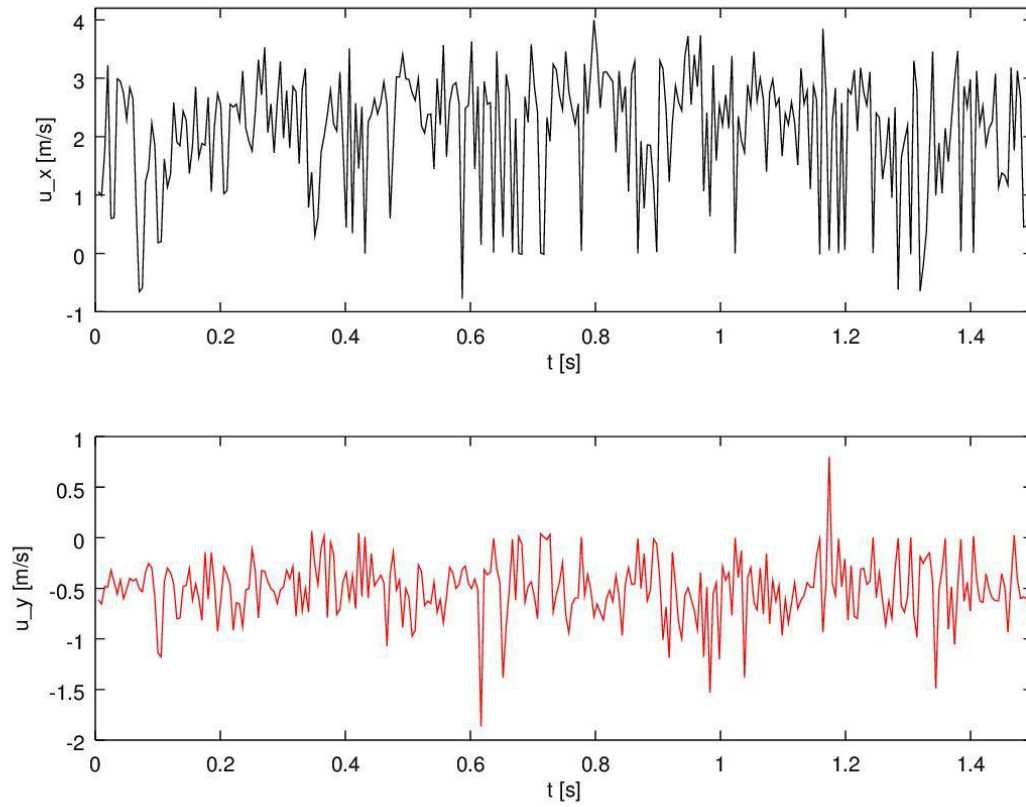


Figure A 12: Temporal velocity distributions in horizontal (x) direction (left panel) and in vertical (y) direction (right panel) for the 20th row and the 10th column of the residual matrices of experiment #6, i.e., for 300 matrices generated for the observation time of 1.5 [s].

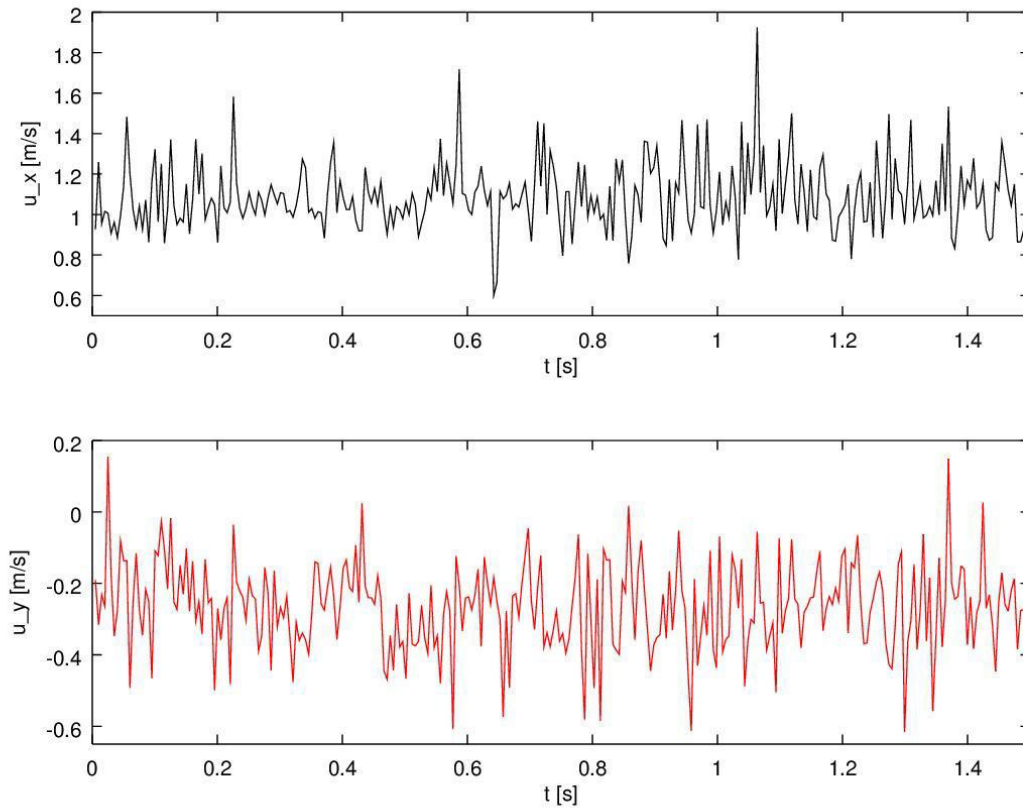


Figure A 13: Temporal velocity distributions in horizontal (x) direction (left panel) and in vertical (y) direction (right panel) for the 20th row and the 10th column of the residual matrices of experiment #7, i.e., for 300 matrices generated for the observation time of 1.5 [s].

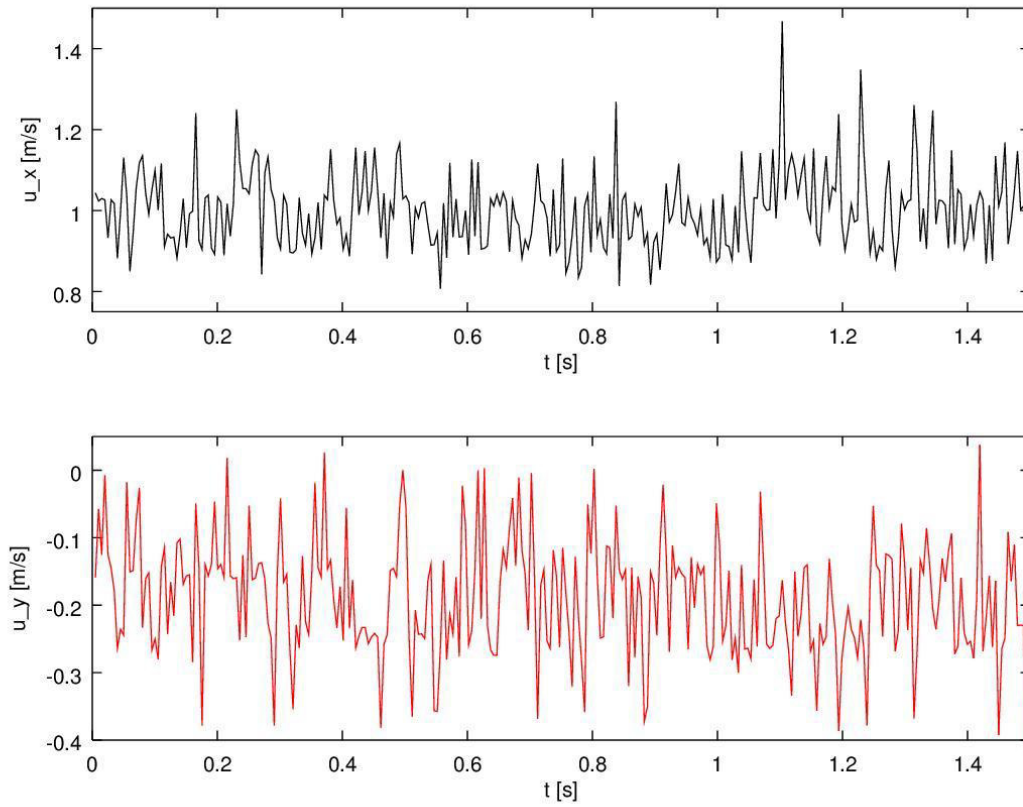


Figure A 14: Temporal velocity distributions in horizontal (x) direction (left panel) and in vertical (y) direction (right panel) for the 20th row and the 10th column of the residual matrices of experiment #8, i.e., for 300 matrices generated for the observation time of 1.5 [s].

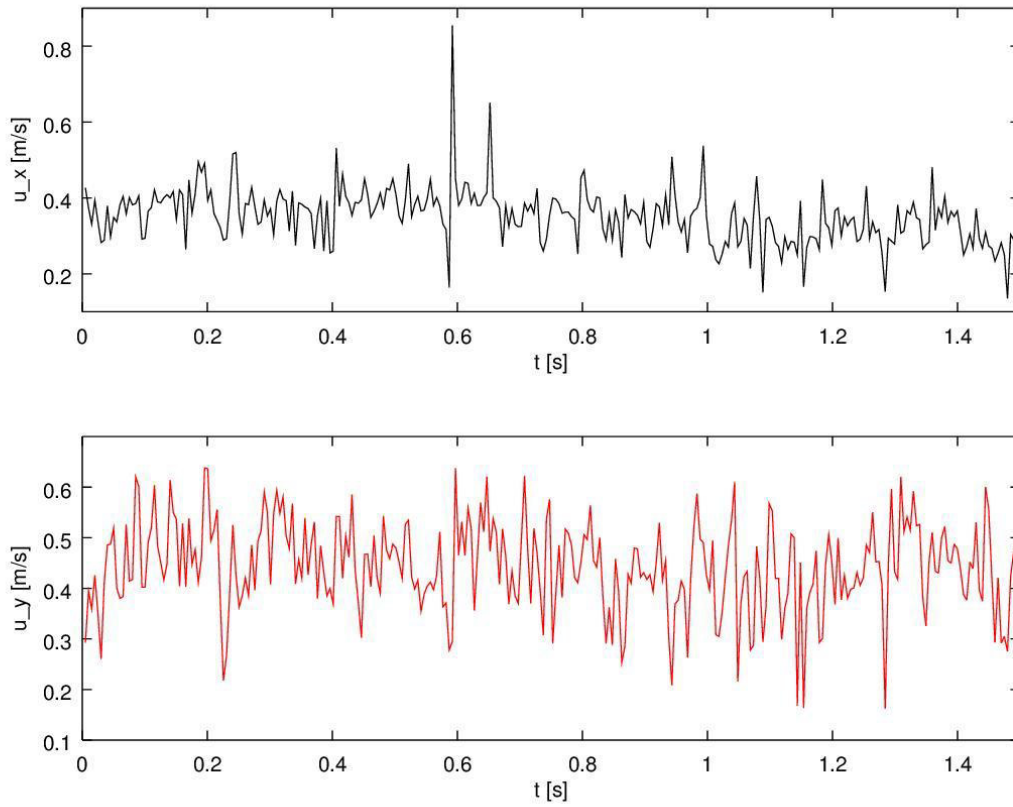


Figure A 15: Temporal velocity distributions in horizontal (x) direction (left panel) and in vertical (y) direction (right panel) for the 5th row and the 25th column of the residual matrices of experiment #9, i.e., for 300 matrices generated for the observation time of 1.5 [s].

E.2 Octave program for temporal velocity analysis

The following Octave program reads the certain velocity matrix out of each generated mat-file. The temporal difference Δt between two files is defined by the overall observation time of 1.5 [s] and by the number of files. Generating the empty matrices before starting the loop reduces the duration of calculation. Within the loop the files are loaded and the time values and the velocity values for each cell are calculated. Thereafter these values are plotted and saved in a graph having the velocity on the y- axis and the time scale on the x- axis.

```

1 %%%%%%%%%%%%%%%%%%%%%%%%%%%%%%%%%%%%%%%%%%%%%%%%%%%%%%%%%%%%%%%%%%%%%%%%%%
2 %           Temporal velocity           %
3 %           analysis                     %
4 %%%%%%%%%%%%%%%%%%%%%%%%%%%%%%%%%%%%%%%%%%%%%%%%%%%%%%%%%%%%%%%%%%%%%%%%%%
5
6
7 more off
8
9 %read filtered .mat-files out of matPIVRes-folder
10 files=dir('res0*vel.mat');
11
12 %define time step
13 nrfiles=length(files);
14 deltat=1.5/nrfiles;
15
16 %create empty matrices for time, velocity in x and y -direction
17 t=zeros(nrfiles,1);
18 velx=zeros(nrfiles,1);
19 vely=zeros(nrfiles,1);
20
21 % read time discrete velocities in x-direction
22 for i=1:nrfiles
23     i
24     load(files(i).name);
25     t(i)    =i*deltat;
26     velx(i) = fu(5,25);
27 end
28 % read time discrete velocities in y-direction
29 for i=1:nrfiles
30     i
31     load(files(i).name);
32     t(i)    =i*deltat;
33     vely(i) = fv(5,25);
34 end
35 % plot temporal velocity distributions over time
36 subplot (2,1,1)
37 plot(t, velx,'k')
38 axis ([0 1.5 0.1 0.9])
39 ylabel ('u_x [m/s]')
40 xlabel ('t [s]')
41 subplot(2,1,2)
42 plot(t, vely,'r')
43 axis ([0 1.5 0.1 0.7])
44 xlabel ('t [s]')
45 ylabel ('u_y [m/s]')
46 % save plot
47 print -djpg u_xy_(5,25).jpg
48
49
50
51

```

E.3 Program add-on for “MatPIV” written by Radl

```

1 %%%%%%%%%%%%%%%%%%%%%%%%%%%%%%%%%%%%%%%%%%%%%%%%%%%%%%%%%%%%%%%%%%%%%%%%%%
2 %           matPIV-TUG Suite           %
3 %  copyright: Stefan Radl, TU Graz, 2016 %
4 %%%%%%%%%%%%%%%%%%%%%%%%%%%%%%%%%%%%%%%%%%%%%%%%%%%%%%%%%%%%%%%%%%%%%%%%%%
5 %   This is the main script to use the %
6 %           matPIV-TUG Suite           %
7 %%%%%%%%%%%%%%%%%%%%%%%%%%%%%%%%%%%%%%%%%%%%%%%%%%%%%%%%%%%%%%%%%%%%%%%%%%
8
9 %add pathes
10 run('E:\Dropbox\matlab\includePathsOctave')
11
12 % Batch File to Process Granular Jet Data
13
14 %% **** INPUT ****
15 close all; clc; clear
16 srcDir      = 'E:\Dropbox\matlab\matPIV\';
17 rasterDir   = 'HFD_demo\CoordinatesAndMask';
18 i=1;
19 caseDirArray{i} = 'HFD_demo'; i=i+1;
20
21 picPrefix   = '';
22 picExt      = '.JPG'; %extension of the images to be processed
23 wocoNumber  = 1;
24
25 timeDelay   = 1/3000; %time delay between a image double
26 interrSize  = 200; %size of the interrogation windows in pixel
27 overlap     = 0.5; %overlap of interrogation windows
28 processingMode = 'multi'; %mode the images are processed
29 noPixStart  = 1; %first image of the two to be used for the crosscorrelation
30 noPixEnd    = 2; %second image of the two to be used for the crosscorrelation
31 deltaPixSeq = 1; %increment of the pix doubles to be processed
32 totalPix    = 2; %total number of pix doubles to be processed <-- change for
33 faster processing
34 totalPixInput = totalPix;
35
36 %Main Processing Switches
37 readRaster   = 0;
38 createMask   = 0; useMask = 1; cutOffBelowZero = [0 0];
39 processData  = 1; forceRecalc = 0; saveFIG = 0; saveEPS = 0; saveJPG = 1;
40 setNaNToZero = 1; %sets all "NaN" values to zero (prior to filtering)
41 calculateAverage= 1;
42
43 %Switches for filter
44 doFilter(1) = 1; %Peak high Filter
45 doFilter(2) = 0; %Signal to Noise Ratio Filter
46 doFilter(3) = 1; %Global Filter
47 doFilter(4) = 1; %Local Filter
48 doFilter(5) = 1; %NaN Interpolation Filter
49
50 vRef = 1;
51
52 xmin      = -0.01;
53 xmax      = 0.01;
54 ymin      = -0.002;
55 ymax      = 0.01;
56 xAxisFlip = 0;
57 yAxisFlip = 0;
58 contourQuantity = 0; %<<-switch to select contour qunty (0...norm, 1...u_x, 2..u_y)
59 plotSkip   = 1; %must be larger 1!
60 headSize  = 0.07;
61 plotVectorsOnly = 1;
62 plotVectorsWithContour = 1;
63 figFontSize = 20; %Font size of the labels in the figure
64 cbarFontSize = 16; %Font size of the labes in the colorbar
65 fontSizeAxis = 20; %Font Size of the plot labels
66 fontSizeLabel = 24;
67 TitleFontSize = 16; %Font Size of the plot title
68 lineWidth   = 1.5;
69 vectorSize  = 0.50; %scale value to change vector size
70 colorVector = 'k'; %color of the vector in the vector plot
71 lengthDimension = 'm';
72
73 %*****
74 %MAIN LOOP OVER CASE DIRS
75

```

```

76 for iCase=1:size(caseDirArray,2)
77     caseDir=caseDirArray{iCase}
78
79 %PRE PROCESSING
80
81 maskFile      = [caseDir,'/', 'polymask.mat']; % dir and name of the mask file
82 saveDir       = [caseDir, '/', 'matpivRes'];
83
84 cAxisMin      = -0.00*vRef;
85 cAxisMax      =  1.00*vRef;
86
87 % *****
88 % ***** PROCESSING SECTION *****
89 % *****
90 % Create Coordinate System
91 if(readRaster)
92     RasterPictureName = 'ImgA000000.tif';
93     RasterType = 'o';
94     cd([srcDir,'/', rasterDir])
95     [comap, A1, world]=definewoco(RasterPictureName, RasterType);
96 else
97     copyfile([srcDir,'/', rasterDir, '/worldcol.mat'], [srcDir,'/', caseDir])
98 end
99
100 % *****
101 % Process the data
102 if(createMask)
103     cd([srcDir,'/', caseDir])
104     B_PIV_Ausschnitte
105 end
106
107 if(processData)
108     cd([srcDir,'/', caseDir])
109     C_PIV_processor
110 end
111
112 if(calculateAverage)
113     cd([srcDir,'/', saveDir])
114     D_PIV_averager
115 end
116
117
118 end
119
120 cd(srcDir)
121 %END MAIN LOOP OVER CASE DIRS
122 %*****
123

```

```
1 grid off
2 box on
3 set(0,'defaultaxesfontsize',fontSizeAxis);
4 set(0,'defaulttextfontsize',fontSizeAxis);
5 set(0,'defaulttextfontname','Times');
6 set(gca,'FontSize',fontSizeAxis);
7 xlhand = get(gca,'xlabel');ylhand = get(gca,'ylabel');
8 set(xlhand,'fontsize',fontSizeLabel); set(ylhand,'fontsize',fontSizeLabel)
9 set(xlhand,'FontName','Times'); set(xlhand,'FontAngle','italic');
  set(xlhand,'FontWeight','bold');
10 set(ylhand,'FontName','Times'); set(ylhand,'FontAngle','italic');
  set(ylhand,'FontWeight','bold');
11 set(gcf, 'paperunits', 'centimeters')
12 colorbar
13 %set(gca, 'Position', [0.21 0.21 0.75 0.75])
14 %set(gcf, 'paperposition', [0 0 20 15])
```

```

1 %% **** CALCULATION AND FILTERING OF VECTORFIELD ****
2 close all
3 currentPix = 0; %set current number of pix already processed to zero
4 currDir = pwd;
5
6
7 %Get List of Files in result dir and filter grid out
8 myFiles=dir(['res',picPrefix,'*.mat']);
9 myGrid =dir(['res',picPrefix,'*grid.mat']);
10 if isempty(myGrid)
11     error('ERROR: No Grid present: please process images first!');
12 else
13     load(myGrid.name)
14 end
15
16 validCount = 0;
17 for fileI=1:size(myFiles,1)
18     tempString = strcat(myFiles(fileI).name);
19     if (~strcmp(tempString,myGrid.name))
20         validCount = validCount +1;
21         validFile{validCount}= tempString;
22     end
23 end
24 if (~exist('validFile','var'))
25     error('ERROR: Could not find a valid time file!');
26 end
27
28 if (~isdir([srcDir,'/',saveDir,'/meanU']))
29     cd([srcDir,'/',saveDir])
30     mkdir('meanU')
31 end
32 cd([srcDir,'/',saveDir,'/meanU'])
33
34 for timeI=1:validCount
35
36     % 1) Load Data
37     currFilteredU = validFile{timeI};
38     load([srcDir,'/',saveDir,'/',currFilteredU]);
39
40
41     % 2) Update the average and Mean
42     if (timeI==1)
43         meanFu=fu;
44         varFu =fu*0;
45         meanFv=fv;
46         varFv =fv*0;
47     else
48         meanFuOld = meanFu;
49         meanFu = meanFu + (fu-meanFu)/timeI;
50         varFu = varFu + (fu-meanFuOld).*(fu-meanFu);
51         meanFvOld = meanFv;
52         meanFv = meanFv + (fv-meanFv)/timeI;
53         varFv = varFv + (fv-meanFvOld).*(fv-meanFv);
54     end
55
56     % 3) Save and plot of last in validFile
57     if (timeI==validCount)
58         varFu = varFu / (length(validFile)-1);
59
60         save([srcDir,'/',saveDir,'/meanU/meanRes',picPrefix,'.mat'], 'x','y',...
61             'meanFu', 'varFu', ...
62             'meanFv', 'varFv');
63
64     disp(['**TIME-AVERAGED QUANTITIES REPORT **'])
65     disp(['mean velocities:          x: ', num2str(mean(meanFu(:)),'% .4f'), ...
66         ' [m/s], y: ', num2str(mean(meanFv(:)),'% .4f'),' [m/s]'])
67     disp(['std. deviation velocities: x: ', num2str(std(meanFu(:)),'% .4f'), ...
68         ' [m/s], y: ', num2str(std(meanFv(:)),'% .4f'),' [m/s]'])
69     disp(['min velocities:          x: ', num2str(min(meanFu(:)),'% .4f')...
70         ' [m/s], y: ', num2str(min(meanFv(:)),'% .4f'),' [m/s]'])
71     disp(['max velocities:          x: ', num2str(max(meanFu(:)),'% .4f')...
72         ' [m/s], y: ', num2str(max(meanFv(:)),'% .4f'),' [m/s]'])
73
74     if (plotVectorsOnly)
75         figure
76         plotQ=quiver(x(1:plotSkip:end,1:plotSkip:end),y(1:plotSkip:end,1:plotSkip:end), ...

```

```

77     meanFu(1:plotSkip:end,1:plotSkip:end), ...
78     meanFv(1:plotSkip:end,1:plotSkip:end),vectorSize, 'k');
79     set(plotQ,'LineWidth',lineWidth);
80     %axis equal
81     if(exist('xmin'))
82         xlim([xmin xmax])
83     else
84         xRange = max(max(x))-min(min(x));
85         xlim([min(min(x))-0.05*xRange max(max(x))+0.05*xRange])
86     end
87     if(exist('ymin'))
88         ylim([ymin ymax])
89     else
90         yRange = max(max(y))-min(min(y));
91         ylim([min(min(y))-0.05*yRange max(max(y))+0.05*yRange])
92     end
93     set(gca,'FontSize',figFontSize)
94     xlabel(['x [' , lengthDimension,']'],'FontSize',fontSizeAxis);
95     ylabel(['y [' , lengthDimension,']'],'FontSize',fontSizeAxis);
96     title(['meanU - ',picPrefix],'FontSize',TitleFontSize)
97     if(xAxisFlip)
98         set(gca,'XDir','reverse');
99     end
100    if(yAxisFlip)
101        set(gca,'YDir','reverse');
102    end
103    makeXYPlotPretty
104    xlhand = get(gca,'xlabel');ylhand = get(gca,'ylabel');
105    % set(xlhand,'Position',get(xlhand,'Position') - [0 1e-5 0])
106    % set(gca,'Position', get(gca,'OuterPosition') + 1 *...
107    % [0.2 0.2 -0.45 -0.25]);
108    set(gcf, 'paperunits', 'centimeters', 'paperposition', [0 0 22 18])
109    saveas(gcf, ['meanRes',picPrefix,'_figVecs'],'fig');
110    if(saveEPS)
111        saveas(gcf, ['meanRes',picPrefix,'_figVecs'],'eps');
112    end
113    if(saveJPG)
114        saveas(gcf, ['meanRes',picPrefix,'_figVecs'],'jpg');
115    end
116    end
117    if(plotVectorsWithContour)
118        figure
119        if(contourQuantity == 0)
120            w = magnitude(x,y,meanFu,meanFv);
121            labelCol = ['\bar{U} [' , lengthDimension,']/s'];
122            fileSuffix = 'magU';
123        elseif(contourQuantity == 1)
124            w = magnitude(x,y,meanFu);
125            labelCol = ['\bar{u}_x [' , lengthDimension,']/s'];
126            fileSuffix = 'uX';
127        elseif(contourQuantity == 2)
128            w = magnitude(x,y,meanFv);
129            labelCol = ['\bar{u}_y [' , lengthDimension,']/s'];
130            fileSuffix = 'uY';
131        end
132        pcolor(x,y,w); hold on
133        shading flat;
134        caxis([cAxisMin cAxisMax])
135        % mycb = COLORBAR('vertical');
136        % xlabel(mycb, 'FontSize',fontSizeAxis);
137        % set(mycb,'FontSize',cbarFontSize);
138        plotQ=quiver(x(1:plotSkip:end,1:plotSkip:end),y(1:plotSkip:end,1:plotSkip:end), ...
139            meanFu(1:plotSkip:end,1:plotSkip:end), ...
140            meanFv(1:plotSkip:end,1:plotSkip:end),vectorSize, colorVector);
141        %axis equal
142        set(plotQ,'LineWidth',lineWidth);
143        if(exist('xmin'))
144            xlim([xmin xmax])
145        else
146            xRange = max(max(x))-min(min(x));
147            xlim([min(min(x))-0.05*xRange max(max(x))+0.05*xRange])
148        end
149        if(exist('ymin'))
150            ylim([ymin ymax])
151        else
152            yRange = max(max(y))-min(min(y));

```



```

153         ylim([min(min(y))-0.05*yRange max(max(y))+0.05*yRange])
154     end
155     hold off;
156     set(gca,'FontSize',figFontSize)
157     xlabel(['x [' , lengthDimension, ']' ],'FontSize',fontSizeAxis);
158     ylabel(['y [' , lengthDimension, ']' ],'FontSize',fontSizeAxis);
159
160     if(contourQuantity==1)
161         countourText='u_x';
162     elseif(contourQuantity==2)
163         countourText='u_y';
164     elseif(contourQuantity==0)
165         countourText='norm';
166     else
167         countourText='unknown';
168     end
169     title(['meanU - ',picPrefix,'.contour.',countourText],'FontSize',TitleFontSize)
170     if(xAxisFlip)
171         set(gca,'XDir','reverse');
172     end
173     if(yAxisFlip)
174         set(gca,'YDir','reverse');
175     end
176
177     makeXYPlotPretty
178     xlhand = get(gca,'xlabel');ylhand = get(gca,'ylabel');
179     % set(xlhand,'Position',get(xlhand,'Position') - [0 1e-5 0])
180     % set(gca, 'Position', get(gca, 'OuterPosition') + 1 *...
181     % [0.2 0.2 -0.45 -0.25]);
182     set(gcf, 'paperunits', 'centimeters', 'paperposition', [0 0 22 18])
183     saveas(gcf, ['meanRes',picPrefix,'_figVecsCont_',fileSuffix],'fig');
184     if(saveEPS)
185         saveas(gcf, ['meanRes',picPrefix,'_figVecsCont_',fileSuffix],'epsc');
186     end
187     if(saveJPG)
188         saveas(gcf, ['meanRes',picPrefix,'_figVecsCont_',fileSuffix],'jpg');
189     end
190
191     end
192
193     end
194
195     end

```

```

1 % A sequence of pictures will be load. this programm compares two
2 % pictures via crosscorrelation and calculates the vectorfield.
3 % Vectorfields are generated. Filters are applied in series.
4
5 %% **** INPUT PARAMETERS ****
6
7 coordinates = [srcDir, '/', rasterDir, '/', 'worldco', sprintf('%1d', wocoNumber), '.mat'];
8 %name of the file including coordinates in [m]
9 load(coordinates)
10
11 %check if there is a file to adjust the offset
12 offsetFile = [srcDir, '/', rasterDir, '/', 'offset.dat'];
13 if(exist(offsetFile)>0)
14     offset=load(offsetFile)
15 else
16     offset=[0 0]
17 end
18
19 if(useMask)
20     mask = [srcDir, '/', maskFile];
21 end
22
23 copyfile([srcDir, '/', rasterDir, '/', 'worldco', sprintf('%1d', wocoNumber), '.mat'],
24 [srcDir, '/', caseDir ])
25
26 if(~exist('filterSnrrange','var'))
27     snrrange = 1.6; % rate for the Signal to Noise Ratio filter
28 else
29     snrrange = filterSnrrange;
30 end
31
32 if(~exist('filterGlobrange','var'))
33     globrange = 3.5; % rate for the global filter
34 else
35     globrange = filterGlobrange;
36 end
37
38 if(~exist('filterLocrange','var'))
39     locrange = 2.5; % rate for the local filter
40 else
41     locrange = filterLocrange;
42 end
43
44 if(~exist('filterPkhrange','var'))
45     pkhrange = 0.4; % rate for the Peak High Filter
46 else
47     pkhrange = filterPkhrange;
48 end
49
50 %% **** END INPUT PARAMETERS ****
51
52 %% **** CALCULATION AND FILTERING OF VECTORFIELD ****
53
54 %Generate Directories if necessary
55 currDir = pwd
56 if(~isdir([srcDir, '/', saveDir]))
57     cd(srcDir)
58     mkdir(saveDir)
59 end
60
61 if(~isdir([srcDir, '/', saveDir, '/fig']) & saveFIG==1)
62     cd([srcDir, '/', saveDir])
63     mkdir('fig')
64 end
65
66 if(~isdir([srcDir, '/', saveDir, '/eps']) & saveEPS==1)
67     cd([srcDir, '/', saveDir])
68     mkdir('eps')
69 end
70
71 if(~isdir([srcDir, '/', saveDir, '/jpg']) & saveJPG==1)
72     cd([srcDir, '/', saveDir])
73     mkdir('jpg')
74 end
75
76 cd(currDir)
77
78 if(totalPixInput<0)
79     imageFiles = dir(['*', picExt])
80     totalPix = str2num(imageFiles(end).name(size(picPrefix,2)+1:end-size(picExt,2)))
81 else

```

```

75 totalPix = totalPixInput;
76 end
77 disp(['Will process ', num2str(totalPix), ' pix.'])
78
79 currentPix = 0; %set current number of pix already processed to zero
80 currDir = pwd;
81 while currentPix < totalPix
82     cd(currDir);
83     close all
84     % 1) Set the pix index and pix file name
85     pix1 = noPixStart + deltaPixSeq * currentPix; %%the first pix for crosscorrelation
86     pix2 = noPixEnd + deltaPixSeq * currentPix; %%the second pix for crosscorrelation
87
88     file0=[picPrefix, sprintf('%.6d',pix1),picExt]
89     file1=[picPrefix, sprintf('%.6d',pix2),picExt]
90
91     %Calculate only if not processed or recalculation is forced
92     if(
~exist([srcDir, '/', saveDir, '/res', picPrefix, sprintf('%.6d',pix1), '_vel.mat'], 'file') ||
forceRecalc )
93
94     % 2a) cut-off pixels of image if desired
95     if(norm(cutOffBelowZero)>0)
96         savePath = pwd
97         %file0
98         [A p1]=imread(file0);
99         if(cutOffBelowZero(1)>0)
100             Anew=A(:,A1(1,2):end); %cut-off xposition
101         else
102             Anew=A;
103         end
104         if(cutOffBelowZero(2)>0)
105             Anew=Anew(1:A1(1,3),:); %cut-off yposition
106         end
107         file0 = 'newTiff_file0.tiff'
108         imwrite(Anew, file0, 'TIFF')
109
110         %file1
111         [A p1]=imread(file1);
112         if(cutOffBelowZero(1)>0)
113             Anew=A(:,A1(1,2):end); %cut-off xposition
114         elseif(cutOffBelowZero(2)>0)
115             Anew=A(:,A1(1,3):end); %cut-off yposition
116         end
117         file1 = 'newTiff_file1.tiff'
118         imwrite(Anew, file1, 'TIFF')
119     end
120     % 2b) Berechnung des Vektorfeldes
121     if(useMask)
122         [x,y,u,v,snr,pkh]=matpiv(file0,file1,interrSize...
123             ,timeDelay,overlap,processingMode,coordinates,mask);
124     else
125         [x,y,u,v,snr,pkh]=matpiv(file0,file1,interrSize...
126             ,timeDelay,overlap,processingMode,coordinates);
127     end
128
129     %2c) Delete the temp tiff files if cut-off was used
130     if(norm(cutOffBelowZero)>0)
131         delete([savePath, '/', file0])
132         delete([savePath, '/', file1])
133     end
134     if(cutOffBelowZero(1)>0)
135         x = x - min(min(x)) + offset(1);
136     else
137         x = x + offset(1);
138     end
139     if(cutOffBelowZero(1)>0)
140         y = y - min(min(y)) + offset(2);
141     else
142         y = y + offset(2);
143     end
144
145     % Now set all NaN's to 0 (causes problems when using a mask)
146     if(setNaNToZero==1)
147         disp('WARNING: SETTING NANS TO ZERO!')
148         NANValue.u=isnan(u);

```

```

149     NANValue.v=isnan(v);
150     u(NANValue.u)=0;
151     v(NANValue.v)=0;
152 end
153 quiver(x,y,u,v)
154
155 % 3) Filterung des Vektorfeldes
156
157 filteredU = u;
158 filteredV = v;
159
160 if(doFilter(1))
161     %Peak high Filter:
162     [pu,pv]=peakfilt(x,y,filteredU,filteredV,pkh,pkhrange);
163     filteredU=pu;
164     filteredV=pv;
165 end
166
167 if(doFilter(2))
168     %Signal to Noise Ratio Filter:
169     [su,sv]=snrfilt(x,y,filteredU,filteredV,snr,snrrange);
170     filteredU=su;
171     filteredV=sv;
172 end
173
174 if (doFilter(3))
175     %Globaler Filter:
176     [gu,gv]=globfilt(x,y,filteredU,filteredV,globrange);
177     filteredU=gu;
178     filteredV=gv;
179 end
180
181 if(doFilter(4))
182     %Lokaler Filter:
183     [lu,lv]=localfilt(x,y,filteredU,filteredV,locrange,'median');
184     filteredU=lu;
185     filteredV=lv;
186 end
187
188 if(doFilter(5))
189     %Interpolation der Ausreißer:
190     [iu,iv]=naninterp(filteredU,filteredV,'linear',x,y);
191     filteredU=iu;
192     filteredV=iv;
193 end
194
195 fu = filteredU;
196 fv = filteredV;
197
198 % 4) Speicherung des Rasters
199 cd([srcDir,'/',saveDir])
200 if currentPix==0
201     save(['res',picPrefix,'_grid.mat'],'x','y')
202 end
203 % 5) Speicherung des ungefilterten und gefilterten Vektorfeldes
204 save(['resUF',picPrefix,sprintf('%d',pixl),'_vel.mat'],'u','v')
205 save(['res',picPrefix,sprintf('%d',pixl),'_vel.mat'],'fu','fv')
206 else
207     load([srcDir,'/',saveDir,'/res',picPrefix,sprintf('%d',pixl),'_vel.mat']);
208     load([srcDir,'/',saveDir,'/resUF',picPrefix,sprintf('%d',pixl),'_vel.mat']);
209     load([srcDir,'/',saveDir,'/res',picPrefix,'_grid.mat']);
210 end
211
212 disp(['mean velocities:          x: ', num2str(mean(fu(:)),'%d'),...
213      ' [m/s], y: ', num2str(mean(fv(:)),'%d'),' [m/s]'])
214 disp(['std. deviation velocities: x: ', num2str(std(fu(:)),'%d'),...
215      ' [m/s], y: ', num2str(std(fv(:)),'%d'),' [m/s]'])
216 disp(['min velocities:          x: ', num2str(min(fu(:)),'%d')...
217      ' [m/s], y: ', num2str(min(fv(:)),'%d'),' [m/s]'])
218 disp(['max velocities:          x: ', num2str(max(fu(:)),'%d')...
219      ' [m/s], y: ', num2str(max(fv(:)),'%d'),' [m/s]'])
220
221
222 % 7) Darstellung des gefilterten Vektorfeldes
223 cd([srcDir,'/',saveDir])
224 if(plotVectorsOnly)

```

```

225 figure
226 %axis equal
227 plotQ = quiver(x(1:plotSkip:end,1:plotSkip:end),y(1:plotSkip:end,1:plotSkip:end),
...
228 fu(1:plotSkip:end,1:plotSkip:end), ...
229 fv(1:plotSkip:end,1:plotSkip:end),vectorSize, colorVector);
230 set(plotQ,'LineWidth',lineWidth);
231
232 if(exist('xmin'))
233     xlim([xmin xmax])
234 else
235     xrange = max(max(x))-min(min(x));
236     xlim([min(min(x))-0.05*xrange max(max(x))+0.05*xrange])
237 end
238 if(exist('ymin'))
239     ylim([ymin ymax])
240 else
241     yrange = max(max(y))-min(min(y));
242     ylim([min(min(y))-0.05*yrange max(max(y))+0.05*yrange])
243 end
244 set(gca,'FontSize',figFontSize)
245 xlabel(['x ', lengthDimension, ''], 'FontSize',fontSizeAxis);
246 ylabel(['y ', lengthDimension, ''], 'FontSize',fontSizeAxis);
247 title([picPrefix,sprintf('%.6d',pixl)], 'FontSize',TitleFontSize)
248 if(xAxisFlip)
249     set(gca,'XDir','reverse');
250 end
251 if(yAxisFlip)
252     set(gca,'YDir','reverse');
253 end
254 makeXYPlotPretty
255 xlhand = get(gca,'xlabel');ylhand = get(gca,'ylabel');
256 % set(xlhand,'Position',get(xlhand,'Position') + [0 1e-5 0])
257 % set(gca, 'Position', get(gca, 'OuterPosition') + 1 *...
258 % [0.2 0.2 -0.45 -0.25]);
259 set(gcf, 'paperunits', 'centimeters', 'paperposition', [0 0 22 18])
260
261 if(saveFIG)
262     saveas(gcf,['./fig/res',picPrefix,sprintf('%.6d',pixl),'_figVecs'],'fig');
263 end
264 if(saveEPS)
265     saveas(gcf,['./eps/res',picPrefix,sprintf('%.6d',pixl),'_figVecs'],'eps');
266 end
267 if(saveJPG)
268     saveas(gcf,['./jpg/res',picPrefix,sprintf('%.6d',pixl),'_figVecs'],'jpg');
269 end
270 end
271 if(plotVectorsWithContour)
272     figure
273     if(contourQuantity == 0)
274         w = magnitude(x,y,fu,fv);
275         labelCol = ['|U| ', lengthDimension, '/s'];
276     elseif(contourQuantity == 1)
277         w = magnitude(x,y,fu);
278         labelCol = ['u_x ', lengthDimension, '/s'];
279     elseif(contourQuantity == 2)
280         w = magnitude(x,y,fv);
281         labelCol = ['u_y ', lengthDimension, '/s'];
282     end
283     pcolor(x,y,w); hold on
284     shading flat;
285     caxis([cAxisMin cAxisMax])
286     mycb = colorbar('vertical');
287
288 %     xlabel(mycb, 'FontSize',fontSizeAxis);
289 % set(mycb,'FontSize',cbarFontSize);
290 plotQ = quiver(x(1:plotSkip:end,1:plotSkip:end),y(1:plotSkip:end,1:plotSkip:end),
...
291 fu(1:plotSkip:end,1:plotSkip:end), ...
292 fv(1:plotSkip:end,1:plotSkip:end), vectorSize, colorVector);
293 %axis equal
294 set(plotQ,'LineWidth',lineWidth);
295 hold off;
296
297 if(exist('xmin'))
298     xlim([xmin xmax])

```

```

299     else
300         xRange = max(max(x))-min(min(x));
301         xlim([min(min(x))-0.05*xRange max(max(x))+0.05*xRange])
302     end
303     if(exist('ymin'))
304         ylim([ymin ymax])
305     else
306         yRange = max(max(y))-min(min(y));
307         ylim([min(min(y))-0.05*yRange max(max(y))+0.05*yRange])
308     end
309
310     set(gca,'FontSize',figFontSize)
311     xlabel(['x [' , lengthDimension,']'], 'FontSize',fontSizeAxis);
312     ylabel(['y [' , lengthDimension,']'], 'FontSize',fontSizeAxis);
313     if(contourQuantity==1)
314         countourText='u_x';
315     elseif(contourQuantity==2)
316         countourText='u_y';
317     elseif(contourQuantity==0)
318         countourText='norm';
319     else
320         countourText='unknown';
321     end
322
323     title([picPrefix, sprintf('%.6d',pix1), '.contour.', countourText], 'FontSize', TitleFontSize)
324     if(xAxisFlip)
325         set(gca, 'XDir', 'reverse');
326     end
327     if(yAxisFlip)
328         set(gca, 'YDir', 'reverse');
329     end
330     makeXYPlotPretty
331     xlhand = get(gca, 'xlabel'); ylhand = get(gca, 'ylabel');
332     % set(xlhand, 'Position', get(xlhand, 'Position') - [0 1e-4 0])
333     % set(gca, 'Position', get(gca, 'OuterPosition') + 1 *...
334     % [0.2 0.2 -0.45 -0.25]);
335     set(gcf, 'paperunits', 'centimeters', 'paperposition', [0 0 22 18])
336
337     if(saveFIG)
338         saveas(gcf, ['./fig/res', picPrefix, sprintf('%.6d',pix1), '_figVecsCont'], 'fig');
339     end
340     if(saveEPS)
341         saveas(gcf, ['./eps/res', picPrefix, sprintf('%.6d',pix1), '_figVecsCont'], 'eps');
342     end
343     if(saveJPG)
344         saveas(gcf, ['./jpg/res', picPrefix, sprintf('%.6d',pix1), '_figVecsCont'], 'jpg');
345     end
346     end
347     % 8) Increment current picture
348     currentPix = currentPix + 1
349 end

```

```
1 % In this file you can cut non important sections of a picture
2
3 %% *****Input*****
4
5 picNum      = 0;
6
7 %% *****cutting non important picture sections*****
8 mask([picPrefix ,sprintf('%06d',picNum),'.tif'], ...
9      [srcDir,'/',rasterDir,'/','worldco',sprintf('%01d',wocoNumber),'.mat']);
10 close;
```

```
1 clear
2 clc
3 close all
4
5 n=5;
6 cd('D:\Gruppe2\Mes1\');
7 files=dir('ImgA0000*');
8
9 A=0;
10 BW=0;
11 for i=1:n
12     [A_one p1]=IMREAD(num2str(files(i).name));
13     BW_one = im2bw(A_one, 0.5);
14     %A=ind2gray(A_one,p1); +A;
15     BW=BW+BW_one;
16 end
17 %A=A./(n);
18 BW=BW/n;
19 %BW = im2bw(A, 0.1);
20 %imshow(A)
21 %figure
22 imshow(BW)
23
24 %%
25
26 sz=size(BW);
27 for i=1:1:sz(1)
28     P(i)=sum(BW(i,:))/sz(2);
29 end
30 y=1:1:length(P);
31
32 figure
33 plot(1-P,max(y)-y)
34
35 %sum(A(1,:))/sz(2)
36 %sum(A(sz(1),:))/sz(2)
```



```
1 % In this file coordinates in x an y Axes will be created for calculations
2 % for the "B_PIV_Ausschnitte.m" and "C_PIV_processor.m" file
3
4 %% **** INPUT ****
5
6 RasterPictureName = 'R003.tif'
7
8 RasterType = 'o'
9
10 %% **** Koordinatentransformation: ****
11
12 definewoco(RasterPictureName,RasterType);
```

```
1 % In this file the Raster can be scaled if it doesn't match with the
2 % expected dimension
3
4 %% *****Input*****
5 ScaleFactor = 0.906
6 worldin = 4
7 worldout = 5
8 %% *****Scale Worldco*****
9 load(['worldco', sprintf('%d', worldin), '.mat']);
10
11 comap_neu(1,:) = comap(1,:)
12 comap_neu(2:3,:) = comap(2:3,:)*ScaleFactor;
13
14 comap = comap_neu;
15
16 save(['worldco', sprintf('%d', worldout), '.mat'], 'comap');
```

Appendix F

F.1 QUICPIC report – fine fraction



Sympatec GmbH
System-Partikel-Technik

QUICPIC-Partikelgrößenanalyse WINDOX 5

QUICPIC (QP0112) & RODOS, 2.00 63.0 mm - M8 (20...6820µm)

Quartz

2016-06-14, 14:56:28.015

$x_{10} = 142.33 \pm 0.00 \mu\text{m}$ $x_{50} = 219.94 \pm 0.00 \mu\text{m}$ $x_{90} = 297.44 \pm 0.00 \mu\text{m}$
 $x_{16} = 157.60 \pm 0.00 \mu\text{m}$ $x_{84} = 283.18 \pm 0.00 \mu\text{m}$ $x_{99} = 368.17 \pm 0.00 \mu\text{m}$
 VMD = 220.56 $\mu\text{m} \pm 0.00 \mu\text{m}$ $C_{\text{opt}} = 0.60 \pm 0.00 \% [0.00 \%]$
 SMD = 199.42 $\mu\text{m} \pm 0.00 \mu\text{m}$ RRSB d' = 240.18 μm RRSB n = 4.22
 Particle number = 1592383

$x_{90}/x_{10} = 2.09$

Polydispersity index: 0.28

StandardDeviation of the PSD: 61.62 μm

Monosized < 1.02

Ultra narrow 1.02 - 1.05

Narrow 1.05 - 1.5

Medium 1.5 - 4

Broad 4 - 10

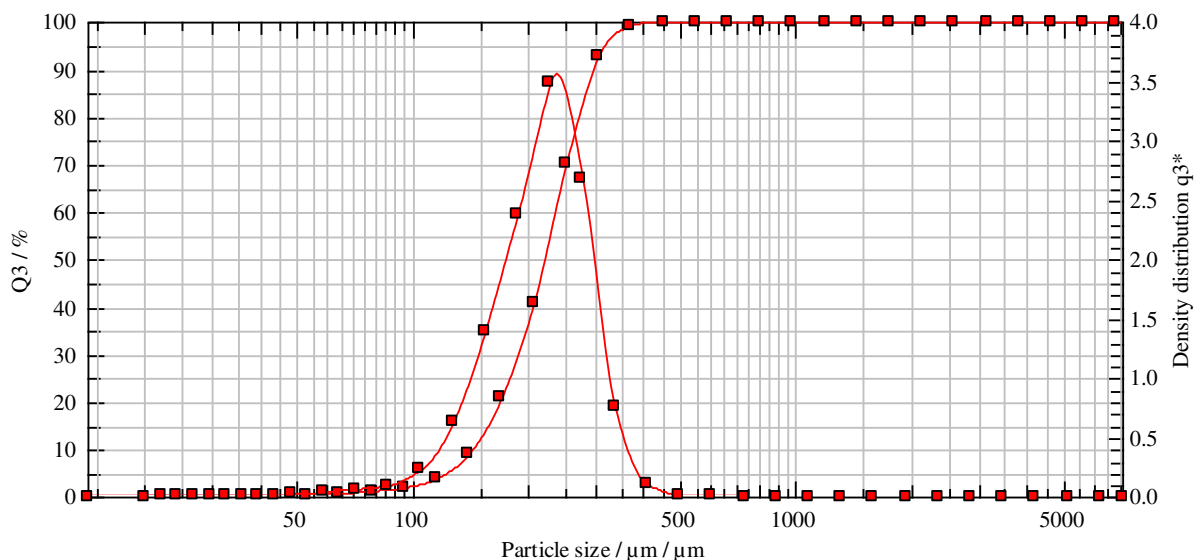
Very broad > 10

Conditions:

Produkt: Quartz
 Auswertung: EQPC (5.6.0.0)
 Trigger: Standard400Hz
 Disp.Meth.: Standard_Trocken 0.5bar..

User parameters:

Benutzer: Piller
 Probenbezeichnung: Fine Fraction
 #Messung: 2
 Förderhöhe:



Cumulative Distribution

$x_3/\mu\text{m}$	$Q_3/\%$	$x_0/\mu\text{m}$	$Q_3/\%$
20,00	0,00	139,73	8,98
24,29	0,02	169,71	20,76
29,50	0,03	206,13	40,83
35,84	0,06	250,36	70,19
43,52	0,14	304,08	92,79
52,86	0,28	369,32	99,11
64,21	0,59	448,57	99,93
77,98	1,09	544,83	99,99
94,72	1,86	661,73	100,00
115,04	3,74	803,73	100,00

F.2 QUICPIC report – coarse fraction



Sympatec GmbH
System-Partikel-Technik

QUICPIC-Partikelgrößenanalyse WINDOX 5

QUICPIC (QP0112) & RODOS, 2.00 63.0 mm - M8 (20...6820µm)

Quartz

2016-06-14, 14:54:10,953

$x_{10} = 218,72 \pm 0,00 \mu\text{m}$	$x_{50} = 285,87 \pm 0,00 \mu\text{m}$	$x_{90} = 389,88 \pm 0,00 \mu\text{m}$
$x_{16} = 232,27 \pm 0,00 \mu\text{m}$	$x_{84} = 359,46 \pm 0,00 \mu\text{m}$	$x_{99} = 533,50 \pm 0,00 \mu\text{m}$
VMD = 297,86 $\mu\text{m} \pm 0,00 \mu\text{m}$		$C_{\text{opt}} = 0,42 \pm 0,00 \% [0,00 \%]$
SMD = 282,60 $\mu\text{m} \pm 0,00 \mu\text{m}$	RRSB d' = 314,01 μm	RRSB n = 4.62
Particle number = 346874		

$x_{90}/x_{10} = 1,78$

Polydispersity index: 0,25

StandardDeviation of the PSD: 71,26 μm

Monosized < 1,02

Ultra narrow 1,02 - 1,05

Narrow 1,05 - 1,5

Medium 1,5 - 4

Broad 4 - 10

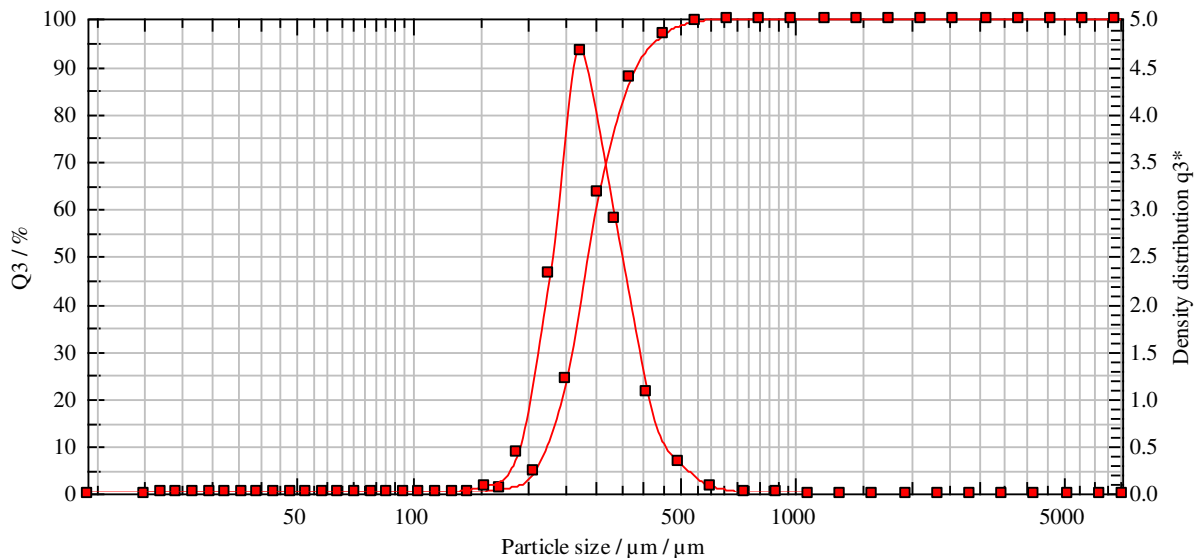
Very broad > 10

Conditions:

Produkt: Quartz
Auswertung: EQPC (5.6.0.0)
Trigger: Standard400Hz
Disp.Meth.: Standard_Trocken 0.5bar..

User parameters:

Benutzer: Piller
Probenbezeichnung: Coarse Fraction
#Messung: 1
Förderhöhe:



Cumulative Distribution

$x_3/\mu\text{m}$	$Q_3/\%$	$x_0/\mu\text{m}$	$Q_3/\%$
20,00	0,00	206,13	4,42
24,29	0,00	250,36	24,01
29,50	0,00	304,08	63,32
35,84	0,00	369,32	87,68
43,52	0,01	448,57	96,61
52,86	0,01	544,83	99,32
64,21	0,02	661,73	99,90
77,98	0,04	803,73	99,97
94,72	0,07	976,19	100,00
115,04	0,11	1185,65	100,00
139,73	0,24	1440,07	100,00
169,71	0,87	1749,08	100,00

F.3 Octave program for particle size analysis

```

1 %%%%%%%%%%%%%%%%%%%%%%%%%%%%%%%%%%%%%%%%%%%%%%%%%%%%%%%%%%%%%%%%%%%%%%%%%
2 % Calculation of separation efficiency %
3 %%%%%%%%%%%%%%%%%%%%%%%%%%%%%%%%%%%%%%%%%%%%%%%%%%%%%%%%%%%%%%%%%%%%%%%%%
4 more off
5
6 clear all
7 close all
8
9 % mass fractions of fines and coarse
10 m_Fine=315; % [g]
11 m_Coarse=534; % [g]
12 m_Feed=m_Fine+m_Coarse;
13 f=m_Fine/m_Feed;
14 c=m_Coarse/m_Feed;
15
16 % read in QICPIC-data from csv-file (cumulative distributions Q(x))
17 data=zeros(32,3);
18 data=csvread('Q_raw.csv');
19 x=data(:,1); % x in [µm]
20 Q_Fine=data(:,2); % Q in [%]
21 Q_Coarse=data(:,3); % Q in [%]
22
23 %interpolate between measured values to smooth cumulative distribution Q(x)
24 x_v=0:0.1:8000; % generate new x-vector for interpolation
25 iQ_Coarse=interp1(x,Q_Coarse,x_v,'spline'); %interpolate between measured values
26 iQ_Fine=interp1(x,Q_Fine,x_v,'spline'); %interpolate between measured values
27
28 % calculate differences dx and dQ within loop
29 for i=1:31
30     dx(i)=x(i+1)-x(i);
31     dQ_Fine(i)=Q_Fine(i+1)-Q_Fine(i);
32     dQ_Coarse(i)=Q_Coarse(i+1)-Q_Coarse(i);
33 end
34
35 % average x-values within loop
36 for i=1:31
37     xm(i)=(x(i)+x(i+1))/2;
38 end
39
40 %calculate density distributions
41 qd_Fine=dQ_Fine./dx;
42 qd_Coarse=dQ_Coarse./dx;
43 qd_Feed=c.*qd_Coarse+f.*qd_Fine;
44
45 % interpolate between measured values to smooth density distribution q(x)
46 x_n=1:0.1:8000; %new x-vector for interpolation
47 iqd_Fine = interp1(xm,qd_Fine,x_n,'spline'); %interpolation
48 iqd_Coarse = interp1(xm,qd_Coarse,x_n,'spline'); %interpolation
49 iqd_Feed = interp1(xm,qd_Feed,x_n,'spline'); %interpolation
50
51 %calculate separation efficiency T(x)
52 m_Feed_x=m_Feed.*qd_Feed;
53 m_Coarse_x=m_Coarse.*qd_Coarse;
54 T_x=m_Coarse_x./m_Feed_x;
55
56
57
58 x_s=1:0.1:1000;
59 iT_x=interp1(xm,T_x,x_s,'spline'); %interpolation
60
61
62 % plot commands
63
64 % cumulative distribution
65 figure
66 plot(x_v,iQ_Fine,'k')
67 hold on
68 plot(x_v,iQ_Coarse,'r')
69 legend('fine fraction','coarse fraction','Location','Northwest')
70 ylabel('Q_3 [%]')
71 xlabel('x [1/10^6 m]')
72 axis([0 500 0 100])
73 print -djpg Cumulative_distribution.jpg
74
75
76 % density distribution

```

```

77 figure
78 plot(x_n,iqd_Fine,'r')
79 hold on
80 plot(x_n, iqd_Coarse,'g');
81 plot(x_n, iqd_Feed,'k');
82 axis ([0 500 0 0.75])
83 xlabel ('x_m [1/10^6 m]')
84 ylabel ('q_3 (x)')
85 legend('Fines','Coarse','Feed')
86 hold off
87 print -djpg Density_distribution.jpg
88
89 % Tromp curve
90 figure
91 plot (x_s,iT_x,'k')
92 ylabel('T(x)')
93 xlabel('x [1/10^6 m]')
94 axis ([120 500 0 1])
95 print -djpg separation_efficiency.jpg
96
97 % find median cut diameter x50
98 a=2400;
99 for i=2400:3000
100     z(i)=iqd_Fine(i)-iqd_Feed(i);
101     z(i);
102     if z(i)>=0.001
103         a=a+1;
104     elseif z(i)<abs(0.001)
105         b=a;
106     endif
107 end
108
109 % display x50, q3 for control purpose
110 disp ("x_50 =", disp (x_n(b)))
111 disp ("q_3_fine =", disp (iqd_Fine(b)))
112 disp ("q_3_coarse =", disp (iqd_Coarse(b)))
113
114 %calculate classifier sharpness index kappa
115
116 f=300;
117 for i=300:length(iT_x)
118     if iT_x(i)<0.25
119         f=f+1;
120     elseif 0.251>iT_x(i)>0.249
121         f;
122     endif
123 end
124
125 disp ("x25 =", disp (x_s(f)))
126
127 g=300;
128 for i=300:length(iT_x)
129     if iT_x(i)<0.75
130         g=g+1;
131     elseif 0.751>iT_x(i)>0.749
132         g;
133     endif
134 end
135
136 disp ("x75 =", disp (x_s(g)))
137
138 disp ("Kappa =", disp (x_s(f)/x_s(g)))

```